

**DOKUZ EYLÜL UNIVERSITY
GRADUATE SCHOOL OF NATURAL AND APPLIED
SCIENCES**

**PROCESSING, CHARACTERIZATION AND
DEVELOPMENT OF RARE EARTH DOPED
LEAD MAGNESIUM NIOBATE
FERROELECTRIC CERAMIC CAPACITORS BY
SOL-GEL TECHNIQUE**

Mehmet Faruk EBEOĞLUGİL

**April, 2011
İZMİR**

**PROCESSING, CHARACTERIZATION AND
DEVELOPMENT OF RARE EARTH DOPED
LEAD MAGNESIUM NIOBATE
FERROELECTRIC CERAMIC CAPACITORS BY
SOL-GEL TECHNIQUE**

**A Thesis Submitted to the
Graduate School of Natural and Applied Sciences of
Dokuz Eylül University
In Partial Fulfillment of
the Requirements for the Degree of Philosophy of Doctora
in Metallurgical and Material Engineering**

**by
Mehmet Faruk EBEOGLUGIL**

**April 2011
İZMİR**

Ph. D. THESIS EXAMINATION RESULT FORM

We have read the entitled “**PROCESSING, CHARACTERIZATION AND DEVELOPMENT OF RARE EARTH DOPED LEAD MAGNESIUM NIOBATE FERROELECTRIC CERAMIC CAPACITORS BY SOL-GEL TECHNIQUE**” completed by **MEHMET FARUK EBEOĞLUGİL** under supervision of **PROF. DR. ERDAL ÇELİK** and we certify that in our opinion it is fully adequate, in scope and in quality, as a thesis for the degree of Doctor of Philosophy



Prof. Dr. Erdal ÇELİK

Supervisor



Prof. Dr. İbrahim AVGIN

Thesis Committee Member



Assoc. Prof. Dr. Mustafa TOPARLI

Thesis Committee Member



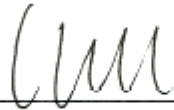
Prof. Dr. İskender İSİK

Examining Committee Member



Prof. Dr. Tevfik AKSOY

Examining Committee Member



Prof. Dr. Mustafa SABUNCU

Director

Graduate School of Natural and Applied Science

ACKNOWLEDGMENTS

First of all, I would like to express my deep sense of gratitude to my advisor Prof. Dr. Erdal ÇELİK for his constructive ideas, help, constant support, guidance and contributions during my PhD research. I would also like to thank my committee members, Prof. Dr. İbrahim AVGIN and Assoc. Prof. Dr. Mustafa TOPARLI for reviewing my work and offering valuable suggestions and sharing their visions about the content of my thesis.

I wish to extend my sincere thanks to Prof. Dr. Tevfik AKSOY, Prof. Dr. Kazım ÖNEL, Prof. Dr. Akın ALTUN and Assoc. Prof. Dr. Bülent ÖNAY, for sharing their valuable knowledge with me in starting lectures in our department. I am especially indebted to Işıl BİRLİK, Esra DOKUMACI, Erhan ÖZKAN, Mustafa EROL, Dr. Süleyman AKPINAR, Dr. Osman ÇULHA, Dr. İ. Murat KUŞOĞLU, Assist. Prof. Dr. Bahadır UYULGAN, and Assist. Prof. Dr. Funda AK AZEM for all of the assistance that they provided me in the times of need. In addition, I would like to thank Şafhak TURAN, Murat ALPASLAN, Burçin VARGEL, Haydar KAHRAMAN, Nihal ALTUĞ and Yiğitalp OKUMUŞ for their invaluable assistance and kind friendship. I would also like to express my genuine gratitude to each of people, although it would be impossible for me to name all.

The successful completion of this work has been aided by a number of people at Dokuz Eylül University. I would like to thank Assist Prof. Dr. Aylin ŞAKAR DELİORMANLI at Celal Bayar University. I would like also thank to The State Planning Organization (DPT), entitled “Processing, development and characterization Lead Magnesium Niobate based ferroelectric ceramic capacitors” for supporting during this study.

A special thank goes to my family for their concern, confidence and support. Finally, I extend my greatest thanks to my wife *Nilüfer* who unconditionally supported me. The successful completion of this study would not have been possible without her constant love and encouragement.

M. Faruk EBEOĞLUGİL

**PROCESSING, CHARACTERIZATION AND DEVELOPMENT OF RARE
EARTH DOPED LEAD MAGNESIUM NIOBATE FERROELECTRIC
CERAMIC CAPACITORS BY SOL-GEL TECHNIQUE**

ABSTRACT

The present thesis demonstrates synthesis, characterization and electrical properties of relaxor ferroelectric pure Lead Magnesium Niobate (PMN) and Rare Earths (RE) (Er, Eu, Dy, Sm and Tb) doped nano scale powders and PMN thin films on n-type Si substrates using sol-gel technique for capacitor applications. With this respect, transparent solutions were prepared from Pb, Mg and Nb based precursors, methyl alcohol and glacial acetic acid (GAA). The obtained solutions were dried at 80 degree celcius for 60 minutes in air to form gel structure of PMN mixture and heat treated at 530 degree celcius for 3 hours and consequently annealed at 950 degree celcius for 2 hours in air. After the sintering, the PMN powders were milled for 12 hours at room temperature to obtain PMN based nano scale powders. Finally, the powders were dispersed in alcohol and the obtained suspensions were deposited on n-type Si substrates using drop and spin coating systems and then annealed at 730 degree celcius for 1 hour in air. Thermal, structural, microstructural, optical, mechanical and electrical properties of the powder and the coatings were characterized through differential thermal analysis-thermogravimetry (DTA-TG), Fourier transform infrared (FTIR), X-ray diffraction (XRD), scanning electron microscopy-energy dispersive spectroscopy (SEM-EDS), atomic force microscopy (AFM), dynamic ultra hardness tester (DUH), scratch tester, refractometer, spectrophotometer, high resolution dielectric analyzer machines and Keithley 2400 for current-voltage characterization. The results showed that it was possible to produce the perovskite phase PMN based thin films at 730 degree celcius using sol-gel derived powder precursor suspension method. The optimum capacitor films were successfully applied to a light emitting diode (LED) flash device for camera for very low filling and draining time (17 ms).

Keywords: PMN, suspension, dielectric, thin film, LED flash

**SOL-JEL TEKNİĞİ KULLANILARAK NADİR TOPRAK KATKILI
KURŞUN MAGNEZYUM NİYOBAT FERROELEKTRİK SERAMİK
KAPASİTÖRLERİN ÜRETİMİ, KARAKTERİZASYONU VE
GELİŞTİRİLMESİ**

ÖZ

Bu tez, kapasitör uygulamalarına sol-jel tekniği kullanılarak elde edilen saf Kurşun Magnezyum Niyobat (PMN) ve Nadir Toprak (Er, Eu, Dy, Sm ve Tb) katkı nano ölçekli tozların ve n-tipi Si altlıklar üzerine kaplanan PMN ince filmlerin relaksör ferroelektrik olarak sentezlenmesi, karakterizasyonu ve elektriksel özelliklerini içermektedir. Bu anlamda, şeffaf solüsyon Pb, Mg ve Nb bazlı başlangıç malzemeleri, metil alkol ve glasiyel asetik asit kullanılarak hazırlanmıştır. Solüsyonlar jel yapılı PMN karışımı oluşturmak için 80 santigrat derecede 60 dakika kurutulmuş ve hava ortamında 530 santigrat derecede 3 saat, 950 santigrat derecede 2 saat ısıtım işlemi yapılmıştır. Sinterlemeden sonra, PMN bazlı nano ölçekli tozlar elde etmek için PMN tozları oda sıcaklığında 12 saat öğütülmüştür. Son olarak, tozlar alkol içerisinde dağıtılmış ve elde edilen süspansiyon damlatma ve spin kaplama teknikleri ile n- tipi Si üzerine kaplanmıştır. Kaplamalara hava ortamında, 730 santigrat derecede, 1 saatte tavlama işlemi uygulanmıştır. Toz ve kaplamaların ısıtım, yapısal, mikroyapı, optik, mekanik ve elektriksel özellikleri diferansiyel termal analiz-termogravimetri (DTA-TG), Fourier transform infrared (FTIR), X-ışını saçınımı (XRD), taramalı electron mikroskop-enerji dağılım spektroskopisi (SEM-EDS), atomic kuvvet mikroskobu (AFM), dinamik ultra sertlik (DUH), kazıma, kırılma indisi, spektrofotometre, yüksek çözünürlüklü dielektrik analiz and akım-voltaj karakterizasyonu için Keithley 2400 cihazları kullanılarak karakterize edilmiştir. Sonuçlar, perovskit faza sahip PMN bazlı ince filmlerin 730 santigrat derecede sol-jel tekniği ile elde edilen tozların süspansiyonu metodu kullanılarak üretilmesinin mümkün olduğunu göstermiştir. En uygun kapasitör filmler fotoğraf makinelerinde kullanılan ışık saçınımı diot (LED) flaş devresinde çok düşük dolma-boşalma süresinde (17 ms) başarılı bir şekilde uygulanmıştır.

Keywords: PMN, süspansiyon, dielektrik, ince film, LED flaş

DEDICATION

To Nilüfer,

My Son Mehmet Abdullah and Daughter Meva Saliha

CONTENTS

	Page
THESIS EXAMINATION RESULT FORM	ii
ACKNOWLEDGEMENTS	iii
ABSTRACT	iv
ÖZ	v
CHAPTER ONE-INTRODUCTION	1
1.1 Organization of the Thesis	11
CHAPTER TWO-THEORETICAL BACKGROUND	13
2.1 Relaxors	14
2.2 Perovskite Structure	15
2.3 Lead Magnesium Niobate	16
2.4 Properties of PMN Produced by Different Techniques.....	21
2.4.1 PMN by Solid State Reactions.....	21
2.4.2 PMN by Sol-Gel Technique.....	23
2.5 Sol-Gel Technique.....	32
2.5.1 The Chemistry of Precursors Solution	32
2.5.2 Hydrolysis and Condensation Reaction	33
2.5.3 Thermodynamics of Nucleation and Crystal Growth	35
2.5.4 Gelation	38
2.5.5 Drying	43
2.5.6 Sintering	46
2.5.6.1 Possible Texture Evolution	47
2.5.6.2 Atomic Transport Mechanisms Operating During Sintering	49
2.5.6.2.1 Atomic Diffusion in Sol-Gel Materials.....	49
2.5.6.2.2 Sintering and Crystallization in Sol-Gel Ceramics.	50
2.6 Milling and Equipment.....	51

2.6.1 Purpose of Milling and Materials.....	51
2.6.2 Dry Milling	52
2.6.2.1 Jaw Crushers	52
2.6.2.2 Roll Crushers.....	53
2.6.3 Milling.....	53
2.6.3.1 Ball Cilling	53
2.6.3.2 Jet Mills	55
2.6.4 Wet Milling	55
2.6.5 Equipments of Mills.....	56
2.6.5.1 Jar Mills.....	56
2.6.5.2 Porcelain Mills	56
2.6.5.3 High Alumina Jar Mills.....	57
2.6.5.4 High Purity Ceramic Mills	58
2.6.6 Milling Media	60
2.6.6.1 Type of Media	60
2.6.6.2 Size and Shape	60
2.6.6.3 Filling	61
2.6.6.4 Milling Rate	61
2.6.6.5 Mill Type.....	61
2.6.6.6 Media Size.....	61
2.6.6.7 Specific Gravity	62
2.6.6.8 Media Wear	62
2.6.7 Mill Racks	65
2.7 Colloidal Processing of Ceramics	68
2.7.1 Ultrasonic Dispersing and Deagglomeration	69
2.7.2 Origin of Surface Charge in Water	70
2.7.3 Interactions in Colloidal Suspensions	72
2.7.4 Van der Waals Interactions	73
2.7.5 Electrostatic Interactions	74
2.7.6 The DLVO Theory	76
2.7.7 Steric Stabilization	77
2.7.8 Depletion Interactions	81

2.8 Coating Techniques	82
2.9 Dielectric Phenomena.....	85
2.9.1 Ferroelectric Materials	89
2.9.2 Conduction Mechanisms in Metal-Dielectric Systems	91
2.9.3 Reverse Bias Schottky Emission.....	93
2.9.4 Poole-Frenkel	94
2.9.5 Fowler-Nordheim (FN) Tunneling.....	95
2.10 Some Application for Capacitor.....	96
2.10.1 Electronic filter	96
2.10.2 Defibrillator.....	96
2.10.3 Flash of Camera	97

CHAPTER THREE-EXPERIMENTAL STUDIES..... 99

3.1 The Aim of Thesis	99
3.2 Materials	100
3.2.1 Substrate Preparation	100
3.2.2 Precursor Materials	101
3.2.3 Device Elements	103
3.2.3.1 Transformator:.....	104
3.2.3.2 Resistance:.....	105
3.2.3.3 Transistor:	106
3.2.3.4 Xenon lamp:	106
3.2.3.5 Diode:	106
3.3 Production Techniques	107
3.3.1 Powder Preparation	107
3.3.2 Ball Milling	111
3.3.3 Colloidal Suspension Preparation	113
3.3.4 Coating Process	114
3.3.4.1 Spin Coating.....	114
3.3.4.2 Drop Coating.....	116
3.3.5 Heat Treatment.....	117

3.4 Characterization.....	119
3.4.1 Solution Characterization.....	119
3.4.1.1 pH Measurement.....	119
3.4.1.2 Turbidity Measurement.....	120
3.4.1.3 Rheometer.....	121
3.4.1.4 Fourier Transform Infrared Spectropy (FTIR).....	121
3.4.2 Material Characterization.....	124
3.4.2.1 Differential Thermal Analysis-Thermal Gravimetric Analysis (DTA-TGA).....	124
3.4.2.2 Particle Size Analyser.....	126
3.4.2.3 X-Ray Diffractometer (XRD).....	127
3.4.2.4 Scanning Electron Microscopy (SEM)/ Energy Dispersive X-ray Spectroscopy (EDS).....	128
3.4.2.5 Atomic Force Microscopy (AFM).....	129
3.4.2.6 Dynamic Ultramicro Hardness (DUH).....	130
3.4.2.7 Scratch Testing Machine.....	132
3.4.2.8 Refractometer.....	134
3.4.2.9 Spectrophotometer.....	135
3.4.2.10 Impedance Measurement.....	135
3.4.2.11 I-V measurement.....	146
3.5 Design and Production of Electronic Devices.....	149

CHAPTER FOUR-RESULT AND DISCUSSION 151

4.1 Solution Characteristics.....	151
4.1.1 pH Results.....	151
4.1.2 Turbidity Results.....	152
4.1.3 Rheological Properties.....	153
4.1.4 Hydrolysis and Condensation Reactions.....	156
4.2 Process Optimization.....	159
4.2.1 Thermal Analysis.....	162
4.2.2 FTIR Analysis.....	166

4.3 Phase Analysis.....	175
4.4 Powder analysis	194
4.5 Microstructure Analysis	195
4.5.1 SEM-EDS Analysis.....	195
4.5.2 AFM Analysis	211
4.6 Mechanical Properties	216
4.6.1 DUH Analysis	216
4.6.2 Adhesion Properties	217
4.7 Optical Properties	219
4.8 Dielectric Properties	219
4.9 Current- Voltage (I-V) Characteristics.....	232
4.10 Device Applications	236
4.10.1 Example Circuit Diagram	238
4.10.2 Camera Flash Circuit	238
4.10.3 Durability of the production.....	239
CHAPTER FIVE-CONCLUSION AND FUTURE PLAN	241
REFERENCES.....	247

CHAPTER ONE

INTRODUCTION

With the advancement of several technologies such as nanotechnology, biotechnology and information technology, a growing interest has been emerging for smart materials. Smart material systems are non-living systems which integrate the functions of sensing, actuation, logic and control to respond adaptively to various changes in a useful and repetitive manner. Smart materials could be passive, responding to external change in a useful manner without assistance or they could be active with feedback capabilities (Deliormanli 2007, Lane and Craig 2000, Newnham & Ruschau 1991, Prasad et al. 1998, Su et al. 2001)

The piezoelectric and electrostrictive materials are smart materials and they can convert electrical energy into mechanical energy, or vice versa (Jordan and Qunaies 2001). Lead magnesium niobate, $\text{Pb}(\text{Mg}_{1/3}\text{Nb}_{2/3})\text{O}_3$ (PMN) is an electrostrictive material that is characterized by a diffuse phase transition over a broad temperature range and a frequency dependent maximum in its relative dielectric permittivity. It is a relaxor ferroelectric such that the term relaxor refers to the significant decrease in dielectric constant with increasing frequency and it demonstrates very high dielectric constant around -10 to -5 °C (Fengbing et al. 2004, Kwon et al. 2001, Heartling 1999). Electrostrictive PMN, like piezoelectrics, exhibits a dimensional change upon the application of an applied electric field or electric polarization when mechanical stress is applied. However, it also exhibits a non linear response as opposed to the linear response of other piezoelectrics such as lead zirconate titanate, $\text{Pb}(\text{Zr}_{0.48}\text{Ti}_{0.52})\text{O}_3$ (PZT) and lead titanate, PbTiO_3 (PT). Electrostrictive materials have almost no hysteresis, a quick response time and high displacements with good reproducibility. These properties make them desired materials for micro-positioner and adaptive optic applications (Deliormanli 2007, Fanning 2000, Shankar and Hom 2000 & Tzou et al. 2004).

PMN based materials are important for applications in multilayer capacitors, actuators and electro-optic devices because of their high dielectric constants, excellent voltage stabilities, good electrostrictive effect and lower sintering temperatures (Kong et al, 2001). The use of PMN ceramics in various applications requires the use of different forms such as thin and thick films, fibers, composites or sintered bodies. In industry, colloidal powder processing is the predominant fabrication method to produce these electroceramic devices (Dogan 2000, Huei & Smay et al. 2002, Lewis 2006 & Luo 2005).

It is well known that single-phase perovskite $(1-x)\text{PMN}-x\text{PT}$ is very difficult to prepare via the conventional solid-state reaction. Several methods such as the two-step columbite, co-precipitation, sol-gel, gel combustion and molten salt have been developed to prepare pyrochlore-free $(1-x)\text{PMN}-x\text{PT}$. More recently, PMN and PMN-PT powders with nanometer size were successfully synthesized via mechanochemical process, the advantage of which is that it can be used to synthesize powders with nano-size scale at room temperature (Kong et al, 2001).

The sol-gel technique offers several advantages for the preparation of ceramic oxides. This method provides high degree of homogeneity and stoichiometry especially for multicomponent systems in addition to allowing doping on a molecular scale. Hence, there is considerable interest in the preparation of PMN ceramics using sol-gel method. The phase formation and electrical properties of piezoelectric ceramics can be easily modified by dopant materials using sol-gel technique. Effects of rare earth elements (RE) doping on the phase formation and electrical properties of piezoelectric ceramics such as barium titanate and lead zirconate titanate are well studied (Deliormanli 2007). The effect of RE addition on the PMN system has also been studied in the literature. Zhong et al. studied the effects of adding a fixed amount of rare earth additives on the microstructure and dielectric properties of PMN-PT ceramics. Their results showed that doping of neodymium (Nd^{+3}) resulted in a slight decrease in the grain size and a lowering of the dielectric constant. In addition to this, effect of lanthanum (La^{+3}) additions on the phase formation of PMN ceramics was demonstrated. The former study indicated that the presence of La^{+3}

cations implied an increase in the short range ordering, resulting negative space-charge balance into the ordered domains in PMN (Branileau et al 2004 & Bhat et al 2005, Kim et al 1991).

In the majority of these reported studies, it is observed that the influences of RE addition into PMN have been studied at fixed RE contents using solid state reactions. With this respect, no published work on the effect of Europium (Eu), Erbium (Er), Dysprosium (Dy), Samarium (Sm) and Terbium (Tb) dopants in the PMN system has been encountered. Generally speaking, perovskite PMN powders were synthesized using a straight forward sol-gel method at room temperature. Hydrolysis conditions as the hydrolysis ratio were observed to influence the phase formation. The structures including %1-20 pyrochlore were obtained by calcination at 950 °C for 2 hours in a lead-rich atmosphere.

As for fabrication of ceramic powders in nano size, high-energy ball milling, which is also known as the mechanical alloying, has been successfully used to produce not only alloys which are non-equilibrium at high temperature but amorphous metals as well. The process has also been used as a vehicle for the solid state reaction. More recently, this mechanochemical ball milling has been employed as a method to synthesize materials for various applications, such as nanocrystalline oxide powders, solid state solutions of ceramics, nanoparticles of the $\text{YBa}_2\text{Cu}_3\text{O}_{7-\delta}$ superconductor, Ni-Zn and barium ferrites, and lead titanate powders (Kong et al, 2001). The advantage of using the high-energy ball milling technique is that it can be used to synthesize the desired compound on a nano-size scale at room temperature. The formation at room temperature is desirable for the synthesis of lead containing materials because the loss of lead can be effectively avoided. However, preparation of ceramic powders needs a long ball milling time (Kong et al, 2001).

The dispersing and deagglomeration of solids into liquids is an important application of ultrasonic devices. Ultrasonic cavitation generates high shear that breaks particle agglomerates into single dispersed particles. The mixing of powders into liquids is a common step in the formulation of various products, such as paint,

ink, shampoo, beverages, or polishing media. The individual particles are held together by attraction forces of various physical and chemical nature, including van der Waals forces and liquid surface tension. This effect is stronger for higher viscosity liquids, such as polymers or resins. The attraction forces must be overcome in order to deagglomerate and disperse the particles into liquid media. The application of mechanical stress breaks the particle agglomerates apart. In addition to this, liquid is pressed between the particles. Different technologies are commonly used for the dispersing of powders into liquids. This includes high pressure homogenizers, agitator bead mills, impinging jet mills and rotor-stator-mixers. High intensity ultrasonication is an interesting alternative to these technologies. This applies mechanical stress on the attracting electrostatic forces (e.g. van der Waals forces). Ultrasonic cavitation in liquids causes high speed liquid jets of up to 1000 km/h (approx. 600 mph). Such jets press liquid at high pressure between the particles and separate them from each other. Smaller particles are accelerated with the liquid jets and collide at high speeds. This makes ultrasound an effective means for the dispersing and deagglomeration but also for the milling and fine grinding of micron-size and sub micron-size particles (WEB1).

Of the three most common passive components in electronic circuitry, resistors, capacitors, and inductors, it is the capacitor that generally dominates the majority of components and printed circuit board space. As an example, the Nokia 6161 cell phone has a 40 cm² circuit board with 15 integrated circuits (ICs), 149 resistors, 24 inductors, and 232 capacitors (Ulrich et al. 2003). The capacitors range in value from 1 to 10 nF. In addition to stand alone devices that are attached separately to complete a circuit board, capacitors are also integrated into standard IC fabrication procedures to produce gate circuitry (Kim et al. 2005 & Lu et al. 1999), dynamic random access memory (DRAM) (Ding et al. 2000, Shaw et al. 2000), microwave electronics (Ding et al. 2000, Morito et al. 2005 & Tsao et al. 2000), and general integrated passives (Aparicio, et al. 2002 & Vayunandana et al. 2007). For DRAM chips at the 1 Gbit level, capacitors are needed with lateral dimensions in the 0.13 μm range with thicknesses between 5 and 30 nm (Shaw et al. 2000). On this front, Motorola, Inc. appears to be leading the commercial field with integrated resistors and capacitors in

many of its newer cell phones (Ulrich et al. 2003). Several Japanese companies are also continuing this trend, and are beginning to introduce products that take advantage of the integrated passives approach. In commercial research, DuPont is developing processes that show potential to produce integrated passives with over 100 nF/cm^2 capacitance, which would be high enough to replace many of the discrete capacitors that currently have to be soldered onto a circuit board (Daniels, et al. 1996 & Ulrich et al. 2003).

Sol-gel technique is commonly employed processes to produce thin and thick films for microelectronic applications. Driving this trend toward integrated passives is the continued development of thin ceramic films with thicknesses between 0.5 and $2 \mu\text{m}$ (Tsao et al. 2000). As these thicknesses are on the same scale as many microstructural characteristics such grain size, ferroelectric domains, and even the electrode interfaces (Daniels, et al. 1996 & Shaw et al. 2000), it can become difficult to ensure property uniformity on a local scale when the device size also continues to decrease. The favored commercial fabrication technique of ceramic capacitors, tape-casting, has advanced over the past 10 years to allow the reliable fabrication of $0.8 \mu\text{m}$ thick dielectrics ($0.5 \mu\text{m}$ thickness on research scales), but has not been able to definitively show that it will be capable of extending its use to thicknesses to $0.2 \mu\text{m}$ and below (Nagata, et al. 2006). This limitation has opened the way for a variety of other thin film deposition methods to be introduced to the field of capacitor research and development.

As dielectric films continue to decrease in thickness due to advances in chemical vapor deposition, physical vapor deposition and sol-gel processing, it becomes increasingly important to control the microstructure to ensure property uniformity. As films become thinner, both intrinsic (i.e. directional response of a single ferroelectric domain) and extrinsic (i.e. phase boundaries, defect densities, etc.) properties become more pronounced (Shaw et al. 2000). Intrinsic size effects result in a ferroelectric transition shift to lower temperatures, a broadening of the temperature dependence of the permittivity (e.g. the development of a Curie region as opposed to a Curie peak), and a drop in the peak permittivity. Extrinsic size effects

have been observed to account for 60 % to 70 % of the dielectric property values in some of the common perovskite materials, and vary depending on the deposition method and chosen materials.

The current challenge for thin film capacitors is the fabrication of devices that exhibit high capacitance, possess high voltage capabilities, and have both high electrical stability and high temperature capability (Nielsen, et al. 1998 & Tsao et al. 2000) all while retaining a compact size and using materials and deposition techniques that are compatible with the materials and processes already in use in standard IC fabrication facilities (Ulrich et al. 2003). For portable power devices (i.e. secondary power supplies, electric vehicles, or battery replacements), capacitors also need to exhibit long life cycles (>100,000 cycles), short charging times in ms to ns range, be safe for consumer handling (simple, robust design), and have a high power density (Lufrano, et al. 2003). For any capacitor technology to be accepted for commercial application, it must exhibit:

- High permittivity (maximized based on material to result in an associated high capacitance density) (Nielsen, et al. 1998)
- High breakdown strength (greater than 1×10^6 V/cm for maximum power density) (Nielsen, et al. 1998)
- Low dielectric loss tangent ($\tan \delta = d$ needs to be at least less than 0.05) (Nagata, et al. 2006)
- Low leakage current density ($< 1 \mu\text{A}/\text{cm}^2$ at 10V) (Nielsen, et al. 1998)
- Low failure rates (2.4 failures or less in 10^9 component hours) (Nielsen, et al. 1998)
- Minimal temperature variance ($\pm 15\%$ or less between 55°C and 125°C) (Nielsen, et al. 1998)

Three capacitor designs are currently used in the electronic industry: in-plane or single layer, electrolytic, and multi-layer capacitors (MLCs). Each design's capacitance can be calculated using:

$$C = \epsilon_0 \epsilon_r (A/d) \tag{1.1}$$

where ϵ_0 is the permittivity of free space (8.854×10^{-12} F/m), ϵ_r is the permittivity of the dielectric material (also referred to as the dielectric constant, k), A is the interaction area of the electrodes (m^2), and d is the distance between the electrodes (m). In-plane capacitors attempt to maximize the capacitance by using large permittivity dielectrics, minimizing layer thicknesses, and increasing the electrode area by rolling the structure into a cylindrical configuration. This simple design allows easy manufacturing, but limits the maximum possible capacitance density by not taking advantage of a 3-dimensional construction methodology. Electrolytic devices maximize the capacitance by significantly increasing the electrode area with porous electrodes submerged within an electrolyte. The drawbacks of electrolytic capacitors are: (1) the distance between the electrodes is set by the conductivity of the electrolyte and tends to be larger than is possible with a solid dielectric, and (2) the use of a liquid electrolyte requires hermetic sealing of the capacitor which precludes the use as an integrated device (Albina, et al. 2007).

MLCs maximize device capacitance by using high permittivity dielectrics (maximizing ϵ_r), minimizing the dielectric thickness (d), and increasing the electrode area (A) by alternating stacks of anode, dielectric, cathode, dielectric, anode, etc. Of the three designs discussed, MLCs are generally able to produce the highest capacitance density due to the use of a 3-dimensional structure that is not inherently limited by dielectric thickness (Moya, et al. 2007). As such, MLCs are the most popular for use in the electronics industry (Nielsen, et al. 1998, Moya, et al. 2007, Pecharroman, et al. 2001) with an estimated 10^{12} units made annually as of 2006 (Nagata, et al. 2006). At present, most commercial MLCs are prepared by tape casting using dispersions of submicron ceramic powders with screen printed metal electrodes that are laminated, co-fired, and terminated with metallic paint (Nagata, et al. 2006). Tape casting, however, has been found to be impractical and not cost efficient for the fabrication of devices with layer thicknesses on the nano-meter scale (Deliormanli 2007, Nagata, et al. 2006 & Ulrich et al. 2003).

Thin film technology allows the optimization of the MLC design to be taken even further with the ability to reliably decrease the dielectric thicknesses into the

nanometer range, thus surpassing traditional tape casting technology. As this thickness minimization occurs, multiple benefits in addition to an increase in capacitance are likely to be seen. Inasmuch as the average AC current path is shorter with thinner films, a smaller series inductance is likely to be measured making a more efficient capacitor with a higher self-resonant frequency (Aparicio, et al. 2002, Itagaki, et al. 2007). A smaller active area also translates to shorter metal lengths, which in turn gives a lower series resistance, and subsequently lower power consumption/loss. On the other hand, as the device areas approach the same size scale as microstructural features (i.e. grain size and/or domain size), the devices are likely to be more susceptible to fractional variations in the measured capacitance (Aparicio, et al. 2002).

Thin film technologies also allow the opportunity to create complex electrode patterns, such as micro-scale fractal patterns, that are not feasible with screen printing technology. By exploiting not only the vertical field components (e.g. minimizing the thickness) but also the lateral, or in-plane, electric field components it is possible to increase the capacitance density even further than with a standard MLC approach (Aparicio, et al. 2002). The capacitance of a device with patterned electrodes can be calculated as:

$$C_{\text{total}} = C_x + C_y + C_z \quad (1.2)$$

$$= \epsilon_0 \epsilon_r [(L_{x,\text{min}}(L_{x,\text{min}} + W_{x,\text{min}}))^{-1} + (L_{y,\text{min}}(L_{y,\text{min}} + W_{y,\text{min}}))^{-1} + (t_{\text{ox}}(t_{\text{ox}} + t_{\text{metal}}))^{-1}]$$

where $L_{x,\text{min}}$ and $L_{y,\text{min}}$ are the minimum in-plane, lateral spacing between the electrodes, $W_{x,\text{min}}$ and $W_{y,\text{min}}$ are the in-plane widths of the metal electrodes, and t_{ox} and t_{metal} are the dielectric and metal thicknesses, respectively. Comparison of theoretical 3-dimensional structures to a standard MLC design has been done by Aparicio (Aparicio, et al. 2002). According to this work, with a dielectric and electrode thickness of 800 nm, the minimum feature sizes (L and W) needed to make complex electrodes more efficient than a standard parallel plate design is between 0.8 μm and 1.0 μm depending on the electrode design used. These feature sizes are well within the capability of standard micro-fabrication facilities, and show promise for

further increasing the maximum capacitance density achievable with thin film technologies.

A wide variety of techniques have been investigated for the deposition of thin ceramic films including chemical vapor deposition (CVD), sol-gel, magnetron sputtering, pulsed laser deposition, among several others. Each process has a set of associated advantages and disadvantages, and any process must be chosen particularly with the disadvantages in mind. Observed size effects associated with varying the dielectric thickness are process dependent. Different deposition processes as well as different processing conditions within each process category are likely to result in different properties in the material adjacent to the electrodes, which in turn contributes to the scatter seen in the experimentally measured size effects on the dielectric properties (Shaw et al. 2000). This is in addition to the differences with the microstructure (e.g. density, grain size, morphology, etc.) of the deposited film from different processes. Based on the literature, it appears that the size effects are controlled more by processing rather than any intrinsic limits on material stability.

Table 1.1 clarifies a brief summary of the more popular thin film deposition techniques and some of the advantages and disadvantages of them. All of the processes have been utilized with success in multiple literature sources. Therefore, the choice in deposition technique must be made with a certain set of constraints. For this research a low deposition temperature was highly desirable due to the prevalence of temperature related issues resulting in cracking or delamination of films during cooling (Wu, et al. 2001 & Yokota, et al. 1998). A process was also desirable that exhibited a large degree of control over film stoichiometry, thickness, uniformity, and step coverage.

Of the above techniques, the majority of research efforts have used CVD and sputtering technologies. CVD techniques, in particular metal-organic CVD (MOCVD), tend to provide excellent composition control with good potential for film homogeneity and conformal coatings of complicated topographies (Tombak, et al. 2003). These benefits have resulted in CVD being regarded as producing the

“highest quality” dielectric films (Laughlin, et al. 2004 & 2005). Unfortunately, CVD methodologies tend to require costly instrumentation and materials and are known for complex process schedules (Laughlin, et al. 2004 & 2005). CVD is also typically performed in a batch process, making the technology less favored for mass production of devices.

Table 1.1 Thin film deposition techniques with associated advantages and disadvantages

Deposition Technique	Advantages	Disadvantages
Magnetron Sputtering	Controllable composition	Many process parameters
	Thin, conformal coatings	Requires vacuum
	Low deposition temperatures	Non-selective coating
Chemical Vapor Deposition	Selective coating	Exotic chemicals
	Low temperatures possible	Thick, rough coatings
	Multiple assisted technologies	Limited coating
Sol-Gel	Conformal coatings	High temperatures
	Ease of processing	Multiple temperature

Comparatively, sputtering requires substantially more simplified equipment (Laughlin, et al. 2005), and the process schedule is generally less complex (Laughlin, et al. 2004). The technique is also capable of producing thin ceramic films with comparable properties to those derived from CVD methods (Laughlin, et al. 2005, Laughlin, et al. 2004) and are generally more reproducible (Tsao et al. 2000, Morito et al. 2005, Stamate, et al. 2003). The process variables of sputtering allow superior residual stress control by modifying the interaction of the energetic particles bombarding the surface of the substrate (Morito et al. 2005), which is effective for avoiding stress-induced mechanical peeling and thus increasing interlayer adhesion between the film and substrate as well as between individual layers of a stacked structure (Morito et al. 2005, Hsi, et al. 2003). Besides, sputtering can be performed at room temperature, potentially allowing the avoidance of high temperatures (Alexandrov et al. 1996, Kim et al. 2005, Kim, et al. 2003, Lin, et al. 2005). Sputtering is commonly used in most IC fabrication facilities resulting in a high potential for mass production, despite being a batch process that is not seen with most of the other deposition techniques (Morito et al. 2005).

Sol-gel method has been widely used in ceramic processing owing to its low cost and simplicity with very good stoichiometry control. Usually metal organic salts are dissolved in small molecule solvents to form a solution which may gel upon heating or shelving. In the case of PT, similarly with PMN, commonly used salts include lead acetate and titanium tetrapropyl and titanium isopropoxide; solvents are usually acetic acid, citric acid (CA), ethylene glycol (EG), or 2-propanol, etc (Luo 2005). Using sol-gel method, many ceramic films can be fired and sintered at much lower temperatures than their bulk counterparts processed by powders. The crystallization temperature for PT from sol-gel is generally in the range of 450~800°C, where many kinds of substrates can be used, such as Si wafer, metal or even low-melting temperature glass slides. For example, ferroelectric PT thin films were obtained on glass substrate from a sol-gel solution after 500°C heat treatment (Cheng et al 2000 & Luo 2005). Thin ceramic films derived from sol-gel are usually tens to hundreds of nanometers thick, similar to those by chemical vapor deposition (CVD). For comparison, those made by suspension method deposition or tape casting, where submicron- or micron-sized powders are involved, are 1 μm ~1 mm thick (Luo 2005).

1.1 Organization of the Thesis

The primary purpose of this thesis is to convey insight into preparation, characterization, development and application of PMN based nanoparticles and films using as a combination of colloidal suspension and deposition methods such as spin and drop coating systems using sol-gel technique. The approach is to explore both the science and technology of how RE dopants influence PMN structure and connect the results to materials properties, and show the engineering concepts that can be used to produce or improve an electronic device by design.

With this context, chapters can be explained in details. Chapter one provides a brief introduction to the area of research and the research objectives of this thesis. In Chapter two, a comprehensive literature review concerning relaxors, perovskite structure, PMN's properties, sol-gel technique, milling system, colloidal processing, coating methods, dielectric phenomena and some applications of capacitor is presented in details. Chapters three, the experimental procedures of PMN with RE

dopants are explained. In Chapter four, the results concerning pure PMN and effect of RE dopants on the stability of PMN structure are demonstrated and discussed in details. Characterization of pure PMN and RE doped PMN powders and thin films and their effect on the electrical properties of PMN is also analyzed in the same chapter. In addition, the optimum PMN based samples were used in electronic applications such as flashing and light emitting diode (LED) devices control depending on PMN capacity. The conclusion and future plans are summarized in Chapter five.

CHAPTER TWO

THEORETICAL BACKGROUND

Ferroelectric ceramics are traditionally made from powders formulated from individual oxides as discussed in the previous chapter, however sol-gel, chemical co-precipitation, reaction sintering (Lion 2004), spray pyrolysis (Marx & Huebner 1995), semi wet hydroxide method (Mohan et al.2001), combustion synthesis (Narendar & Messing 1997) and hydrothermal techniques are utilized in production of the newer materials. The processing method that one selects to prepare the powder depends to large extent on cost but even more important is the final application (Haertling 1999). A sintering temperature of 1200 °C is needed to produce PMN based materials as a dense ceramic part. At this sintering temperature, PbO is very volatile. The volatile nature of PbO could cause imprecise composition and deteriorates the properties of final product. Also, too much PbO evaporation is very harmful to the environments. Furthermore, at such a high sintering temperature, expensive electrode materials such as Pt or Pd have to be used in Multi-Layer-Capacitor (MLC) industry instead of the cheaper Ag and Cu electrodes. In order to use Ag and Cu as electrodes, the sintering temperature cannot be higher than 1000 °C.

Targeting to decrease the sintering temperature and reduce the processing steps, several processing methods have been investigated. For instance, it was found that an excess of 5-21 wt% of PbO could decrease the sintering temperature to 950 °C. 1-4 at% of SrO doping would result in the sintering temperature to be as low as 800-900 °C (Yang et al.2001).

By using thermal spray, pre heat-treatment, and reactive sintering, the sintering temperature could be decreased to 1050 °C. Liou et al found that directly pressing the columbite phase and PbO into green bodies and reactively sintering it could reduce the total processing steps of PMN dense part to 2 steps of ball millings, 1 step of calcination, and 1 step of sintering. Nevertheless, the sintering temperature of this

method was 1250 °C. Later, with the same method, Kwon et al succeeded in reducing the sintering temperature to 1000 °C by using nano size TiO_2 , more reactive $(\text{PbCO}_3) \cdot 2\text{Pb}(\text{OH})_2$ instead of PbO and O_2 sintering atmosphere.

Supon and Thomas (1998) synthesized the PMN powders using modified two stage mixed oxide route. According to their results, PMN ceramics with high density and optimized dielectric properties may be produced by use of a sintering method employing platinum foil and a PMN atmosphere powder. Furthermore, straightforward sintering conditions are appropriate, i.e. a temperature of 1275°C for 2 h.

The method of S. Kwon et al. is one of the best efforts that have been published about PMN. It prevented the pyrochlore phase from formation, decreased the sintering temperature, and reduced one ball-milling and one calcination step from the processing. But nanosize reactant is used in this technique and it needs O_2 sintering atmosphere.

In the topics presented below, important literature knowledge of relaxor materials and perovskite structures depending on PMN ceramics have tried to describe. In addition, PMN ceramics will be presented depending on literature. After aforementioned issues, fabrication of PMN ceramics having different techniques will be described in the following parts of this chapter such as solid state reactions and sol-gel technique. In the other part, we will discuss our knowledge about sol-gel ceramics fabrication and grinding techniques for sol-gel delivered powders on literature. Colloidal phenomena and properties of nano scale powders have vital important our studies. The mechanism and interactions between the particles are very important for this thesis. Dielectric properties and electronic applications will be tried to explain in the last part of the chapter.

2.1 Relaxors

Relaxor is a sub-group of ferroelectrics. In relaxor systems, the dielectric response has a broad peak as a function of temperature, rather than a sharp peak in a normal

ferroelectric, and a frequency dependent response (Cohen 2000). Therefore, relaxor ferroelectrics are characterized by a frequency dependent dielectric response which has a broad maximum as a function of temperature. In addition, relaxors possess a local polarization at temperatures above their dielectric maximum (Fanning 2000, Ravez 2000). The phase of the bulk material throughout the Curie temperature range from cubic to orthorhombic structure is responsible for the 0.1 % volume expansion of the crystal lattice upon application of the electric field (Blackwood & Ealey 1993).

Relaxor ferroelectrics belong to the class of materials which show strong chemical disorder (Kircher and Bohmer 2002). They are generally expressed by $\text{Pb}(\text{B}_1, \text{B}_2)\text{O}_3$ with high permittivity and relatively small temperature coefficient (Kelly et al. 1997 & Kobune et al. 2004).

PMN belongs to a class of relaxor ferroelectrics. Therefore, it exhibits a strong dispersion of dielectric permittivity with frequency and displays no macroscopic polarization even at temperatures well below the temperature of the maximum dielectric constant (Blackwood & Ealey 1993, Kim & Cha 1997). Because of the absence of the remanent polarization, PMN displays very little hysteresis above the Curie temperature range (Hood 1996). Relaxor behavior is very common among lead-based perovskites, suggesting that the “lone pair” electrons of Pb^{2+} play a role in the micro domain process, possibly by adjusting their orientations (Newnham et al. 1999).

2.2 Perovskite Structure

Many of the ferroelectric materials possess perovskite-type structure which can be expressed mostly ABO_3 in formula (Schwartz 1997). The unit cell of perovskite structure is shown in Figure 2.1. In the structure A-site cations occupy the corners of a cube, while B-site cations sit in the body center. Three oxygen atoms per unit cell rest on the faces (Burton 2000 & Swartz 1990). The lattice constant of these perovskite is always close to 4 Å due to the rigidity of the oxygen octahedra network and the well defined oxygen ionic radius of 1.35 Å. Another common ferroelectric

structure is the layered perovskite structure which consists of a varying number of perovskite unit cells separated by an oxide layer.

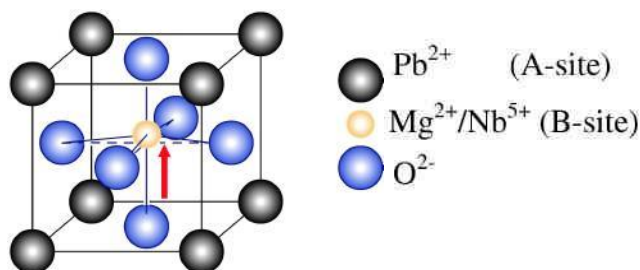


Figure 2.1 Schematic presentation of the PMN perovskite unit cell. (Deliormanli 2007)

This structure is also found in many high T_c superconductors (Bhalla et al. 2000). The crystal structure of PMN is controversial and following models explain the order-disorder behavior observed in this material (Mathan et al. 1990).

According to this model ordered regions has an ordered $Mg^{+2}: Nb^{+5}$ compositional distributions. The $Mg^{+2}: Nb^{+5}$ (1:1) ordered region will have negative charge relative to the Nb^{+5} rich matrix. The disordered matrix around these ordered regions has to be Nb^{+5} rich to maintain the overall stoichiometry (Burton 2000 & Yan et al. 1998).

In this model, B'' sites are occupied by Nb^{+5} cations, and B' sites are occupied randomly by $2/3Mg^{+2}$ and $1/3Nb^{+5}$ cations, for the $Pb(Mg_{1/3}Nb_{2/3})O_3$ complex perovskite. The structural formula can be written as $Pb(Mg_{1/3}Nb_{1/3})_{1/2}Nb_{1/2}O_3$. This inherent randomness results in relaxor properties even for fully (1:1) ordered systems (Burton 2000, Fanning 2000 & Yan et al. 1998).

2.3 Lead Magnesium Niobate

$Pb(Mg_{1/3}Nb_{2/3})O_3$ (PMN) is one of the most widely studied relaxor ferroelectric ceramic because of its superior dielectric constant, electrostrictive coefficient. PMN has a very high dielectric constant ($\epsilon_{max}=15000-30000$ at 1 kHz) near the room temperature (Cho et al. 2000, Fanning 2000 & Swartz et al. 1990). Curie temperature of the material is about $-10\text{ }^\circ\text{C}$ (Gentil et al. 2004). Figure 2.2 denotes the frequency dependency of the dielectric constant of PMN at various temperatures.

It was first synthesized by Smolenskii and Agranovskaya in 1958 (Fanning 2000, Kircher & Bohmer 2002 & Mohan et al. 2001). The study of relaxor materials continue in the early 1960`s with work on single crystal $\text{Pb}(\text{Mg}_{1/3}\text{Nb}_{2/3})\text{O}_3$ materials. More recent work in 1980`s with PMN based relaxor ceramics has led to their successful applications such as high strain electrostrictive actuators and high dielectric constant capacitors (Haertling 1999 & Zhong et al. 2005).

The highest symmetry phase for PMN is cubic with $\text{Pm}3\text{m}$ space symmetry and lattice constant $a=4.04 \text{ \AA}$. PMN undergoes a diffuse phase transition with a maximum temperature, T_m , from -3 to $-15 \text{ }^\circ\text{C}$ (Fitzgerald et al. 2000, Babooram et al. 2004). No structural change can be detected in PMN as it passes through the diffuse transition (Gu 2003). In its crystal structure, Pb^{+2} occupies the corner A-site and the B-site can be Mg^{+2} or Nb^{+5} (Swartz 1990). However, it does not exist with an idealized perovskite lattice structure as shown in Figure 2.1, where an ordered distribution of $\text{Mg}(\text{II})$ and $\text{Nb}(\text{V})$ ions in the next-nearest neighbor B-site octahedra exists (Fitzgerald et al. 2000). PMN has either partial or complete B-site disorder of the $\text{Mg}(\text{II})$ and $\text{Nb}(\text{V})$ B-site ions as it is discussed in the previous section. B-site cation order influences the crystallography, phase transitions and other physical properties. The broad diffused phase transition in PMN is due to the presence of two cations of very different ionic radii and the valences at the octahedral B-site of the perovskite (Das et al. 2003). The atoms are located in the ideal cubic sites but continually shift off these positions. The origin of these effects is a partial ordering of the PMN perovskite structure in which the niobium and the magnesium atoms of PMN alternate in position over only a few unit cells (usually $30\text{--}50 \text{ \AA}$). Within these ordered regions, an external field acts upon fluctuating dipoles to make large electrostrictive motions (Newnham & Amin 1999).

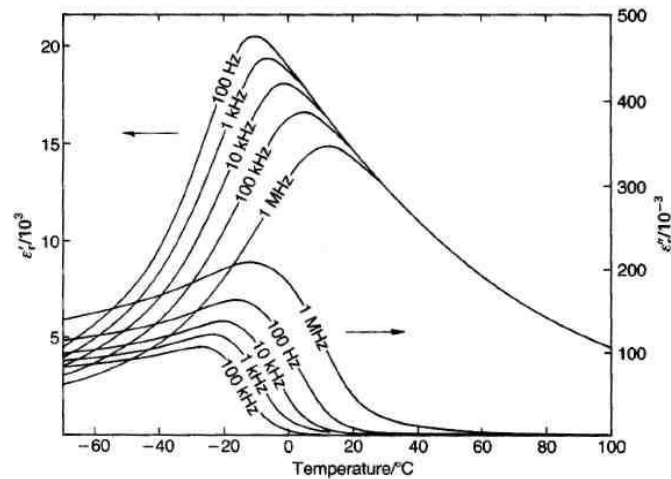


Figure 2.2 Dielectric constant (left) and dielectric loss (right) of the relaxor PMN as a function of temperature (Fanning 2000).

PMN has temperature-sensitive micro domains that result from the many different “active” ion linkages in the disordered octahedral framework. Each NbO_6 octahedron may be bonded to zero to six other NbO_6 octahedra (with the remaining connections involving MgO_6 octahedra). Connections between these octahedra are assumed to be essential to ferroelectricity and high anisotropy coefficients. As the temperature decreases from the high-temperature paraelectric state, ferroelectric micro domains gradually coalesce to macro domains, giving rise to a diffuse phase transformation. These polarization fluctuations are also dependent on bias field and the frequency used to measure the dielectric or piezoelectric constant. The dielectric constant drops off rapidly with increasing frequency (hence the name “relaxor”) because it takes time for the polarization fluctuations to respond (Egami et al. 1998, Newnham & Amin 1999,).

The main problem in PMN production is the formation of a lead-niobate based pyrochlore phase with low dielectric constant (~ 200 compared to the 20000 for PMN single crystal) during the heating process (Costa et al. 2001). Although the pyrochlore phase is composed mainly of PbO and Nb_2O_5 , it may contain a small amount of MgO in the lattice. The ratio of $\text{Pb}:\text{Nb}$ in the pyrochlore phase is less than or equal to the ratio of $\text{Pb}:\text{Nb}=1.5$ in the perovskite phase (Gu 2003). The pyrochlore can be formed by decomposition of the PMN perovskite phase as a consequence of

PbO volatilization during sintering. The widespread method to synthesize pure perovskite was introduced by Swartz and Shrout in 1982, known as columbite method (Costa et al. 2001). In addition to mixed oxide method, solution synthesis methods such as sol-gel are used to synthesize high purity PMN powders and thin films (Brailenau et al. 2004, Deliormanli et al. 2007 & Wu and Liou 1995).

PMN forms a solid solution with lead titanate (PT) as seen in Figure 2.2 providing many compositions that have excellent electromechanical properties (Kelly et al. 1997). The composition near 0.9PMN-0.1PT has a high dielectric constant ($>20,000$) and also has a very high electrostrictive coefficient ($3.6 \times 10^{-16} \text{ m}^2/\text{V}^2$). The composition 0.65PMN-0.35PT has a very high piezoelectric coefficient of $560 \times 10^{-12} \text{ C/N}$. Additionally, high electromechanical properties such as $\sim 0.1\%$ longitudinal strain and $>0.03\%$ transverse strain at 1 MV/m and 0.1 Hz have been reported (Cho et al. 2000, Deliormanli 2007).

Lucas and Petuskey investigated the ternary phase diagram of PbO-MgO-Nb₂O₅ at 1000 °C. Figure 2.3 shows the phase diagram of this ternary system. Two ternary compounds were observed in the PbO–MgO–Nb₂O₅ system: Pb(Mg_{1/3}Nb_{2/3})O₃ and the cubic pyrochlore phase. In Figure 2.4, PMN is the perovskite phase, the black domain represents the pyrochlore (Py) solid-solution range, the light gray areas correspond to diphasic domains, and the dark gray area represents the extent of the liquidus at 1000°C (Lucas & Petuskey 2001).

As conclusion, general properties of PMN ceramics are summarized in the following paragraph:

- Electrostrictive PMN exhibits a negligible hysteresis ($<1\%$), which is essential in repeatedly locating and maintaining a set-point accuracy (Deliormanli 2007).
- PMN requires no poling, which means it remains stable with no aging or creep commonly found in piezoelectric devices (Deliormanli 2007).
- PMN has a very high elastic modulus ($17 \times 10 \text{ Psi}$) which produces relatively high stiffness, enhancing the force/deflection capability (Deliormanli 2007).

- PMN actuators have negligible thermal growth because the thermal expansion coefficient dissipates very little power (Deliormanli 2007).
- PMN also has improved strain sensitivity that reduces the operating voltage below 150 V (Deliormanli 2007).
- PMN produces little or no electrical or magnetic interference with other components (Deliormanli 2007).

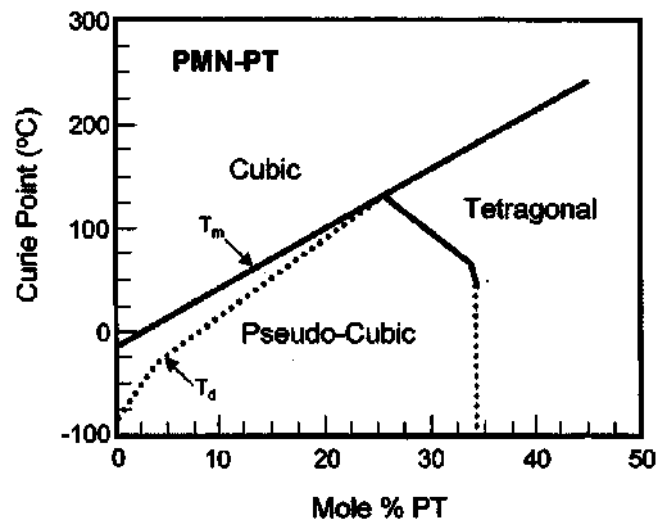


Figure 2.3 PMN-PT phase diagram (Gu 2003)

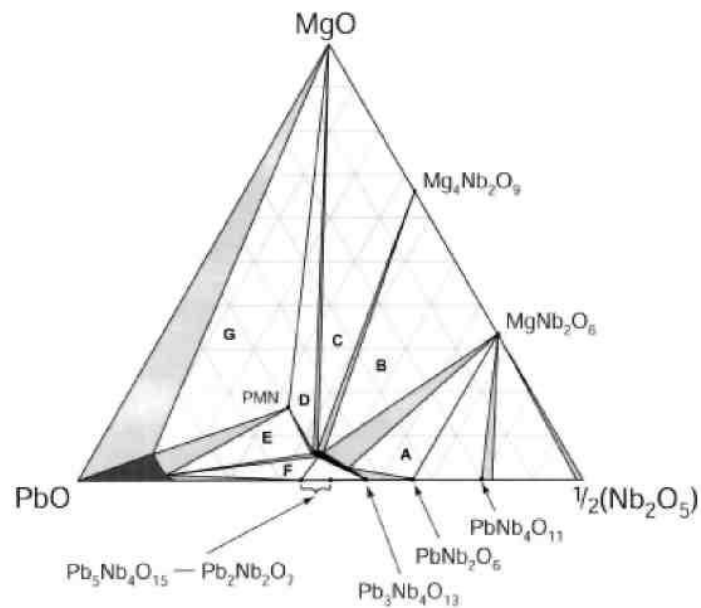


Figure 2.4 Ternary phase diagram of the PbO-MgO-Nb₂O₅ system at 1000°C (axes are given in cation fractions) (Lucas & Petuskey 2001).

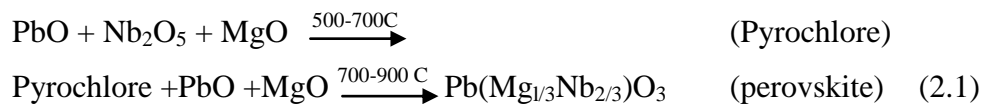
Accordingly, today PMN components have replaced many piezoelectric actuators used in precision apparatus because the PMN drift is less than 3 % over two days compared with 10–15 % of a comparable piezoelectric device under loading. Therefore, precision actuators and displacement transducers are ideal applications of PMN-based materials (Shankar and Hom 2000 & Tzou et al. 2004).

2.4 Properties of PMN Produced by Different Techniques

2.4.1 PMN by Solid State Reactions

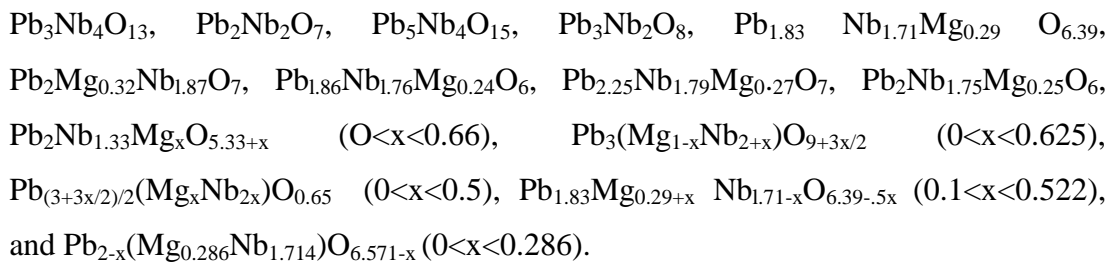
Most direct method of making mixed oxides is to react a mixture of metal oxides, hydroxides or salts in the solid state. Conventional processing to prepare multicomponent mixed oxide ceramic powders involves three consecutive steps of mixing, solid-state reaction and milling. Particles can be formed either in a structured fashion or randomly. Then the multicomponent phases are formed via solid-state reactions (Su 2001).

Unlike most other ferroelectric ceramics, the desired perovskite phase of PMN or PMN-PT cannot be synthesized by simply calcining the component oxides mixture. It has been shown that the following equations are the reaction sequence during the calcinations of the oxide mixture of PbO, MgO, and Nb₂O₅:



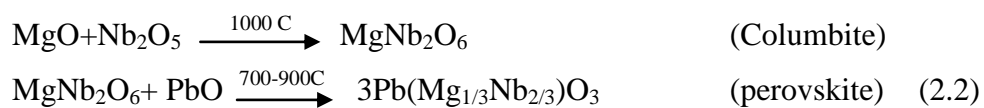
In these two reactions, the first reaction is not complete, indicating that the pyrochlore phase is not completely converted into perovskite phase. The final product is a mixture of both pyrochlore and perovskite phase. The presence of the pyrochlore phase degrades the dielectric and electromechanical property significantly as mentioned before.

Pyrochlore compounds have the general formula $A_2B_2O_7$, where A and B are cations and X are anions. There are different types of pyrochlores that correspond to different combinations of A, B and X ions; such pyrochlores are not limited to the ideal stoichiometric (Beltran et al. 2003). The exact composition of the pyrochlore phase is still not clear. Many possible formulas have been proposed by some groups (Ananta and Messing; Beltran et al. 2003, 2000; Mergen and Kaye 2004) as follows:



The common features of these formulas are that the pyrochlore phase is composed mainly of PbO and Nb₂O₅. It may contain a small amount of MgO in the lattice. The ratio of Pb:Nb in the pyrochlore phase is less than or equal to the ratio of Pb:Nb=1.5 in the perovskite phase. Thus, in essence, the transformation reaction from the pyrochlore to perovskite phase is a process of MgO and maybe some PbO diffusing into the lattice of the pyrochlore phase. In so far as the PbO melting temperature is low at 888 °C, the diffusion rate of PbO in the pyrochlore phase is quite high. Therefore, the critical factor in this reaction is controlled by the slower diffusion of MgO (Koyuncu & Pilgrim 1999).

A procedure to limit the amount of pyrochlore to <5 wt% was developed to address this problem the columbite precursor method developed by Swartz and ShROUT. This method has been used extensively in many syntheses of PMN (Koyuncu & Pilgrim 1999):



In the first calcination step, mixtures of Nb_2O_5 and MgO were heat-treated at around 1000°C to form the columbite phase, MgNb_2O_6 . In the second calcination step, MgNb_2O_6 was mixed and heat-treated with PbO . In this way, Nb_2O_5 and MgO are pre-reacted and mixed uniformly at atomic level. Due to the fact that PbO are relative easy to diffuse, last reaction can be completed at a relative low temperature. Also the direct contact and reaction of Nb_2O_5 and PbO are eliminated, thus the formation of pyrochlore phase are prevented (Ananta & Thomas 1999).

Cavalheiro et al. (2004) studied the effects of excess PbO on the formation of PMN by the columbite via polymeric precursor's method. Liou, 2004 used reaction sintering method to obtain pyrochlore free PMN powders and studied the effect of heating rate. The obtained results showed that density increases as heating rate increased from 5 to $10^\circ\text{C}/\text{min}$ and reach a maximum $8.06\text{ g}/\text{cm}^3$ at $10^\circ\text{C}/\text{min}$. It decreases at heating rates of 20 and $30^\circ\text{C}/\text{min}$.

Solid state reactions typically result in the formation of aggregates that require a comminution process to reduce particle size to micrometer level. But, milling to particle size below $1\mu\text{m}$ is technically difficult for some hard materials, contaminates the product and is energy intensive. The homogeneity and purity of the powder thus are poor whereas the particle size distribution is broad (Su 2001). Conventional technique of solid phase reactions allows obtaining material with admixture of about 10-20 % of the pyrochlore phase. The latter can be reduced to 5-10 % using MgCO_3 as the source of MgO . Similar result is achieved by the columbite method (Dambekalne et al.).

2.4.2 PMN by Sol-Gel Technique

The sol-gel method is widely employed to prepare perovskites at low temperature. There is considerable interest in making electroceramic materials by sol-gel processes as they offer numerous potential advantages for PMN formation compared to solid-state routes. Solvents such as methanol (MeOH), ethanol (EtOH) and butanol (BuOH) are usually used in sol-gel syntheses. Of these solvents, 2- methoxyethanol

is also extensively used in the synthesis of perovskite materials and is beneficial in assisting the dissolution of carboxylate precursors such as lead acetate (Schmidt 1988). The key reactions leading to the formation of the precursor species are hydrolysis and condensation of the alkoxide reagents, leading to formation of metal-oxygen-metal (M-O-M) bonds (Beltran et al.2003).

Beltran et al (2000) successfully synthesized the perovskite PMN powders by a simple sol-gel method at room temperature using minimum quantity of solvent. In the study, a multicomponent alkoxide solution was prepared by mixing lead acetate $\text{Pb}(\text{CH}_3\text{COO})_2 \cdot 3\text{H}_2\text{O}$, anhydrous magnesium acetate $\text{Mg}(\text{CH}_3\text{COO})_2$, and niobium ethoxide $\text{Nb}(\text{OC}_2\text{H}_5)_5$. The solvents used in the study were 2-methoxyethanol $\text{CH}_3\text{OCH}_2\text{CH}_2\text{-OH}$, methanol CH_3OH , and ethanol $\text{CH}_3\text{CH}_2\text{OH}$ (absolute, extra pure 99%). The general scheme for preparation is shown in Figure 2.5.

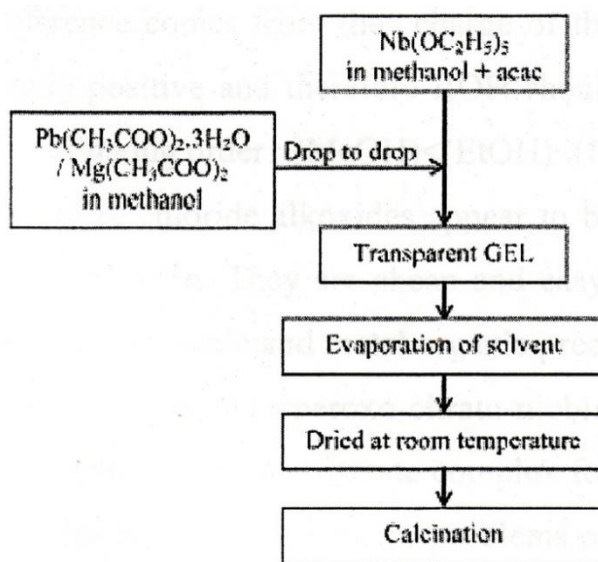


Figure 2.5 Powder preparation procedure by sol-gel (Beltran et al 2000).

However, phase analysis by X-ray powder diffraction (XRD) showed that perovskite PMN was the final phase to appear, crystallizing above 650°C ; at lower temperatures a pyrochlore phase was detected. Beltran et al used the following procedure in the recent study (Figure 2.6). The dried gels were heated in air in a furnace for $10^\circ\text{C}/\text{min}$ to 650°C to ensure the total removal of organic material and

then were heated at 5 °C/min to 800 °C and held at these temperatures for 4 hours in air. Samples were removed from the furnace, crushed, pressed into pellets, and reheated at 800 °C for 3 h in Au foil. According to the results of the study, it can be concluded that an excess of Pb and Mg is necessary in order to form compositions near the stoichiometric.

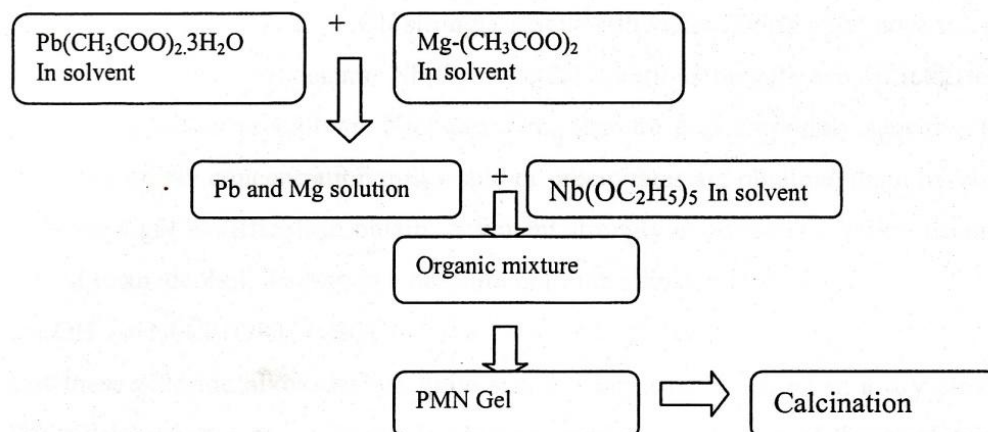


Figure 2.6 Procedure for sol-gel synthesis of PMN (Beltran et al. 2003).

It may be also possible to use metal chloride alkoxide as precursor rather than alkoxides. They are very easy to synthesize and can be used as molecular precursors to make oxide gels. According to Sanchez et al. 1988, NbCl_5 strongly reacts with water giving gelatinous precipitates of $\text{Nb(OH)}_3\text{Cl}_2$ while HCl gas occurs. Nb_2O_5 colloidal solutions or gels are difficult to obtain through peptization of the precipitate. Niobium alkoxides are also extremely sensitive towards water. Depending on Nb concentration milky sold or precipitates are obtained upon hydrolysis of Nb(OEt)_5 . Again a gel is difficult to obtain. A violent strongly exothermic reaction occurs when NbCl_5 is added to an alcohol, leading to a niobium chloride alkoxide such as:



Solutions of these chloride alkoxides are quite stable. They can be stored in a dry atmosphere without any special care. Gels can be easily obtained through hydrolysis of these solutions with the excess water. The rate of gelation depends on the alcohol.

Gelation occurs within a few seconds with propanol (PriOH), a few hours with EtOH and several days with MeOH. Chemical analysis of these gels shows that chlorine is still present after hydrolysis while all OR groups have been removed.

NbCl_5 is more rapidly hydrolyzed than Nb(OR)_5 . The positive charge of Nb in NbCl_5 is quite large ($\delta = +0.66$), therefore nucleophilic addition of H_2O is easy. Hydrolysis and condensation are fast, leading to the departure of the positively charged HCl molecule. The positive charge of Nb ($\delta = +0.53$) in Nb(OEt)_5 is smaller and hydrolysis is not fast. The positively charged ROH molecule is removed. The positive charge of the niobium atom in the mixed chloride alkoxide $\text{Nb(OR)}_3\text{Cl}_2$ is intermediate between them. Therefore hydrolysis should be rather fast. The main difference comes from the charge of the alkoxy groups in the hydrated transition states. It is highly positive and therefore ROH should be removed through hydrolysis and condensation in the following order: $(\text{MeOH}) < (\text{EtOH}) < (\text{PriOH})$.

Therefore chloride alkoxides appear to be very convenient molecular precursors for the sol-gel polymerization. They are cheap and easy to synthesize and also they offer a good compromise between inorganic and metal organic precursors (Sanchez et al). Similarly Narendar and Messing (1997) synthesized a peroxy-citrato-niobium, a novel aqueous precursor of niobium and Nas et al. (2000) used niobium tartarate complex for this purpose. They claim that use of niobium tartarate complex can avoid the major problems of moisture sensitivity of other niobium sources such as niobium pentachloride and niobium ethoxide, during the reaction period.

W.F-A Su was synthesized the PMN according to the method of Roy group with some modifications. In the procedure, lead oxide was added a flask and purged with argon overnight. Acetic acid was then into the flask. The mixture was heated to 130 °C to distil out of water and acetic acid. After solution was cooled below 40 °C, methoxyethanol was added to the flask. It was heated again and subsequently pH was adjusted to 8.2. Magnesium ethoxide and niobium ethoxide were added into the solution. The solution was heated to 130 °C until about 50 g of distillate was collected. 10 g of deionized water was added to 100 g of PMN solution and a

gelation occurred. The gel was dried at 130 °C for 18 hours and calcined at 350 °C for 18 hours.

Komerneni et al (1999) have developed a process utilizes lead acetate, magnesium ethoxide and niobium ethoxide as starting precursors. Figure 2.7 describes the procedure to obtain the powders. The PMN powder prepared by calcining the gel at 900 °C for 2 hours showed a small amount of pyrochlore. Nevertheless the particle size and morphology of PMN powder reveals that the particle size is very large which was reflected in its surface area of 0.4 m²/g.

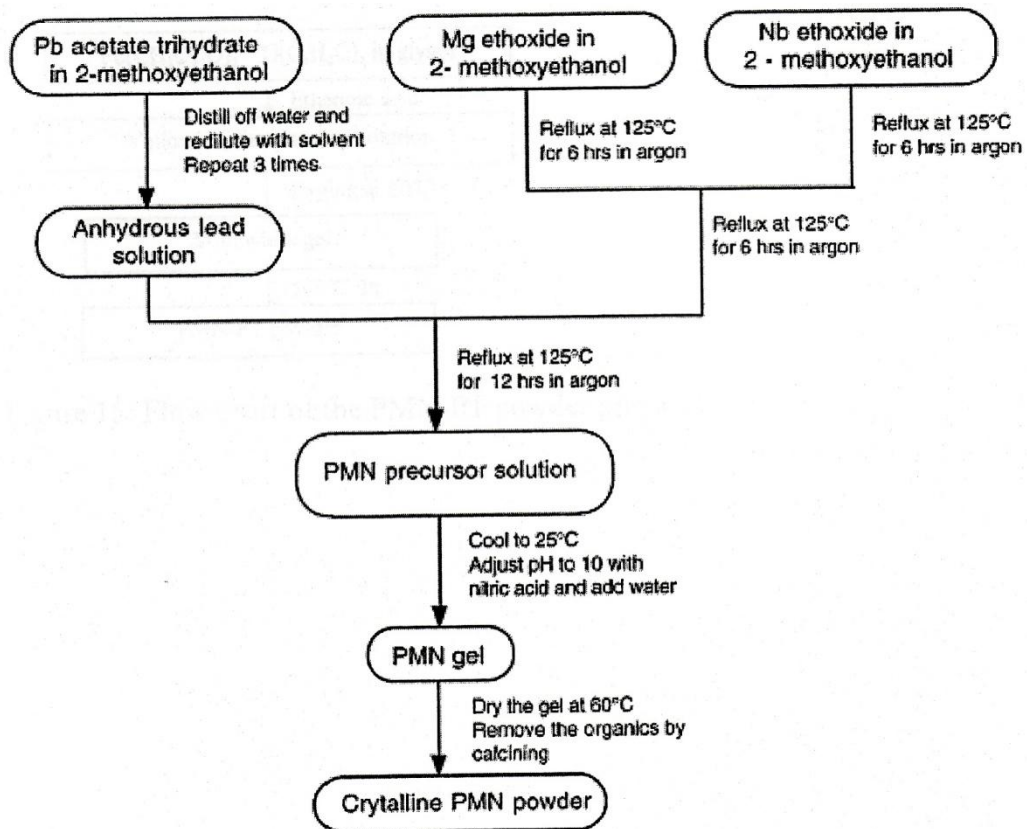


Figure 2.7 Flow chart for the synthesis of PMN powder by sol-gel processing (Komerneni et al. 1999).

Jiwei et al (2000) reported the preparation and dielectric properties of PMN-PT powders prepared by sol-gel method. According to their observations, the metal alkoxides such as Nb(OC₂H₅)₅ and Mg(OC₂H₅)₂ are the starting materials for sol-gel method and all of the reaction must be carried out in flowing argon atmosphere. This

method is expensive and difficult for preparation powders as well as ceramics. Therefore they used the salt precursor and followed the procedure shown in Figure 2.8. Results showed that the formation of pure perovskite phase at 1100 °C via the intermediate formation of pyrochlore phase. A maximum dielectric constant of 24,014 was obtained for the pellets sintered at 1250 °C at 1 kHz. All of the samples exhibited frequency dispersion behavior of both dielectric constant and loss factor.

The sol-gel process means the synthesis of an inorganic network by a chemical reaction in solution at low temperature (Schmidt, 1988). The method can be used to prepare a variety of materials, including: glass, powders, films, fibers, and monoliths. The sol-gel method leads to homogeneous stoichiometric and high purity fine particles, offer great flexibility because of the large variety of organic precursors that are available (Beltran et al. 2003).

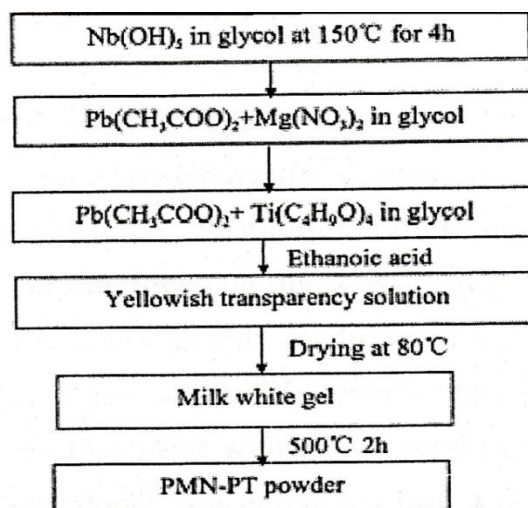


Figure 2.8 Flow chart of the PMN-PT powder preparation (Jiwei et al 2000).

There are two important sol-gel processes, namely the alkoxide and the colloidal methods (Guglielmi & Carturan 1988). Traditionally, sol-gel process involves hydrolysis and condensation of metal alkoxides (Deliormanli 2007).

Metal alkoxides have the general formula $M(OR)_x$ and they are compounds in which elements are bonded to a hydrocarbon moiety through oxygen (Guglielmi and

Carturan 1988). The general synthesis of metal alkoxides involves the reaction of metal species (a metal, metal hydroxide, metal oxide, or metal halide) with an alcohol. Metal alkoxides are good precursors because they readily undergo hydrolysis; that is, the hydrolysis step replaces an alkoxide with a hydroxide group from water and a free alcohol is formed. They have many advantages compared to inorganic and organic salt precursors (Schmidt 1988).

Sol-gel-derived thin films are favored for production of PMN films due to the flexibility in the characteristics of solution precursors, the variety of deposition methodologies, and the reduction of the sintering temperatures. The standard solution approach to generating PMN thin films typically involves either using commercially available precursors and dissolving them in 2-methoxyethanol, which acts as both a solvent and a chemical modifier, or synthesizing large metal organic "soap-derivative" (neo-decanoate) compounds using organic solvents such as xylenes (Pierre 1998). Although other alcohols have also been utilized, the solvent, 2-methoxyethanol ($\text{CH}_3\text{-OCH}_2\text{CH}_2\text{OH}$), is most extensively used in the chemical synthesis of perovskite materials. Processes based on 2-methoxyethanol are most appropriately considered sol-gel processes and the key reactions leading to the formation of the precursor species are hydrolysis and condensation of the alkoxide reagents, in which metal-oxygen-metal (M-O-M) bonds are formed (Ananta & Thomas 1999):

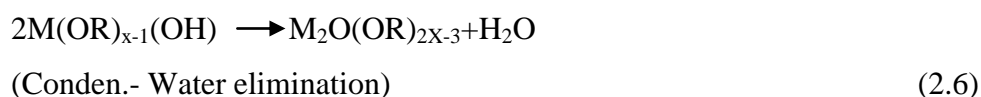
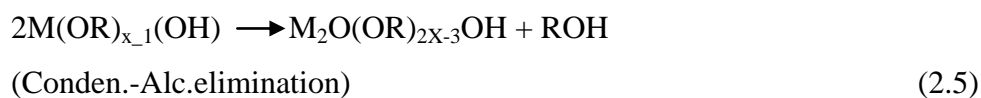


Once hydrolysis has occurred, the sol can react further and condensation (polymerization) occurs. The hydrolysis reaction can be considered as a source for reactive monomers or oligomers (Schmidt 1988; Schwartz 1997).

Prehydrolysis of less reactive alkoxides may also be used to improve solution compositional uniformity. Another key reaction in the use of this solvent is the alcohol-exchange reaction that results in a decrease in the hydrolysis sensitivity of starting reagents such as zirconium n-propoxide and titanium isopropoxide used in

the production of PZT films: where OR is a reactive alkoxy group and OR' is the less reactive methoxyethoxy group. 2-Methoxyethanol has also been found to be beneficial in the dissolution of carboxylate precursors such as lead acetate. In this case, by refluxing the lead acetate precursor in 2-methoxyethanol, one of the acetate groups is replaced, resulting in the formation of the soluble lead precursor, $\text{Pb}(\text{OOCCH}_3)(\text{OCH}_2\text{CH}_2\text{OCH}_3)\cdot 0.5\text{H}_2\text{O}$. Lead carboxylate compounds are usually employed due to the instability of lead alkoxides and their limited commercial availability. A typical process involves refluxing lead acetate and the alkoxide compounds in methoxyethanol in separate reaction vessels. This is followed by combining the solutions, further refluxing, distillation, and dilution to the desired volume. Prior to film formation, the stock solution prepared by the above process is then hydrolyzed to promote oligomerization. The reactions that occur during PZT solution preparation have been extensively studied using spectroscopic techniques (Ananta & Thomas 1999). Similar reactions between precursor compounds and 2-methoxyethanol have been also noted in the processing of $\text{Pb}(\text{Zn}_{1/3}\text{Nb}_{2/3})\text{O}_3$ (Ananta & Thomas 1999). These studies have elucidated certain aspects of the structure of the solution precursors. Some studies have indicated that the precursors formed in the lead zirconate titanate and lead titanate deposition solutions are apparently small, mixed metal oligomers, (Ananta & Thomas 1999) while others have indicated that the A-site precursor may not be intimately involved in the formation of the gel network (Ananta & Thomas 1999). In particular, the results of Sengupta and co-workers (Ananta & Thomas 1999) for EXAFS (extended X-ray absorption fine structure) investigations of PZT gels indicate that separate networks of Ti-O-Ti, Zr-O-Ti, and Pb-O-Pb exist within the gel structure. This would seem to indicate that "intimate" mixing of the starting reagents has not taken place. In terms of controlling the extent of intermixing and stoichiometry of the precursor species, there have been a number of efforts to synthesize stoichiometric precursors with structures similar to the final crystal structure of the desired perovskite phase. The motivation behind these efforts is that stoichiometric precursors with structures similar to the crystalline phase should undergo crystallization at lower heat treatment temperatures. Most attempts have resulted in mixed metal species with a cation stoichiometry different than that of the perovskite material (Es-Souni et al. 2003). These results indicate the

importance that thermodynamic sinks can play in the synthesis of these materials (Ananta & Thomas 1999). Nonetheless, while the stoichiometry of the precursor species may not match that of the crystalline perovskite, this has not inhibited the production of high quality perovskite films by this processing route (Deliormanli 2007).



These condensation reactions lead to gel formation after hydrolysis process. In condensation two hydrolyzed fragments join together and either an alcohol or water is released. Condensation occurs by either nucleophilic substitution or nucleophilic addition. Reactions (2.3)-(2.4) may simultaneously occur so that it is impossible to describe the process by the separate and independent of hydrolysis and condensation reactions (Guglielmi & Carturan 1988). Nevertheless, the real chemistry is not as simple as that. Chemical additives are used to improve the process and obtain better materials. Additives can be solvent molecules, acid/base catalysts, stabilizing agents or drying control chemical additives. Hydrolysis may perform in an acid catalyst that allows experimental control of the rate and the extent of the hydrolysis reaction (Doeuffs et al.1987). Most common additives such as acetic acid and acetylacetone may chemically react with alkoxides at a molecular level giving rise to new molecular precursors. Then the whole hydrolysis and condensation processes are modified (Sanchez et al 1988). Therefore factors that are need to be considered in a sol-gel process are solvent, temperature, precursors, catalysts, pH, additives, and mechanical agitation (Chow & Schmidt 1988). These factors can influence the kinetics, growth reactions, hydrolysis, and condensation reactions. The solvent influences the kinetics and conformation of the precursors, and the pH affects the hydrolysis and condensation reactions. Acidic conditions favor hydrolysis, which means that fully or nearly fully hydrolyzed species are formed before condensation begins. Under acidic conditions there is a low cross-link density which yields a

denser final product when the gel collapses. Basic conditions favor condensation reactions, therefore, condensation begins before hydrolysis is completed. The pH also affects the isoelectric point and the stability of the sol. By varying the factors that influence the reaction rates of hydrolysis and condensation, the structure and properties of the gel can be changed in sol-gel processing (Deliormanli 2007).

A typical process involves refluxing metal acetate and the alkoxide compounds in 2-methoxyethanol in separate reaction vessels. This is followed by combining the solutions and further refluxing, distillation, and dilution to the desired concentration. Prior to film formation, the stock solution prepared by the above process is partially hydrolysed to promote oligomerization (Babooram et al. 2004). Solution processes based on the use of methoxyethanol are widely used due to the ability of this solvent to solubilize a variety of different precursors. Once properly carried out, the process offers excellent control and reproducibility of process chemistry, and non-hydrolyzed solutions exhibit minimal ageing effects. Further, 2-methoxyethanol is a known teratogen, which presents a significant safety concern and inhibits its use in most manufacturing facilities. Hence 2-butoxyethanol, which is less toxic, has been introduced into the sol-gel processing of lead zirconium titanium oxide (PZT) thin films (Babooram et al. 2004). Ravindranathan et al. teach a methoxyethanol approach to generating PMN thin films. In that method, commercially available acetates and alkoxides are heated in the presence of methoxyethanol in order to convert them to the methoxyethoxide derivatives. Ravindranathan's alcohol (methoxyethanol) necessarily serves both as solvent and modifier of precursor material (Deliormanli 2007 & Pierre 1998).

2.5 Sol-Gel Technique

2.5.1 The Chemistry of Precursors Solution

If inorganic sols and gels can be obtained by various methods, they are often directly synthesized from chemical reactants dissolved in a liquid medium. The chemical reactants which contain the cation M (metal) present in the final inorganic

sol or gel is called the chemical precursor. Its chemical transformations are complex and involve a competition at the molecular level between the reaction responsible for the formation of open structures and the one leading to dense solid. Those same reactions are responsible for the controlled dispersion of dense colloidal particles in a sol or their agglomeration into a gel (Pierre 1998). All types of precursors can be used, provided they are miscible. For powder and thin film production, metal alkoxides are better than its salts as a precursor to achieve crack-free, pinhole-free, homogeneous and textured films.

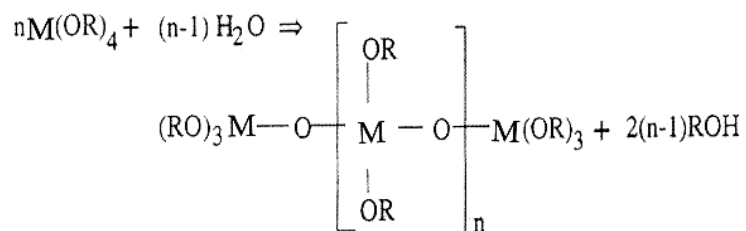
Solvents which dissolve precursor have a molecular structure characterized both by a permanent dipole moment μ and by a relative dielectric constant ϵ_r . A high relative dielectric constant ($\epsilon_r > 40$) is often due to the existence of a permanent dipole moment. Such molecules have good ionizing properties and can therefore dissolve other polar solute. On the other hand when the solvent's relative constant is low ($\epsilon_r < 20$), it has a weak ionizing property and can only dissolve less polar solute (Pierre 1998).

Sol-gel precursors undergo chemical reaction with solvents and the other species present in the solution. One of the most efficient models used to predict those reactions is the Partial Charge Model. Various atomic or molecular groups called ligands can bind to a complex C or cation M either directly or by substituting another ligand. The mechanism of the transformation depends on the partial charge of the different atoms in the species. Those with a negative partial charge are nucleophilic, and those with a positive charge are electrophilic. Similarly, in a substitution reaction, the the new ligands with the highest partial charge is the nucleophile while the group in the metal complex with the highest positive charge is the leaving group (Pierre 1998).

2.5.2 Hydrolysis and Condensation Reaction

Hydrolysis can be expressed by deprotonation of a solvated M cation and it consists in the loss of a proton by one or more of the water molecules that surrounds

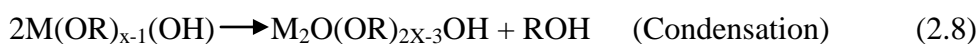
the M in the first solvation shell during hydrolysis process. As a consequence, the aquo ligand molecule, H₂O that is bonded to the metal is either transformed into an hydroxo ligand, OH⁻, if only one proton leaves, or into an oxo ligand O⁻², if two protons detaches.



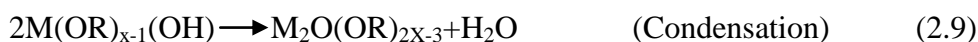
(Hydrolysis)

(2.7)

After hydrolysis, condensation reaction occurs to form a polynuclear complex consisting of two metal atoms. Condensation, in aqueous solutions, is the result of either an olation or an oxolation reaction. In either case, one must be quite careful as the oxygen present sometimes speeds the reaction to a point where it becomes necessary to work in the neutral atmosphere of argon in order to control it (Pierre 1998). In the first case, transfer of the H to an OR ligand according to the reaction below (olation process);



In the second case, transfer of the H to an OH group according to Reaction (2.9), condensation is called oxolation.



Hydrolysis and condensation both keep on going thus gradually building up a tridimensional network that, at the end, often forms a solid phase. This process is accelerated by heat as the rate of the both reactions increases together with the temperature. Since the kinetics of hydrolysis and condensation, and hence the overall reaction and the type of polymers formed, depends on the pH, a great variety of

materials with different structures can be obtained. These include linear polymers as well as dense colloidal particles and smaller ones with more or less weakly bonded cross-linked clusters of polymers.

Hydrolysis is complex technique that, depending on the conditions, gives rise to a great variety of colloidal structures ranging from metals to hydroxides and including oxides and oxihydroxides. The behavior of cations in aqueous solutions can be summarized according to their nature and with respect of their final type of ligands as depicted in Figure 2.9 (Pierre 1998).

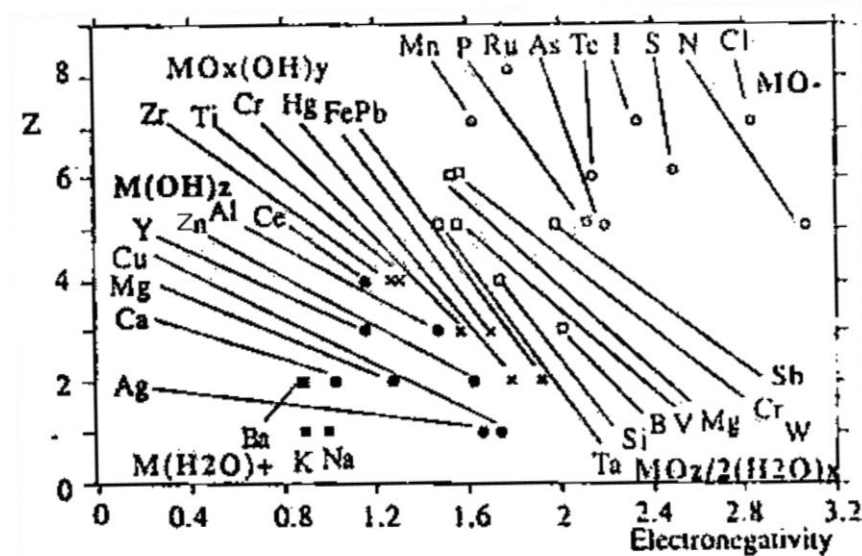


Figure 2.9 Charge versus electronegativity. This relation shows the species formed by cations in aqueous solutions (Pierre 1998).

2.5.3 Thermodynamics of Nucleation and Crystal Growth

The chemical reactions which transform a precursor solution, produce a large variety of complexes. The formation of solid particles can be described as a process of nucleation and growth, according to the sequence (2.10);



Solid particles can form as the results of heterogenous on foreign inclusions, such as dusts, or the products from uncontrolled hydrolysis (Pierre 1998).

The transformation from the amorphous to the crystalline state can be considered with phenomenological thermodynamics. The most favorable site for the nucleation can be derived by classical nucleation theory. It should be noted that much of the volume is not far from the surface and the interface with the substrate and heterogeneous nucleation is more likely to occur in the thin films. Assuming for simplicity that regions of crystalline PMN is spherical with a radius r , a free energy change ΔG , due to homogeneous nucleation is given by

$$\Delta G = 4\pi r^2 \gamma + \frac{4}{3} \pi r^3 \Delta G_v \quad (2.11)$$

where γ is the interfacial energy between the amorphous and the crystalline PMN and ΔG_v the free energy change per unit volume. In case of solid-solid transformation, a nucleus usually undergoes distortion in atomic arrangement as a result of contact with surrounding matrix and/or the substrates. Consequently, a distortion energy term must be added in a right-hand side of Equation 2.11. In the present case, however, both the matrix and the substrate are amorphous giving incoherent interfaces, and the nucleus is not affected by them in terms of the atomic arrangement. Therefore, the distortion energy can be regarded as zero (Fujihara et al, 2001).

From the nucleation $\partial(\Delta G)/\partial r=0$, a free energy barrier, ΔG_c , which subcritical embryos must overcome to come supercritical nuclei, is derived as follows:

$$\Delta G_c = \frac{16\pi\gamma}{3(\Delta G_v)^2} \quad (2.12)$$

Thus, the heterogeneous nucleation at the substrate surface is more likely to occur. Consideration of a polyhedron nucleus leads to a similar tendency.

When the nucleus is formed on a flat substrate characterized by contact angle, θ , the reduced barrier, ΔG_c^* , can be expressed by:

$$\Delta G_c^* = f(\theta)\Delta G_c \quad (2.13)$$

where

$$f(\theta) = \frac{1}{4}(2 + \cos\theta)(1 - \cos\theta)^2 \quad (2.14)$$

The θ value is determined by the surface energy of the substrate (γ_s) and the nucleus (γ_n) and the interfacial energy between them (γ_{sn}):

$$\cos\theta = \frac{\gamma_s - \gamma_{sn}}{\gamma_n} \quad (2.15)$$

Figure 2.10 clarifies a relationship between $f(\theta)$ and θ . The $f(\theta)$ value increasing the contact angle θ . Therefore ΔG_c^* in Equation 2.13 is lower with smaller contact angle of the nucleus. $\gamma_s = \gamma_n$ and $\gamma_s = 0$ in homoepitaxial systems give $\cos\theta = 1$, $f(\theta) = 0$, and accordingly $\Delta G_c^* = 0$. On the other extreme, $\gamma_{sn} = \gamma_s + \gamma_n$ gives $\Delta G_c^* = \Delta G_c$, where the homogeneous nucleation occurs without the effect of the substrate. γ_{sn} is generally less than the sum of γ_s and γ_n . When γ_s is constant as for the glass substrates, γ_n is determined by γ_{sn} as follows:

$$\gamma_{sn} = \alpha\gamma_n \quad (0 < \alpha < 1) \quad (2.16)$$

From Equations 2.15 and 2.16,

$$\cos\theta = \left(\frac{\gamma_s}{\gamma_n} \right) - \alpha \quad (2.17)$$

Assuming that α is constant, the lowest γ_n gives the latest $\cos\theta$ and hence, the smallest ΔG_c^* .

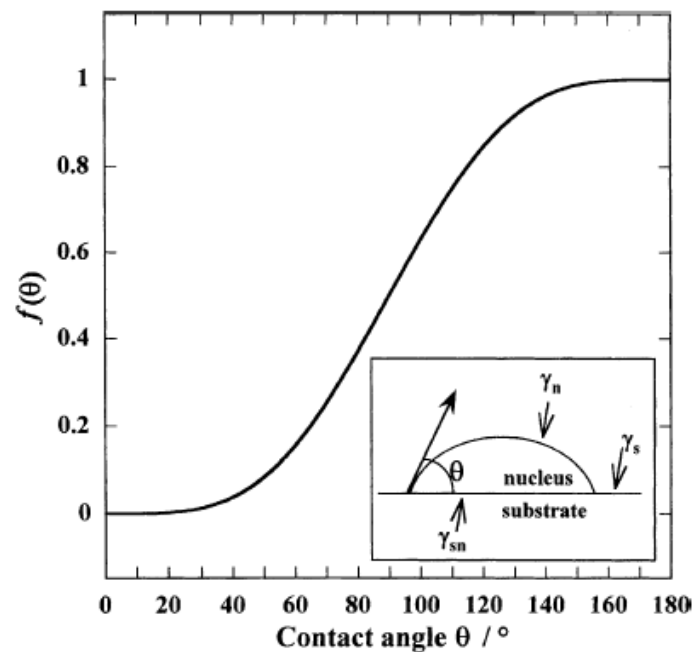


Figure 2.10 A relationship between $f(\theta)$ and contact angle, θ (Fujihara et al, 2001)

2.5.4 Gelation

Gelation is a process according to which a sol or solution, transforms to a gel. It consists of establishing links between the sol particles or the solution molecules so as to form 3-dimensional solid network. Gelation occurs when the extent of polymerization reactions ξ reaches a critical value ξ_c . This precise critical stage, when for the first time a polymer of infinite size is formed by comparison with the molecular scale, defines the gel point. In a practical manner, at this point the product resulting from polymeric condensations transforms suddenly from a viscous liquid to a material with elastic properties (Pierre 1998).

Gelation can be described in a more abstract fashion within the frame work of critical phenomena in thermodynamics in particular by the percolation theories. The most simple of the percolation models is isotropic such as the bond percolation and the site percolation (Figure 2.11). In these models, either a bond is established or a

site is occupied with probability p , in a completely random fashion throughout a geometrical network (Pierre 1998).

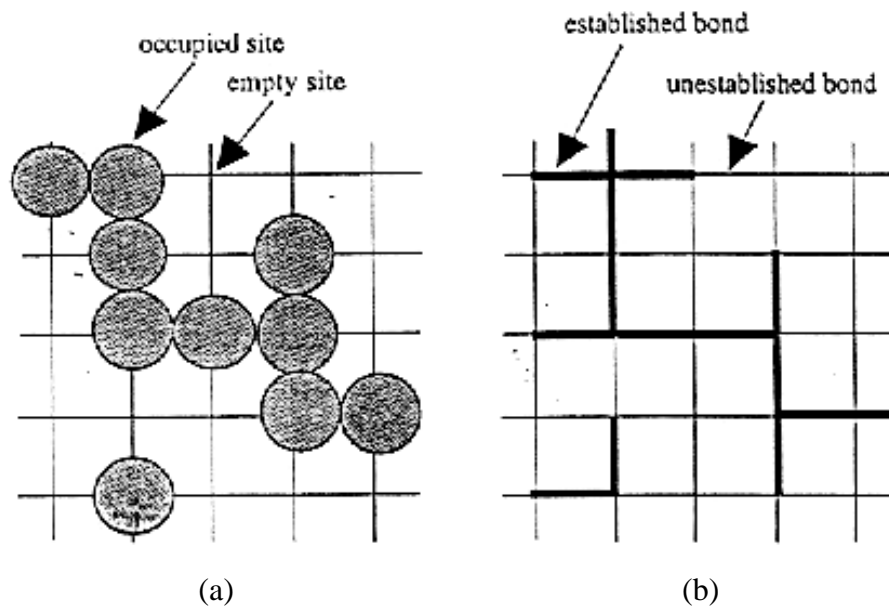


Figure 2.11 (a) Site percolation and (b) bond percolation on a square bi-dimensional network (Pierre 1998).

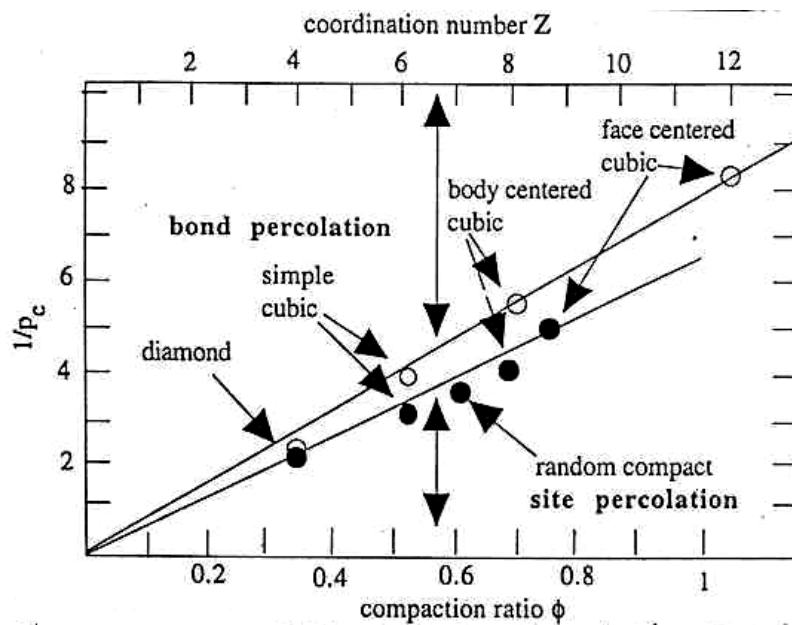


Figure 2.12 Empirical correlation between the percolation threshold and the lattice coordination for various three dimensional structures (Pierre 1998).

Another critical parameter is the percolation threshold probability p_c as shown in Figure 2.12. However, its value depends on the coordination number Z in the case of a regular site network or on the volume fraction ϕ occupied by the sites if they are replaced by hard spheres packed in a random fashion. Critical probability p_c is related to the coordination number Z by equation 2.18;

$$P_c = \xi_c = \frac{1}{Z-1} \quad (2.18)$$

Its main default is to neglect the formation of closed loops contrary to what occurs in real gelation (Pierre 1998).

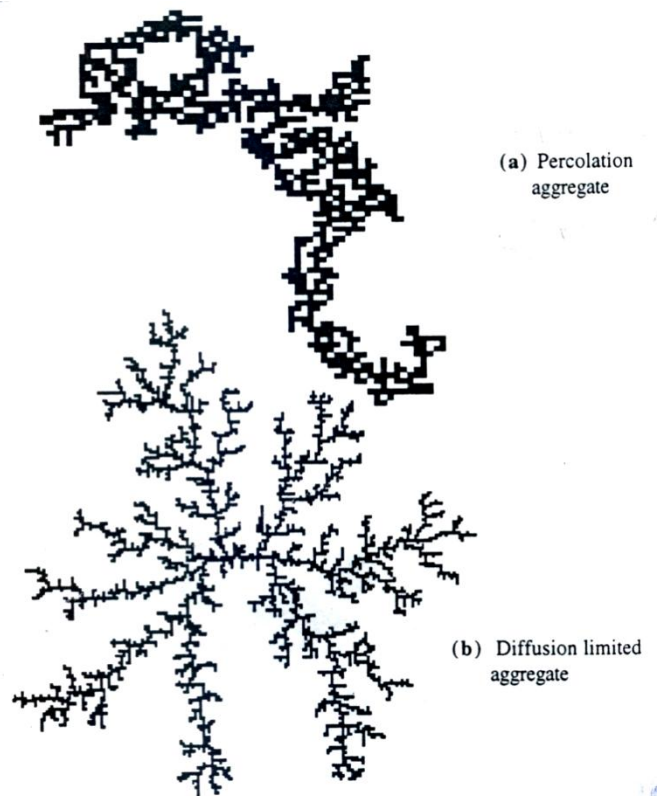


Figure 2.13 Bi-dimensional aggregates on a square lattice with different fractal dimensions: (a) aggregate near the percolation thresholds in site percolation and (b) diffusion-limited aggregation cluster comprising 3600 particles (Pierre 1998).

Diffusion limited aggregation models (DLA model) can be also described the happening. The sites at a given distance from the original nucleus are allowed to walk randomly. They may therefore either avoid meeting a nucleus or reach one of them and participate to its growth. As soon as some branches of the aggregate statistically start to grow around this nucleus, the possibility for sites to diffuse up the corridors without hitting a tendency to keep growing so that the aggregates becomes even more ramified than in the percolation models (Figure 2.13) (Pierre 1998).

Ramified structures can be observed when a large number of primary particles have aggregated. Nevertheless, a linear bonding between colloidal particles is possible in some conditions as soon as the first contacts occur and this phenomenon can be described within the Derjaguin-Landau-Verwey-Overbeek (DLVO) theory. Figure 2.14 demonstrates condition for the formation of a stable sol, gelation and coagulation as a function of the non-potential determining electrolyte C . If the concentration C of non-potential determining electrolyte is smaller than the existence of a critical concentration for gelation C_g a sol is stable. If $C_c > C > C_g$ where C_c is the existence of a critical electrolyte concentration the sol slowly gels (Pierre 1998).

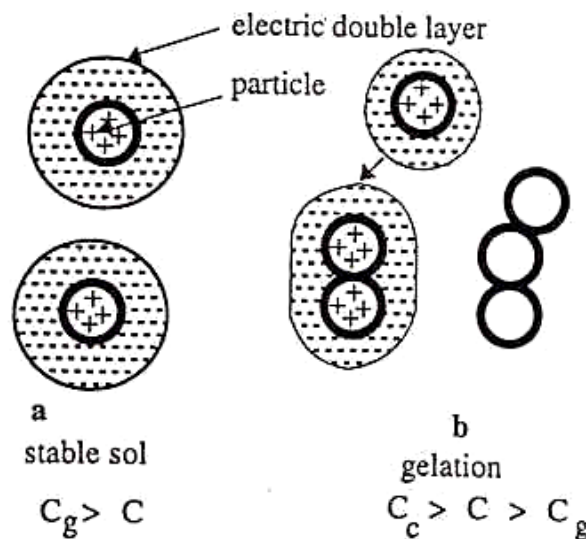


Figure 2.14 Conditions for the formation of: (a) stable sol; (b) gelation as a function of the non-potential determining electrolyte (Pierre 1998).

The molecular groups which constitute the solid network of a gel can present a more or less strong affinity for molecules in the liquid which impregnates them. This affinity can be strong enough, in some cases, to overcome the mechanical strength of the network without destroying it. That is to say, the gel swells or shrinks and in some gels such as organic polymeric gels, this change in gel volume is reversible. A polymeric gel can practically adapt one of two possible states: a shrunken state and a swollen state. These two states can coexist, exactly as a liquid and a gas state can coexist in a classical liquid-gas phase transformation.

Moreover, a critical point exists above which the gel passes gradually from one state to the other. Below the critical point is possible to obtain either one of these two states; or the coexistence of both, as in classical liquid-gas state transition. The critical point corresponds to critical conditions where the compressibility of the gel network becomes infinite; this is a true critical point in a thermodynamic sense. Overall, the state transition of a covalent polymeric gel network can be described within the theory of critical phenomena, and a state diagram can be drawn as in Figure 2.15 (Pierre 1998).

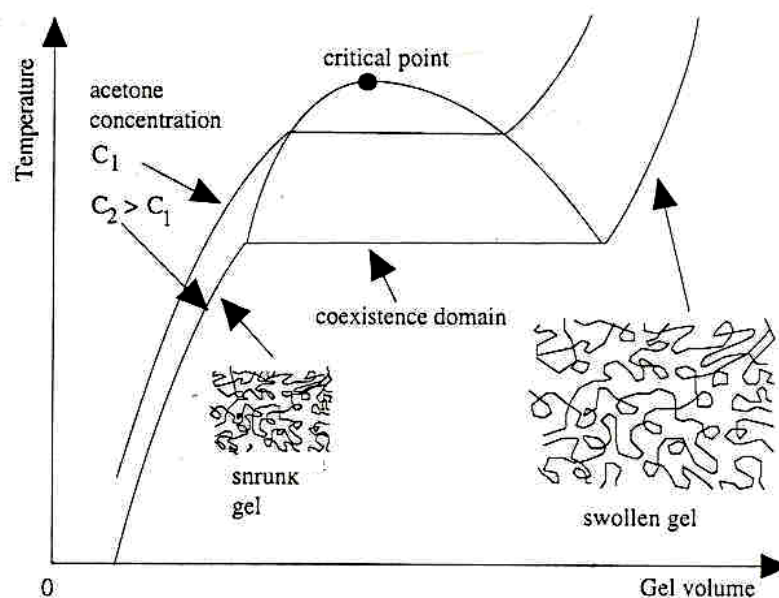


Figure 2.15 State diagram of an organic polymer gel (Pierre 1998).

2.5.5 Drying

Drying rate per unit area of gels follows two successive regimes: a “constant-rate” period, followed by a “falling-rate” period (Figure 2.16, curves a and b). The transition between these two regimes occurs at a very sharp point named the “critical-point” (Pierre 1998).

Drying is irreversible transformation of the gel which is composed of a solid network and liquid matrix. The capillary mechanism explains well the reproducible adsorption hysteresis curves of water in silica gels. This mechanism can be summarized as follows:

- ✓ Evaporation creates a liquid vapor meniscus at the exit of pores in the gel.
- ✓ This induces a hydrostatic tension in the liquid, which is balanced by an axial compression on the solid.
- ✓ The latter compression makes the gel shrink.
- ✓ As a result of shrinkage, more liquid is fed to the menisci at the exit of the gel pores, where it is evaporated and so on (Pierre 1998).

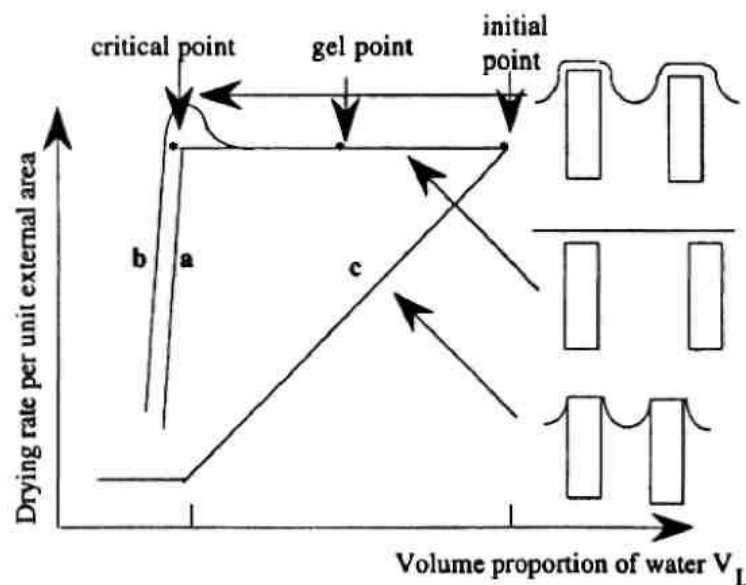


Figure 2.16 Evolution of the drying-rate per external unit area of wet gel as a function of the liquid volume proportion V_L : (a) and (b) experimental graphs; (c) graph if the drying rate was proportional to the relative surface of menisci (Pierre 1998).

Branch IC in Figure 2.17a corresponds to the initial drying of the gel. At point C, the meniscus is as in Figure 2.17b. Furthermore, it penetrates inside the gel pores which stop shrinking. Along CD, the meniscus is deeper inside the pores (Figure 2.17c), but this is a spherical meniscus with two radii of curvature equal to the radius of the pore r_{por} . Its curvature is therefore $2/r_{\text{por}}$. From D to S, only a thin layer of water remains on the cylindrical walls of the pores. The cylindrical configuration of point S maintains if water is re-adsorbed in the gel and curve SDF is followed during re-adsorption. At point F, the gel pores again full of water. Along FC, during the second desorption cycle, a spherical meniscus is formed again (Pierre 1998).

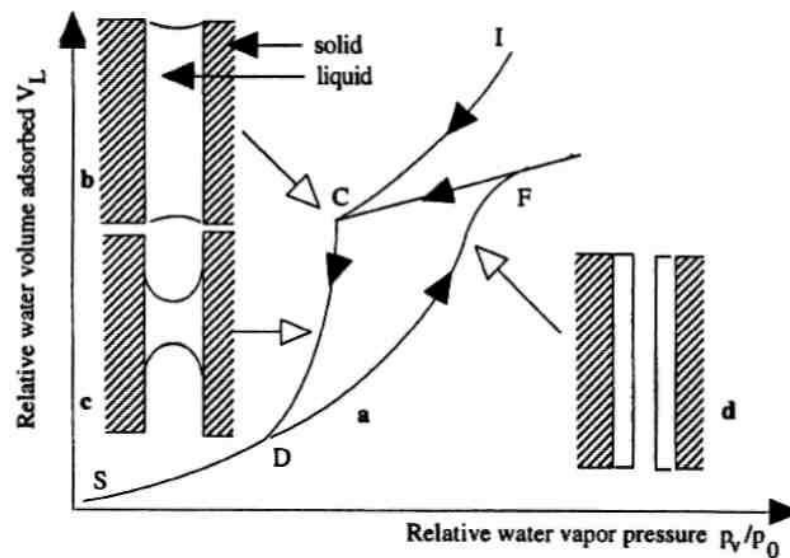


Figure 2.17 Adsorption-desorption isotherms of water vapor in a silica gel (Pierre 1998).

The equilibrium meniscus radius r_m at any instant, is given by the compressive stress that the solid network of the gel can support. The contact wetting angle at the liquid–solid–vapor interface is undetermined along a sharp solid edge. Higher stresses are required for higher compression states of the solid, which requires higher hydrostatic tension in the liquid. It follows therefore that the menisci are sharper and sharper (smaller radius r_m) when contraction increases. This keeps a gel shrinking until the meniscus radius r_m reaches the pores radius r_{por} . The latter event defines the

drying critical-point. Beyond this critical-point, capillarity cannot increase the compressive stresses anymore on the solid network (Pierre 1998).

Hence the drying rate per unit area should decrease linearly with the liquid content c . The experimental existence of a “constant-rate” period before the critical-point is therefore generally interpreted as being due to evaporation of a continuous liquid film, which covers the entire surface of the gel. Obviously, the existence of such a film can be related to the affinity of oxides for water, which depends largely on the nature of the oxide (Pierre 1998).

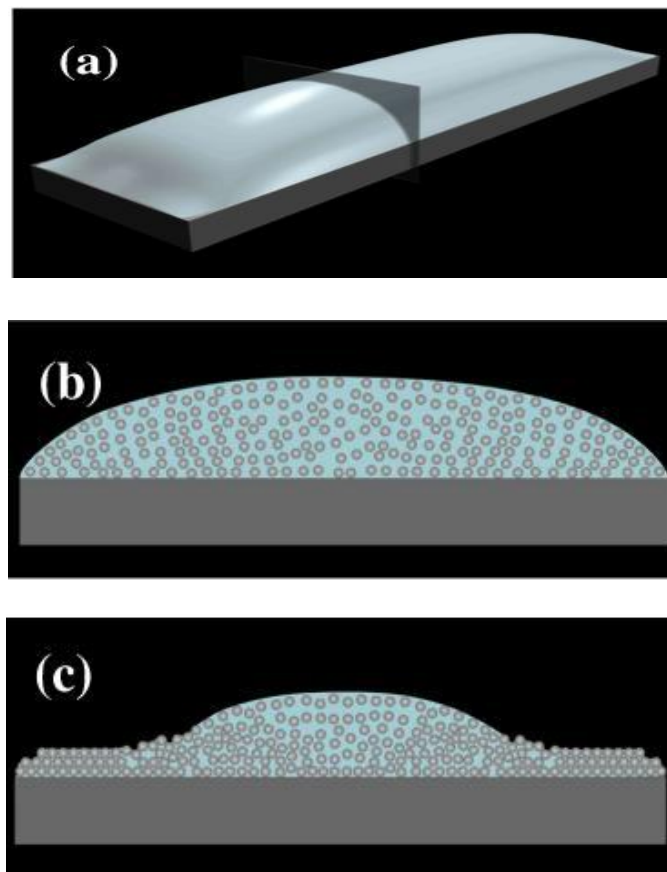


Figure 2.18 Schematic illustration of the shape evolution of ceramic films during drying (a) macroscopic view of deposited film (b) cross sectional view of the deposited film (c) cross-sectional view of the film after drying partially (Deliormanli 2007 & Martinez 2002).

Drying of ceramic films is a complex process. After casting the film is in a super-saturated state which means that there is excess liquid to fill the pores between the particles. Therefore, ceramic particles move freely in the liquid phase under the influence of the Brownian motion and capillary flow. As the evaporation starts the solids loading of the film increases and it continues until a particle network forms that can support the capillary tension created by the liquid. This tension induces compressive stress on the solid network. Since the film adheres to the substrate, contraction is allowed only in the z direction, which results in a stress in the x-y plane. The saturated state is reached when the liquid content equals the pore volume and the radius of the menisci formed by the alcohol is equal to the pore radius.

As the evaporation proceeds large pores drain first from the particle network followed by the smaller pores. Further evaporation causes a pendular state and beyond this point alcohol removal occurs by gas phase diffusion within the internal pore network (Chiu and Cima 1993, Scherer 1988 & 1990 & Rahaman 1995). Figure 2.18 denotes schematically the stages of the drying of colloidal films.

2.5.6 Sintering

The specific surface area of the porosity is an evolution named sintering. In terms of thermodynamics, sintering originates from the specific surface area S_a of a porous material, which introduces a positive contribution G_s due to the surface of pores, to the Gibbs free energy of a material:

$$G_s = \gamma S_a \quad (2.19)$$

Since states with a lower Gibbs free energy are more stable at a given temperature and pressure, the specific surface area should tend to decrease, an evolution which can proceed according to two types of pore evaluation:

- ✓ by changing the shape of pores but not their volume.

✓ by eliminating the pores.

The first type of evolution does not produce any material densification, contrary to the second one which makes a material shrink without losing any mass. Moreover, sintering is not the only transformation which involves Gibbs free energy of surface origin. Grain boundaries constitute another type of surfaces which contribute another Gibbs free energy term G_{gb} . In order to reduce this free energy contribution, the specific grain boundary area S_{gb} must decrease. Hence another evolution named grain growth enters in competition with sintering (Pierre 1998).

Sol-gel ceramics just after drying and even after heat treatments at intermediate temperatures often have a very high specific surface area and an extremely small grain size. Hence, both sintering and grain growth tend to be vigorous (Pierre 1998).

2.5.6.1 Possible Texture Evolution

If the external pressure in the pores outside the solid is p_o and the two principal curvature radii of the surface are r_1 and r_2 , the local pressure inside the solid, just under the surface is

$$p = p_o + \gamma \left(\frac{1}{r_1} + \frac{1}{r_2} \right) \quad (2.20)$$

When the local surface is convex, that is to say when the solid is on the same side as the center of curvature, a radius r must be taken with a positive value. On the other hand, when the local surface is concave, that is to say when the solid is on the opposite side to the center of curvature, the radius r must be taken with a negative sign. For sake of simplicity, it is possible to consider the case where $p_o=0$ (treatment under vacuum). In such conditions, when two spherical particles of radius r are linked by a neck with principal radii x (convex radius) and p (concave radius) at the neck tip and such that in absolute value $p \ll x$, (Figure 2.19), the mechanical stresses states inside the solid near the external surface are (Pierre 1998).:

✓ a compression far from the neck, at point A where:

$$p_A = \sigma_c = \frac{2\gamma}{r} > 0 \quad (2.21)$$

✓ a tension near the neck at point N where:

$$p_N = \sigma_t = \gamma \left(\frac{1}{x} - \frac{1}{\rho} \right) \approx \gamma \frac{1}{\rho} < 0 \quad (2.22)$$

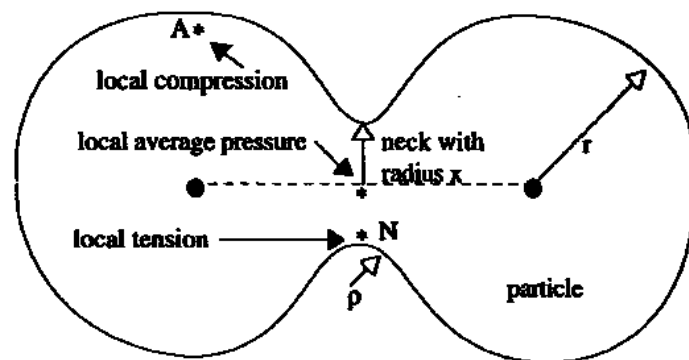


Figure 2.19 Initial sintering stage of two spherical particles (Pierre 1998).

The mechanical stress difference between points A and N is equivalent to a difference in the local Gibbs free energy of mechanical nature and it tends to attenuate by transfer of matter. Finally, the surface energy happens to be at the origin of atomic transport (Pierre 1998).

The transport of atoms to sinter a material can proceed along several different types of paths. Some of these paths actually result in densification, in particular when the atoms originate from sources, that is to say local parts of the material located along dislocations and grain boundaries, or when atoms are transported by a cooperative phenomenon known as viscous flow. Other transport paths only change the pore shape, in particular when the matter comes from the pore surface (Pierre 1998).

2.5.6.2 Atomic Transport Mechanisms Operating During Sintering

When sintering proceeds by atomic diffusion in the case of a ceramic which comprises several types of ions, each ion has to diffuse in proportion to its stoichiometry in the ceramic. Consequently, sintering is controlled by the slowest ion transported along its fastest path. If one species, for instance the anions, has the smallest diffusion coefficient, it is possible to accelerate its diffusion with the help of cations additives which have a lower valence and a size close to that of the host cation. To balance the electric charges in the compound, anion vacancies are then often created, which accelerates anions diffusion. In oxide, this concerns the oxygen anions which diffuse significantly at high temperature only. The formation of oxygen vacancies increases their mobility and can help sintering. The proportion of additives must remain below but can be close to the solid solution limit (Pierre 1998).

2.5.6.2.1 Atomic Diffusion in Sol-Gel Materials. It is possible to question whether transport mechanisms such as atomic diffusion can be extrapolated from the conventional ceramics, to the colloidal sizes. Atomic transport by diffusion in the vapor phase rests on an evaporation-condensation process due to differences in the equilibrium vapor pressure near a solid surface, depending on the local surface curvature. The equilibrium vapor pressure is lower near a neck between two particles where the solid surface is essentially concave, than far from a neck, at atomic scales. The resulting vapor pressure gradient induces a vapor phase diffusion which keeps feeding the neck. It modifies the pore shape but does not induce densification which in a gel often occurs between 900 and 1200 oC. At these temperatures, the equilibrium vapor pressure of oxygen is very low for an oxide. On the other hand, the residual hydration water usually absent in conventional ceramics is much more volatile relatively low temperatures. Hence, this mechanism cannot be completely rejected for the sol-gel processes, as water is known to be a general sintering aid. Surface atomic diffusion does not induce densification neither. However, it is like to operate at a lower temperature than usual, because of the extremely high special area of sol-gel and also because of the special nature of the gel surface which easily adsorbs water molecules or OH groups (Pierre 1998).

Overall, the atomic transport mechanisms which make the pore shape become spherical without producing any densification are likely to be common in sol-gel materials. If this is the case, these mechanisms can be strongly modified by tailoring the nature of a sol-gel solid surface, for instance by adsorbing hydrophobic molecules. Hence the liquid sol-gel chemistry can have a marked influence on the sintering behavior (Pierre 1998).

As seen previously, lattice atomic diffusion can actually densify a material, depending on the source from where the atoms originate. In a crystalline material such as an oxide, this mechanism begins to significantly operate when the atomic mobility of oxygen atoms is high enough that is to say at high temperatures. It requires the presence of atomic point defects such as vacancies, interstices or dislocations. However gels are far from being very well crystallized; they have at best very small grains with a high defects density. Consequently, depending on the compound, lattice diffusion can often operate at a much lower temperature than conventional ceramics. Actually, a distinction between the different atomic diffusion paths, such as on a surface, inside a lattice, along dislocations or along grain boundaries may be difficult in sol-gel materials, in so far as it becomes difficult to distinguish between dislocations, grain boundaries and surfaces. It would seem appropriate to consider a global diffusion process through a very disordered gel or transition phase structure (Pierre 1998).

2.5.6.2.2 Sintering and Crystallization in Sol-Gel Ceramics. In so far as densification can be considered to occur in sol-gel ceramics by global atomic diffusion, the corresponding diffusing species are also likely to enhance the crystallization by nucleation and growth of the most thermodynamically stable crystalline phase. Densification of sol-gel ceramics often occurs concurrently with their crystallization of a stable phase usually occurs at a relatively low temperature, the crystallization of a stable phase usually occurs at a slightly lower but very close temperature (Liu et al 2002).

2.6 Milling and Equipment

2.6.1 Purpose of Milling and Materials

This section includes information on equipment and procedures for milling ceramic material. Milling produces a particular particle size distribution and deagglomeration of fine powders. Physical processes include impact, shear between two surfaces, and crushing by a normal force between two hard surfaces. When a solid is fractured, energy is given off as heat from fracture, friction in the equipment, and energy necessary to create additional surface area. It is the energy from creating additional surface area that does the work sought (King 2002).

There are two broad types of ceramic raw materials that require milling. These are classified as lumpy and powdered ceramics. Lumps result from mining, fusion, and sintering. These are usually premilled by the supplier and are available in various screen sizes. Depending on technical requirements, these may require further milling in the lab. Mined materials include talc, shale (clays), bauxite, and quartz. Fused materials include fused alumina, magnesia, mullite, and zirconia. Tabular alumina, and polycrystalline grogs (coarse granules) made from alumina, mullite, and zirconia. One way of making Si_3N_4 is to heat silicon material in a nitrogen atmosphere. Carbo-thermal reactions at a high temperature are a common way to make a variety of carbides (King 2002).

Powdered raw materials usually come from chemical processes where the material in solution chemically reacts to form particles in suspension. An important class is Bayer alumina that starts as bauxite mineral. The Hall Cell fuses the bauxite with the cryolite flux forming a sodium aluminate that is then leached with caustic and washed to produce a moderately pure alumina powder. The powder is agglomerated and then milled for ceramic formulations. Several varieties are available according to crystallite size and purity (King 2002).

In other processes, the material is dissolved and is then precipitated chemically as a powder. High purity ceramic powders are sometimes made from an organic precursor decomposed to make the ceramic powder (King 2002).

Much of this knowledge is about ball mills used for processing ceramic slips. Emphasis is on fine-grained slips, with limited information on equipment for coarse materials. Some materials are more difficult to mill than others. Generally, the order of difficulty from the most difficult to the least difficult is dense-fused materials, sintered materials, and precipitated powders. Even though one might not expect this, glasses are very difficult to mill to micrometer sizes, but they are easy to crush to granules (King 2002).

2.6.2 Dry Milling

Production milling is sometimes performed dry as this avoids a separate drying step. Dry milling also avoids the formation of hard agglomerates as there is no liquid present. Dry milled ceramics are usually used in pressing operations to make a shape and to consolidate the particles. Crushing and milling are sequential processes for particle size reduction. They will be enlightened separately (King 2002).

Related to fusion is the Acheson furnace for making SiC. A pile of mix: sand, partially reacted material from a previous run, and coke is reacted by resistance heating at a very high temperature to form a "pig" of SiC that has to be crushed. Sintered raw materials include sintered clays, crushing helps reduce the particle size of hard materials to about 80 mesh using Tyler Sieves. After achieving this size reduction, other finer reduction techniques can be used in the lab. Two types of crushers are most commonly used: jaw crushers and roll crushers (King 2002).

2.6.2.1 Jaw Crushers

Jaw crushers possess two hardened steel jaws, a stationary and a moving jaw. The moving jaw reciprocates in and out while exerting a crushing force on the granules. The cavity between the two jaws is tapered so that the finer particles drop down into

the taper where they are then crushed to an even finer size. An adjustment on the width of the gap enables a jaw crusher to reduce the size of particles to about 10 mesh. Embedded particles on the jaw surfaces will contaminate subsequent batches. One can reduce contamination by running part of the new batch through the crusher and subsequently discarding it (King 2002).

2.6.2.2 Roll Crushers

Roll crushers have two counter rotating steel rolls that are about 6 inches in diameter with an adjustable gap through which the material is crushed. These crushers can crush materials to about 80 mesh. Particles that press onto the roll surfaces will contaminate future batches. Wire brushing the roll surfaces reduces contamination, but the only way to completely clean the roll surfaces is to have them machined though this is not at all practical. Roll crushers are dangerous as loose clothing such as sleeves, neckties, necklaces, or gloves can be caught between the rolls. One should avoid wearing or using anything that can be caught between the rolls (King 2002).

2.6.3 Milling

2.6.3.1 Ball Milling

Usually dry milling is done in a ball mill with a milling media. Ball mills and media are discussed later in this chapter. Portland cement is dry milled commercially using steel balls for efficiency. An alumina media about three inches in diameter is used for milling white cement where the color has to be controlled. Hard ferrites are also dry milled in air swept ball mills. Bayer aluminas are dry milled by the producer (King 2002).

In the lab, dry milling is not as common since the cost of drying is not a factor. However, when the product, which is originally wet milled in the lab, is transferred to production where it is dry milled, the properties of the powders will be different

and will cause start-up problems. Dry milling is not effective in small diameter mills as it lacks enough energy to fracture the particles. Mills with about a 12-inch diameter are suitable. Higher energy mills such as planetary and stirred mills are also available (King 2002).

A serious problem with dry milling is that the powder will cake onto the sides of the mill and will not receive further size reduction. Scraping the mill down periodically helps to reduce this caking problem. Another way to reduce the caking problem is to add a surface active agent. It is believed that Bayer alumina dry milling involves the use of ethylene glycol. Bone-dry powders have less of a caking tendency than a powder exposed to humidity. Generally, powders can be dried and immediately put into the mill while still hot (King 2002).

A stable colloid with well-dispersed particles, an optimised deposition process and the best sintering conditions are necessary if we wish to obtain a final product with the desired properties. It is known, for example, that the electrosteric stabilization of ceramic particles is easier in water, but that water-based suspensions are prone to the hydrolysis of water at potentials above 2 V. For the processing of PMN–PT thick films by electrophoretic deposition, therefore, non-aqueous suspensions are preferable over water-based suspensions since the hydrolysis of water at the electrodes can be avoided in this way. Moreover, it was shown that in water, both lead and magnesium ions preferentially dissolve from the PMN's surface in the pH range between 2 and 10. Therefore, the leaching of Pb^{2+} and Mg^{2+} in water is a major issue in the colloidal processing of PMN–PT using an aqueous medium (King 2002).

The electrophoretic deposition of $0.8\text{Pb}(\text{Mg}_{1/3}\text{Nb}_{2/3})\text{O}_3$ – 0.2PbTiO_3 particles onto platinum foils has been reported by Chen et al. The micron-sized powder was dispersed in ethanol using only an ultrasound treatment, and for the deposition they used a constant voltage of 100 V for 2 minutes. A dense, 16 μm thick film with a dielectric permittivity of 26,000 was obtained after sintering at 1100 °C. In the colloidal processing of ceramic powders, ammonium polyacrylate is a widely used

dispersant in aqueous media. The adsorption mechanism of polyacrylic acid on PMN particles in an aqueous medium was proposed by Sakar-Deliormanli in 2007. For the adsorption process above the isoelectric point, pHIIEP (pH dependence isoelectric point), chemical interactions between the ionized carboxyl group and the $M^{2+}OH$ as well as the hydrogen bonds are responsible. Below the pHIIEP the carboxylic group is bonded to the positively charged PMN particles due to the hydrogen bonds and the electrostatic interactions. However, ammonium polyacrylate is not soluble in ethanol and therefore some modifications are reported. Popa et al studied the colloidal stability of Al_2O_3 and ZrO_2 particles in ethanol (Deliormanli, 2007). They used an ammonium salt of poly-methacrylic acid that enables particle charging and the electrosteric stabilization of the suspension. An organic base n-butylamine was used to dissociate the ammonium salt of the poly-methacrylic acid (King 2002).

2.6.3.2 Jet Mills

Jet mills have two opposed jets of air that collide. These air jets also contain the ceramic particles. Often these mills are connected with an air classifier and a cyclone for recovering the fine particles. This set up is much more capital intensive than ball mills. It is also more difficult to clean between batches. Jet mills require a lot of high pressure air (80 Psi). As the particles are in free flight, there is little contamination. Nonetheless, a white powder will turn grey after milling due to the polymeric mill lining (King 2002).

2.6.4 Wet Milling

Wet milling is more frequently applied in the laboratory than dry milling. Wet milling is usually used to make a coarse-grained slip or a fine grained slip. A slip consists of a liquid vehicle, usually water, and suspended ceramic particles. Fine-grained particles are held in suspension by dispersants and other surface active chemicals. Settling is basically by Stoke`s law where larger and denser particles will settle out faster in a low viscosity liquid. This will be explained further in a later

section. Wet milling reduces the particle size for fine grained slips and disperses the agglomerates in both fine and coarse grained slips (King 2002).

2.6.5 Equipments of Mills

2.6.5.1 Jar Mills

Jar mills are cylinders with a capacity of about 0.5 liters to 2.0 liters. Many labs have larger equipment depending on their specific needs. Generally speaking, slips in the lab are made up in smaller quantities. Jar mills are generally rotated on mill racks rather than with an individual drive (King 2002).

2.6.5.2 Porcelain Mills

These mills are made from an alumina fortified porcelain. Porcelain has dispersed alumina particles in a glassy matrix. Mills and lids are slip cast, dried, and fired. The porcelain body has a composition of about 60-70 % alumina with the remainder being a glass mostly silica with some alkaline earths, usually magnesia and sometimes some baria. Bayer processed aluminas are used in the formulation. These contain about 0.4 % Na_2O in the glassy phase and about 2-3 % Na_2O that provides some fluxing and softening of the glass. Microstructure shows that there is about 10% residual porosity in the body. Porcelain bodies are not as wear resistant as 85-90 % aluminas by a factor of about four. However, most of the batch contamination during milling is from media wear rather than from the mill body. Porcelain mills are tolerable when the contamination by alumina and silica is acceptable (King 2002).

Figure 2.20 shows both porcelain and rubber jar exteriors. Porcelain has to be rotated on rubber rollers to obtain enough friction. Rubber exteriors can be rotated on either steel or rubber rollers. Hand tightening the closure is all that is required if the mill lip, gasket, and lid are kept clean. Most mill leakages occur due to failure to keep the sealing surfaces clean. Unclean surfaces can lead to over tightening and a deformation of the cross bar. Slips containing a binder dry harder though the binder

can be scraped away. Porcelain is brittle and can break if it is dropped or falls off the mill rack (King 2002).



Figure 2.20 Typical Alumina Fortified Jar Mill (courtesy of E.R. Advanced Ceramics & King 2002).

2.6.5.3 High Alumina Jar Mills

High alumina jar mills possess an alumina content of 85-90 % with the remaining being silica, alkaline earths, magnesia, and sometimes baria. Calcia is also, but rarely, used in some compositions. Bayer alumina is the principal source of alumina. It contains about 0.4 % Na_2O , which is appreciable when dissolved in the glassy bond. The microstructure has small (3-5 mm long) alpha alumina crystallites faceted in a glassy matrix. Dealers often do not distinguish between porcelain and high alumina, but there is a way to distinguish them. Porcelain is more translucent with a light grey cast, but high alumina is white and opaque. This difference is evident when the jars are held up to bright light. There is some residual porosity in the body. These pores are unusual in that they are large (10 mm) and are scattered throughout the structure in fully dense regions of crystallites and glass. These pores are probably caused by degassing the ceramic after the structure sinters to an impervious state; when gas can no longer escape and causes the body to bloat. Wear resistance of high alumina is dependent upon the alumina content, volume percent porosity, and

crystallite size. Optimum wear resistance is approached with 90 % alumina, less than 5 % porosity, and a 3 mm alumina grain diameter. Crystallite size depends on the firing temperature, which can be reduced when the green density is high. The manufacturer may have photomicrographs for perusal, or a piece which can be polished and observed. Like porcelain, alumina is a brittle ceramic and can break if it is dropped (King 2002).

2.6.5.4 High Purity Ceramic Mills

These mills are very expensive, but commercial sources can be found. The problem being that it is very difficult to slip cast relatively large shapes from these fine sized slips. However, jars made from high purity alumina, yttria stabilized zirconia, or silicon nitride have been made and used. One example is the milling of silicon nitride (Si_3N_4) where steel milling is not preferred because the acid leach affects the ceramic powder. In this case, a silicon nitride mill and media are used (King 2002).

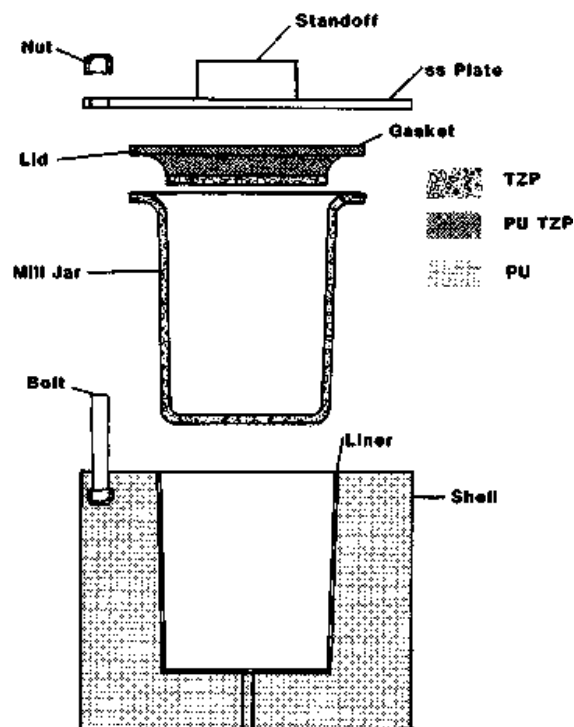


Figure 2.21 Ball Mill Assembly (courtesy of E.R. Advanced Ceramics & King 2002).

Figure 2.21 depicts experimental design; it is included here because it addresses some problems with jar mills. The ceramic-yttria-stabilized zirconia is often referred to as Tetragonal Zirconia Polycrystal (TZP). Casting grade polyurethane was used for the encasement. The gasket is polyurethane filled with TZP powder mixed on a three roll mill. By casting the gasket in place on the mill jar, a perfect fit is achieved. Most gaskets are not this tight and some slip penetrates into the join and is therefore not milled. When this happens, agglomerates get into the slip lowering the ceramic strength. This design allows the jar to be lifted out of the encasement for a clean recovery of the slip (King 2002).

With most jar mills, the slip is poured out over the lip and the top of the mill body; this adds contamination to the batch. Nevertheless, contamination does not occur here as the seal is dry and with the jar removed, the slip is not poured over the top of the mill body. Another design of vibratory mill is shown in Figure 2.22 (King 2002).

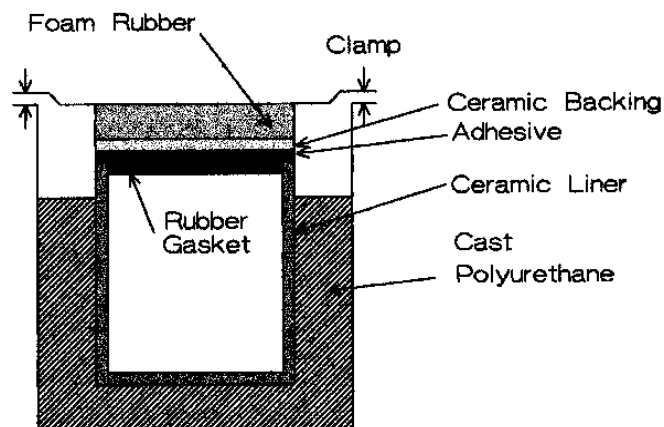


Figure 2.22 High Purity Vibratory Mill (courtesy of E.R. Advanced Ceramics & King 2002).

There are several parts to the mill: a ceramic jar, a lid with a gasket, a polyurethane casting that holds the jar in place, a foam rubber piece that holds the lid in place, and the stainless steel can and lid. The jar is removable. The milling media in this application is 3 mm in diameter and is half filled with TZP. The mill is clamped to a vibrating base. Milling is not nearly as intense as in a ball mill. In this

case, the batch is not contaminated partially due to the design and partly due to the TZP media that is extraordinarily wear resistant. During vibration, the batch does not splash up to the gasket; eliminating another source of contamination. As was stated earlier, this design is not readily utilized due to the deagglomeration of soft particles. Incidentally, stainless pots and trays are a lot less expensive when bought from a restaurant equipment supply house or department store (King 2002).

2.6.6 Milling Media

The jars hold the batch and the milling media along with the liquid that is usually water. It is the milling media that does the grinding. There are a substantial number of media choices (King 2002).

2.6.6.1 Type of Media

Composition of the media includes the following: porcelain, high alumina, pure alumina, TZP, MgO stabilized zirconia, silicon nitride, silicon carbide, steel, modified fused zircon, and a variety of mineral products such as flint, agate, or the material that is ground by itself (autogenous milling). Mineral products are cheap and can be surprisingly wear resistant. When processing fine ceramics, a general rule is to use the same composition of the media as that of the batch, if possible. For general lab applications, high alumina is perhaps the most commonly used media (King 2002).

2.6.6.2 Size and Shape

Depending on which media is selected, the size ranges from 1 mm to 3 inches in diameter. The choice of size depends on the material being milled. A general rule is to use the smallest size that has sufficient energy to fracture the particles in the batch (King 2002).

The best media shape, to obtain optimum grinding efficiency, is debatable in current literature. Most common shapes are spheres, satellite spheres, cylinders, and

round-ended cylinders. Media with sharp edges should be prerun in the mill to round off the edges; otherwise, they will tend to chip and contaminate the batch. Stirred mills present a special problem as the media can pack and overload the drive. In such cases, spherical or satellite spheres are preferred (King 2002).

2.6.6.3 Filling

Jar mills are filled about half full with grinding media. When the jar is over filled, there is not enough space for the media to tumble. When under filled, there is excessive media wear. Media that cascade with too much energy can chip or break. Sand mills have a vertical mill case and a vertical stirrer. These mills use small spheres such as quartz sand, alumina, or zirconia media. When the media is too dense, the weight of the media can prevent churning (the action that does the milling). However, horizontal stirred mills do not have this problem (King 2002).

2.6.6.4 Milling Rate

The milling rate for a given batch formulation is affected by several factors such as the mill type, media size, and media specific gravity (King 2002).

2.6.6.5 Mill Type

Stirred mills are faster than jar mills. Large diameter jar mills are faster than small diameter mills as the media cascade drops over a greater height. Speed depends on the amount of energy in the media created by the agitation. However, media energy is limited when the media starts to fracture (King 2002).

2.6.6.6 Media Size

There are more points of contact per unit volume for smaller diameter media than for larger diameter media. This increases efficiency. Stirred mills impart additional energy, and they can get away with using smaller diameter media. Lots of stirred mills use media that are 2-3 mm in diameter. However, small diameter media are more expensive than larger diameter media as the cost curve is logarithmic to

diameter size reduction. Due to cost concerns, newly designed stirred mills try to use a lesser quantity of media. However, it is important to consider the strength of the media. If the media is too weak, it will fracture and contaminate the batch. In this respect, TZP media is often the best choice, though expensive. High quality TZP is very strong and thus highly wear resistant. Inasmuch as TZP lasts a long time and results in minimal contamination, it is sometimes the preferred media and should be regarded as an excellent investment (King 2002).

2.6.6.7 Specific Gravity

The specific gravity of the media dictates the energy in the mill. High density mill balls have more energy because of their mass. Table 2.1 gives the specific gravity of commonly used materials (King 2002).

Table 2.1 Specific Gravity of Commonly Used Materials (courtesy of E.R. Advanced Ceramics & King 2002).

Material	Specific Gravity g/ml
WC/Co	13.0 - 15.0
Iron	7.8
TZP	± 6.2
Zircon	4.7
Alumina	3.98
Silicon Carbide	3.21
Silicon Nitride	3.18
Porcelain	± 2.7
Flint	± 2.62

2.6.6.8 Media Wear

Wear tests can be done by placing a specific number of specimens in a small jar mill with a 3 mm TZP media (see Figure 2.23 for details). These specimens are about the same size as the TZP media, but they vary in shape from spheres to cubes depending on what is available (King 2002).

The data that follows is based on two slips: A-16 alumina and 600 grit Silicon Carbide (SiC). After each run, the specimens were picked out with tweezers, washed, dried, and weighed. Each type of media in the test was identifiable by its color, shape, or size. As many as 8 types of grinding media can be run together and a fresh slip was used for each cycle. Table 2.2 summarizes the ceramic material and slips (King 2002).

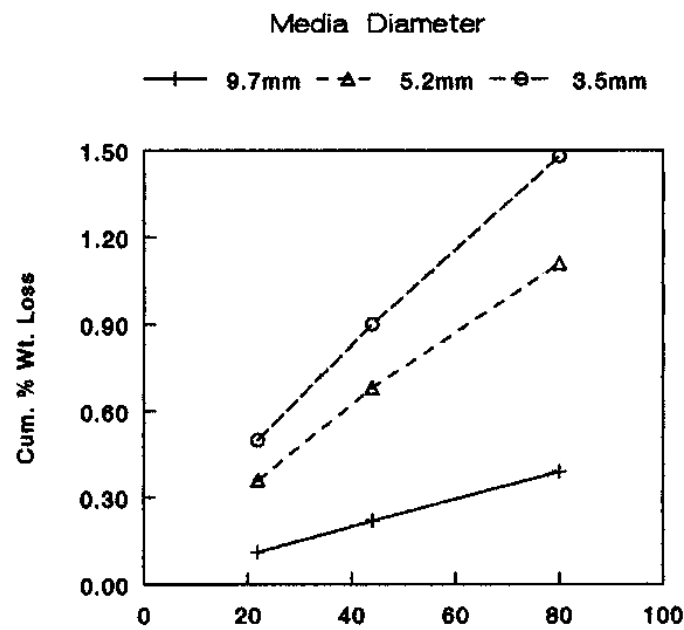


Figure 2.23 Wear of TZP vs Media Diameter (courtesy of E.R. Advanced Ceramics & King 2002).

Table 2.2 Ceramic Material vs Slips Used (courtesy of E.R. Advanced Ceramics & King 2002).

Ceramic Material	Slip
Aluminas	A-16
Zirconias	A-16
Silicon Carbide & Silicon Nitride	A-16
Aluminas	SiC
Zirconias	SiC
Silicon Carbide & Silicon Nitride	SiC

Data using commercial spherical grinding media of the modified fused zircon is shown in Figure 2.24 (Courtesy of SEPR). This material has the advantage of being cheap relative to other higher purity types. It is also durable in many applications when compared to those of severe attrition. The microstructure is of interest as it suggests a reason for the good wear resistance (King 2002).



Figure 2.24 SEPR Beads (Courtesy of SEPR & King 2002).

The microstructure of the SEPR beads is shown in Figure 2.25. Zirconia dendrites are seen in the microstructure radiating out from central sources. The matrix is a glass with silica and other constituents added during manufacture (King 2002).

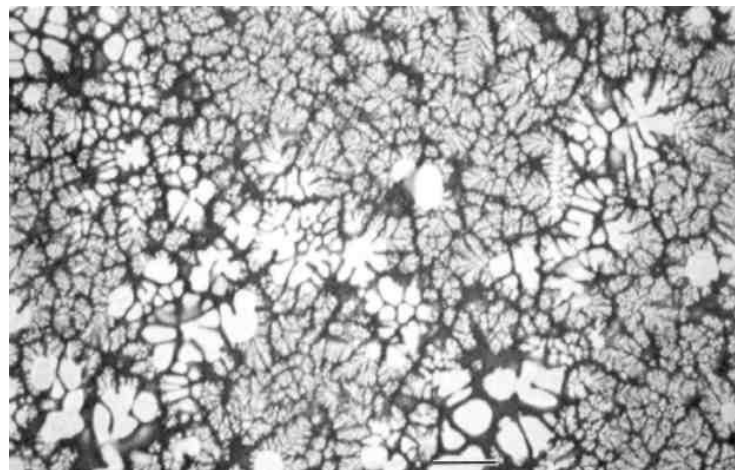


Figure 2.25 Microstructure of SEPR Beads in Polished Section (courtesy of E.R. Advanced Ceramics & King 2002).

The TZP media is much more wear resistant under highly innocuous conditions. This media has a pearly luster owing to a fully dense microstructure and a very high index of refraction. When this takes place, the wear mechanism is on a molecular scale producing the high polish. This polish is retained on the media surfaces. These TOSOH beads are shown in Figure 2.26 (King 2002).

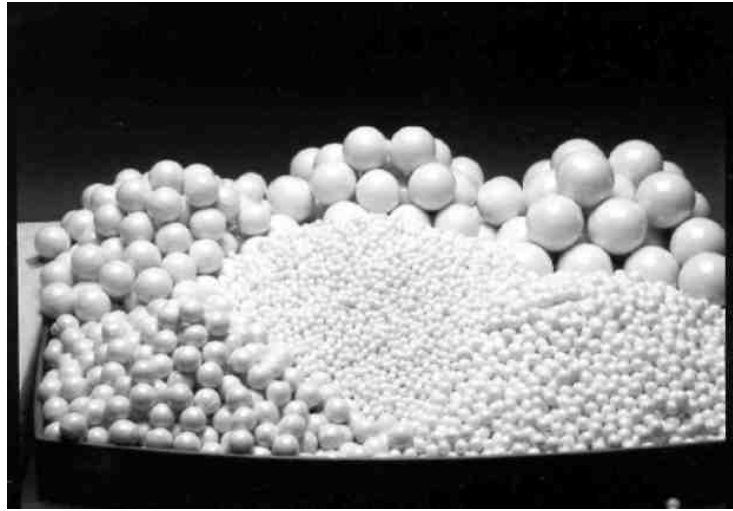


Figure 2.26 TOSOH Beads (Courtesy of TOSOH & King 2002).

2.6.7 Mill Racks

Laboratory jar mills are usually rotated on a mill rack. The rack is a steel frame with two rollers per tier with usually one to three tiers (King 2002).

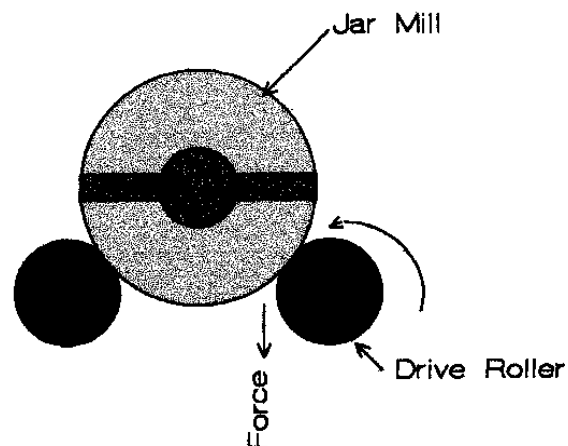


Figure 2.27 Mill Roller Direction (courtesy of E.R. Advanced Ceramics & King 2002).

On each tier, there are two rollers: a drive roller and an idler. The drive roller is usually driven with a chain and sprocket connected to a gear reduction motor. Now that mills come in different diameters, it is advantageous to have a variable speed drive and a tachometer for each tier. The drive roller must have a force vector pulling down on the mill body, as shown in Figure 2.27 (King 2002).

When the drive roller force vector pulls up, the mill will slip and not roll at the proper speed. The proper speed is 60-70 % of the critical speed. As the mill rotates, the grinding media is subjected to two accelerations: gravitational force and centrifugal force. When these are equal or when centrifugal acceleration is the greater, the media will just ride around and not do any grinding. This limiting factor is the critical speed given in the equation below (King 2002):

$$a = v^2/r \quad (2.23)$$

where a is the acceleration due to rotation, v is the velocity around the mill's internal diameter (ID), and r is the mill's ID. In most labs, there are mills of different internal diameters, therefore the mention of a variable speed drive. For each diameter, there will be an optimum rack speed. In design, there are six important factors: a gear ratio of the mechanism, a gear motor in the right speed range, a variable speed drive, a separate speed control for each tier, a tachometer for each tier, and a timer for each tier. The idler roller should be adjustable laterally to accommodate different diameter mills. Commercial mill racks usually do not have all these features, but they can be added if requested (King 2002).

There are two types of rollers: steel and rubber. For the mill to rotate properly, there should be enough friction to turn the mill body. Rubber against steel is satisfactory, where either the rubber or the steel can be on the mill or on the roller. Steel does not have enough friction against either rigid polymers or itself to turn the mill. Rubber rollers are available with molded on-end flanges that are a great help to keep the mill on the rack. Jar mills will always migrate to the end of the rack, where they will fall off without the flanges or other restraining mechanisms (King 2002).

With more than one mill on the rack, the jar mills will all migrate to one end and will rub against each other. As a result, either the closure mechanism on one mill can flip the other off the rack, or the closure on one mill can unscrew the closure on the other. If this occurs, the batch will spill over the mill-rack, onto the lower tiers, and onto the floor where it will harden. This is not an uncommon phenomenon as the jar mill diameters are different, causing the end closures to get entangled. Additionally, the mills are rotating at different centers and at different speeds; causing the closure screw to unwind, the lid to open and the batch to spill (King 2002).

The temperature of the mill batch can increase due to the friction in the mill. This in turn will cause the internal pressure to increase and possibly cause the batch to leak out of the mill. Since each ceramicist's experimental needs vary, multiple users can further complicate the management of these problems. These problems are manageable if only one person uses the mill rack at a time (King 2002).

There is an additional problem associated with the jar mills. Layers of dried slip can build up on the lid, gasket, and top of the mill body. This build-up makes it difficult to maintain a leak-proof seal. Additionally, as the bolt in the cross bar clamp is repeatedly tightened, the cross bar bends into an arc and no longer fits the ears on the mill-body. This in turn can cause the slip to spill. Keep the lid, gasket, and top of the mill body clean. Hardened slip can be hard to remove and a scraper is often needed (King 2002).

To obtain the desired particle size, the milling time is specified. Any change in that time will produce a different particle size distribution with a coarser size when the time is shorter and a finer size when the time is longer. Problems arise whenever there is a power failure or when someone turns off the mill rack to remove a mill. With the mill rack off, the time is compromised. It is not so bad if this is evident, but it is a serious problem when not evident. There has to be an understanding among people using the mill rack that the speed cannot be changed or the rack left off other than momentarily when someone else has a mill running. It would be wise to

measure the particle size distribution. If the particle size is not reasonable, one should start over (King 2002).

A commercial mill rack is depicted in Figure 2.28 (Courtesy of E.R. Advanced Ceramics). This mill rack possesses a variable speed, but the speed is the same for both tiers. This is not a problem provided the mills are all of the same diameters (King 2002).

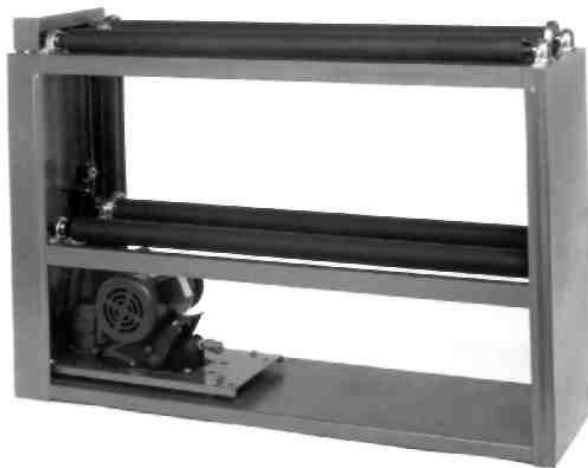


Figure 2.28 Commercial Mill Rack (courtesy of E.R. Advanced Ceramics & King 2002).

Mill racks are noisy and are generally placed in an enclosure with a door in front. A mill enclosure helps reduce noise that emanates from the mill rack, but it also makes it difficult to clean the spills and to move the mill due to its weight. The enclosure is shown for a single tier. Since the lid on the enclosure is double hinged, it is lifted away providing easy access to the rack and a better angle. This enables one to lift the mill using one's legs and not one's back (King 2002).

2.7 Colloidal Processing of Ceramics

The solid-liquid dispersions within the particle size range of 1 nm to 1 μm are generally referred to as colloidal suspensions. On the other hand, systems in which a significant fraction of particles cover a range that is greater than the colloidal range,

i.e. greater than 1 μm , are termed suspensions (Tadros 1986). Colloidal suspensions are used in widespread applications. Colloid based products include ceramics, inks, paints, cosmetics and pharmaceutical compositions (Shaw 2003, Lewis 2000). Agglomeration is a natural process for all ceramic powders because of the Van der Waals forces. This is responsible for inhomogeneities in microstructures that results in reduced mechanical and electrical properties (Deliormanli, 2007).

On the other hand, colloidal processing methods can minimize the number of heterogeneities during fabrication due to use of stable particle suspensions. The colloidal processing approach for ceramic fabrication involves: (1) de-agglomeration and stabilization of colloidal suspensions (2) preparation of slurries that include other processing additives, with desired rheological properties (3) consolidation of the slurry to pack the particles to a high density (4) drying and densification by heat treatment (Su et al. 2001, Reed 1995, Rahaman 1995). Therefore, by controlling the interparticle forces, the agglomeration between the ceramic particles can be prevented and this may result in improved ceramics with better final properties (Deliormanli, 2007).

2.7.1 Ultrasonic Dispersing and Deagglomeration

The dispersing and deagglomeration of solids into liquids is an important application of ultrasonic devices. Ultrasonic cavitation generates high shear that breaks particle agglomerates into single dispersed particles (WEB1).

The mixing of powders into liquids is a common step in the formulation of various products, such as paint, ink, shampoo, beverages, or polishing media. The individual particles are held together by attraction forces of various physical and chemical nature, including Van der Waals forces and liquid surface tension. This effect is stronger for higher viscosity liquids, such as polymers or resins. The attraction forces must be overcome in order to deagglomerate and disperse the particles into liquid media (WEB1).

The application of mechanical stress breaks the particle agglomerates apart. In addition, liquid is pressed between the particles. Different technologies are commonly used for the dispersing of powders into liquids. This includes high pressure homogenizers, agitator bead mills, impinging jet mills and rotor-stator-mixers (WEB1).

High intensity ultrasonication is an interesting alternative to these technologies. When sonicating liquids the sound waves that propagate into the liquid media result in alternating high-pressure (compression) and low-pressure (rarefaction) cycles. This applies mechanical stress on the attracting electrostatic forces (e.g. Van der Waals forces). Ultrasonic cavitation in liquids causes high speed liquid jets of up to 1000 km/h (approx. 600 mph). Such jets press liquid at high pressure between the particles and separate them from each other. Smaller particles are accelerated with the liquid jets and collide at high speeds. This makes ultrasound an effective means for the dispersing and deagglomeration but also for the milling and fine grinding of micron-size and sub micron-size particles (WEB1).

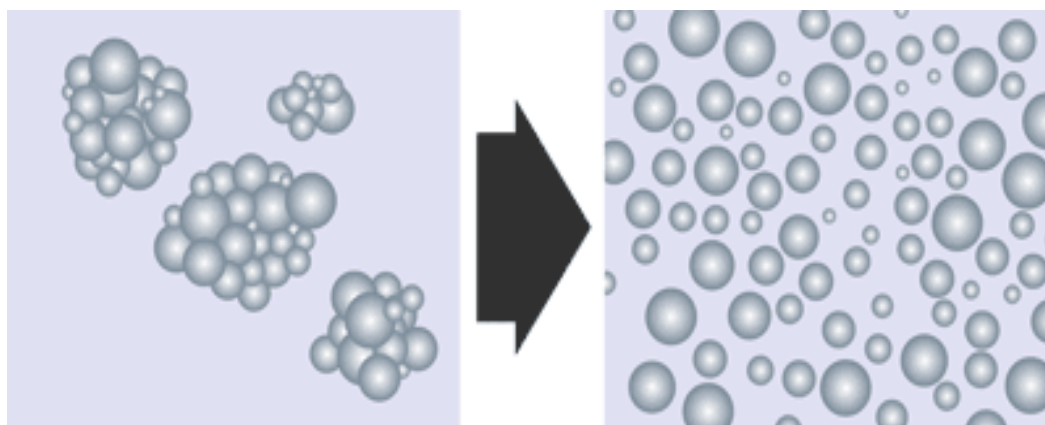


Figure 2.29 Dispersed particles using an ultrasonic cleaner machine (WEB1).

2.7.2 Origin of Surface Charge in Water

An interface may acquire an electrical charge by one or more of several mechanisms. The most common of which include (1) preferential solution of surface ions, (2) direct ionization of surface groups, (3) substitution of surface ions, (4)

specific ion adsorption, and (5) charges deriving from specific crystal structures (Myers 1999, Reed 1995).

Once a particle is immersed in an aqueous solution, it usually acquires a surface charge, either by adsorbing or desorbing ions according to some chemical equilibrium with the surrounding solution. To illustrate this, the surface of an oxide particle is hydroxylated when coming into contact with water, and undergoes proton association-dissociation reactions (Hunter 1995). As soon as the surface is exposed to water, chemical surface reactions take place between the oxygen ions and the water molecules resulting in a surface charge. The amount of surface charge depends on various parameters as the number of deprotonable surface sites per surface area and the acidity / basicity of the oxide surface (Rezvan 2005). The deprotonation of the oxide surface is illustrated in Figure 2.30 using alumina as an example.

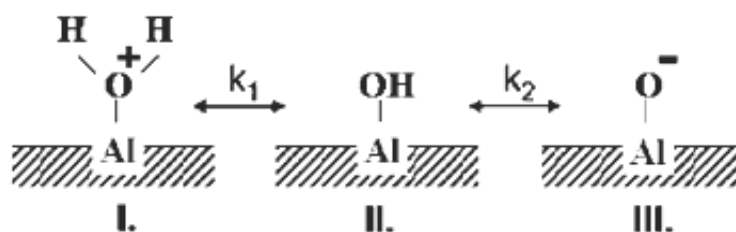


Figure 2.30 Reaction of water at the alumina surface: I. Protonated, II. Neutral, III. Deprotonated state (Rezvan 2005).

The surfaces of metal oxides contain OH-groups which are amphoteric and can either take up a proton at low pH or leave one proton at a high pH. At low pH the surface is positively charged while at high pH the surface is negatively charged. At a certain intermediate pH level, the oxide surface is neutral and the point of zero charge can be expressed as a pH value. The PZC is usually measured in the presence of electrolytes. In many cases, one or both of the ions can adsorb on the surface. The PZC is then dependent on both the proper surface properties and also the content of the dispersion medium. If the medium does not contain any ions which specifically adsorb on the surface, the PZC is only dependent on the material in the colloidal particles. Such a PZC is known as a pristine point of zero charge (PPZC) (Holmberg et al. 2002).

As it is discussed before the net surface charge of a hydrous oxide is determined by the proton transfer and reactions with other cations and anions. In general, the net surface charge density of a hydrous oxide is given by:

$$C_p = F[\Gamma_H - \Gamma_{OH} - \Sigma(Z_M \Gamma_M) - \Sigma(Z_A \Gamma_A)] \quad (2.24)$$

where C_p is the net surface charge in Coulombs m^{-2} , F is the Faraday constant, Z is the valency of the sorbing ion, Γ_H , Γ_{oh} , Γ_m and Γ_a is the sorption densities of H, OH, metal ions and anions respectively. The point of zero charge can be given as where $C_p=0$ (Stumm 1992).

The net proton charge, the charge due to binding of protons or H^+ ions is given by:

$$C_H = F[\Gamma_H - \Gamma_{OH}] \quad (2.25)$$

The aquatic particles has electric charge and this charge is balanced by the charges in the diffuse layer which move freely in solution and remain near enough to colloid surface to create the effective (counter) charge C_d that balances C_p therefore $C_p+C_d=0$. This is often referred to as isoelectric point. It is the point where particles do not move in an applied electric field (Stumm 1992).

2.7.3 Interactions in Colloidal Suspensions

Ceramic suspensions can be either stable or flocculated depending on the interactions between the colloidal particles. The total interparticle potential V_{tot} is given by the following equation:

$$V_{total} = V_{VDW} + V_{elec} + V_{steric} + V_{dep} \quad (2.26)$$

where V_{VDW} is the attractive potential energy due to long-range Van der Waals interactions between particles, V_{elec} , is the repulsive potential energy arising from electrostatic interactions between charged particle surfaces, V_{steric} is the repulsive

potential energy arising from steric interactions between particles coated with adsorbed polymers, and, V_{dep} is the potential energy created by the presence of nonadsorbed polymeric species in solution (Lewis 2000, Israelachvili 1991).

2.7.4 Van der Waals Interactions

The origin of Van der Waals forces lies in the dipole or induced–dipole interactions at the atomic level. There are three major types of Van der Waals forces: Debye, Keesom and London (Dispersion) forces. These three terms describe permanent dipole–induced dipole, permanent dipole–permanent dipole and induced dipole–induced dipole interactions. The London (Dispersion) force is always present, like the gravitational force, as it does not require the existence of permanent polarity or charge–induced polarity. The contribution of the Van der Waals attraction to the total interaction depends to a large extent on the separation distance between the particles and the magnitude of the repulsive force at this separation (Tadros 1986, Larson 1999, Napper 1977, Rezvan 2005).

The strength of Van der Waals forces increase for interactions between colloidal particles as typically each particle has a large number of atoms or molecules. But Van der Waals forces are only effective over short distances of typically 0.2–3 nm which is the reason why colloidal suspensions do not coagulate instantly (Rezwan 2005).

In 1937 Hamaker, derived equations for these forces on the basis of additivity of Van der Waals energies between pairs of atoms or molecules, and assuming these energies to be proportional to the inverse sixth power of the distance. Casimir and Polder introduced the influence of retardation at large separations (Overbeek 1977). The Van der Waals interaction energy between two spherical interacting particles (see Figure 2.31) of the same material separated by a distance, H , is given by (Pashley and Karaman 2004):

$$V_{\text{VDW}} = -A_{121} \cdot a / 12H \quad (2.27)$$

where A_{121} is the Hamaker constant .

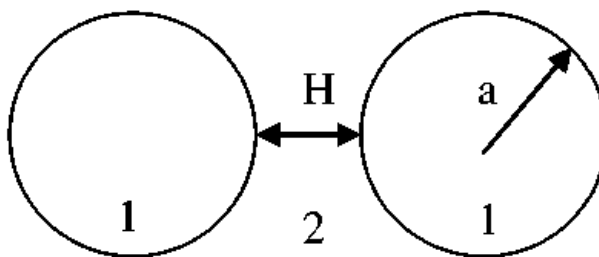


Figure 2.31 Diagram of two colloidal spheres separated by a distance H (Rezvan 2005).

2.7.5 Electrostatic Interactions

The ions of opposite charge which are dissolved in water, known as counterions, are attracted towards the surface. Nonetheless, they do not simply stick to the surface, but form a diffuse layer of charge adjacent to the surface due to the balance between their electrostatic and entropic energy. The surface charge plus the diffuse layer of opposite charge constitute an electric double layer. When two particles approach each other, the two double layers interpenetrate, causing a repulsive force between them. Figure 2.32 denotes schematically the model including the Stern layer and diffuse double layer (Hunter 1995, Pashley and Karaman 2004, Rezvan 2005).

In Figure 2.32 the surface potential (ψ_o) is defined as the potential found at the surface (x_o). The zeta potential (ψ_ζ) is defined as the potential obtained at $x = x_\zeta$. The zeta potential can be obtained from electro kinetic potential measurements such as electrophoresis but never directly the surface potential. However, at very low ionic strengths, the surface potential can be approximated by the zeta potential, that is $\psi_o \approx \psi_\zeta$ (Hunter 1995). Therefore, the stability of aqueous colloidal systems can be controlled by generating like-charges of sufficient magnitude on the surfaces of suspended ceramic particles. The resulting repulsive Velect exhibits an exponential distance dependence whose strength depends on the surface potential induced on the interacting colloidal particles (Lewis 2000, Kingery et al. 1976). For the diffuse layer the Poisson-Boltzmann equation can be written in one dimension:

$$d^2\Psi / dx^2 = -(e / \varepsilon) \sum z_i n_{i_0} \exp(z_i e\Psi / kT) \quad (2.28)$$

where ψ is the potential at a distance x from the surface, ε is the permittivity of the medium, n_{i_0} is the bulk concentration of ions of charge z_i , e is the electronic unit charge, k is the Boltzman constant and T is the absolute temperature. For the assumption of low charge ($z_i e\Psi / kT < 1$) cases this equation can be written as:

$$\Psi(x) = \Psi_\delta \exp(-KX) \quad (2.29)$$

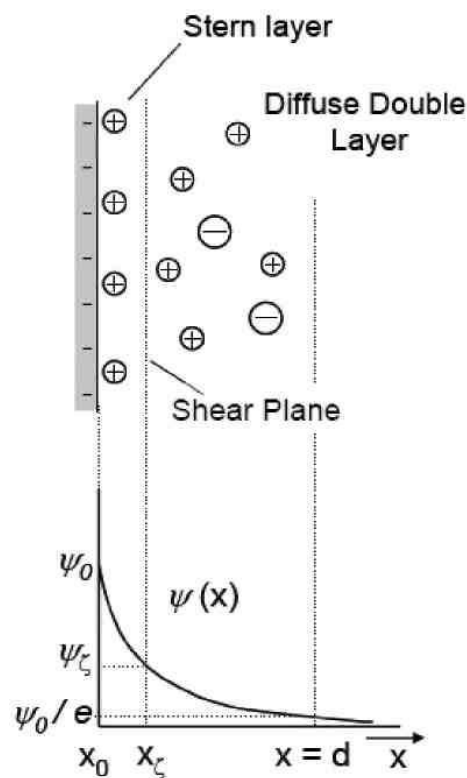


Figure 2.32 Schematic presentations of the electrical potentials develop through the electrical double layer (Rezvan 2005).

In the low surface potential limit electrostatic potential between two particles is given by Derjaguin approximation:

$$V_{elect} = 2\pi\varepsilon_r\varepsilon_0 a\phi_0^2 \exp(-Kh) \quad (2.30)$$

where K is known as the inverse Debye length (Overbeek 1977).

2.7.6 The DLVO Theory

The interaction potential in charged stabilized systems can be described approximately by the Derjaguin-Landau-Verwey-Overbeek (DLVO) theory (Myers 1999, Hunter 1995, Su 1997). DLVO theory determines the stability of a given colloid in a suspension through the balance between the repulsive and attractive forces as they approach each other. Figure 2.33 signifies the total interaction potential graph of a system in the presence of electrostatic repulsive and Van der Waals attractive terms (Ma et al. 2003, Yoshioka et al. 1997).

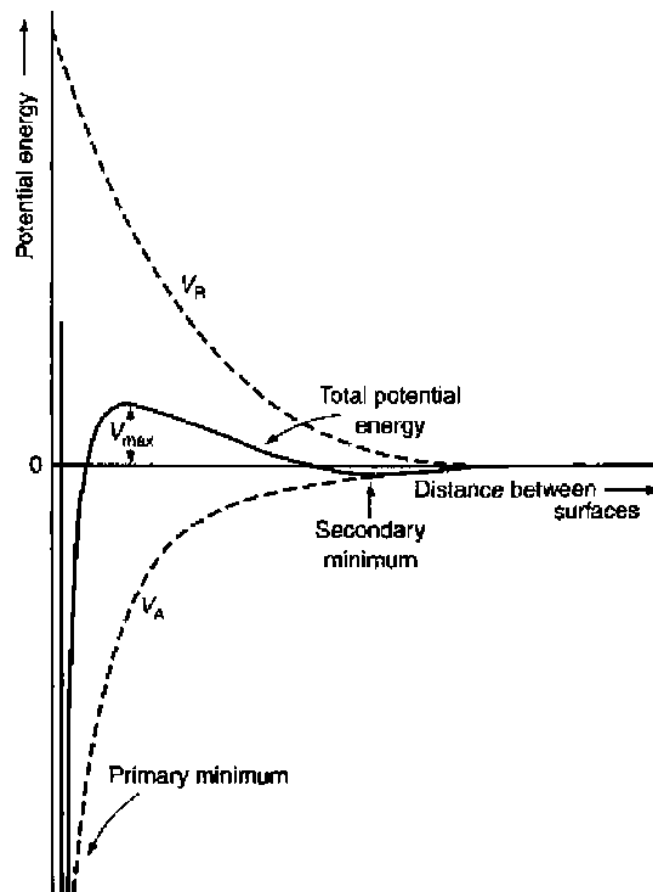


Figure 2.33 Schematic presentation of the total interparticle potential in the presence of attractive van der Waals and repulsive electrostatic forces. (Source: Adapted from Sato and Ruch 1980), (Deliormanli 2007).

The sharp increase of VR at very close approach is due to the repulsion between the electron clouds of atoms of the particles and is referred to as the Born repulsive energy. In the dispersed state, particles that exist in the suspension repel each other on close approach, provided the repulsive barrier is greater than kbT. In the weakly flocculated state, particles aggregate in a shallow secondary minimum (well depth ~ 2– 20 kbT), forming flocs in suspension (Lewis 2000, Polat M and Polat H 2000). Yoshioka and co-workers reported that suspended particles coagulate when the minimum of the potential curve becomes smaller than -5 kT. The particles that are in weak flocculation have a tendency to disperse again, with aid of the mechanical energy when the value approximately above 5 kT (Yoshioka et al. 1997, Deliormanli 2007).

2.7.7 Steric Stabilization

When two particles with adsorbed polymer layers approach each other at distances of separation of their surfaces of less than twice the thickness of the adsorbed layer, interaction of two particles takes place (Sato and Ruch 1980). The degree of stabilization can be defined in terms of the energy change occurring during the interaction. The free energy of change for the interaction can be written as (Hesslink 1971):

$$\Delta G = \Delta H - T\Delta S \quad (2.31)$$

where ΔH is the enthalpy change, ΔS is the entropy change and T is the temperature.

Steric stabilization can be achieved when one (or more) of the following conditions are met: good solvent conditions, good surface coverage, thick adsorbed layer, strongly bound adsorbed layer (Myers 1999). Good solvent conditions (When Flory Huggins parameter, $\chi < 0.5$) are desired, due to the fact that the interaction energy between the polymer chains is repulsive. The repulsive interaction arises since the polymer segments prefer to be surrounded by solvent rather than by other polymers. Therefore, good solvent conditions results in a greater coil size which

yields a thicker layer. Nevertheless, in poor solvent conditions ($\chi > 0.5$) the polymer prefers to be surrounded by itself rather than solvent owing to the attractive interactions between segments (Ogden 1996, Netz and Andelman 2003). Effect of solvent quality on the polymer coil size is shown schematically in Figure 2.34.

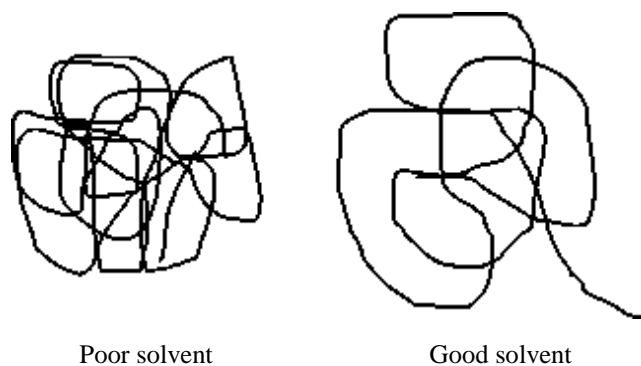


Figure 2.34 Schematic presentation of the effect of solvent quality on polymer coil size (Deliormanli 2007).

Linear polymer molecules in solution in general form random coils, which may be described as three-dimensional random walks in space. For "ideal" chains, consisting of non-interacting statistical units (segments), with molecular weight M , polymer in solution has a Gaussian segment density distribution and the coil radius of gyration is proportional to M . However, real segments possess volume and interact with each other. For a pair of segments, an interaction (or excluded) volume can be defined in terms of the (effective) segment-segment interaction energy. In theta solvents ($\chi = 0.5$), chains behave "ideally". In better solvents, segments repel each other and a more realistic model for that case is a chain without self-intersections, the statistical analog of which is called a "self-avoiding walk". In this model radius of gyration is proportional to M (Cohen-Stuart et al. 1986, Napper 1977).

In concentrated solutions, coils overlap and interpenetrate so that the interaction between segments becomes even more important. In the "classical" polymer solution theory of Flory and Huggins, the thermodynamic properties of the solution were calculated assuming that, for the interaction of a segment with its surroundings, all other segments could be considered as "smeared out" (i.e., a segment would have the

same probability of meeting a segment of its own chain as one from a different chain). This is referred to as a mean field approach. As soon as chain overlap occurs, a polymer solution can be understood as a transient network with an average "mesh size", which depends on the extent of overlap and hence on the concentration. For distances smaller than the mesh size, the distribution of segments is correlated because segments interacting with each other will experience the full excluded volume. For distances larger than mesh size the correlation is lost because segments are screened from each other by other chains and the behavior is that of an ideal chain. The description of overlapping coils ("semi-dilute" solutions) in terms of mesh size is commonly referred to as the "scaling theory" of semi-dilute polymer solutions (Cohen- Stuart et al. 1986, Napper 1977).

Many theories have been proposed to explain the adsorption of charged polymers and steric stabilization mechanism (Vincent 1974). According to the Sato and Ruch, most of these theories may be divided into two major categories. The first one is the entropic stabilization theory and the second is the osmotic (or heat-mixing repulsion) stabilization theory (Sato & Ruch 1980 & Shaw 2003).

In the entropic stabilization theory, it is assumed that the second surface approaching the adsorbed layer is impenetrable. Therefore, the adsorbed layer is compressed and the polymer segments contained in the interaction area loose configurational entropy. This reduction in entropy increases ΔG and this produce repulsion between the particles. In this theory, the enthalpic interaction between the adsorbed molecules and the dispersion medium is neglected, therefore the equation becomes, $\Delta G = -T\Delta S$. The theory was first initiated by Mackor and van der Waals. Then Hesselink, Vrij and Overbeek described this entropic effect as the volume restriction effect (Sato & Ruch 1980, Shaw 2003, Overbeek 1977 & Vincent 1974).

In contrast, the osmotic repulsion theory assumes that adsorbed layers can overlap each other when the two particles collide. It also assumes that no desorption occurs on collision. In this model the polymer segments are in contact with molecules of the dispersion medium. This contact is reduced as a result of the contact between the

segments in the overlapped region and this result in the enthalpy of mixing, ΔH_{mix} . On the other hand, as a result of the segment concentration in the overlapped region, there is also reduction in the configurationally entropy of the adsorbed molecules. Therefore, the total free energy changes due to overlap of the adsorbed layers can be expressed as a function of both enthalpic and entropic change (Hesselink et al. 1971):

$$\Delta G_M = \Delta H_M - T\Delta S_m \quad (2.32)$$

In other words, as the segment density increases the segment-segment interaction increases and the segment-dispersion medium interaction decreases. The change in the mixing free energy depends on the magnitude of these two interactions. Figure 2.35 shows schematically the steric potential between two particles as a function of particle separation (Sato & Ruch 1980 & Shaw 2003).

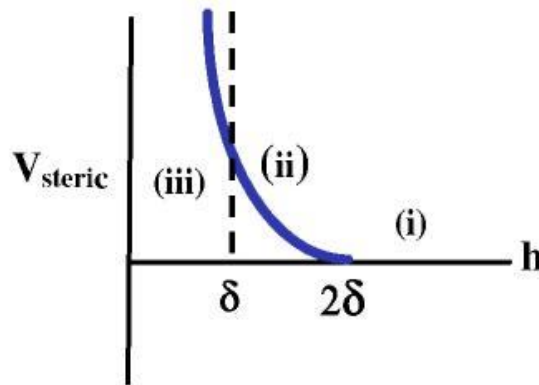


Figure 2.35 Schematic presentation of (a) $h \gg 2\delta$, no interaction, $V_{\text{steric}} = 0$, (b) $h \sim 2\delta$ or less and $\delta < h \leq 2\delta$ repulsion due to entropic, mixing effects, (c) $h < \delta$ repulsion due to mixing + strong repulsions due to elastic restoring forces (Deliormanli 2007).

To summarize, the interaction between the polymer chains on the particles may be separated into (a) mixing effect that produces either repulsion or an attraction and (b) an elastic effect that is always repulsive. The mixing effect is also described as osmotic effect, whereas the elastic effect is described as an entropic effect or volume

restriction effect (Figure 2.36). The free energy of the polymeric interaction can be written as (Napper 1977, Rahaman 1995):

$$\Delta G_{steric} = \Delta G_{mix} + \Delta G_{elastic} \quad (2.33)$$

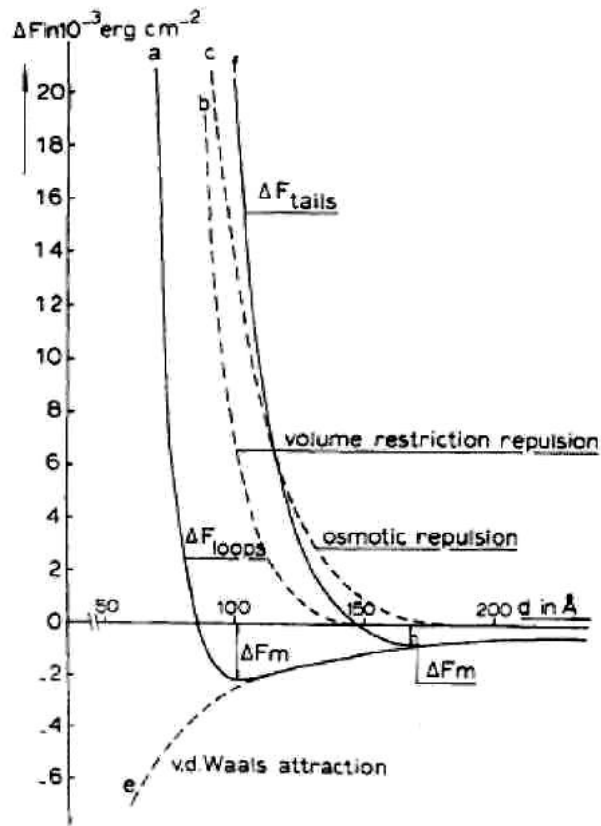


Figure 2.36 Total interaction potential graph that demonstrates the effect of osmotic repulsion and volume restriction components (Hesselink et al. 1971, Deliormanli 2007).

2.7.8 Depletion Interactions

This type of interactions arises when polymeric species are in the non-adsorbed state or free in solution (Lewis 2000). Depletion interactions can be attractive or repulsive, depending on the polymer concentration. At low concentrations, when particles approach each other at separation distances less than the effective coil diameter ($2R_g$) the coils are excluded from their gap. As a result, an osmotic pressure

difference occurs between the surrounding bulk polymer solution and the pure solvent in the gap. This osmotic pressure difference drives the particles together and induces flocculation. On the other hand, at high polymer concentrations the coils will begin to overlap in solution and prevent a close approach of particles hence will create stabilization (Blackman 1996, Vincent et al. 1986). The depletion potential depends on the size of the polymer and can be approximated by:

$$V_{depletion} = -\rho R_g kT \quad (2.34)$$

where p is the number density of the polymer, R_g is the radius of gyration of the polymer, k is the Boltzmann's constant, and T is the temperature.

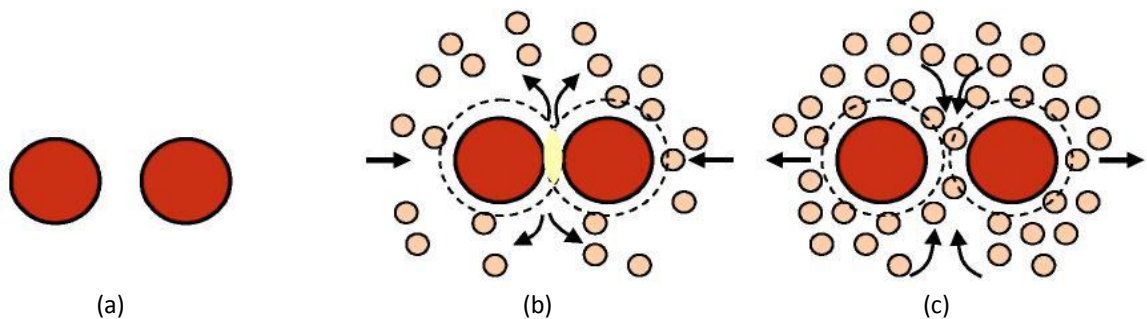


Figure 2.37 Schematic representation of the interactions in the presence of free polymer (a) initial, (b) flocculated and (c) restabilized states (Deliormanli 2007).

Vincent and co-workers reported that addition of free (non-adsorbing) polymer chains to the continuous phase causes a weak, reversible flocculation occurs beyond some critical volume fraction of free polymer, however restabilisation occurs at an even higher volume fraction of polymer (Vincent et al.1986). This phenomenon is presented schematically in Figure 2.37, showing the interactions in the presence of free polymer indicating initial, flocculated and restabilized states (Deliormanli 2007).

2.8 Coating Techniques

Among the continuous coating, drop and spin coating seems to be a simple and suitable method for coated electronic materials such as conductors, semiconductors

and insulators. The general steps of drop and spin coating include immersion of the substrate into the drop coating solution, start-up, where withdrawal of the substrate from the solution begins, film deposition, solvent evaporation and continued drainage as the substrate is completely removed from the liquid bath. The film thickness formed in drop coating is mainly governed by the viscous drag, and surface tension. The final thickness of the drop or spin coated capacitor film depends on the concentration of the coating solution and the substrate withdrawal speed during the coating process. For coating long length tapes or large area films at industrial scale, dropping and spin coating techniques are very suitable to minimize the use of solution and both faces can be coated simultaneously (Araki et al.2003).

Spin coating has been used for several decades for the application of thin films. A typical process involves depositing a small puddle of a fluid resin onto the center of a substrate and then spinning the substrate at high speed (typically around 3000 rpm). Centripetal acceleration will cause the resin to spread to, and eventually off, the edge of the substrate leaving a thin film of resin on the surface. Final film thickness and other properties will depend on the nature of the resin (viscosity, drying rate, percent solids, surface tension, etc.) and the parameters chosen for the spin process. Factors such as final rotational speed, acceleration, and fume exhaust contribute to how the properties of coated films are defined.

One of the most important factors in spin coating is repeatability. Subtle variations in the parameters that define the spin process can result in drastic variations in the coated film. The following is an explanation of some of the effects of these variations.

A typical spin process consists of a dispense step in which the resin fluid is deposited onto the substrate surface, a high speed spin step to thin the fluid, and a drying step to eliminate excess solvents from the resulting film. Two common methods of dispense are Static and Dynamic dispenses.

Static dispense is simply depositing a small puddle of fluid on or near the center of the substrate. This can range from 1 to 10 cc depending on the viscosity of the

fluid and the size of the substrate to be coated. Higher viscosity and or larger substrates typically require a larger puddle to ensure full coverage of the substrate during the high speed spin step. Dynamic dispense is the process of dispensing whilst the substrate is turning at low speed. A speed of about 500 rpm is commonly used during this step of the process. This serves to spread the fluid over the substrate and can result in less waste of resin material since it is usually not necessary to deposit as much to wet the entire surface of the substrate. This is a particularly advantageous method when the fluid or substrate itself has poor wetting abilities and can eliminate voids that may otherwise form.



Figure 2.38 Schematic illustration of the commonly used coating techniques (Schwartz, 2004).

In spin coating process, the substrate is held in place on the spinner by applying a vacuum to the back side of the wafer through a chuck that is attached at the end of the spinner motor shaft. The wafer is typically flooded with solution during a “static dispense” using a syringe. The wafer is then accelerated rapidly to 1000-6000 rpm and the spinning time can vary from seconds to few minutes. Spin coating is a very convenient technique for the laboratory scale production of PMN capacitor films because a very small volume of solution is used, and an accurate control of the film thickness can be achieved by controlling the precursor viscosity, spinning rate and time. Higher speed and longer spin time results in thinner film, but at very high spin speed and long spin time, the film thickness becomes constant.

2.9 Dielectric Phenomena

The most basic defining electrical property of dielectric materials is the permittivity (ϵ_r), also known as the “dielectric constant”. This characteristic value illustrates the ability of a material to be polarized under an applied electric field (E). The permittivity depends considerably on the frequency of the applied electric field, the chemical structure, the defects of the material, and on external parameters such as ambient pressure and temperature (Kao 2004).

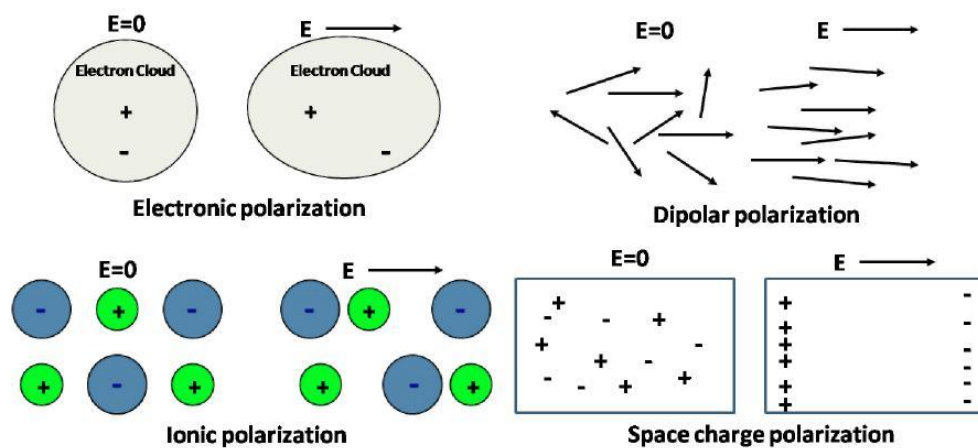


Figure 2.39 Schematic representations of various polarization mechanisms (Moulson & Herbert 2003).

A dielectric material is made up of atoms or molecules that exhibit at least one of the following types of polarization schematically represented in Figure 2.39: electronic polarization (P_{el}), in which the applied field displaces the electronic charge relative to the atom nucleus to give a dipole, ionic polarization (P_{ion}), in which cations and anions are displaced in opposite directions from their original equilibrium bonded positions in the crystal structure and this gives rise to ionic dipoles, dipolar orientation (P_{dip}), in which polarization is due to alignment of permanent dipoles, and space charge polarization (P_{sc}), the migration of charged internal defects when an electric field is applied (Moulson & Herbert 2003). The total polarization under an applied electric field is given by Equation 2.35 and this arithmetically sums the contribution:

$$P_{tot} = P_{el} + P_{ion} + P_{dip} + P_{sc} \quad (2.35)$$

Now that each type of polarization requires time to respond, the degree of total polarization depends on the time variation of the electric field. Dipoles cannot keep shifting orientation direction when the frequency of the applied electric field exceeds their relaxation frequency, and therefore, will not make a contribution to the permittivity.

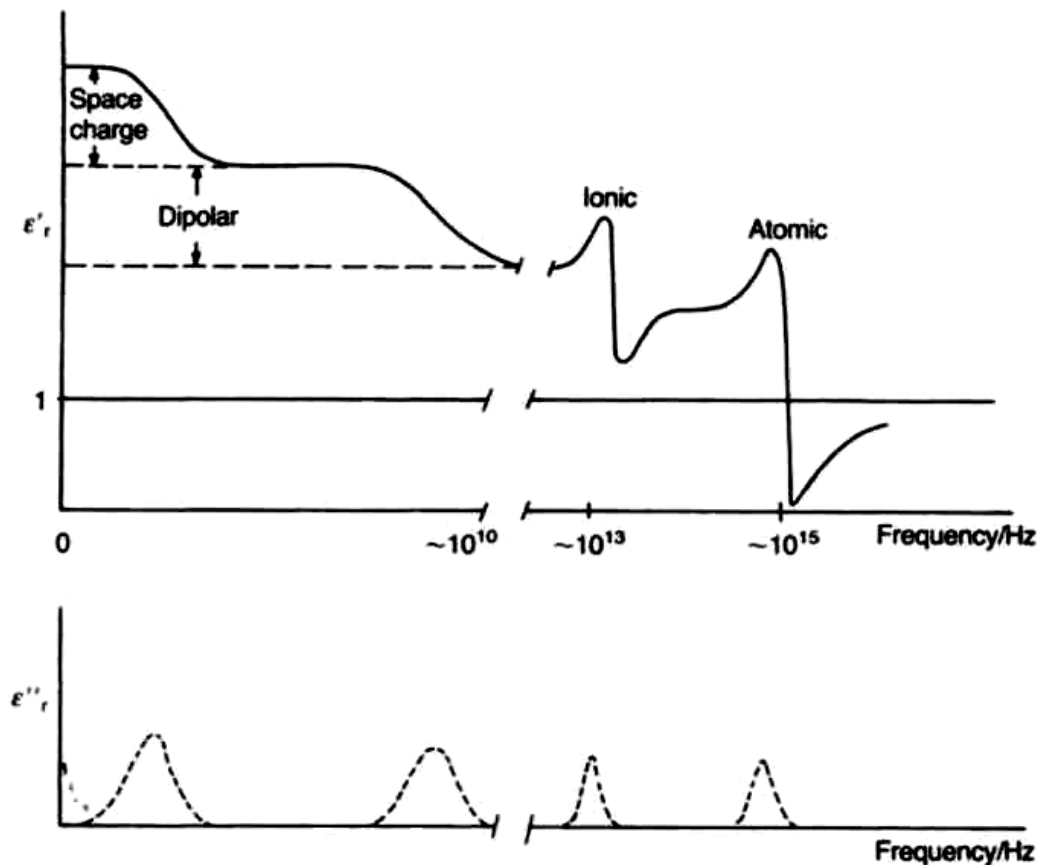


Figure 2.40 Frequency dependence of real and imaginary part of the permittivity. (Moulson & Herbert 2003).

While for the electronic and ionic mechanisms a resonance can be observed when the frequency matches the natural angular frequency of the oscillating mobile species, relaxation processes are characteristic of dipolar and space charge polarization at low frequencies. The real and imaginary components of the

permittivity for a material that shows the four types of polarization are shown in Figure 2.40.

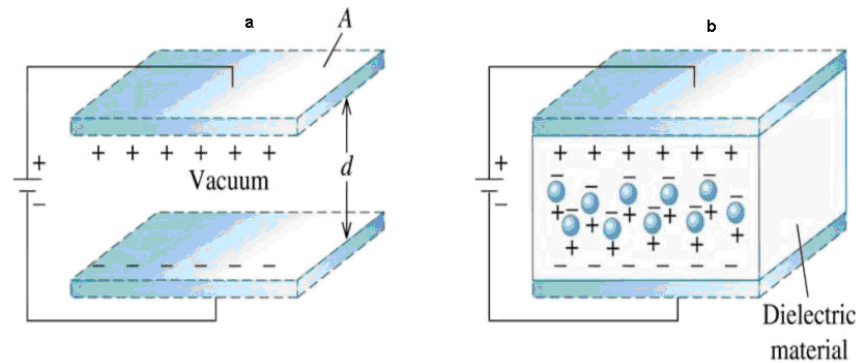


Figure 2.41 Parallel plates capacitors (a) with vacuum between plates and (b) with a dielectric material (Moulson & Herbert 2003).

The relationship between the permittivity and the polarization of a material can be understood in terms of the dielectric displacement (\vec{D}). This parameter represents the surface charge density and is proportional to the applied electric field in a parallel plates capacitor as represented in Figure 2.41.

When a dielectric material is present between the plates, the displacement is given by Equation 2.36:

$$\vec{D} = \epsilon_0 \epsilon_r \vec{E} \quad (2.36)$$

where ϵ_0 is the permittivity of the vacuum ($8.85 \times 10^{-12} \text{F/m}$). In the presence of a dielectric, the surface charge density on the plates of a capacitor may also be represented by:

$$\vec{D} = \epsilon_0 \vec{E} + \vec{P} \quad (2.37)$$

By manipulating Equations 2.36 and 2.37 the polarization can be shown to be proportional to the applied field (Equation 2.38).

$$\vec{P} = \epsilon_0 (\epsilon_r - 1) \vec{E} \quad (2.38)$$

When a time varying electric field is applied across a parallel-plate capacitor, the polarization does oscillate with the field. In order to properly describe the dielectric losses produced by the effective friction of the electric dipoles during reorientation, the permittivity is expressed as a complex number as described in Equation 2.39 (Moulson & Herbert 2003):

$$\epsilon^* = \epsilon' - j\epsilon'' \quad (2.39)$$

where $j = \sqrt{-1}$.

In an AC circuit, the dielectric loss is a function of a phase angle between the current and the applied voltage. The loss is usually expressed in terms of $\tan\delta$, given by the ratio between the imaginary and the real part of the permittivity, as represented in Figure 2.42. For a perfect insulator material $\tan\delta=0$. For practical applications, it is desired to have $\tan\delta$ values as close to 0 as possible. The losses have various origins: the internal inelastic scattering of charge carriers during their migration, the friction in the polarization processes and in ferroelectrics, domain walls motion can provide significant contribution to dielectric losses in poly domain materials (Kao 2004).

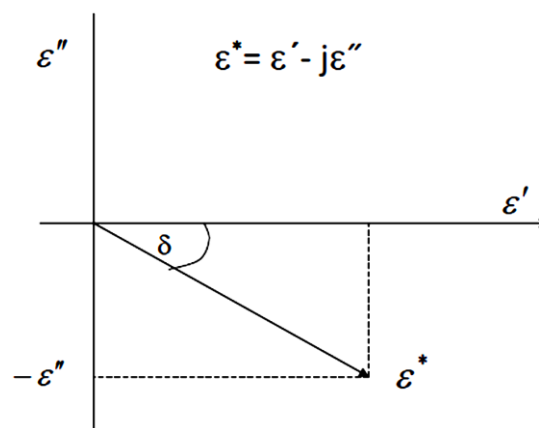


Figure 2.42 Schematic of the real vs. imaginary component of permittivity (Kao 2004).

2.9.1 Ferroelectric Materials

The polarization induced by an applied field in regular dielectric materials is relatively small, yielding a permittivity in most cases smaller than 100. However, a number of crystals with a non-centrosymmetrical structure can display permittivity values up to 105. Those materials, ferroelectrics, satisfy the conditions as shown in Figure 2.43 (necessary conditions but not sufficient): poled materials exhibit piezoelectric behavior, upon the application of mechanical stress, electricity can be generated in the crystal, and pyroelectricity, meaning heat generated electricity in structures with a spontaneous polarization.

Materials that exhibit these effects must be polar, thus when undergo a small change in dimension electric polarization occurs and have an electrical order meaning that they may be crystalline. A ferroelectric material is defined as being a polar dielectric for which a spontaneous dipole polarization can be switched between two or more equilibrium symmetry equivalent states by the application of an appropriate electric field at certain temperatures (Damjanovic 1998).

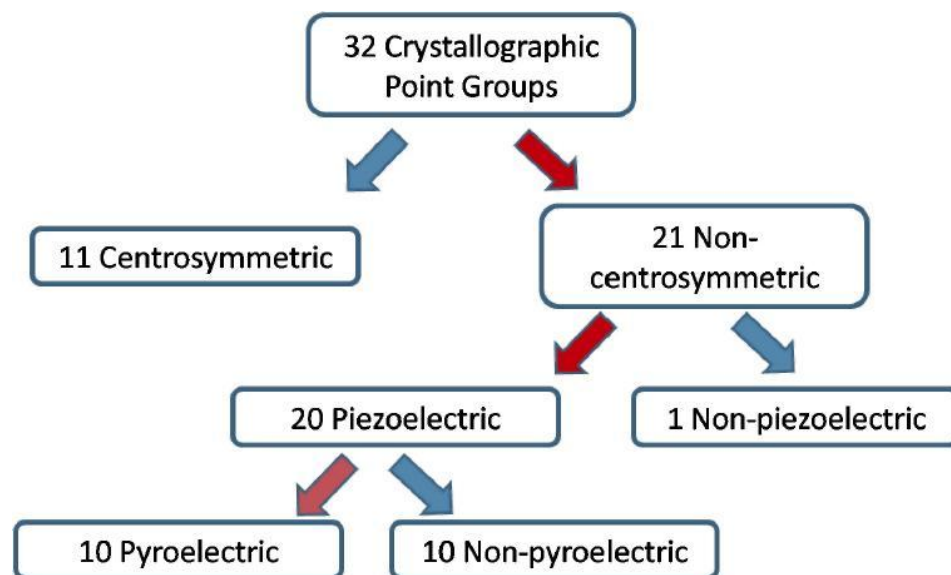


Figure 2.43 Classification of crystals according to their structure and properties. Ferroelectric materials have to be pyroelectrics and piezoelectrics (Moulson & Herbert 2003).

In addition to reversible spontaneous polarization, ferroelectric materials exhibit hysteresis loops that can be appreciated at temperatures below the paraelectric-ferroelectric transition temperature as schematically represented in Figure 2.44.

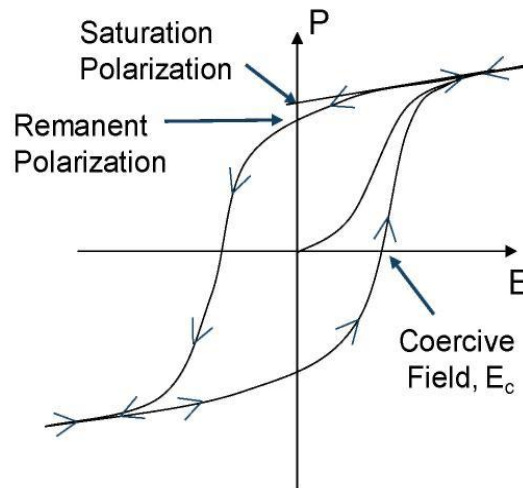


Figure 2.44 Characteristic (P-E) hysteresis loops for a ferroelectric material (Moulson & Herbert 2003).

The spontaneous polarization in a ferroelectric crystal is in most cases not homogeneously aligned all over the crystal along the same direction. The directions along which the polarization will extend depend on the mechanical and electrical boundary conditions across the specimen. The uniformly oriented spontaneous polarization regions of the sample are called ferroelectric domains, the region between domains is called domain wall. These domains are created to reduce the electrostatic energy of depolarizing fields and the elastic energy related with mechanical constraints to which the material is exposed as it is cooled through the paraelectric-ferroelectric phase transition (Newnham 1975).

The occurrence of the hysteresis loops in ferroelectric materials can be considered in terms of domain-wall orientation. At small values of the AC electric field, the polarization increases linearly with the applied field, at this point the field is not strong enough to switch domains not aligned with the field direction. As the field increases in value, the polarization of domains with other orientations will start to

switch in the direction of the field, in this region the polarization response is nonlinear. Nonetheless, once the majority of the domains are aligned the behavior becomes linear again. When the field strength decreases the domains will start to switch back, but at zero field some polarization remains (remanent polarization). To reach a zero polarization the sign of the field have to be reversed (coercive field). In an ideal hysteresis loop this pattern is symmetrical having the remanent polarization and coercive field the same value at positive and negative values of the applied field. The mechanism of polarization switching is complex and has been analyzed by many authors in terms of domain-wall motion by nucleation and growth (Jaffe et al. 1971). It is believed that domain wall motion is the principal contributor to dielectric losses in ferroelectric materials with well controlled resistivities (Uchino & Hirose 2001).

The first ferroelectric material was reported in 1921 by Valasek (single crystal Rochelle salt) (Valasek 1921). Some years later, in 1935 Busch and Scherrer in 1935, reported ferroelectricity in potassium dihydrogen phosphate, but it was not until the second world war when the more stable compound, BaTiO_3 , was discovered simultaneously in the United States, Russia and Japan that ferroelectricity begun to be studied systematically for practical applications (Randall et al. 1971). Since then, hundred of ferroelectric materials have been discovered. Among the oxide ferroelectrics, many are titanates, niobates and tantalates with a perovskite crystal structure or a similar one based on oxygen octahedra.

2.9.2 Conduction Mechanisms in Metal-Dielectric Systems

As the thickness of the dielectric layers decreases to improve the volumetric efficiency of the capacitors, the electrical behavior of the thin films is expected to differ from that of the bulk materials. Two main reasons can be anticipated to cause this variation. The first one is that at very thin layers the conductivity will be more dependent on the interface. In addition to that, the thin dielectric layers are prepared by different routes than bulk materials leading to variations in the physical properties.

The leakage current mechanisms are usually considered, in the literature, in terms of the metal-semiconductor junctions' theory (Nagata et al. 2006). It was Wilson (1931) who first formulated the transport theory of semiconductors based on the band theory of solids (Dechakupt 2008). This theory was applied to the metal-semiconductor contacts. Some years later Schottky (1938) suggested that a potential barrier could arise from space charges in the semiconductor side of the contact. This model will be known as the Schottky barrier (Sze 1981).

When a metal is making contact with a semiconductor, the Fermi level (E_f) in the two materials line up at thermal equilibrium. The barrier height (Φ_B) will be given, as represented in Figure 2.45 by the difference between the metal work function (Φ_m) and the electron affinity of the semiconductor (χ_s). The metal work function is the energy difference between the vacuum level (E_o) and the Fermi level, the electron affinity in the semiconductor is the energy difference between the bottom of the conduction band (E_c) and the vacuum level.

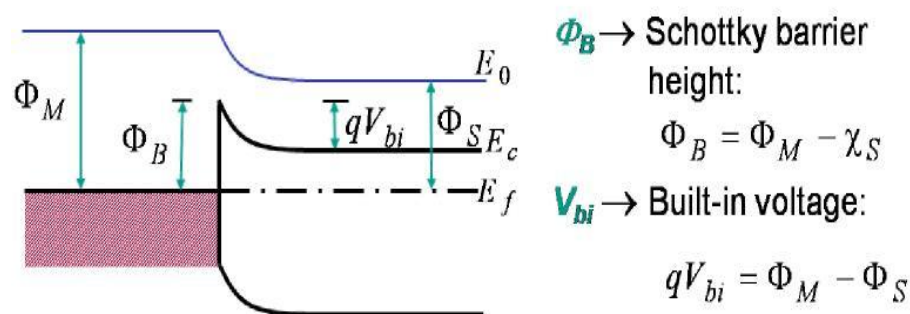


Figure 2.45 Metal-semiconductor junction at equilibrium (Sze 1981).

The mechanisms controlling conduction in perovskite-titanate based thin films capacitors have been investigated by a few groups in the last years, mainly on $\text{Ba}_x\text{Sr}_{1-x}\text{TiO}_3$ for use in dynamic random access memory devices (DRAM) (Wilson 1931). Several mechanisms have been proposed in the literature to govern the leakage current of metal-oxide-metal films.

2.9.3 Reverse Bias Schottky Emission

Probably the most common mechanism for leakage current in base metal multilayer BaTiO₃ capacitors is Schottky conduction (Yang et al. 2004, Chazono and Kishi 2001, Morita et al. 2007), with the high oxygen vacancy concentration in BaTiO₃ leading the dielectric to act as an n-type semiconductor. This mechanism results from the thermionic emission of an electron from a metal electrode into the conduction band of a semiconductor.

When an electron is situated near the metal in the semiconductor, a positive charge is induced on the metal surface, creating an attraction of the electron to the metal. The resultant attraction force is called the image force. Whilst the image force tends to attract the emitted electrons back to the metal, the driving force due to the applied field tends to drive the electrons away from the metal (Kasap and Capper 2006). This effect is schematically represented in Figure 2.46. The result is a lowering in the barrier height given by:

$$\Delta\Phi_B = \alpha E^{1/2} = \left(\frac{q^3 E}{4\pi\epsilon} \right)^{1/2} \quad (2.40)$$

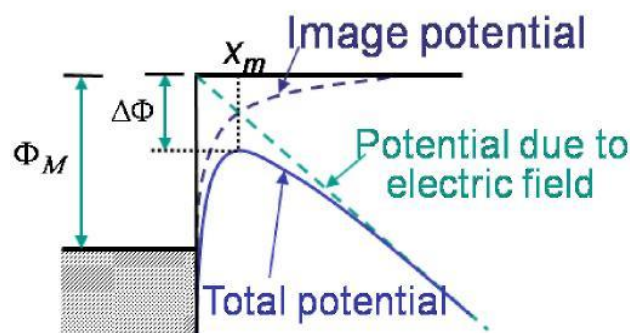


Figure 2.46 The effective barrier is lowered when an electric field is applied to the surface (O'Dwyer 1973).

The current density (J) under the reverse bias Schottky effect control is given by Equation 2.41 when $qV > 3k_B T$

$$J = A^* T^2 \exp\left(\frac{\alpha E^{1/2} - \Phi_B}{k_B T}\right) \quad (2.41)$$

where A^* is the Richardson constant modified to take into account the semiconductor properties. Further refinements can be made to this basic theory, such as corrections for interfacial surface states and images forces, to model the potential energy barrier (O'Dwyer 1973).

2.9.4 Poole-Frenkel

The Poole-Frenkel effect may be the dominant mechanism when electric conduction is bulk limited. Poole-Frenkel conduction involves trapped electrons or holes. The traps are generally close to the edge of the bandgap. The conduction method is dependent on the presence of an electric field. The effect of the applied field is to lower the potential barrier enough to allow a trapped electron to escape. In this conduction mechanism electrons jump from trap to trap under the influence of the electric field. The Poole-Frenkel effect is similar to the Schottky effect, but the amount of barrier lowering due to the Poole-Frenkel effect is twice that of the Schottky effect as the Coulombic attractive force to an electron is twice as large for the Poole-Frenkel effect (Kao 2004). The lowering of the barrier height resultant from the Poole-Frenkel effect is given by Equation 2.42

$$\Delta\Phi_B = \beta E^{1/2} = \left(\frac{q^3 E}{\pi\epsilon}\right)^{1/2} \quad (2.42)$$

The field and temperature dependence of the Poole-Frenkel dominated conduction is described in Equation 2.43

$$J = BE \exp\left(\frac{\beta E^{1/2} - \Phi_B}{k_B T}\right) \quad (2.43)$$

where Φ_B in this case represents the Poole-Frenkel potential barrier and B is a constant dependent on the properties of the semiconductor material.

2.9.5 Fowler-Nordheim (FN) Tunneling

Under high field, the quantum mechanical tunneling of electrons through a potential barrier from a metal to a semiconductor is a strong possibility. Tunneling through thin dielectric films can take place if the barriers are sufficiently thin or contain a large number of defects (Dietz et al. 1997). In that case electrons can tunnel directly from one electrode into the other without charge carrier movement in the conduction band of the dielectric. A schematic representation of an electron tunneling is shown in Figure 2.47. This kind of emission described by Fowler and Nordheim in 1928 was reported to be the main conduction mechanism at a particular range of fields and temperatures (mainly high fields and low temperatures) for $\text{Ba}_{1-x}\text{Sr}_x\text{TiO}_3$ (Ahn et al. 2003 & Hwang et al. 1999,) and BaTiO_3 (Morita et al. 2007) films.

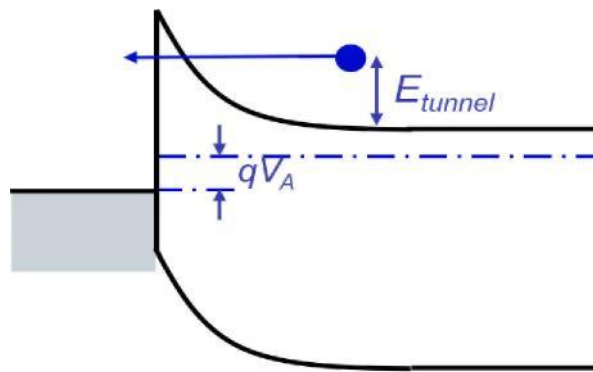


Figure 2.47 Schematic diagram illustrating an electron tunneling through a potential barrier (Kao 2004).

The current density due to FN tunneling can be described by (Kao 2004):

$$J = CE^2 \exp(-E_o/E) \quad (2.44)$$

C and E_o are constants related to the effective mass of the electron and the potential barrier respectively.

2.10 Some Application for Capacitor

2.10.1 *Electronic filter*

Electronic filters are electronic circuits which perform signal processing functions, specifically to remove unwanted frequency components from the signal, to enhance wanted ones, or both. Electronic filters can be:

- ✓ passive or active,
- ✓ analog or digital,
- ✓ high-pass, low-pass, band-pass, band-reject (band reject; notch), or all-pass,
- ✓ discrete-time (sampled) or continuous-time,
- ✓ linear or non-linear, and
- ✓ infinite impulse response (IIR type) or finite impulse response (FIR type).

The most common types of electronic filters are linear filters, regardless of other aspects of their design. The oldest forms of electronic filters are passive analog linear filters, constructed using only resistors and capacitors or resistors and inductors. These are known as RC and RL single-pole filters respectively. More complex multipoled LC filters have also existed for many years, and their operation is well understood.

Hybrid filters are also possible, typically involving a combination of analog amplifiers with mechanical resonators or delay lines. Other devices such as CCD delay lines have also been used as discrete-time filters. With the availability of digital signal processing, active digital filters have become common.

2.10.2 *Defibrillator*

An automated external defibrillator (AED) is a portable electronic device that automatically diagnoses the potentially life threatening cardiac arrhythmias of ventricular fibrillation and ventricular tachycardia in a patient, and is able to treat

them through defibrillation, the application of electrical therapy which stops the arrhythmia, allowing the heart to reestablish an effective rhythm. AEDs are designed to be simple to use for the layman, and the use of AEDs is taught in many first aid, first responder and basic life support (BLS) level CPR classes.

Defibrillation is the definitive treatment for the life-threatening cardiac arrhythmias, ventricular fibrillation and pulseless ventricular tachycardia. Defibrillation consists of delivering a therapeutic dose of electrical energy to the affected heart with a device called a defibrillator. This depolarizes a critical mass of the heart muscle, terminates the arrhythmia, and allows normal sinus rhythm to be reestablished by the body's natural pacemaker, in the sinoatrial node of the heart. Defibrillators can be external, transvenous, or implanted, depending on the type of device used or needed. Some external units, known as automated external defibrillators (AEDs), automate the diagnosis of treatable rhythms, meaning that lay responders or bystanders are able to use them successfully with little, or in some cases no training at all.

2.10.3 Flash of Camera

Capacitor stores the energy to work a flash. A flash is a device used in photography producing a flash of artificial light (typically 1/1000 to 1/200 of a second) at a color temperature of about 5500 K to help illuminate a scene. A major purpose of a flash is to illuminate a dark scene. Other uses are capturing quickly moving objects or changing the quality of light. Flash refers either to the flash of light itself or to the electronic flash unit discharging the light. Most flash units are electronic, having evolved from single-use flashbulbs and flammable powders. Modern cameras often activate flash units automatically.

Flash units are commonly built directly into a camera. Some cameras allow separate flash units to be mounted via a standardized "accessory mount" bracket (hot shoe). In professional studio equipment, flashes may be large, standalone units, or studio strobes, powered by special battery packs or connected to mains and

synchronized with the camera from either a flash synchronization cable, radio transmitter, or are light-triggered. Only one flash unit needs to be synchronized with the camera, which in turn triggers the other units.

CHAPTER THREE

EXPERIMENTAL STUDIES

3.1 The Aim of Thesis

Now that PMN based materials and related topics possess a huge potential for future electro-ceramic applications, the present research is challenging as the main interest of this thesis. In the project, we are intending to produce very fine, pure PMN based powders with perovskite structure (pyrochlore-free) using sol-gel method. Effects of the rare earth (Eu, Er, Sm, Tb and Dy) dopants on the characteristic properties such as crystal system, surface morphology, mechanical and electrical properties of the PMN ceramics have been studied in details. With this respect, the aim of this thesis is to clarify preparation, characterization, development and application of PMN based nanoparticles and films using as a combination of colloidal suspension and deposition methods such as spin and drop coating systems using sol-gel technique. The new approach is to explore both the science and technology of how RE dopants affect PMN structure and connect the results to materials properties, and show the engineering concepts that can be used to produce or improve an electronic device by design.

In order to determine solution characteristics which influence thin film structure; turbidity, pH values and rheological properties of the prepared solutions were measured by turbidimeter, pH meter and rheometer machines before drying and heating processes. Prior to coating process, substrates which were used such as silica glass and Si(100) were cleaned in 1:1 methanol-water medium with ultrasonic cleaner. In order to use suitable process regime and to define chemical structure and reaction type of intermediate temperature products, DTA-TG and FTIR analyses were performed in the powder production using xerogels produced at different temperatures. Structural analysis of the powders was performed through multipurpose XRD. The other objective of this study was to synthesis and characterization of PMN thin films by a suspension containing PMN nanoparticles

derived from sol-gel process technique. Surface morphologies of the films were investigated using SEM/EDS and AFM. Thickness measurements of the films were investigated through refractometer and spectrophotometer. The mechanical properties of the PMN films were scrutinized by means of DUH and scratch testing machines. The dielectric properties and I-V characteristics of the films were evaluated with the help of impedance and Keithley machines. After producing optimum PMN based films, the samples were applied to electronic devices such as electronic filter, defibrillator and flash of camera thanks to their high dielectric constants.

3.2 Materials

3.2.1 Substrate Preparation

The substrates used in the experiments must be thermally and chemically stable at the elevated temperatures which PMN MOS capacitor coating is carried out. In addition, there should not be any chemical interaction at the interface between coating and substrate due to the fact that it influences device performance.

Thermal expansion coefficients of the substrate and PMN based film must be similar in electronic applications. If the substrate has a higher thermal expansion coefficient than PMN, it will contract more upon cooling from the deposition temperature, causing a compressive stress in PMN layer. For substrates with a lower thermal expansion coefficients, PMN layer will be in tension. Any stress may lead to a degradation of PMN films. Hence a substrate should ideally possess a thermal expansion coefficient which is matched to, or slightly higher than PMN film.

Table 3.1 Properties of substrates.

Substrate	Surface	Crystal structure	Preperation for coating process
n-Phos Si <100>	Single slide polished	Cubic –Textured	Cutting with diamond pen
Glass	Polished	Amorphous	Ready for coating process

In the current research, Si(100) and glass were used as substrate materials. All the substrates used were in high purity. The properties of the substrates were illustrated in Table 3.1.

The surface of the substrate must be suitably polished and suitable for coating materials. When the substrate surface is highly rough, the PMN based layers will not be able to form a smooth, continuous well-oriented film. <100> oriented commercial phosphorus doped from Si-Mat Silicon Wafers, CZ Company with radius of 3 inches were used as substrates in order to prepare PMN MOS capacitor thin films.

Before deposition, substrates such as silica glass and Si(100) were cleaned in an ultrasonic bath using 1:1 methanol-water or acetone media in order to eliminate impurities from the sample surface inasmuch as cleaning is a main issue in science and technology.

3.2.2 Precursor Materials

General properties of the elements used for production of both PMN powders and PMN thin films are listed in Table 3.2. Alkoxide precursors, solvents, chelating agents and surface modifier were used to prepare PMN based powders and thin films. All chemical materials which were used for production of both PMN based powders and thin films are listed in Table 3.3, indicating chemical types, names, formulas and purity percentages. Precursor materials were used from alkoxide-based chemical materials which can be easily dissolved in solvents. These powder precursors were diluted by different solvents which are generally alcohol-based liquids such as methylalcohol, 2-methoxyethanol and ethylene glycol. Chelating agent, glacial acetic acid, was used to dissolve powder precursors. In order to circumvent adhesion or wettability problems between coating and substrate and obtain highly textured surfaces, modifying liquid material such as triethanolamine (TEA) was utilized in some solutions.

Table 3.2 All elements used for production of PMN powders and thin films (WEB4).

<i>Element</i>	<i>Atomic Number</i>	<i>MP (°C)</i>	<i>Relative Atomic Mass (gr)</i>	<i>Radius</i>		<i>Electro negativity</i>	<i>Crystal Structure</i>
				<i>Atomic (10⁻¹⁰m)</i>	<i>Ionic (nm)</i>		
Pb	82	327,5	207,2	1,81	0,119(+2)	2,33	F Cubic
Mg	12	648,8	24,31	1,72	0,065(+2)	1,31	Hexagonal
Nb	41	2468	92,91	2,08	0,007(+5)	1,60	Cubic
O	8	-218	16	0,65	0,14 (-2)	3,44	Cubic
Er	68	1522	167,25	2,45	0,088(+3)	1,24	Hexagonal
Eu	63	822	151,96	2,56	0,095(+2)	1,20	Cubic
Dy	66	1409	162,5	2,49	0,091(+3)	1,22	Hexagonal
Sm	62	1072	150,36	2,59	0,096(+3)	1,17	Rombohedral
Tb	65	1356	158,93	177pm	0,092(+3)	1,20	Hexagonal

To obtain of the PMN powders following precursors were used in three different combinations. Lead (II) acetate trihydrate, 99.5 %, $\text{Pb}(\text{CH}_3\text{COO})_2 \cdot 3\text{H}_2\text{O}$ (Carlo Erba), Magnesium acetate, $[(\text{CH}_3\text{COO})_2 \cdot \text{Mg} \cdot 4\text{H}_2\text{O}]$, Niobium (V) ethoxide, $[\text{Nb}(\text{OC}_2\text{H}_5)_5]$ (Aldrich, Alfa Aesar), Acetic acid, glacial, $\text{C}_2\text{H}_4\text{O}_2$, 2-methoxyethanol ($\text{CH}_3\text{-OCH}_2\text{CH}_2\text{OH}$), (Aldrich, Alfa Aesar), Ethylene glycol, $\text{C}_2\text{H}_6\text{O}_2$. >99.5 %, and Methylalcohol, 99.9 % (assay) (Riedel). Table 3.4 shows unique combinations of precursor materials in preparation of solutions.

For the sol-gel synthesis, ethoxide precursors were utilized. In spite of the fact that alkoxides have important advantages over the salt precursors, the cost of Nb-ethoxide and its moisture sensitivity makes difficult the synthesis process. With no doubt, the success of the sol-gel process depends on many parameters such as type of precursors, addition sequence, hydrolysis and condensation rates. As the starting

point for the experiments the following combinations have been used as shown in Table 3.4, which will be explained in details just later.

Table 3.3 All chemicals used for production of PMN based powders and thin films

Chemical Type	Chemical	Formula	Purity
Precursor	Lead (II) acetate trihydrate	$\text{Pb}(\text{CH}_3\text{COO})_2 \cdot 3\text{H}_2\text{O}$	99.5 % (REO)
	Magnesium acetate	$(\text{CH}_3\text{COO})_2 \cdot \text{Mg} \cdot 4\text{H}_2\text{O}$	99.9 % (REO)
	Niobium (V) ethoxide	$\text{Nb}(\text{OC}_2\text{H}_5)_5$	99.9 % (REO)
Doping precursor	Erbium pentanedionate	$\text{Er}(\text{CH}_3\text{COCHCOCH}_3)_3 \cdot \text{XH}_2\text{O}$	99.999 %
	Europium pentanedionate	$\text{Eu}(\text{CH}_3\text{COCHCOCH}_3)_3 \cdot \text{XH}_2\text{O}$	99.999 %
	Dysprosium pentanedionate	$\text{Dy}(\text{CH}_3\text{COCHCOCH}_3)_3 \cdot \text{XH}_2\text{O}$	99.999 %
	Samarium pentanedionate	$\text{Sm}(\text{CH}_3\text{COCHCOCH}_3)_3 \cdot \text{XH}_2\text{O}$	99.999 %
	Terbium pentanedionate	$\text{Tb}(\text{CH}_3\text{COCHCOCH}_3)_3 \cdot \text{XH}_2\text{O}$	99.999 %
Solvent	Methyl alcohol	CH_3OH	99.90 %
	2-methoxyethanol	$\text{CH}_3\text{-OCH}_2\text{CH}_2\text{OH}$	99.90 %
	Ethylene glycol	$\text{C}_2\text{H}_6\text{O}_2$	>99.5 %
Chelating Agent	Acetic acid, glacial	$\text{C}_2\text{H}_4\text{O}_2$	99.90 %
Surface Modifier	Triethanolamine (TEA)	$(\text{HOCH}_2\text{CH}_2)_3\text{N}$	97 % (Assay)

Table 3.4 The precursor combinations of PMN solutions.

Name of solution	Type of precursors	Type of solvents	Stirring time	Drying Temp. (°C)
Comb1	Pb(II)-ac, Mg-ac, Nb(v)-Eth	2-methoxyethanol, GAA	5 hours	120
Comb2	Pb(II)-ac, Mg-ac, Nb(v)-Eth	Ethylene glycol, GAA	5 hours	120
Comb3	Pb(II)-ac, Mg-ac, Nb(v)-Eth	Methanol, GAA	1 hours	25

3.2.3 Device Elements

For the simple device, circuit diagram is chosen “flash circuit”. This flash is used before in other words waste flash. Circuit diagram is schematically shown in Figure 3.1. Circuit components are below;

- ✓ 2 transformers,
- ✓ 2 resistances (10 kΩ),
- ✓ Transistor,
- ✓ LED,

- ✓ Xenon bulb,
- ✓ SR 96 diode,
- ✓ 02K400SC diode,
- ✓ 2 x 1.5 battery, and
- ✓ PMN based capacitor.

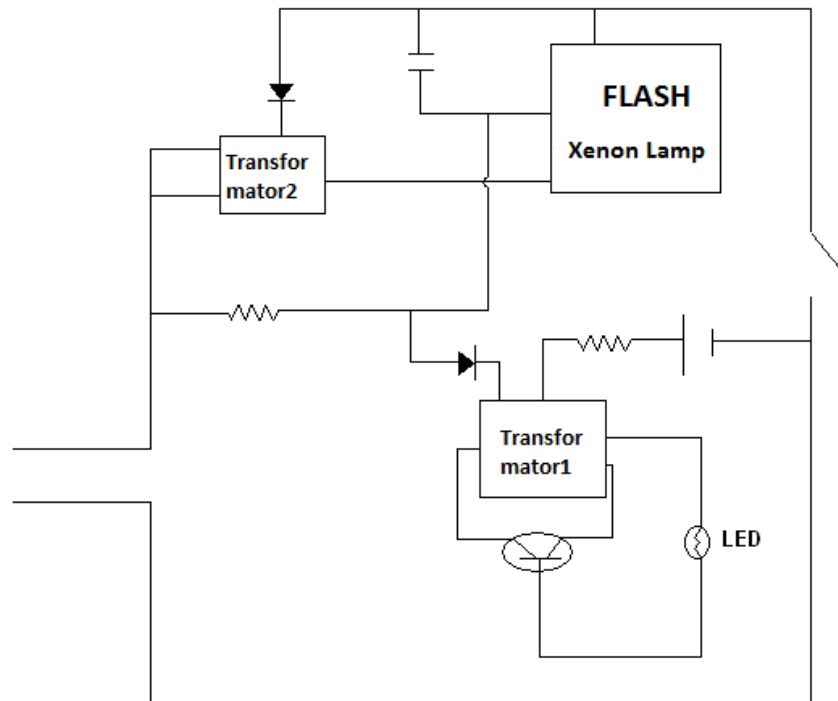


Figure 3.1 Flash circuit diagram.

3.2.3.1 Transformer:

A transformer is a device that transfers electrical energy from one circuit to another through inductively coupled conductors—the transformer's coils. A varying current in the first or primary winding creates a varying magnetic flux in the transformer's core, and thus a varying magnetic field through the secondary winding. This varying magnetic field induces a varying electromotive force (EMF) or "voltage" in the secondary winding. This effect is called mutual induction.

If a load is connected to the secondary, an electric current will flow in the secondary winding and electrical energy will be transferred from the primary circuit

through the transformer to the load. In an ideal transformer, the induced voltage in the secondary winding (V_S) is in proportion to the primary voltage (V_P), and is given by the ratio of the number of turns in the secondary (N_S) to the number of turns in the primary (N_P) as follows:

$$\frac{V_S}{V_P} = \frac{N_S}{N_P} \quad (3.1)$$

By appropriate selection of the ratio of turns, a transformer thus allows an alternating current (AC) voltage to be "stepped up" by making N_S greater than N_P , or "stepped down" by making N_S less than N_P .

3.2.3.2 Resistance:

The electrical resistance of an object is a measure of its opposition to the passage of a steady electric current. An object of uniform cross section will have a resistance proportional to its length and inversely proportional to its cross-sectional area, and proportional to the resistivity of the material.

Discovered by Georg Ohm in 1827, electrical resistance shares some conceptual parallels with the mechanical notion of friction. The SI unit of electrical resistance is the ohm (Ω). Resistance's reciprocal quantity is electrical conductance measured in Siemens.

For a wide variety of materials and conditions, the electrical resistance does not depend on the amount of current through or the potential difference (voltage) across the object, meaning that the resistance R is constant for the given temperature and material. Therefore, the resistance of an object can be defined as the ratio of voltage to current, in accordance with Ohm's law:

$$R = \frac{V}{I} \quad (3.2)$$

In the case of a nonlinear conductor (not obeying Ohm's law), this ratio can change as current or voltage changes; the inverse slope of a chord to an I–V curve is sometimes referred to as a "chordal resistance" or "static resistance".

3.2.3.3 Transistor:

A transistor is a semiconductor device used to amplify and switch electronic signals. It is made of a solid piece of semiconductor material, with at least three terminals for connection to an external circuit. A voltage or current applied to one pair of the transistor's terminals changes the current flowing through another pair of terminals. In so far as the controlled (output) power can be much more than the controlling (input) power, the transistor provides amplification of a signal. Nowadays, some transistors are packaged individually, but many more are found embedded in integrated circuits. The transistor is the fundamental building block of modern electronic devices, and its presence is ubiquitous in modern electronic systems. Following its release in the early 1950s, the transistor revolutionized the field of electronics, and paved the way for smaller and cheaper radios, calculators, and computers, amongst other things.

3.2.3.4 Xenon lamp:

A flashtube, also called a flash lamp, is an electric glow discharge lamp designed to produce extremely intense, incoherent, full-spectrum white light for very short durations. Flashtubes are made of a length of glass tubing with electrodes at either end and are filled with a gas that, when triggered, ionizes and conducts a high voltage pulse to produce the light. Flashtubes are used mostly for photographic purposes but are also employed in scientific, medical and industrial applications.

3.2.3.5 Diode:

In electronics, a diode is a two-terminal electronic component that conducts electric current in only one direction. The term usually refers to a semiconductor diode, the most common type today. This is a crystalline block of semiconductor

material connected to two electrical terminals. A vacuum tube diode (now little used except in some high-power technologies) is a vacuum tube with two electrodes; a plate and a cathode.

The most common function of a diode is to allow an electric current to pass in one direction (called the diode's *forward* direction) while blocking current in the opposite direction (the *reverse* direction). Thus, the diode can be thought of as an electronic version of a check valve. This unidirectional behavior is called rectification, and is used to convert alternating current to direct current, and to extract modulation from radio signals in radio receivers.

However, diodes can have more complicated behavior than this simple on-off action, due to their complex non-linear electrical characteristics, which can be tailored by varying the construction of their p-n junction. These are exploited in special purpose diodes that perform many different functions. For instance, specialized diodes are used to regulate voltage (Zener diodes), to electronically tune radio and TV receivers (varactor diodes), to generate radio frequency oscillations (tunnel diodes), and to produce light (light emitting diodes).

Diodes were the first semiconductor electronic devices. The discovery of crystals' rectifying abilities was made by German physicist Ferdinand Braun in 1874. The first semiconductor diodes, called cat's whisker diodes were made of crystals of minerals such as galena. Today most diodes are made of silicon, but other semiconductors such as germanium are sometimes used.

3.3 Production Techniques

3.3.1 Powder Preparation

For PMN based powder synthesis, 3.81 g lead acetate was dissolved in 10 ml methanol and 2 ml acetic acid until completing dissolution which was accomplished within few minutes. At this stage, rare earth precursors such as Er^{+3} , Eu^{+3} , Sm^{+3} ,

Dy⁺³ and Tb⁺³ based starting chemical materials were separately incorporated into this solution as dopant matters in order to prepare six different solutions. Subsequently, 0.388 g magnesium acetate was added along with additional 10 ml methanol and acetic acid. The solutions were rigorously and continuously stirred until completing dissolution of the precursors. Finally, a 1.67 ml aliquot of Nb-ethoxide, which was already cooled down to 5 °C, was added to the main suspensions, resulting in transparent solutions which mean very clear liquids. In this stage, hydrolysis, condensation and complexiation reactions were formed after preparation of transparent solutions. More details regarding as how to prepare PMN based powders and coatings can be clearly seen in Figure 3.2, which specifically presents whole procedure for the sol-gel synthesis of the powders using alkoxide precursors.

Gelation, which is a process according to which a sol, or a solution, transforms to a gel, occurred within 1 day (24 hours) in these experiments when methanol was used in all solutions as a solvent. More homogeneous and strongly bonded gel network was accomplished in the case of doped samples compared to undoped species. Gels were initially dried at room temperature, and followed by drying at 80 °C for few minutes in air. PMN based xerogels were produced after drying process. Their colors varied from light brown to dark one. Figure 3.3 demonstrates PMN based gels having very strong gel network prepared at 80 °C in air.

In these experiments, the heat treatment schedule including calcining and sintering, and atmosphere have to be precisely controlled to obtain the required oxidation states and perovskite structure. Under these circumstances, calcination of the samples was performed at 500 °C at a heating rate of 10 °C /min for 3 hours in air in an electrical furnace to ensure the total removal of organic materials. These samples were then heated to various temperatures, namely 800, 900, 950, and 1 100 °C at a heating rate of 5 °C /min and were kept at these temperatures for 2–8 hours in air in order to form perovskite structure. During heat treatment, double alumina crucible system with cover was used to prevent the lead loss from the samples as

shown in Figure 3.4. To provide a lead rich atmosphere, extra lead zirconate (PbO) powder was used in the outer crucible.

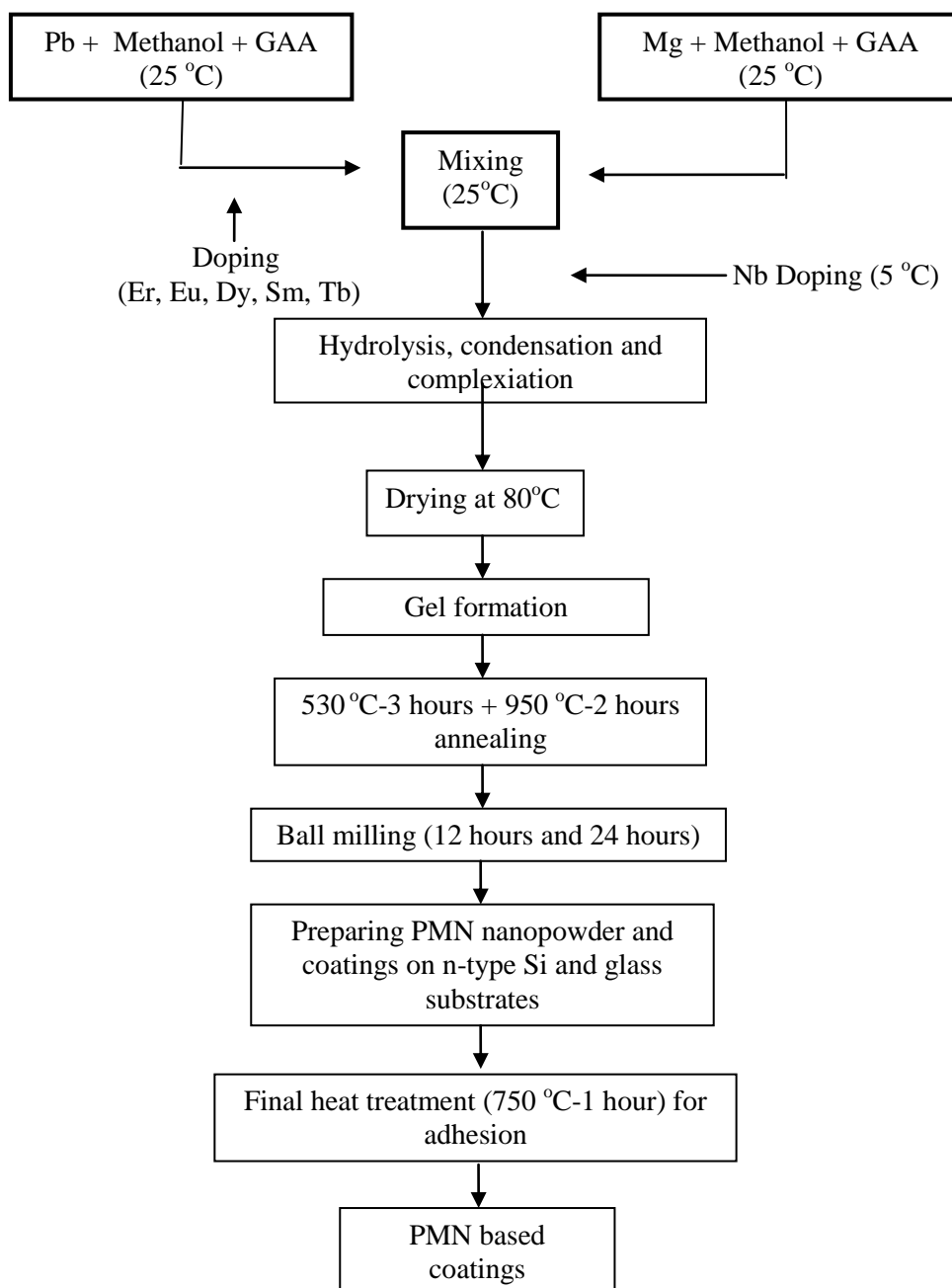


Figure 3.2 Flow chart for the sol-gel synthesis of PMN powders using alkoxide precursors.

In the case of RE^{+3} doping, the RE^{+3} content (x) in the final samples was varied in the range of 0.01 and 0.07. When the samples were doped with RE^{+3} , it was necessary to account for the charge imbalance. One way was to keep the ratio of Mg:Nb content fixed which would result in the A site vacancies

$\text{Pb}_{1-3x/2}\text{RE}_x(\text{Mg}_{1/3}\text{Nb}_{2/3})\text{O}_3$. However, in this study, Mg:Nb ratio was increased to balance the donor charge of RE^{+3} and to prevent A site vacancies. Hence, the compositions were expressed by the following formula:



Figure 3.3 PMN xerogels having very strong gel network.



Figure 3.4 The PMN powder samples after annealing process.

During synthesis of the PMN based powders, most of the reactions were carried out at given temperatures for several hours in air. In all methods, the dried gels were calcined at various temperatures up to 950 °C in air. Figure 3.5 indicates the position of the samples inside furnace. It is important to note here that extra purchased PbO powder from company was used in the electrical furnace to avoid PbO loss in the final samples. It is actually necessary in heat treatment procedures by virtue of high volatility of PbO from final PMN based samples. It facilitates experimental progress.



Figure 3.5 The position of the samples inside the furnace.

After successfully synthesis of the pure perovskite PMN powders (see Figure 3.4), the same procedure was to be utilized for the addition of the rare earth elements to the structure. As the starting point for the experiments, the given procedures in Figure 3.2 have been used for PMN based materials. As can obviously seen from Figure 3.2, thin film samples were heated up at 750 °C for 1 hour in air to achieve high adhesion strength of PMN based coatings on the substrates and improve performances of electronic devices.

3.3.2 Ball Milling

In order to obtain PMN based powders with nano size, home-made ball milling system was designed and successfully set up as a machine in our Lab as shown in Figure 3.6. This machine basically includes a container, alumina balls, an electric

motor, metal plates, cylindrical rods and some plastic materials. Having optimized design of the machine, it was devised to use in milling the powders. The container from plastic bottle possesses a volume of 100 ml which is placed into the PMN based powder after heat treatment process. The electric motor transfers energy to cylindrical long rods to mill the powders at room temperature. Nano powders were prepared after turning 12 hours in air. The machine stimulated the intensive research and development of PMN based powders and coatings.

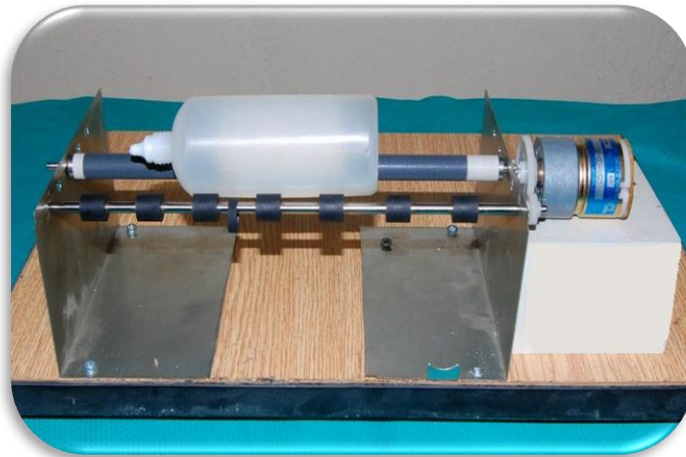


Figure 3.6 The ball milling machine (Electronic Materials Lab., DEU).



Figure 3.7 The high energy ball milling machine (Ceramic Engineering Lab., DPU).

Knowledges in literature (Hiemenz 1997) were used for container rates determined from the grinding process, and then a mixture among powder, methanol and alumina balls was accordingly prepared in this system. A volume of 1/3 ratio of the powder was set up for grinding alumina ball. The volume rate of methanol which contains the PMN based powder is 1/3. The remaining of 1/3 the luxury part is left blank. After turning for 12 hours in air, the powder of the vessels are regarded to come to the nano size. Yellow color of the powder on a very good solution in methanol and the mixture well on its own has become a yellow color. In addition to this, Fritsch Premium line Pulverisette 7 model High Energy Ball milling machine in Figure 3.7 was used for grinding the powders. PMN based powders was ground at rate of 800 rpm at room temperature for 15 minutes in air. With the aid of this concept of the ball milling systems, PMN based nanoparticles were produced to use in thin film fabrication for electronic devices.

3.3.3 Colloidal Suspension Preparation

Sedimentation is one of techniques in separation of PMN based powders from sub-micron to nano scale. The aim of sedimentation was to focus on how PMN based nanoparticles can first separate from the solution and show how nano scaled particles can separate from micron scaled particles. Generally speaking, sedimentation is the tendency for nanoparticles in suspension to settle out of the fluid. In this research, sedimentation may pertain to PMN based powders of various sizes, ranging from large particles to nanoparticles. With the sedimentation method, nano scaled particles stay upper side of the prepared solution and micron scaled particles descended underside of the solution in terms of its density. This behavior leads to the separation of PMN based powders. Suspended PMN based particles is the mass of dry solids retained by a filter of a given porosity related to the volume of the liquid sample (Levi 2009).

Inasmuch as the sedimented particles in suspension can not be seen with naked eyes, it is easy to take nanoparticles with liquid using an injector. After separating the alumina balls from all mixtures, approximately 30 ml PMN based solution were

received from milling tank in order to smoothly deposit on n-type Si and the glass substrates. The obtained suspension was kept to evaporate methanol at 60 °C for 90 minutes in air. The suspension which contains nano scaled pure or doped PMN powders was incorporated into a mixture of 8 ml methanol and 0.2 g tri ethanolamine (TEA). The prepared new suspensions from different PMN based powders were dispersed at room temperature for 1 hour in air using an ultrasonic bath/cleaning machine as shown in Figure 3.8. In order to homogenously and continuously deposit PMN based nanoparticles on the substrates, the solutions including very fine particles in the suspension were injected to glass bottles using an injector and therefore colloidal suspensions were prepared for coating systems.



Figure 3.8 The ultrasonic bath/cleaning machine (Chemistry Lab., DEU).

3.3.4 Coating Process

Prior to coating process, the substrates which were used as silica glass and Si(100) were cleaned in 1:1 methanol-water medium in order to eliminate impurities, oil or dirty materials on the surface using ultrasonic cleaning machine (see Figure 3.8).

3.3.4.1 Spin Coating

The PMN based films were spin coated on the glass and Si(100) metallic substrates from the prepared suspension solutions through Cookson Electronics

Equipment SCS G3P-8 model spin coater, as is evident from Figure 3.9. Different spinning parameters such as spinning rate, acceleration time were used to control the film thickness in this system. A spinning rate of 1000-3000 rpm for 10 to 30 seconds and an acceleration time of 10 seconds were used for PMN based films as optimum parameters.



Figure 3.9 G3P-8 Cookson model spin coater (Ceramics Lab., DEU).

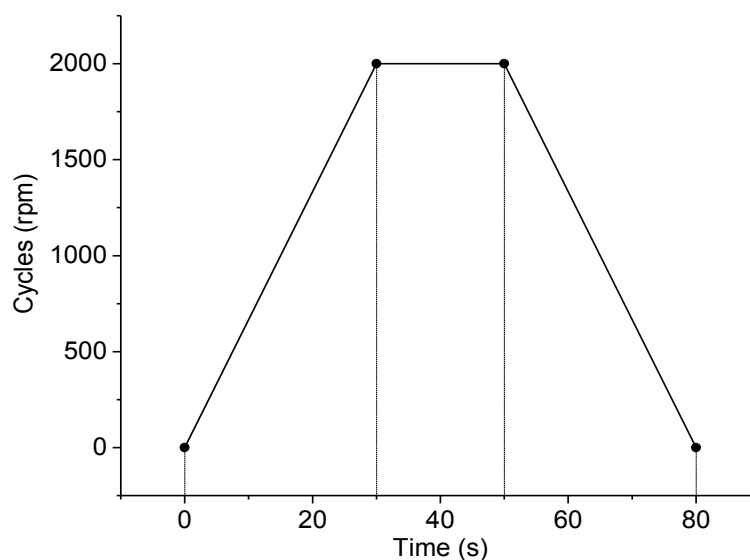


Figure 3.10 Spin coating regime for PMN based suspension.

The coating spinning regime which was used in this technique is diagrammatically presented in Figure 3.10. As shown in the figure spin coating process which is

executed at air atmosphere possess three steps. At first 30 seconds the spinner accelerates up to 2000 rpm to spread the solution and remove the excess of solution. In the range of 30th sec. to 50th sec., spinner turns in a constant speed at 2000 rpm. At this step of operation, the deposited solution easily spreads on the substrate.

There exists a unique relationship among deposition quality and solution parameters such as film thickness, wettability, viscosity, pressure etc. Each parameter is expected to improve surface quality depending on solution characteristics. Third step is the deceleration step here vaporizing of the volatiles and residual solutions were removed to improve surface quality and homogeneity in 30 seconds at 25 °C in air.

3.3.4.2 Drop Coating

Solution dropping method is simpler and hand-operated if compared with spin coating. This procedure has several steps such as taking solution into an injector, dropping solution drops at equal numbers on substrates, and giving a tilt of approximately 20° to the substrates with the help of a clean pincer to help whole wetting on substrate surface.

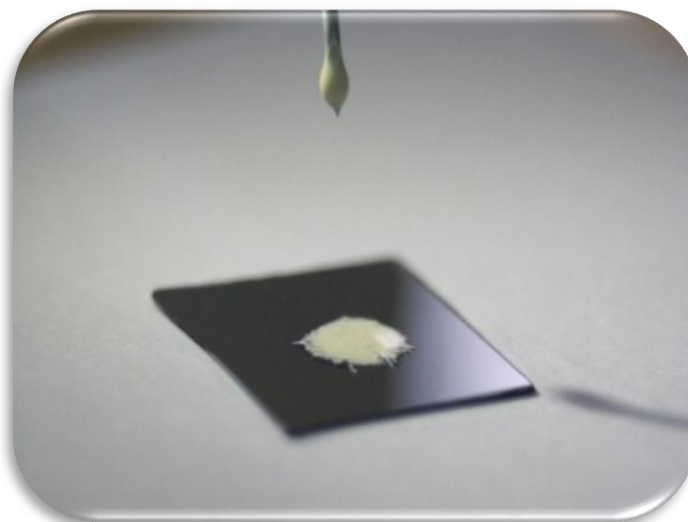


Figure 3.11 Dropping solution/suspension on the Si (100) substrate.

PMN based suspensions were coated using solution dropping procedure as seen in Figure 3.11. The smooth, homogeneous and continuous PMN based films with high dielectric constant were successfully produced by this method.

3.3.5 Heat Treatment

A Protherm tube furnace in Figure 3.12 was effectively used for the calcining and annealing processes of pure and doped PMN powders. The heating profile for the powders is illustrated in Figure 3.13.



Figure 3.12 Protherm tube furnace (Ceramics Lab. DEU).

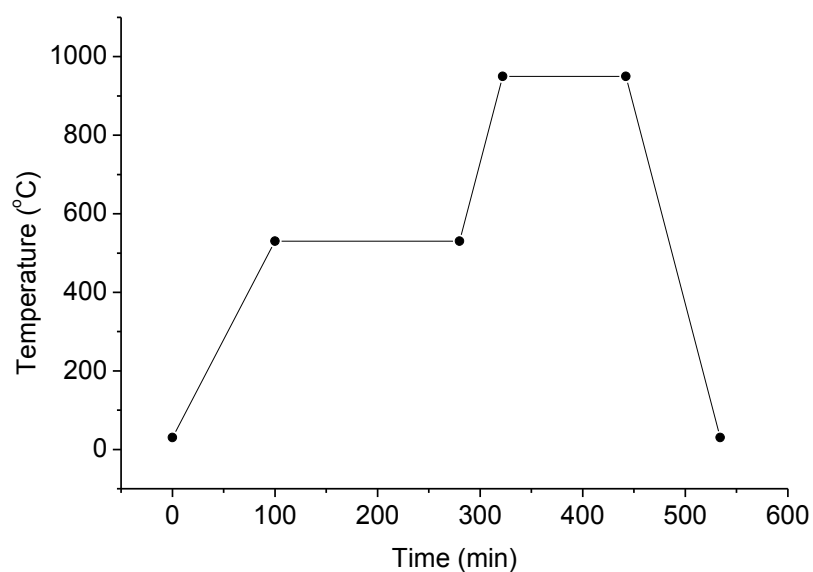


Figure 3.13 Heating regime of PMN based powders for calcinations and annealing processes.

For the heat treatment regime of the samples, the temperature of the furnace was raised to 530 °C with heating rate of 5°C/min and then kept at this temperature for 3 hours in air. After the calcinations process, the annealing/sintering temperature was raised from 530 °C to 950 °C with heating rate of 10°C/min and subsequently it was kept at 950 °C for 2 hours in air to form perovskite structure from PMN based powders. End of this procedure, a cooling process was performed to take out the powder samples from the tube furnace.

A box furnace for heat treatment of the thin films as depicted in Figure 3.14 was used to improve adhesion strength of pure and doped PMN coatings on the substrates.



Figure 3.14 Illustration of PMN based thin films in the box furnace.

To greatly improve mechanical properties of PMN based coatings such as hardness and adhesion strength, efforts about annealing were realized as is evident in Figure 3.15, illustrating the heating regime. In this case, the furnace temperature was raised to 730 °C with speed of 10 °C/min and the kept at the same temperature for 1 hour in air. Finally the obtained samples opened up the possibility of practical electronic applications, particularly electronic filter, defibrillator and flash of camera.

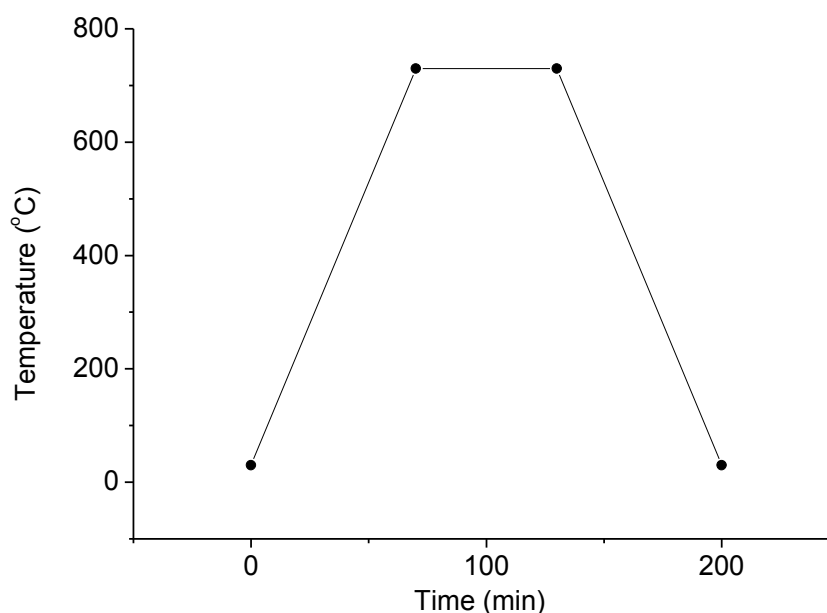


Figure 3.15 Heating regime for PMN based thin films.

3.4 Characterization

3.4.1 Solution Characterization

In order to determine solution characteristics which affect the final products thin film properties, pH values, turbidity, rheological properties and spectroscopic properties of the prepared solutions were respectively measured by pH meter, turbidimeter, rheometer machines and FTIR before powder and thin film fabrication.

3.4.1.1 pH Measurement

The pH measurement refers to determination of the activity of hydrogen ions in an aqueous solution. Many important properties of a solution can be determined from an accurate measurement of pH, including the acidity of a solution and the extent of a reaction in the solution. Many chemical processes and properties, such as the speed of a reaction and the solubility of a compound, can also depend greatly on the pH of a solution. In the study, pH values of the sol solutions were determined through Mettler Toledo Inlab 412 pH meter.

3.4.1.2 Turbidity Measurement

Turbidity (or the relative cloudiness of a liquid) measurement gives the optical characteristics of suspended particles in a liquid. Light is passed through the sample and is scattered in all directions. The light that is scattered at a 90° angle to the incident light is then detected by a photo diode and is converted into a signal linearized by the analyzer and displayed as an NTU (Nephelometric Turbidity Units) value. The more suspended particles there are in a liquid, the more light will be scattered, resulting in a higher NTU value. In the experiment, turbidity measurements of the prepared precursor solutions were performed by using TB1 Turbidimeter just like in Figure 3.16.



Figure 3.16 TB1 Turbidimeter, VELP, Scientifica Srl, Italy (Chemistry Lab., DEU).

The sample was placed in the vessel with a dimension of Ø25 mm and height of 50 mm. Formazine is recognized throughout the world as a primary standard. Formazin solution was used to calibrate the turbidity. It was determined whether powder based precursors are well-dissolved in the used solvent.

3.4.1.3 Rheometer

The rheological properties that lead to further characteristic knowledge concerning coating quality without depositing PMN based coatings include viscosity, gelation time, shear, elastic and viscous modulus. The rheological measurements of PMN based solutions were conducted with the help of a Bohlin Instruments CVO 100 Rheometer (see Figure 3.17 for details) with 2° conic plate geometry 60 mm in diameter and 0.7 μm gap sizes between plates. The viscosity values of PMN based solutions were performed at constant 300 Hertz frequency and single shear mode at 20 °C. As far as the elastic and viscous moduli were concerned, these parameters were determined using oscillatory shear at 1 Hertz frequency for all PMN based solutions/suspension. The rheological properties of the PMN based solutions were comparatively studied to characterize their gelation behaviours.



Figure 3.17 Bohlin Instruments CVO 100 Rheometer (Ceramics Lab., DEU).

3.4.1.4 Fourier Transform Infrared Spectroscopy (FTIR)

An analytical technique, Fourier Transform Infrared (FTIR or IR) spectroscopy is generally a non-destructive technique, which is used to measure the absorption of various infrared light wavelengths of organic or inorganic materials of interest. The infrared absorption bands identify the specific molecular components or structures,

and provide chemical bonding information of the PMN based materials because of the vibrational motions of the chemical bond showing frequencies in the infrared regime. Infrared spectra record the infrared intensity (transmission percentage or absorption) versus wavelength (wavenumber) of light. The IR spectrum can be generally divided into three frequency (or wavenumber/wavelength) regions: the far IR (10~400 cm^{-1}), the middle IR (400~4,000 cm^{-1}) and the near IR (4,000~14,000 cm^{-1}), with the middle IR region being employed in most IR spectroscopic investigations. The basic infrared experiment is to measure the changes of infrared light intensity after interacting with the sample (Almeida, & Marques, 2004). Intensity can be expressed as percent transmittance (%T) or absorbance (A) (Marcott, 1998). If I_0 is the energy, or radiant power, reaching the infrared detector with no sample in the beam, and I is the energy detected with a sample present, transmittance is,

$$T = \frac{I}{I_0} \quad (3.4)$$

And percent transmittance:

$$\%T = \frac{I}{I_0} \times 100 \quad (3.5)$$

Absorbance is:

$$A = \log\left(\frac{1}{T}\right) = \log\left(\frac{I_0}{I}\right) \quad (3.6)$$

The technique of Attenuated Total Reflectance (ATR) has in recent years revolutionized solid and liquid sample analyses because it combats the most challenging aspects of infrared analyses namely sample preparation and spectral reproducibility. An ATR accessory operates by measuring the changes that occur in a

totally internally reflected infrared beam when the beam comes into contact with a sample as indicated in Figure 3.19 (Ak, 2008).



Figure 3.18 Schematic illustration of FTIR system having ATR apparatus (Electronic Materials Lab., DEU).

An infrared beam is directed onto an optically dense diamond crystal with a high refractive index at a certain angle. This internal reflectance creates an evanescent wave that extends beyond the surface of the crystal into the sample held in contact with the crystal. It can be easier to think of this evanescent wave as a bubble of infrared that sits on the surface of the crystal.

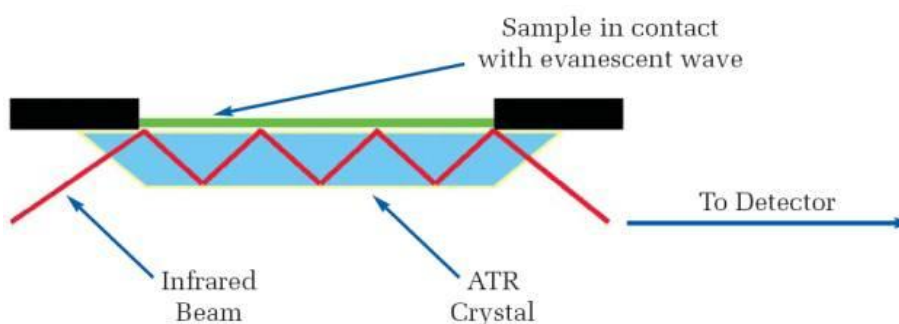


Figure 3.19 Schematic illustration of FTIR detection (WEB2).

This evanescent wave protrudes only a few microns ($0.5\text{-}5\ \mu\text{m}$) beyond the crystal surface and into the sample. Consequently, there must be good contact between the sample and the crystal surface. In regions of the infrared spectrum where the sample

absorbs energy, the evanescent wave will be attenuated or altered. The attenuated energy from each evanescent wave is passed back to the IR beam, which then exits the opposite end of the crystal and is passed to the detector in the IR spectrometer. The system then generates an infrared spectrum.

The infrared spectra of all liquid and coated samples were recorded with a Perkin Elmer Spectrum BX instrument equipped with ATR (Figure 3.18) apparatus in the spectra range between 4000 and 650 cm^{-1} with a resolution of 4 cm^{-1} . With this concept, we were particularly interested in what happened to PMN based xerogels and films when they regularly heated up from 25 $^{\circ}\text{C}$ from perovskite formation temperatures. Based on this, it was determined the chemical ingredient of dried and annealed samples.

3.4.2 Material Characterization

In order to determine powder and thin films characteristics of PMN based materials which affect the last application products, thermal behavior of xerogel powders, particle size distribution of PMN powders and phase analyses of PMN powders and thin films. In addition, thin film morphologies were observed by the way of microscopic techniques. Mechanical properties of PMN based thin films were measured for optimum samples. Finally, optical characteristics and dielectric properties were determined for PMN based thin films.

All of above mentioned measurement and tests were respectively made by DTA-TG, particle size analyzer, XRD, SEM, AFM, DUH, Scratch tester, refractometer, spectrophotometer, Dielectric analyzer, I-V measurement system after powder and thin film fabrication process.

3.4.2.1 Differential Thermal Analysis-Thermal Gravimetric Analysis (DTA-TGA)

The thermal analysis of the gel was studied under N_2 flowing by means of Shimadzu 60H Model Differential Thermal Analysis-Thermal Gravimetry (DTA-

TG) as shown in Figure 3.20 in order to obtain information about the decomposition behaviour of the gels and adjust the thermal treatment accordingly. More precise data regarding as process optimization in PMN based powder and film production depending on temperature were obtained after DTA-TG analysis. Thermal data were analyzed using TA60 software program supplied with the instruments. In this experiment, heating regime was selected as 10 °C/min from 25 °C to 1000 °C.

Thermal analysis is defined as a group of techniques in which a physical thermal analysis is defined as a group of techniques in which a physical property of the substance and its reaction products are measured as a function of temperature whilst the substance is subjected to a controlled temperature program (Hill, 1991). In addition to these, thermal methods are based upon the measurement of the dynamic relationship between temperature and some property of the system such as mass and heat absorbed by or evolved from it. Differential Thermal Analysis (DTA) and Thermogravimetry (TG) are the most important thermal methods used in characterization of materials (Kayatekin, 2006).

DTA is a technique in which the difference in energy between the sample and the reference material is measured against time or temperature. The DTA curve is generally a plot of the difference in energy as the ordinate against temperature T, as the abscissa. By convention, in DTA endothermic peaks are drawn downwards and exothermic upwards (Ak, 2008). As for TG, it is a technique in which the mass of the sample is monitored against time or temperature while the temperature of the sample is programmed. A plot of mass loss or percent loss versus temperature or time can be obtained. The reaction is shown as one or more steps, each of which represents a mass change.

Temperature change in the samples brings about the chemical (phase transition, reduction, oxidation and decomposition) and physical (boiling, melting and sublimation) changes of a sample and these can be endothermic or exothermic. DTA is able to be used to study any process in which heat is absorbed or evolved. The number, shape and position of the various endothermic and exothermic peaks in

DTA curve can be used for qualitative identification of the substance. Simultaneous techniques refer to the application of two or more techniques to a sample at the same time. In the present study, DTA-TG simultaneous techniques are used. It is an advantage to use simultaneous techniques because it saves time and sample and it gives an opportunity to set an experiment at the same conditions (Ak, 2008).



Figure 3.20 Shimadzu DTG-60H/TA-60WS simultaneous thermal analyzer (Ceramics Lab, DEU).

3.4.2.2 Particle Size Analyser

The particle size distribution (PSD) of a powder, or granular material, or particles dispersed in fluid, is a list of values or a mathematical function that defines the relative amounts of particles present, sorted according to size (Jillavenkatesa, 2001). PSD is also known as grain size distribution. There are different types of measurement techniques for size distribution analysis, they are arranged as follow: (a) sieve analysis, (b) optical counting methods, (c) electrical counting methods, (d) sedimentation techniques, (e) laser diffraction methods, and (f) acoustic spectroscopy.

In this work, laser diffraction method is used to determine particle size of PMN based powders. These methods depend upon analysis of the "halo" of diffracted light produced when a laser beam passes through a dispersion of particles in air or a liquid. The angle of diffraction increases as particle size decreases, so that this

method is particularly good for measuring sizes below 1 μm . Advances in sophisticated data processing and automation have allowed this to become the dominant method used in industrial PSD determination. A particular advantage is that the technique can generate a continuous measurement for analyzing process streams. The machine used as laser diffraction was called Malvern Instruments, Mastersizer 2000 as seen in Figure 3.21.



Figure 3.21 Mastersizer 2000 particles size distribution system (Malvern Instruments, DEU).

3.4.2.3 X-Ray Diffractometer (XRD)

X-ray diffraction (XRD) is one of the primary techniques to analyze all kinds of materials such as powders and crystals. XRD can provide information about crystalline structure and structural phases. It is extensively used to investigate the structural properties of PMN based powders and thin coatings on substrates. Synthesized coatings were analyzed by means of XRD in Figure 3.22 with a grazing angle attachment and an incident angle of 1° (Rigaku, D/Max-2200/PC). X-Ray radiation of $\text{CuK}\alpha$ was set at 40 kV and 36 mA with a scanning speed of 2° $2\theta/\text{min}$, from 15° to 80° .



Figure 3.22 X-Ray Diffractometer, Rigaku, D/Max-2200/PC (X-Ray Lab., DEU).

3.4.2.4 Scanning Electron Microscopy (SEM)/ Energy Dispersive X-ray Spectroscopy (EDS)

Scanning electron microscopy (SEM), as depicted in Figure 3.23, is one of the most common analytical methods to examine surface morphology of the solid-state specimen. In SEM, a tiny high-energy electron beam is scanned across the sample surface. Series of radiations can be produced in terms of the interaction between the electron beam and the sample. Normally, two types of radiation are utilized for image formation: primary backscattered electrons and secondary electrons. Backscattered electrons reveal the compositional and topographical information of the specimen.

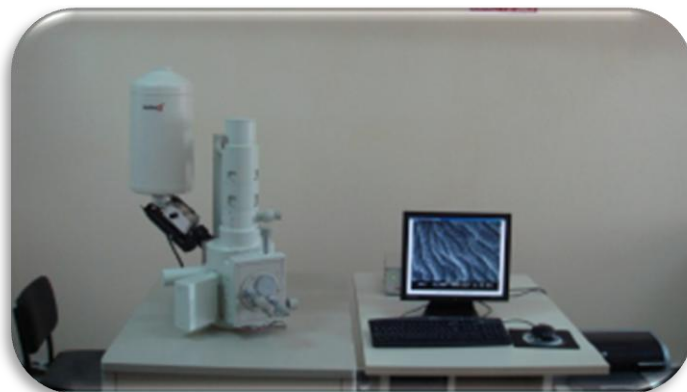


Figure 3.23 JEOL JSM-6060 (SEM Lab., DEU).

The secondary electron images produce a depth of field which shows the surface topography. The signal modulation of the two types of radiation is viewed as images in the CRT and provides the morphology, surface topology and composition of the specimen surface. The energy dispersive spectroscopy (EDS) is often attached to the SEM. The X-rays generated from the interaction between the electron beam and the specimen is used to identify and measure quantitatively the elemental composition of the specimen. Therefore, SEM/EDS can detect the elemental composition and obtain the morphology of the specimen simultaneously. In this study, the surface and elemental composition of the PMN based films were examined by using JEOL JSM-6060 instrument operating at an accelerating voltage of 15 kV.

3.4.2.5 Atomic Force Microscopy (AFM)

Atomic Force Microscopy is a powerful tool for assessing the three dimensional surface topography and morphological quality of PMN based films. A Digital Instruments Nanoscope III as denoted in Figure 3.24 was used in tapping mode to obtain AFM images of at least one film in each batch measured. In ‘Tapping Mode’ technique the probe is oscillated at a constant frequency as the AFM head scans across the surface. The amplitude of oscillation of the tip varies as it moves nearer to the surface of the film, this change is used as feedback to control the sample-tip distance and deduce the surface height of the film. In general AFM measurements revealed that it was difficult to obtain vicinal films with as high a quality as the best



Figure 3.24 Nanoscope III AFM machine (Metallography Lab., DEU).

c-axis films. Even the best films exhibited pin-hole defects or outgrowths. The AFM employed was well-calibrated in the z-axis, a maximum error of ± 2 nm was observed imaging 180 nm deep pits on a calibration sample. The AFM was therefore be used to obtain film thickness by measuring the height of chemically etched steps.

3.4.2.6 *Dynamic Ultramicro Hardness (DUH)*

Shimadzu DUH-W201, DUH-W201S model Dynamic Micro-Hardness Tester, as can be seen in Figure 3.25, was used for indentation tests of PMN based coatings on the substrates with a working range 0.1–1961 mN.



Figure 3.25 Shimadzu DUH-W201 ultra micro hardness testing machine (Metallography Lab., DEU).

In this study, all the ultramicro hardness tests for chosen optimum samples were realized under 10 mN applied load.

The conventional micro hardness value can be determined from the optical measurement of the residual impression left behind upon load release. In recent decades, the development of depth-sensing indentation equipment has allowed the easy and reliable determination of two of the most commonly measured mechanical properties of materials, the hardness and Young's modulus. The depth-sensing (or dynamic) micro indentation method offers great advantages over conventional Vickers micro hardness testing in two aspects. Firstly, apart from micro hardness (or micro strength), the method can also provide well-defined mechanical parameters such as elastic modulus of the interfacial zone. Secondly, as load and depth of an indentation are continuously monitored, optical observation and measurement of diagonal length of the indent/impression, which can be difficult and subjected to inaccuracy, is no longer required (Güçlü 2006, Ebeoğlugil 2010).

Two mechanical properties, that is, elastic modulus E and micro hardness H can be obtained with the load and penetration depth data. A typical load–penetration depth curve is shown in Figure 3.26. During indenter loading, test material is subjected to both elastic and plastic deformation. The three key parameters needed to determine the hardness and modulus are the peak load (P_{\max}), the contact area (A_c) and the initial unloading contact stiffness (S) as formulated Equation (3.7). Similar to the conventional micro hardness testing, the micro indentation hardness is usually defined as the ratio of the peak indentation load, P_{\max} , to the projected area of the hardness impression, A_c , i.e (Güçlü 2006, Ebeoğlugil 2010).

$$H = \frac{P_{\max}}{A_c} = \frac{P_{\max}}{26.43h_c^2} \quad (A_c = 26.43h_c^2) \quad (3.7)$$

Different approaches for deducing the contact depth, h_c , from the resultant load displacement curve have been purposed and perhaps the most widely used one is that of Oliver and Pharr. The Oliver and Pharr (Oliver 1992) data analysis procedure begins by fitting unloading curve to an empirical power-law relation:

$$P = \alpha(h - h_f)^m \quad (3.8)$$

in which P is the indentation load, h is the penetration depth, h_f is the final unloading depth and α and m are empirically determined fitting parameters. Using the initial part of the unloading curve, both stiffness and contact depth are determined by differentiating Equation 3.8 at the maximum depth of penetration, $h=h_{\max}$. Then, the stiffness of the contact is given by Equation 3.9.

$$S = \frac{dP}{dh} = \frac{2}{\sqrt{\pi}} E_r \sqrt{A_c} \qquad \frac{1}{E_r} = \frac{1-\nu^2}{E} + \frac{1-\nu_0^2}{E_0} \qquad (3.9)$$

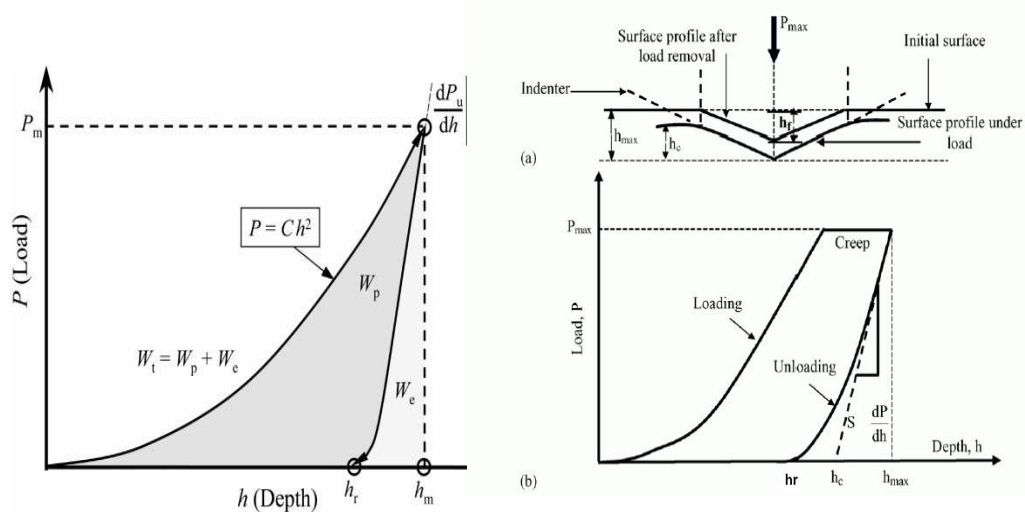


Figure 3.26 Schematic illustration of a typical P - h response of an elasto-plastic material to instrumented sharp indentation (Dao 2001).

E_r is called reduced modulus or combined modulus, $S=dP/dh$ is the experimentally measured stiffness of the upper portion of the unloading data, which is the slope of the curve fitted straight line of the initial part of unloading, A is the projected contact area of the indenter at maximum loading condition, E and ν are Young's modulus and Poisson's ratio for the specimen, and E_0 and ν_0 are the same parameter for the indenter.

3.4.2.7 Scratch Testing Machine

Adhesion properties of PMN based coatings were measured by using Shimadzu Scanning Scratch Tester SST-W101 in Figure 3.27 (Instruction Manual, Shimadzu

Scanning Scratch Tester SST-W101, 2002, Shimadzu Corporation.) equipped with a standard off-line Zeis metallographic microscope. In this technique, the load on a Rockwell C diamond with tip radius of stylus (R) of 15 μm was linearly increased from 0 mN to 98 mN at loading speed of 1 $\mu\text{m/s}$ and scratch speed of 2 $\mu\text{m/s}$ as the diamond is drawn across the coating surface. The testing temperature and humidity percentage are 20.3 $^{\circ}\text{C}$ and 50 %, respectively. During the test, a stylus was drawn on coating surface with a sliding speed of 5 $\mu\text{m.s}^{-1}$ keeping scanning amplitude of 10 μm which perpendicular to the scratching direction at the same time. Friction on the stylus increases with increasing load, which causes a delay in movement between cartridge body and stylus. This delay is defined as a cartridge output. As a result of tests, test force versus cartridge output (%) curves are obtained and compared results.



Figure 3.27 Shimadzu, SST-W101 scratch testing machine (Metallography Lab., DEU).

The scratch was examined with an optical microscope and critical force (W_c) value at which the coating is removed from substrate was determined. After microhardness value of metal substrate was converted to Brinell Hardness (H) from Vickers Microhardness by using Standard Hardness Conversion Tables for Metal (Culha 2009), the adhesion strength (F) of the coatings was calculated as MPa unit by using Equation 3.10 (Culha 2009).

$$F = \frac{H}{\left[\frac{\pi R^2 H - W_c}{W_c} \right]^{1/2}} \quad (3.10)$$

where H is Brinell hardness value in kg/mm² of the Si substrate and R is radius of stylus in μm. In addition, it is possible to evaluate adhesion of coatings using Equation (3.10). As the test force applied to coating increases, speling of coating occurs. At this time peeled pieces of coating cause a high frequency noise in a cartridge output signal. Detecting this noise makes it possible to determine a critical force. Normally, this critical force can be used the adhesion value of coating. Nonetheless, in the case that a hardness of the substrate has been known, Equation (3.10) can show adhesion strength. As a result of this, test force–cartridge output graph is obtained from this measurement. Cartridge output (%) represents percentage of indentation of the stylus as a function of loading during the test. The percentage increases with a increasing load, that applied by stylus, due to the adhesion resistance of the coating to substrate (Culha 2009).

3.4.2.8 Refractometer

Refractive indexes of PMN based films were measured at selected wavelengths in the VIS region by a high-accuracy Abbe refractometer (Figure 3.28) at room temperature.



Figure 3.28 Abbe refractometer (Electronic Materials Lab, DEU).

All PMN based thin films on glass substrates were measured refractive indexes using refractometer. These values were used to measure their thickness by the help of spectrophotometer.

3.4.2.9 Spectrophotometer

Film thicknesses of PMN based coatings were measured by using V-530 JASCO UV/VIS spectrophotometer as shown in Figure 3.29. Refractive indexes were used to determine film thickness values of PMN based coatings and to determine band gap values using the spectrophotometer.



Figure 3.29 Spectrophotometer, V-530 JASCO UV/VIS (Electronic Materials Lab., DEU).

3.4.2.10 Impedance Measurement

Dielectrical properties of PMN based coatings were determined using Novocontrol Alpha-N High Resolution Dielectric Analyzer (Figure 3.30). With this respect, dielectric constant, loss factor ($\tan\delta$) and capacitance were measured as dielectric parameters. Since sample cells were utilized as a plate capacitor, the sample material was placed between two external capacitor plates as shown in Figure 3.31. This technique has the advantage, that the sample preparation is very easy and straightforward. External electrodes with several diameters can be used for optimal

adaptation of the sample material to the impedance measurement system. In addition, the sample cell electrodes are not contaminated by the sample material.

The material dielectric function is calculated by;

$$\varepsilon^* = \varepsilon' - i\varepsilon'' = \frac{C_p^*}{C_0} \quad (+) \quad (3.11)$$

from the measured complex sample capacity, C_p^* . C_0 is a constant determined by the sample geometry. Equation 3.11 refers to evaluation of data for details. Equation 3.11 will be only exact, if the electrical field distribution is homogenous inside the sample capacitor and zero outside. In practice, there will be some field inhomogenitites at the capacitor borders reducing the sample capacity. In addition the field outside the capacitor will not be zero. Instead there will be a stray field, which contributes as an additional external capacity to the measured sample capacity. Both contributions can be considered by an additional capacity which is edge capacity (C_{edge}). The measured capacity can be written as;

$$C_m^* = C_p^* + C_{edge} \quad (3.12)$$

in which C_p^* is the capacity of the ideal capacitor.



Figure 3.30 Alpha-N High Resolution Dielectric Analyzer, Novocontrol (Electronic Materials Lab., DEU).

The edge capacity can be reduced, if a sample cell with guard ring is used. The disadvantage of this set-up is that the sample preparation becomes more difficult as no external electrodes can be used. In addition, at high frequencies technical problems arise. On the other hand, the errors in a non guarded set-up can be easily kept below other error sources if either a convenient sample cell geometry is chosen and/or the edge capacity is taken into account in the evaluation. Comparing the benefits of a guarded set-up with its disadvantages, novocontrol system favors the second solution without guarding.

C_{edge} can be exactly calculated for round capacitor plates centered in an evacuated and grounded metallic sphere with infinite radius (capacitor not filled with sample material).

$$\frac{C_{edge}}{C_0} = \frac{2d}{\pi D} \ln \frac{8\pi D}{d} - 3 + z(x) \quad (3.13)$$

$$z(x) = (1 + X) \ln(1 + X) - x \ln(x) \quad (3.14)$$

$$X = t/d \quad (3.15)$$

$$C_0 = \epsilon_0 \frac{\pi D^2}{d} \quad (3.16)$$

in which, D: electrode diameter, d: spacing between electrodes, t: electrode thickness, and $\epsilon_0 = 8,85 \cdot 10^{-12} \text{ As/Vm}$.

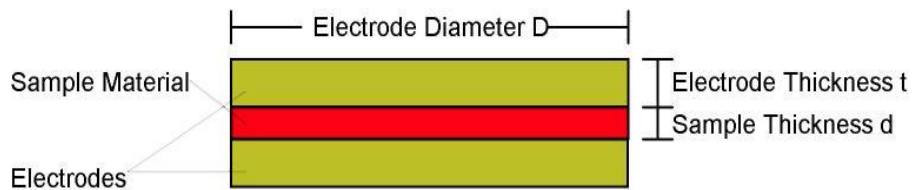


Figure 3.31 Illustration of dielectric sample between capacitor plates.

If the volume between the capacitor plates is filled with a dielectric material, which does not exceed the capacitor plates as shown above in Figure 3.31, one can approximately assume the edge capacity not to be changed by the material. In this case, the ideal sample capacity C_p^* can be calculated from Equations 3.12 and 3.15. This was verified for several geometries and dielectric materials by the result that the residual errors of this method are $< 1.1\%$ of the measured values for all tested samples. This residual error is at least in the same region as other errors of the measurement set-up (e.g. inexact sample geometry, contact problems and device uncertainties).

The above method of edge correction is automatically applied by WinDETA program if edge compensation in sample specification dialog of the measurement menu is activated. Nevertheless, there are some limitations of the method which should be considered. In practice, the sample capacitor is surrounded by additional grounded conductors. These are for the low frequency sample cell BDS 1200 e.g. the walls of the cryostat and for the RF sample cell BDS 2100 the walls of the cell. In addition, for the RF sample cell, a part of the edge capacity is already compensated by the open sample cell calibration. Therefore Equation 3.15 will hold in practice only approximately. Especially for large ratios C_{edge}/C_o (Equation 3.15) may become inaccurate.

As a general rule, the sample geometry should be selected in such a fashion that unnecessary large edge capacities are avoided. This can be done by making the sample diameter large and the spacing thin (see Equation 3.15).

The ratio C_{edge}/C_o can be used to guess the maximum error without edge compensation. The error $\Delta\varepsilon'$ of a measured dielectric function due to edge effects (without compensation) is

$$\frac{\Delta\varepsilon'}{\varepsilon'} = \frac{C_{edge}}{C_p} = \frac{C_{edge}}{C_o\varepsilon'} \quad (3.17)$$

The residual error with edge compensation enabled will be smaller. Nevertheless, highest accuracy will be achieved, if a sample geometry with a small ratio C_{edge}/C_0 is selected. C_{edge}/C_0 is displayed for the actual sample geometry in the Sample Specification dialog of the Measurement menu. This method may be used for other sample geometries too (e.g. if the lower electrode exceeds the upper electrode). In this case, slightly different equations to Equation 3.15 apply, but the order of magnitude for the edge capacity will be the same. To illustrate this, for 40 mm sample diameter and 0.1 mm thickness, C_{edge}/C_0 is 0.016. For a typical dielectric material with a dielectric function of $\epsilon' = 4$, the error without edge correction would be $0.016/4 = 0.4\%$ of measured value. This can be clearly neglected against other sources of inaccuracies. If edge compensation is enabled the error maybe even be reduced to 0.1 % under the assumption, that the calculated edge capacity is accurate within 30 % of the real edge capacity. On the other hand, for 4 mm sample diameter and 1 mm sample thickness, C_{edge}/C_0 is 0.56 and the relative error $0.56/4=14\%$ without edge correction.

In a dielectric or impedance measurement a voltage U_0 with a fixed frequency $\omega/2\pi$ is applied to a sample cell which contains the sample material under test. U_0 causes a current I_0 at the same frequency in the sample cell. In addition, there will generally be a phase shift between current and voltage described by the phase angle.

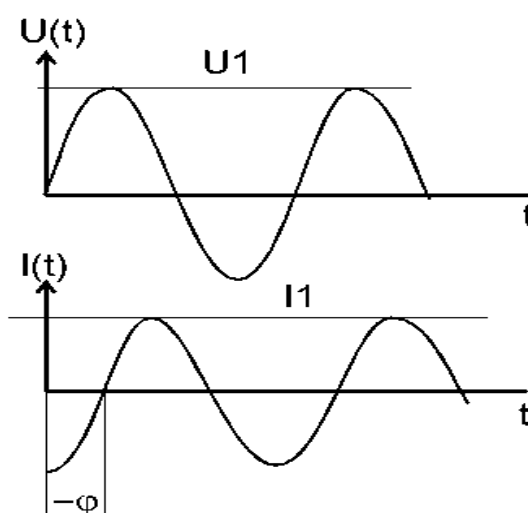


Figure 3.32 Illustration of voltage-frequency and current-frequency relations.

The ratio of U_1 and I_1 and the phase angle are determined by the electromagnetic properties of the sample material and the sample geometry. For easy calculation and representation of the formulas, it is convenient to use complex notation.

$$u(t) = U_1 \cos(\omega t) = \text{Re}(U^* \exp(i\omega t)) \quad (3.18)$$

$$i(t) = I_1 \cos(\omega t + \varphi) = \text{Re}(I^* \exp(i\omega t)) \quad (3.19)$$

with

$$U^* = U' + iU'', \quad U' = U_1, \quad U'' = 0$$

and

$$I^* = I' + iI'', \quad I' = I_1 \cos(\varphi), \quad I'' = I_1 \sin(\varphi)$$

For a sample with linear electromagnetic response, the sample impedance

$$Z^* = U^* / I^* \quad (3.20)$$

depends on the material properties and the sample geometry but not on the voltage amplitude U^* . This information can be expressed instead as Z^* in various other equivalent representations (dependent variables) which are described below in detail.

The values of U^* and I^* directly refer to the voltages and currents at the sample cell. Possible device calibration procedures which consider errors due to lines and non ideal sample cells are already included at this point.

WinDETA program supports the following three types of sample cells:

1. Dielectric sample cell with a round plate capacitor filled with the sample material (Figure 3.33):

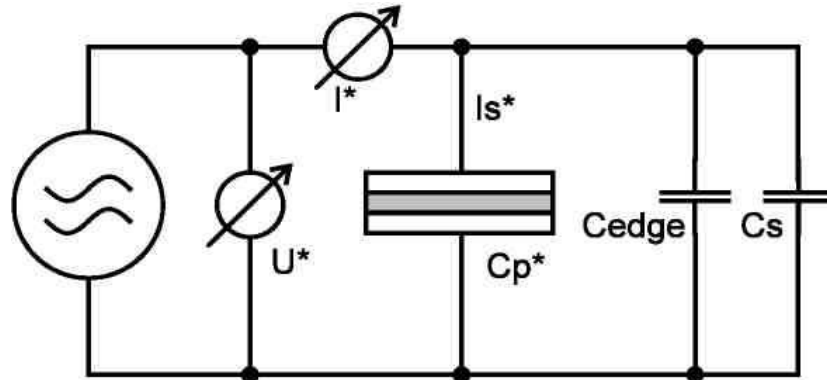


Figure 3.33 Illustration of dielectric sample cell with a round plate capacitor filled.

C_p^* denotes the complex parallel capacity of the filled sample capacitor without the influence of spacers. C_s denotes the additional capacity caused by the external sample cell stray capacity and the capacity of optional spacers in the sample capacitor. The sample cell stray capacity is due to the capacity of the electrode connection wires which is about 1 pF. For the liquid sample cell BDS 1308, an additional stray capacity of about 5.5 pF from the Teflon isolation and the upper and lower mounting plates has to be taken into account.

C_{edge} is an additional capacity because of electrical stray fields from the borders of the sample capacitor. C_{edge} will be only considered, if Use Edge Compensation in the Sample Specification dialog of the Measurement menu is active, referring to Edge Compensation for details of calculations of edge capacity.

The sample capacity is related to the measured voltage and current by

$$C_P^* = -i \frac{I^*}{\omega U^*} - C_{edge} - C_s \quad (3.21)$$

2. Dielectric sample cell with an interdigit electrode capacitor covered by the sample material (Figure 3.34).

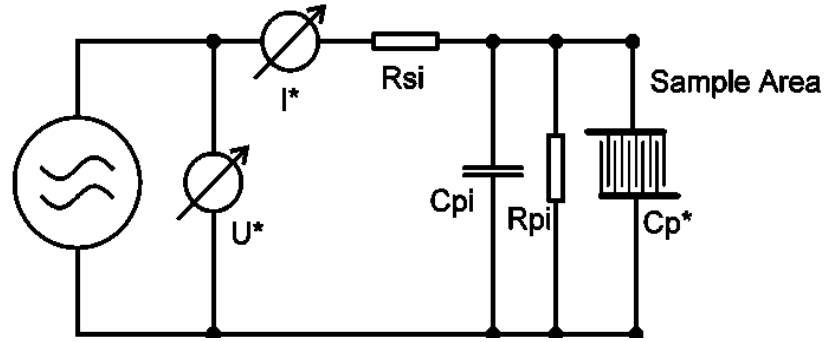


Figure 3.34 Illustration of dielectric sample cell with an interdigit electrode capacitor covered.

The complex capacity C_p^* of the sample area is corrected by the three elements Pre-Resistance R_{si} corresponding to the resistance of the evaporated electrode material, Parallel Resistance R_{pi} corresponding to the resistance of the object carrier material, Parallel Capacity C_{pi} corresponding to parallel the capacity due to the object carrier material.

Both for the round plate capacitor and for the interdigit electrode, the sample impedance Z_s^* and the admittance Y_p^* is calculated from complex parallel sample capacity C_p^* by;

$$Z_s^* = \frac{1}{Y_p^*} = -\frac{i}{\omega C_p^*} \quad (3.22)$$

The complex dielectric constant is ϵ^* related to the complex sample capacity by

$$\epsilon^* = \epsilon' - i\epsilon'' = \frac{C_p^*}{C_0} \quad (3.23)$$

with the empty cell capacity C_0 . For a sample cell consisting of round parallel plates with diameter D and spacing d , C_0 is calculated by;

$$C_0 = \epsilon_0 \frac{\pi \left(\frac{D}{2}\right)^2 - A_{spacer}}{d} \quad (3.24)$$

where A_{spacer} designates the average area inside the sample capacitor occupied by the spacer material. For the interdigit electrode, the value of C_0 has to be measured before the sample material is attached to the electrode.

The complex dielectric modulus is defined as:

$$M^* = M' + iM'' = \frac{1}{\epsilon^*} \quad (3.25)$$

The specific conductivity σ^* is related to the dielectric constant by

$$\sigma^* = \sigma' - i\sigma'' = i2\pi f\epsilon_0(\epsilon^* - 1) \quad (3.26)$$

The specific resistance of the material is calculated by

$$\rho = \frac{1}{\sigma} \quad (3.27)$$

Instead of the complex sample impedance Z_s^* , the electrical response of the sample in Figure 3.35 may be represented by the series or parallel resistance, conductance, capacity or inductivity as shown in Figure 3.36 below.

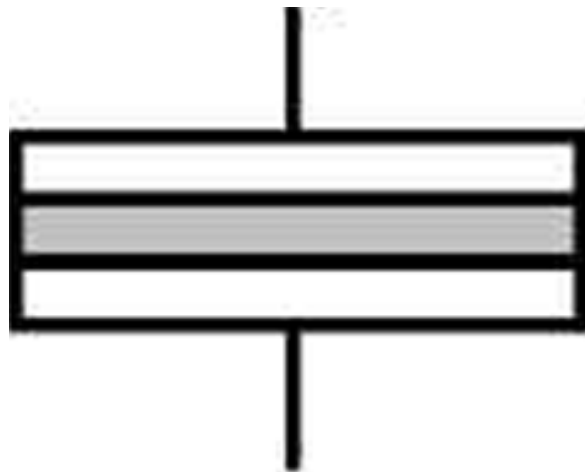


Figure 3.35 Illustration of dielectric sample cell.

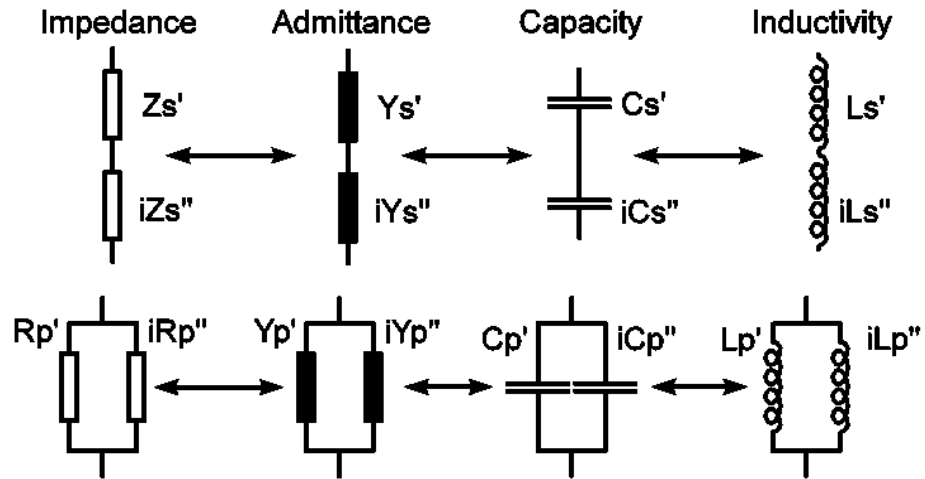


Figure 3.36 Illustration of series or parallel resistance, conductance, capacity or inductivity.

For the serial parts, the components are connected to the sample impedance by;

$$Z_s^* = Z_s' + iZ_s'' = \frac{1}{Y_s'} + i\frac{1}{Y_s''} = \frac{1}{i\omega C_s'} + i\frac{1}{i\omega C_s''} = i\omega L_s' + i\omega L_s'' \quad (3.28)$$

For the parallel parts, the components are connected to the sample admittance by

$$Y_p^* = \frac{1}{Z_p'} + i\frac{1}{Z_p''} = Y_p' + iY_p'' = i\omega C_p' + i\omega C_p'' = \frac{1}{i\omega L_p'} + i\frac{1}{i\omega L_p''} \quad (3.29)$$

The absolute values are calculated for Z_s , L_s , Y_p , and C_p . The loss factor, $\tan(\delta)$ is calculated by;

$$\tan(\delta) = \frac{\epsilon''}{\epsilon'} = \frac{\mu''}{\mu'} = \frac{Z_s'}{Z_s''} \quad (3.30)$$

From the loss factor, the loss angle δ is calculated by;

$$\delta = \frac{180^\circ}{\pi} \arctan\left(\frac{\epsilon''}{\epsilon'}\right) \quad (3.31)$$

In contrast to the loss angle δ , the phase angle

$$\varphi = \frac{180^\circ}{\pi} \arctan \left(\frac{Z_s''}{Z_s'} \right) \quad (3.32)$$

specifies the angle in the complex plane between the applied voltage U^* and the sample cell current I_s^* (without the stray capacity and spacer contribution) φ is shifted by 90° with respect to δ .

In the above formulas, the following symbols are defined as:

$\omega = 2\pi$ frequency	Circular frequency
$\pi = 3.14\dots$	Circle constant
$i = \sqrt{-1}$	Imaginary unit
$\epsilon_0 = 8.85 \cdot 10^{-12} \text{ As/V}$	Vacuum permittivity
D	Diameter of the sample capacitor's plates
d	Distance of the sample capacitor's plates
$\mu_0 = 4\pi 10^{-7} \text{ Vs/Am}$	Vacuum inductivity

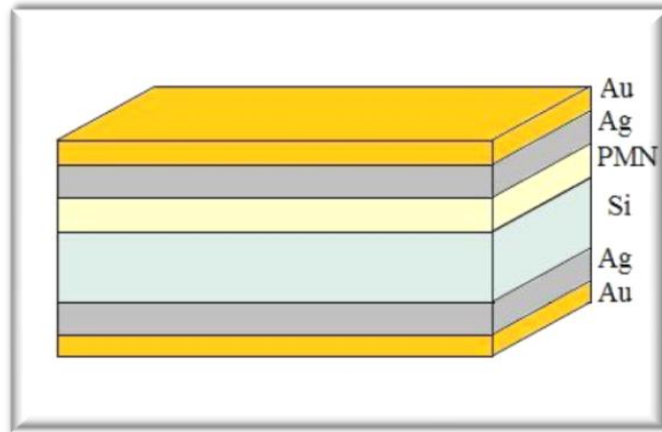


Figure 3.37 MOS structured PMN based samples for measurement.

Electrical testing in this research was performed in two stages, direct current (DC) and alternating current (AC). Basic, initial DC testing was conducted with a Wavetek Meterman 10XL multimeter to determine device yield per wafer. Alternating current (AC) testing of PMN based coatings was conducted with two pieces of Au plates equipment. The system measures at a V_{rms} or 0.1 V AC bias was used from 10^{-1} Hz to 10^7 Hz at room temperature.

3.4.2.11 I-V measurement

A current–voltage characteristic is a relationship, typically represented as a chart or graph, between an electric current and a corresponding voltage, or potential difference. In electronics, the relationship between the DC current through an electronic device and the DC voltage across its terminals is called a current–voltage characteristic of the device. Electronic engineers use these charts to determine basic parameters of a device and to model its behavior in an electrical circuit. These characteristics are also known as I-V curves, referring to the standard symbols for current and voltage.

A more general form of current–voltage characteristic is one that describes the dependence of a terminal current on more than one terminal voltage difference; electronic devices such as vacuum tubes and transistors are described by such characteristics (Bijl, 1919).

Figure 3.38 shows an I–V curve for a p–n junction diode. Figure 3.39 shows a family of I–V curves for a MOSFET as a function of drain voltage with overvoltage ($V_{GS}-V_{th}$) as a parameter.

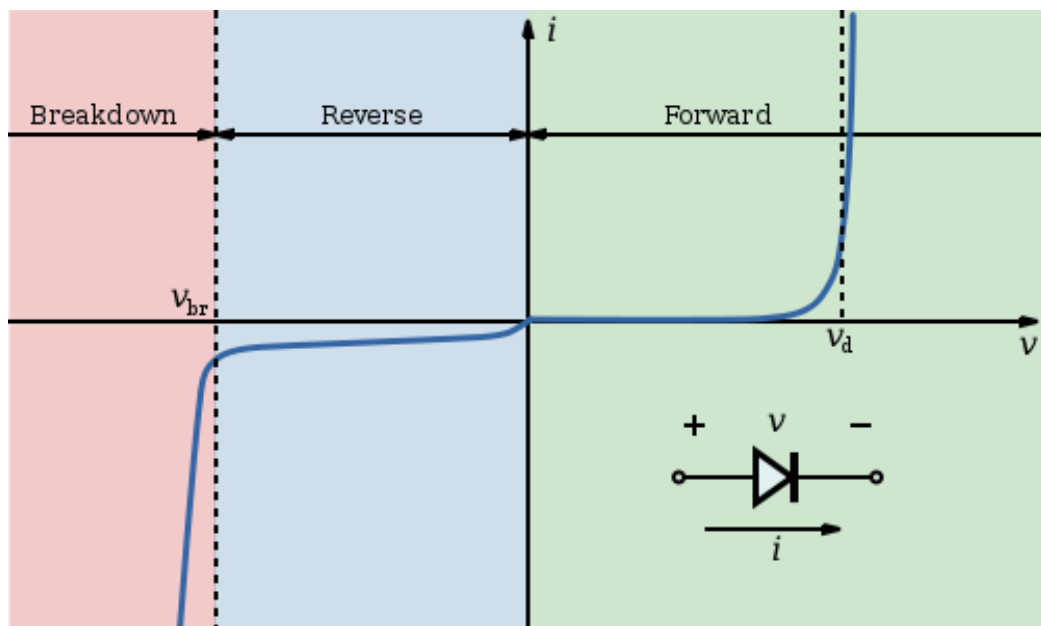


Figure 3.38 I–V curve of a p–n junction diode (not to scale).

The simplest I–V characteristic involves a resistor, which according to Ohm's Law exhibits a linear relationship between the applied voltage and the resulting electric current. Nonetheless, even in this case environmental factors such as temperature or material characteristics of the resistor can produce a non-linear curve.

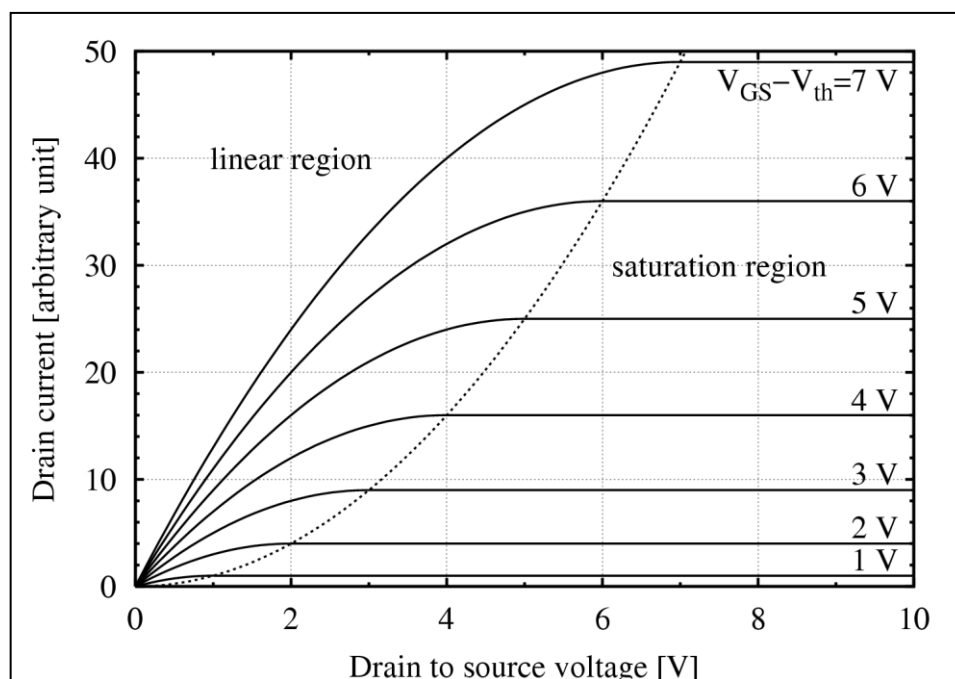


Figure 3.39 MOSFET drain current vs. drain-to-source voltage for several values of the overdrive voltage, $V_{GS} - V_{th}$; the boundary between linear (ohmic) and saturation (active) modes is indicated by the upward curving parabola.

The transconductance and early voltage of a transistor are examples of parameters traditionally measured with the assistance of an I–V chart, or laboratory equipment that traces the charts in real time on an oscilloscope (Bijl, 1919).

The Wavetek could measure a maximum of 20 M Ω , and was found to be a suitable initial test of the sputtered devices. More in-depth DC analysis was conducted using a Keithley 2400 (Figure 3.40) to obtain current-voltage (I–V) plots between -50 and +50 V in both positive and negative polarities.



Figure 3.40 Keithley 2400, I-V characterization unit (Electronic Materials Lab., DEU).

I-V testing on the Keithley 2400 was conducted in a specially fabricated Schottky barrier from MOS structured PMN based samples with two coaxial throughputs for electrical connections (Figure 3.41). The image also shows the positioning needles used to make contact with the anode and cathode of all devices during electrical testing.



Figure 3.41 Illustration of Schottky barrier from MOS structured PMN samples with two coaxial throughputs for I-V measurement connection.

3.5 Design and Production of Electronic Devices

After obtaining optimum PMN based film on Si substrates, a LED flash device was designed and produced from two transformers, two resistances ($10\text{ k}\Omega$), a transistor, a LED, a xenon bulb, a SR 96 diode, a 02K400SC diode, a battery with 2×1.5 dimension, and PMN based capacitor. From RC circuit as shown in Figure 3.42 for giving a square wave from AC power source to measure capacitor filling-drain time was calculated as experimental data. As an example, 3 % Dy doped PMN coated capacitors are used. Output was obtained by means of oscilloscope (TT T-ECHNI-C Oscilloscope MOS-620CH) image of the PMN capacitor. The difference between two peaks as discharge of the filling is set to 350 Hz. Power supply was used for applying load in ranging from 10 Hz to 10 kHz.

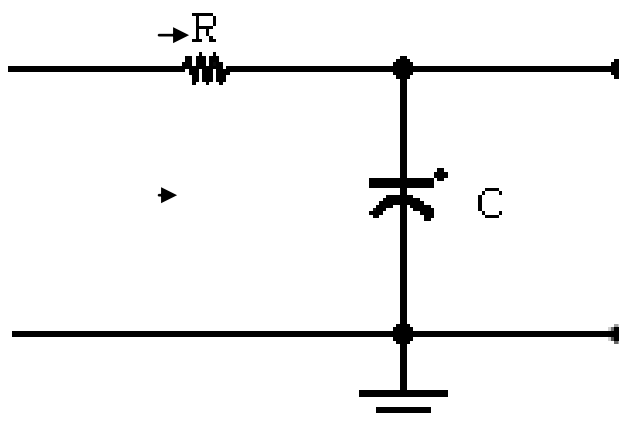


Figure 3.42 R-C device.

LEDs can be significantly more efficient than incandescent lamps at lower power levels, and therefore they use less battery energy than incandescent lightbulbs. Such flashlights have longer battery lifetimes than incandescent lamps of comparable light output. Moreover, LEDs are less fragile than conventional glass lamps.

Some LED flashlights electronically regulate the voltage supplied to the LEDs to stabilize light output as the batteries discharge. By contrast, the light output of non-regulated flashlights changes proportionally to the voltage supplied by the battery, resulting in a significant decline in output as battery voltage declines. LEDs also

have the advantage of maintaining a specific color temperature regardless of input voltage or current, while the color temperature of an incandescent bulb declines with the power available.

LED flashlights may consume 1 watt (W) or more from the battery, producing heat as well as light. Heat dissipation for the LED often indicates that LED flashlights have aluminum bodies to dissipate heat and can become warm during use.

CHAPTER FOUR

RESULT AND DISCUSSION

4.1 Solution Characteristics

4.1.1 pH Results

The pH values of the solutions were found to be in the range of 5.85 and 6.00 as shown in Table 4.1. The pH values of the solutions decreased as a function of acetic acid content in the solution. Their pH values are a significant issue to determine transparent solutions. It is also clear from Table 4.1 that the solutions exhibit an acidic character which influences hydrolysis, condensation and complexation reactions in the solutions. Sol-gel processing offer the amazing possibility to synthesize complex oxides such as PMN by mixing several alkoxide precursors. Those elaborate precursors can be established by mixing, after having previously and separately produced them by hydrolysis, the different solutions containing each a metal precursor Owing to this reality, acidic or basic characters of the complex solutions should be controlled before starting thin film fabrication.

Table 4.1 The pH and turbidity values of the PMN precursor solutions.

Number of test	pH range	Turbidity value (ntu)
1	5.85-6.00	8.26
2	5.85-6.00	8.45
3	5.85-6.00	8.47
4	5.85-6.00	8.51
5	5.85-6.00	8.68
6	5.85-6.00	8.68

The importance of the pH values of the solutions depending on time can be appreciated from Table 4.1. According to this result, acidity of the solutions does not

change within first 15 minutes because they stabilize. It was estimated that the pH values of the solutions comes to stable state in terms of PMN precursor. Since pH value of the solution is an important factor influencing the formation of the polymeric three-dimensional structure of the gel during the gelation process, it should be taken into consideration while preparing solutions. While ramified structure is randomly formed in acidic conditions, separated clusters are formed from the solutions showing basic characters (Culha et al. 2009). The other factor is dilution of the solution using solvent. The excess solvent physically affects the structure of the gel, because the liquid phase mainly consists of the excess solvent during the aging procedures. The changes in the gel structure at this stage partly influence the final structure (Culha et al. 2009).

4.1.2 Turbidity Results

Most modern instruments measure 90° scatter and they are called nephelometric turbidimeter. Turbidity measured in this way is stated in nephelometric turbidity units (ntu). In the current turbidity measurements were performed using nephelometric ratio method and the obtained results were recorded in terms of ntu with ± 2 of value or ± 0.01 ntu accuracy.

With turbidity experiments, whether powder precursor materials are dissolved very well in solutions is understood by looking ntu values before coating process. As mentioned before, the turbidity values of the solutions vary in the range of 0 ntu and 1,000 ntu. It is interpreted that powder based precursors are completely dissolved as turbidity value approaches to 0 ntu and they are not dissolved and some powder particles are suspended in a solution as it approaches to 1000 ntu. The fabrication of pure perovskite PMN powder or thin films is directly related to turbidity values of the solutions, which is 0 ntu. In this experiment, turbidity value of the solutions was measured as 8.42 ntu (Table 4.1). Based on the turbidity value, it can be pointed that powder based precursors are completely dissolved in the solutions. Moreover, these values present an important clue for further processing. It is worth noticing that optimum structural, thermal, microstructural, mechanical, optical and high dielectric properties are not obtained using undissolved solutions.

4.1.3 Rheological Properties

Rheological behaviour can be an important property to characterize sols and sol-gel transition. With this context, the viscosity of PMN ideal solution was measured as a function of time for different temperatures. Figure 4.1 shows the flow behavior of the PMN precursor solution. The increasing temperature caused a gradual decrease in viscosity value.

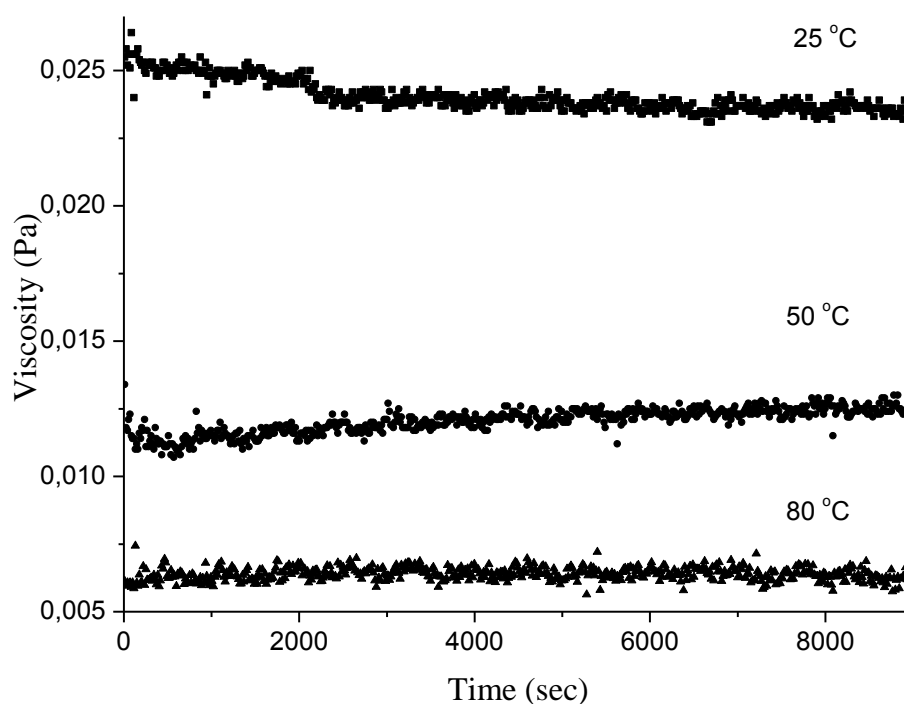


Figure 4.1 Viscosity values of ideal PMN precursor solution.

Gelation occurs when aggregation of particles or molecules takes place in a liquid, under the action of Van der Waals forces or via the formation of covalent or non covalent bonds. The process can be investigated using rheological measurement techniques (Culha et al. 2009). Figures 4.1, 4.2 and 4.3 clarify rheological properties such as viscosity, phase angle, viscous and elastic modulus for the solutions prepared from methanol as a function of temperature and time. Figure 4.2 depicts phase angle values of the solutions as a function of time. Figure 4.3 denotes viscosity values of the solutions as a function of time at 25°C, 50°C and 80 °C for 9000 s in air. Viscosity values of the solution for 25°C, 50°C and 80 °C were found to be 0.26

mPa.s, 0.12 mPa.s and 0.04 mPa.s, respectively. The striking property of the solution performed rheological experiment at 80 °C is the pronounced changes in its viscosity due to heating compared to others at 25°C and 50°C.

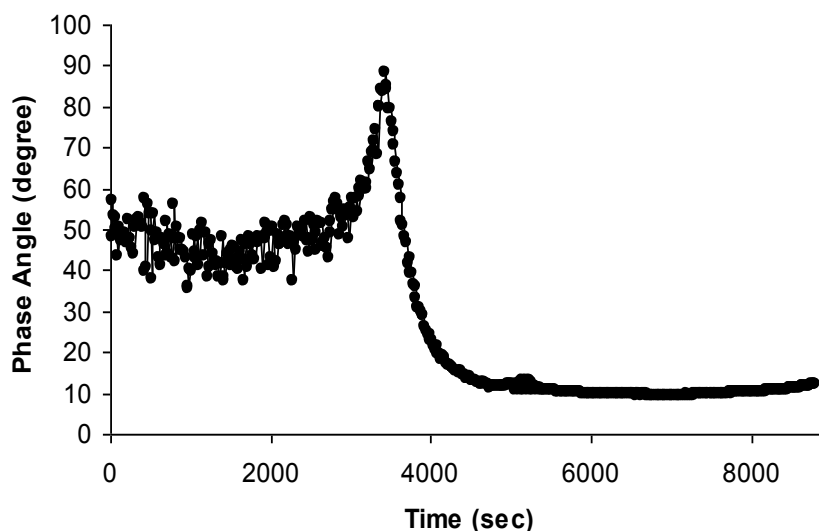


Figure 4.2 Viscosity values of ideal PMN precursor solution.

Solution exhibits continuously tendency of formation gel network depending on time. Therefore, the solution changed to the gel network structure after 3500 second. Insight into complex gelation mechanism can be gained from the following analysis having viscoelastic behaviors of the solution. Figure 4.1 denotes viscous and elastic moduli of the solution at 25°C, 50°C and 80 °C for 9000 s in air. Here, the experiment was performed at 25 °C for 3000 s and then at 50 °C for period between 3000 and 6000 s. After that, the experiment was completed at 80 °C for period between 6000 and 9000 s. As clearly seen from Figure 4.3, elastic and viscous moduli have an intersection point at 4703 s on x-axis. It can be indicated that viscous and elastic moduli can be changed depending on time and temperature for our cases. The time necessary to reach the intersection depends on the oscillations frequency (ω). Therefore, this intersection could be used to define the experimental gel point (Gentil et al. 2004).

Table 4.2 Chemical formulas and gelation times of the mixtures depending on additives rates.

Additives	Doping rates (%mol)	Chemical formulas	Gelation times (sec)
Pure PMN	0	$\text{Pb}(\text{Mg}_{0,333}\text{Nb}_{0,667})\text{O}_3$	3500-4000
Erbium	0,01	$\text{Pb}_{0,99}\text{Er}_{0,01}(\text{Mg}_{0,337}\text{Nb}_{0,663})\text{O}_3$	400-450
	0,03	$\text{Pb}_{0,97}\text{Er}_{0,03}(\text{Mg}_{0,343}\text{Nb}_{0,657})\text{O}_3$	450-500
	0,05	$\text{Pb}_{0,95}\text{Er}_{0,05}(\text{Mg}_{0,350}\text{Nb}_{0,650})\text{O}_3$	500-550
	0,07	$\text{Pb}_{0,93}\text{Er}_{0,07}(\text{Mg}_{0,357}\text{Nb}_{0,643})\text{O}_3$	600-700
Europium	0,01	$\text{Pb}_{0,99}\text{Eu}_{0,01}(\text{Mg}_{0,337}\text{Nb}_{0,663})\text{O}_3$	50-60
	0,03	$\text{Pb}_{0,97}\text{Eu}_{0,03}(\text{Mg}_{0,343}\text{Nb}_{0,657})\text{O}_3$	100-120
	0,05	$\text{Pb}_{0,95}\text{Eu}_{0,05}(\text{Mg}_{0,350}\text{Nb}_{0,650})\text{O}_3$	150-200
	0,07	$\text{Pb}_{0,93}\text{Eu}_{0,07}(\text{Mg}_{0,357}\text{Nb}_{0,643})\text{O}_3$	300-400
Dysprosium	0,01	$\text{Pb}_{0,99}\text{Dy}_{0,01}(\text{Mg}_{0,337}\text{Nb}_{0,663})\text{O}_3$	300-350
	0,03	$\text{Pb}_{0,97}\text{Dy}_{0,03}(\text{Mg}_{0,343}\text{Nb}_{0,657})\text{O}_3$	400-450
	0,05	$\text{Pb}_{0,95}\text{Dy}_{0,05}(\text{Mg}_{0,350}\text{Nb}_{0,650})\text{O}_3$	400-450
	0,07	$\text{Pb}_{0,93}\text{Dy}_{0,07}(\text{Mg}_{0,357}\text{Nb}_{0,643})\text{O}_3$	400-450
Samarium	0,01	$\text{Pb}_{0,99}\text{Sm}_{0,01}(\text{Mg}_{0,337}\text{Nb}_{0,663})\text{O}_3$	300-350
	0,03	$\text{Pb}_{0,97}\text{Sm}_{0,03}(\text{Mg}_{0,343}\text{Nb}_{0,657})\text{O}_3$	400-450
	0,05	$\text{Pb}_{0,95}\text{Sm}_{0,05}(\text{Mg}_{0,350}\text{Nb}_{0,650})\text{O}_3$	400-450
	0,07	$\text{Pb}_{0,93}\text{Sm}_{0,07}(\text{Mg}_{0,357}\text{Nb}_{0,643})\text{O}_3$	400-450
Terbium	0,01	$\text{Pb}_{0,99}\text{Tb}_{0,01}(\text{Mg}_{0,337}\text{Nb}_{0,663})\text{O}_3$	300-350
	0,03	$\text{Pb}_{0,97}\text{Tb}_{0,03}(\text{Mg}_{0,343}\text{Nb}_{0,657})\text{O}_3$	420-450
	0,05	$\text{Pb}_{0,95}\text{Tb}_{0,05}(\text{Mg}_{0,350}\text{Nb}_{0,650})\text{O}_3$	600-650
	0,07	$\text{Pb}_{0,93}\text{Tb}_{0,07}(\text{Mg}_{0,357}\text{Nb}_{0,643})\text{O}_3$	720-800

Table 4.2 shows the effect of time on the gelation behavior PMN and doped PMN solutions. Solutions exhibit continuously tendency of formation gel network rapidly with addition of rare earths. Thus, the doped PMN solutions changed to the gel network structure after a few minutes. For instance, it can be noticed from Table 4.2

that in spite of the fact that gelation time of pure PMN was in the range of 3500 sec and 4000 sec which are very long times, that of doped PMN was found to 50-800 sec. In practical applications, a very long gelation time is desirable during sol-gel processing.

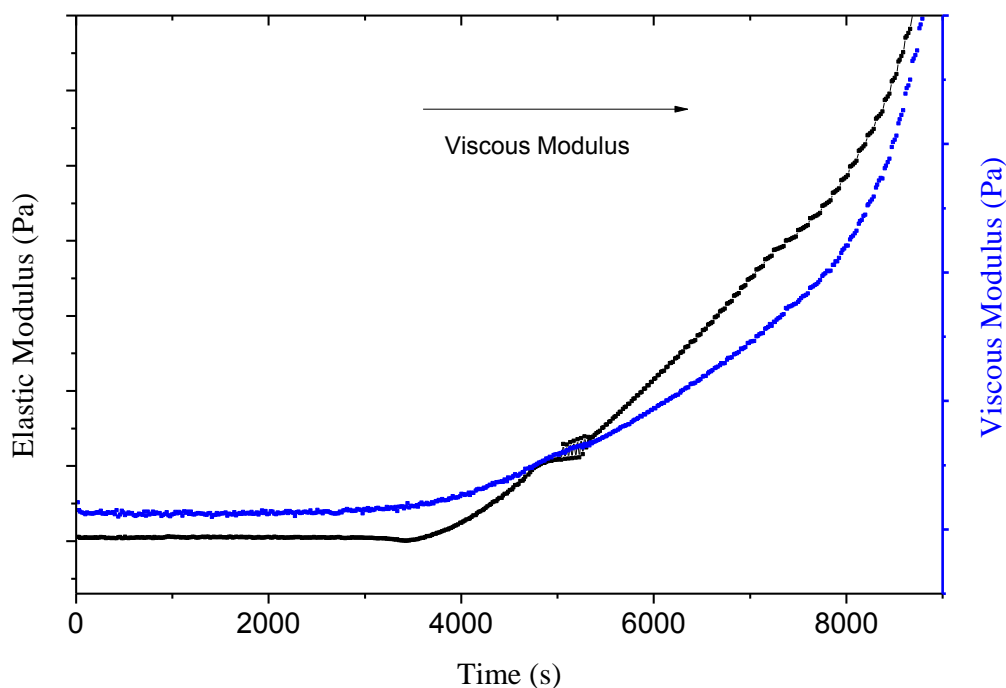


Figure 4.3 Viscosity values of ideal PMN precursor solution.

A very interesting gelling behavior was observed to be directly related to the content of RE^{+3} doping, as shown in Table 4.2. The solutions with RE^{+3} doping became colloids, and the more the RE^{+3} content, the faster it gelled. The 1 %, 3 %, 5 % and 7 % RE-doped PMN solutions are liquid while Nb was added. A semi-solid gel which could be flowable upon shaking up. The shaken up gel would gel again when shelved for another.

4.1.4 Hydrolysis and Condensation Reactions

To circumvent some of the problems mentioned above about the obtaining pure PMN and doped PMN perovskite structure, we have investigated the synthesis of PMN by a simple sol-gel method at room temperature using a minimum quantity of solvent; slow drying leads to a monolithic gel, thereby avoiding many of the

problems that often arise on drying due to accelerated evaporation. This work also has the aim of investigating the range of MgO, PbO, and Nb₂O₅ compositions in which PMN is obtained as a single phase; even though non-stoichiometric compositions are usually used to synthesize PMN, it is generally assumed that the product has the ideal stoichiometry Pb(Mg_{1/3}Nb_{2/3})O₃.

Solvents such as MeOH, EtOH, and BuOH, are usually used in sol-gel syntheses. 2-methoxyethanol is also extensively used in the synthesis of perovskite materials and is beneficial in assisting the dissolution of carboxylate precursors such as lead acetate. The key reactions leading to the formation of the precursor species are hydrolysis and condensation of the alkoxide reagents, leading to formation of metal-oxygen-metal (M-O-M) bonds (Beltran et al. 2000).

A multicomponent alkoxide solution was prepared by mixing lead acetate (Pb(CH₃COO)₂·3H₂O), anhydrous magnesium acetate (Mg-(CH₃COO)₂), and niobium ethoxide (Nb(OC₂H₅)₅). The solvents which were investigated with the objective of preparing a transparent solution, were 2-methoxyethanol (CH₃OCH₂CH₂-OH), methanol (CH₃OH), and ethanol (CH₃CH₂OH). The general scheme for preparation is shown in Figure 3.4; in Table 4.2 the compositions of the samples prepared are given, based on PMN stoichiometry; with an 5-10 % excess of Pb and Mg over the PMN stoichiometry.

First, 2-methoxyethanol was performed in our experiments. Although Ramamurthi et al. prepared a solution by first refluxing 1 mol of lead acetate trihydrate with 8 mol of methoxyethanol at ~118 °C, and then repeated distillations were conducted to remove the byproducts (Beltran et al. 2000). Ethylene glychol was the second solvent which was used, but neither lead acetate nor niobium ethoxide were soluble in it.

In our working conditions at room temperature, lead acetate did not dissolve, but on adding lead acetate to a solution of magnesium acetate in methanol, a transparent

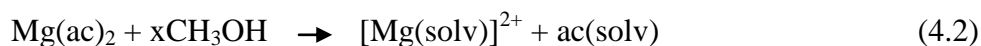
solution was obtained. This solution was added drop-wise to the stirred niobium ethoxide solution in methanol at 5 °C; after a few minutes, a white gel was obtained.

Even though processes based on methanol are considered to be sol-gel processes, in which M-O-M bonds are formed by hydrolysis and condensation of the alkoxide reagents, another key reaction with the use of this solvent is the alcohol exchange:



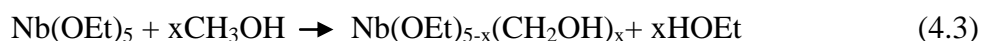
In this sense, the following reactions could be described in our system.

First:



where solv = CH₃OH and ac = CH₃COO⁻. The formation of CH₃COO⁻ could explain the dissolution of Pb(ac)₂ when it was added to the solution of magnesium acetate forming a [Pb(ac)_{2+x}]⁻ complex.

Second:



where OEt = CH₃CH₂O⁻. However, inasmuch as this reaction results in the generation of a certain amount of ethanol, the methanol was undried prior to use and the lead acetate contained water of crystallization, it is possible that H₂O from the sources contributed to the explanation of the precipitation of Nb(V) hydrous oxides (Beltran et al. 2000).

On addition of niobium ethoxide to methanol a white precipitate was observed, probably caused by the hydrolysis of Nb(V) ions, because undried methanol was used or because there are alcohol exchange reactions that form insoluble species.

However, this precipitation could be prevented by adding glacial acetic acid, $C_2H_4O_2$, (GAA) is a rather strong chelating ligand that has often been reported in the sol-gel literature as a stabilizing agent for nonsilicate metal alkoxide precursors. Complexing ligands such as GAA lead to less-hydrolyzable Me-acac bonds. The procedure used to prepare gels with methanol as solvent was as follows.

The niobium ethoxide (1.67 ml), which was already cooled down to 5 °C, was added to a mixture of methanol (20 ml) and GAA (2 ml). Separately, lead acetate (3.81 g) was added to a vessel with 10 ml of methanol and stirred until dissolution of the lead acetate. To this solution, if the sample was to be doped, RE^{+3} precursors was added to this solution at this stage. The magnesium acetate (0.388 g) was added to a vessel with 10 ml of methanol with continuously stirring, followed by dropwise addition of the niobium ethoxide solution. The solution hydrolyzed and was cured at room temperature; gelation occurred within a few minutes. Since this method using methanol as solvent gave transparent gels, it was used for all subsequent work.

4.2 Process Optimization

For the sol-gel synthesis of the PMN powders some combinations were prepared previously using 3 different solvents such as 2-methoxyethanol, ethylene glycol and methyl alcohol. These methods were described in Table 4.3. In addition to this, Figure 3.4 describes the production process in detail. According to this production procedure, in doped PMN production process, the first, stoichiometric amounts of Pb-acetate was prepared in 10 ml methanol and then 2 ml GAA were added to the solution. To prepare each solution, the dopands were separately incorporated into mixtures obtained from Pb-acetate and 12 ml methanol. Similar to the previous mixture process, to the mixture of 12 ml methanol and GAA was added Mg-acetate precursor as determined before. This process is that both additives was repeated separately for the Eu, Er, Dy, Sm and Tb doping. Following this, doped Pb solutions and Mg solutions combined with the help of magnetic mixer were held to one another in the resolution. Finally, to the obtained solution, Nb ethoxide was added at 5 °C to form rare earth doped PMN gel structures. For Er, Eu, Dy, Sm and Tb doped

PMN coatings were made contributions in ratio of 0.01 %, 0.03 %, 0.05 % and 0.07 %. In Table 4.2, PMN chemical formulas and gelation time are listed depending on the amount of additives.

Table 4.3 Chemical formulas and gelation times of the mixtures depending on additives rates.

<i>Combination</i>	<i>Chemical</i>	<i>Formula</i>	<i>Result</i>
1	Lead (II) acetate trihydrate	$Pb_{1.83}Mg_{0.29}Nb_{1.71}O_{6.39}$	Unsuccessful
	Magnesium acetate		
	Niobium (V) ethoxide		
	2-methoxyethanol		
	GAA		
2	Lead (II) acetate trihydrate	$Pb_{1.83}Mg_{0.29}Nb_{1.71}O_{6.39}$	Unsuccessful
	Magnesium acetate		
	Niobium (V) ethoxide		
	Ethylene glycol		
	GAA		
3	Lead (II) acetate trihydrate	$Pb(Mg_{0.333}Nb_{0.667})O_3$	Successful
	Magnesium acetate		
	Niobium (V) ethoxide		
	Methyl alcohol		
	GAA		

The following combinations were expresses as below:

Combination 1;

Pb(II)-acetate (3.81 g) and Mg-ethoxide (0.4 g) precursors were dissolved in 20 ml 2-methoxyethanol at room temperature in air. After Niobium (V) ethoxide (1.81 g) was directly incorporated into the former solution drop by drop, totally 10 ml acetic acid was used as a chelating agent in this experiment. Suspension was stirred for 5 hours and gelation occurred after 6 hours. The obtained gel was dried at 120 °C for 24 hours in air. The final sample was heat treated at 500 °C for 3 hours and 950°C for 2 hours in air.

Combination 2;

Pb(II)-acetate (3.81 g) and Mg-ethoxide (0.4 g) precursors were dissolved in 20 ml ethylene glycol at room temperature in air. Niobium (V) ethoxide (1.81 g) was directly added to the former solution drop by drop. After that, totally 2 ml acetic acid was used to accelerate reactions in the solution. Suspension was stirred for 5 hours and gelation occurred after 6 hours. Gel was subsequently dried at 120 °C for 24 hours in air. As a final procedure, a heat treatment for this sample was performed at 500 °C for 3 hours and 950°C for 2 hours in air.

Combination 3;

Similar procedure was applied in preparation of combination 3 and summarized here. Pb(II)-acetate (3.81 g) and Mg-ethoxide (0.4 g) precursors were dissolved in 20 ml methyl alcohol at room temperature in air. Niobium (V) ethoxide (1.81 g) was directly incorporated into the former solution drop by drop. Totally 2 ml acetic acid was used. Suspension was stirred for 1 hour and gelation occurred after 1 hour. Gel was dried for 24 hours at 120 °C. Here a heat treatment was applied at 500 °C for 3 hours and 950°C for 2 hours in air.

Complete gelation occurred within one day if the solvent was methanol. More homogeneous and strongly bonded gel network was obtained in the case of doped samples compared to undoped species. Gels were initially dried at room temperature and followed by drying at 80 °C in air. Calcination of the samples was performed in air at 500 °C at a heating rate of 10 °C /min for 3 hours to ensure the total removal of organic materials. These samples were then heated to various temperatures, namely 800, 900, 950 °C, and 1100 °C at a heating rate of 5 °C /min and were kept at these temperatures for 2–8 hours. During heat treatment, double alumina crucible system with cover was used in order to prevent the lead loss from the samples. To provide a lead rich atmosphere lead oxide (PbO) powder was used in the outer crucible.

In the case of RE^{+3} doping, the RE^{+3} concentration (x) in samples was varied between 0.01 and 0.07. When the samples were doped with RE^{+3} , it was necessary to account for the charge imbalance. One way was to keep the ratio of Mg:Nb concentration fixed which would result in the A site vacancies $\text{Pb}_{1-3x/2}\text{RE}_x(\text{Mg}_{1/3}\text{Nb}_{2/3})\text{O}_3$. However, in this study, Mg:Nb ratio was increased to balance the donor charge of RE^{+3} and to prevent A site vacancies. Hence, the compositions were expressed by the following formula $\text{Pb}_{1-x}\text{RE}_x(\text{Mg}_{(1+x)/3}\text{Nb}_{(2-x)/3})\text{O}_3$.

4.2.1 Thermal Analysis

Simultaneous thermal analysis (DTA-TG, SHIMADZU) measurements were carried out in oxygen atmosphere from room temperature to 950 °C at heating rate of 10 C/min. Cylindrical Pt crucibles of diameter 4 mm and depth 2 mm were used. Prior to measurements, PMN xerogel powders were firstly dried at room temperature for 24 hours. Approximately 59 mg of the obtained powders was heated and Al_2O_3 powder was used as a reference material.

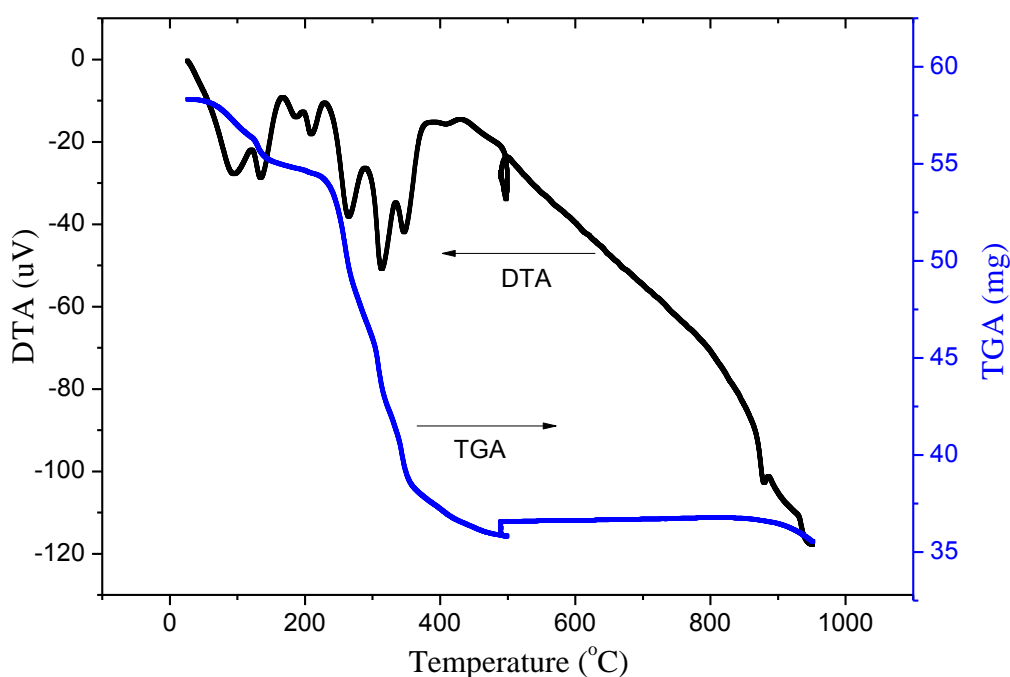


Figure 4.4 DTA-TGA curves of the PMN xerogel powders dried from a fresh solution at 25°C for 24 hours in air.

It is important to appreciate the process optimization mechanism leading to thermal behavior of PMN based powder xerogel to obtain regular heat treatment regime from room temperature to phase formation temperature. Figure 4.4 depicts DTA-TGA curves of the PMN powder xerogel, which were dried from a fresh solutions at room temperature (25°C) for 24 hours in air. As is evident from these figures, DTA curves of dried gel powders are differ from pure perovskite powder. Exothermic and endothermic peaks were found until 400 °C and other thermal effects were not observed above these temperatures until 500 °C. Three thermal phenomena in the xerogel were determined. One of them was the solvent removal at temperature of approximately 130 °C. At this temperature, the endothermic reaction is mostly due to evaporation of volatile organic components. The second effect was the combustion of OR groups in the samples between 150 and 280 °C. Two exothermic peaks were found at this temperature range. Organic materials coming from Pb-Mg-Nb based precursor, solvent, and chelating agent started to burn out at ~150 °C and the combustion was completed at ~400 °C. The strongest exothermic reaction of all samples took place approximately 370 °C. These reactions caused weight loses with increasing temperature. Approximately, totally weight loss percent is 42 %. Generally speaking, the last stage should have been the formation of ceramic oxides at 500 °C. However, we could not determine oxidation peaks with high intensity in the range of these temperatures. On the contrary, the exothermic peak at 880°C was determined. This peak may responsible the formation point of pyrochlore phase or phases.

Figure 4.5 shows DTA-TGA curves of the PMN powder heat treated at 950 °C for 2 hours in air. As can be simply seen in this figure, DTA curve of PMN oxide powders are differ from PMN xerogel powder. Thermal effects were not observed above these temperatures until 750 °C. Pure perovskite powders show the formation of pyrochlore phase at 730 °C. Above this temperature, formation of pyrochlore phase has been supported by XRD performing at different temperature as will be explained in XRD results.

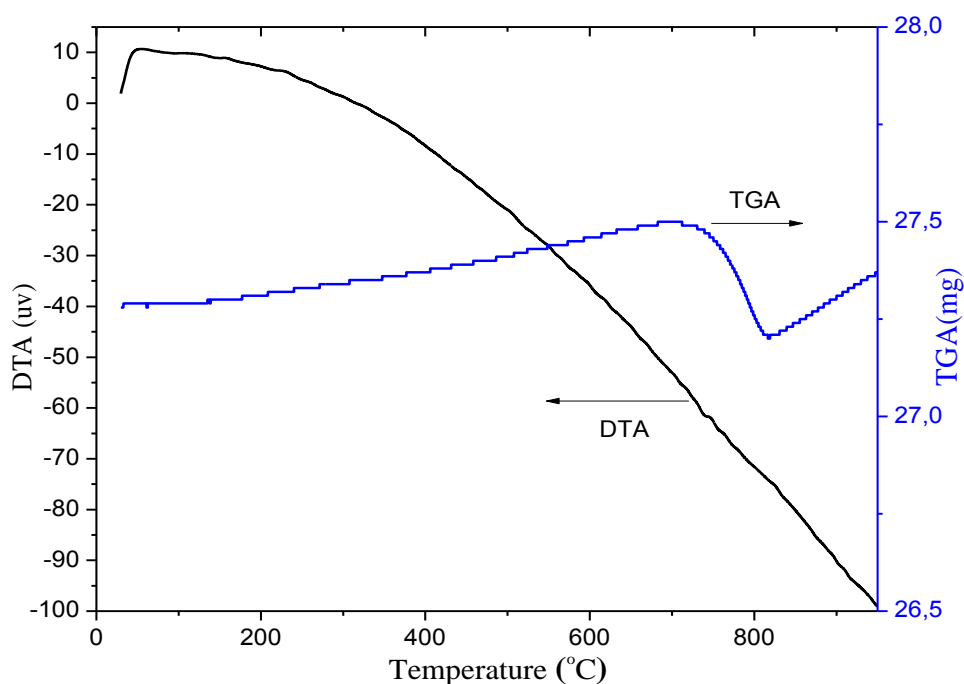


Figure 4.5 DTA-TGA curves of the pure PMN powders heat treated at 950 °C for 2 hours in air.

As for DTA-TGA curves of the PMN based xerogel powders, which were dried from a fresh solution at 25°C for 24 hours in air, it can be comparable for the effect on rare earth dopants in PMN structure. As can be seen in Figure 4.6, DTA curves of the gel powders containing rare earth elements are different from those of pure PMN gel powder. In spite of the fact that exothermic and endothermic peaks were found until 400 °C in this sample, other thermal effects were not observed above these temperatures until 500 °C. Note that three thermal phenomena in the xerogel sample were determined. The thermal behavior of such a sample resembles that of other ones. For instance, one of them was the solvent removal at a temperature of approximately 190 °C. At this temperature, the endothermic reaction is mostly due to the evaporation of physical water and solvent in the gel coming from liquid alkoxides, solvent, and chelating agent. The second effect was the combustion of OR groups in the samples at temperatures between 200 and 400 °C. This effect is referred to as the combustion of organic groups. It is clear from the figure that two exothermic peaks were found in this temperature range. Notably, organic materials coming from Pb, Mg, and Nb based precursors, solvent, and chelating agent started to burn out at ~150

°C and the combustion was completed at ~400 °C. The strongest exothermic reaction of the sample took place approximately 330 °C. These reactions caused weight losses

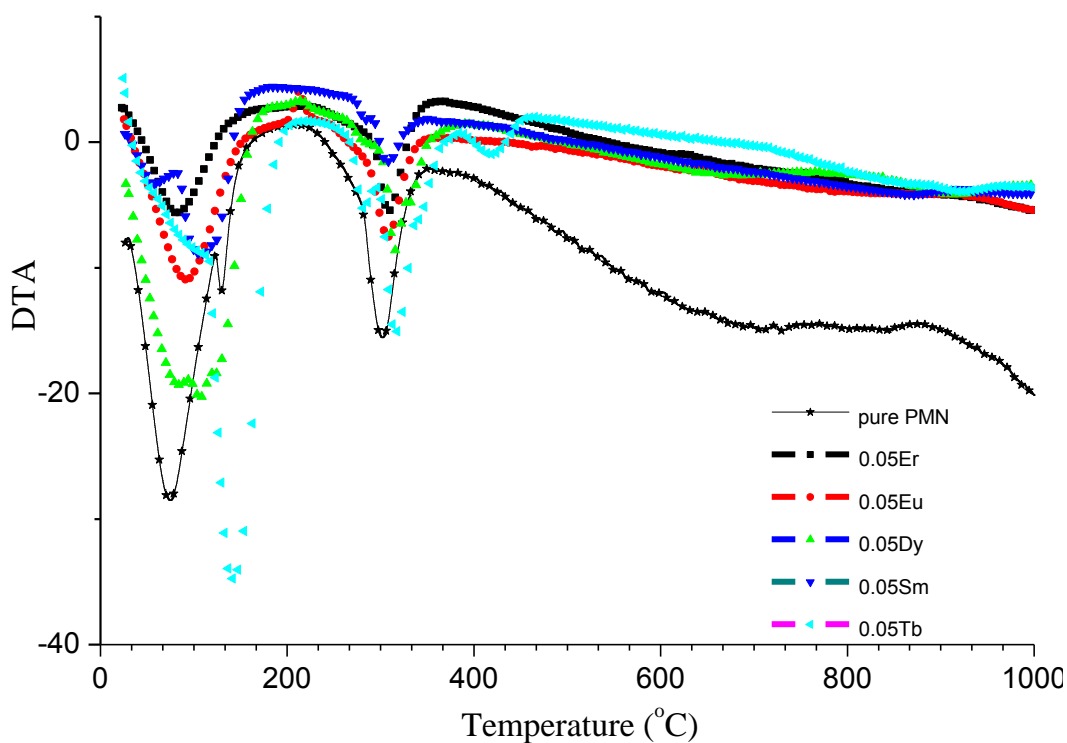


Figure 4.6 DTA curves of the pure PMN and doped PMN xerogel samples.

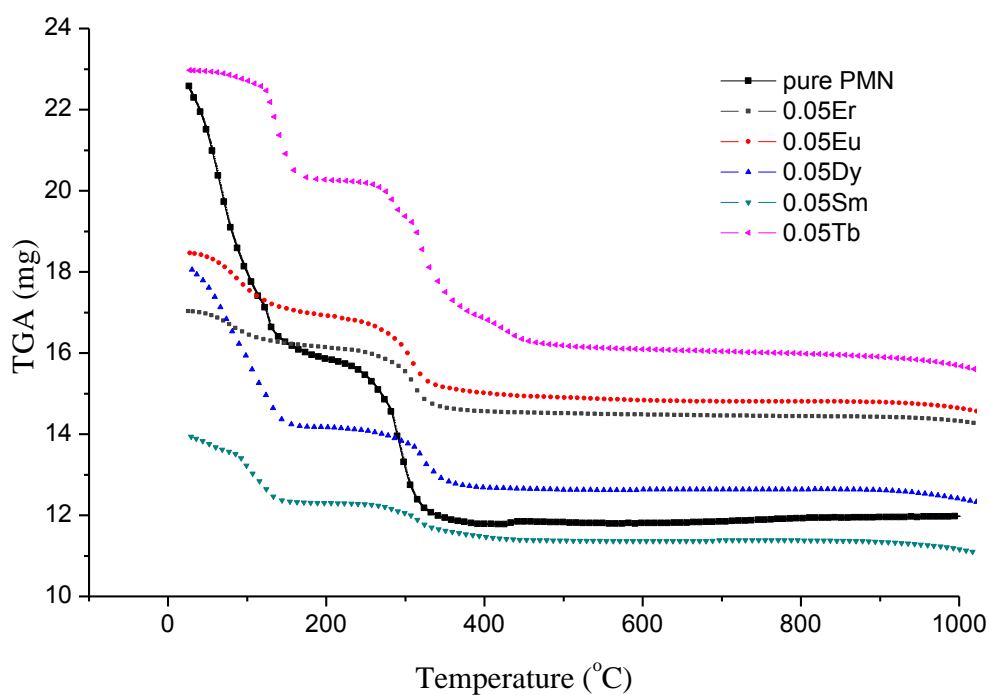


Figure 4.7 TGA curves of the pure PMN and doped PMN xerogel samples.

with increasing temperature. It can be easily expressed from these points of DTA curves that we have a good agreement with TGA. From this point of view, totally weight loss percentage is obtained to be approximately 46 % as seen in Figure 4.7. The last stage should have been the formation of ceramic oxides at 500 °C. Nevertheless, we could not determine oxidation peaks with high intensity in the range of these temperatures. On the contrary, the exothermic peak at 950°C was determined. This peak may be responsible for the formation point of perovskite phase or phases. Thus an understanding of the perovskite phase formation of PMN based ceramics greatly assists the control of sintering/annealing conditions using DTA-TGA. Depending on these data, process optimization concerning heat treatment regimes of the PMN based samples can be revealed, but not enough, and it can be supported by the virtue of FTIR and XRD results in detail.

4.2.2 FTIR Analysis

The aim of this section is to elucidate what type bonding can occur during heat treatment of PMN based materials, to understand the nature of their bonds, and thus to assist to be determined their process optimization. For that reason, FTIR spectrum of precursors, PMN gel and PMN coating samples for various temperature were recorded with FTIR spectrophotometer (Perkin Elmer). For each sample 25 scans were recorded with a resolution of 4 cm^{-1} . The spectra were represented as relative absorbance versus the wave number (cm^{-1}). Figures 4.8, 4.9 and 4.10 involve FTIR absorbance spectra of Mg, Pb and Nb based precursors. It is clear from the figures that Mg and Pb acetate precursors showed the nearly similar spectra corresponding to acetate bonds, whereas Nb ethoxide precursor exhibited ethoxide bonds.

Figure 4.11 displays FTIR absorbance spectra of undoped PMN solution and gel sample dried at room temperature for 24 hours in air. The bands at 2800 and 3700 cm^{-1} are because of O-H species in all doped PMN gel samples which were dried at 25°C, and those at 2350 cm^{-1} is due to C-H stretching frequencies. The band seen at 1450 cm^{-1} is due to C=O arising in terms of bridging type metal-acetate bonding (M-OCOO-M). The band at 1000 and 1300 cm^{-1} is the C-O stretching frequencies and

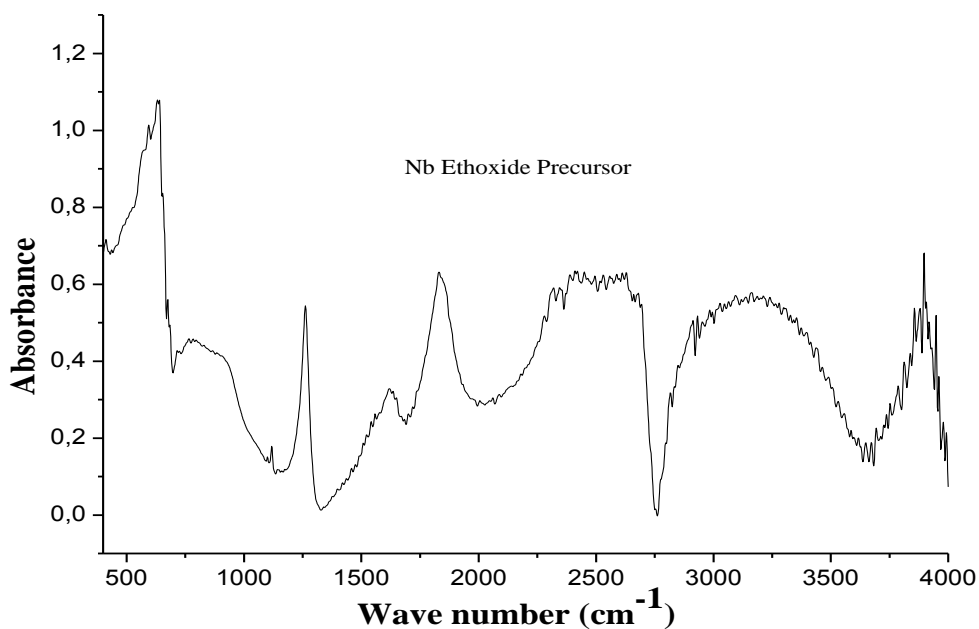


Figure 4.10 FTIR absorbance spectrum of Nb ethoxide precursor.

that at $650\text{--}900\text{ cm}^{-1}$ is due to weakly bound acetic acid molecule (HOOC-R). The spectra of the samples which were dried at 25°C in air, were nearly similar. But, the OH band has shifted slightly towards lower frequencies as seen in Figure 4.11. Upon increasing the gel network bonding of PMN solution, the absorbance peaks of O-H, C-H, C=O, C-O and M-OCOO-M bands increased.

Another method for determining the heat treatment regime depending on material structure is to investigate how properties of PMN alter in the temperature range of 25°C and 700°C with the help of FTIR analysis. In this case, Figure 4.12 indicates the FTIR absorbance spectra PMN based powders, which were dried at $25, 100, 200, 300, 400, 500$ and 600°C for 30 minutes in air. The spectra show characteristic vibrations in the region of $650\text{--}4000\text{ cm}^{-1}$. Apparently, the bands at 2800 and 3750 cm^{-1} 3600 and 4000 cm^{-1} are due to O-H species in the Pb-Mg-Nb based xerogel, which was heat treated at $25\text{--}300^\circ\text{C}$, respectively and those at $2200\text{--}2500\text{ cm}^{-1}$ is due to C-H stretching frequencies. We have a similar result with the literature (Culha et al. 2009). Notably, a broad band between $3,200$ and $4,000\text{ cm}^{-1}$ for all dried and heat treated samples was possible because of residual water present in the samples. The band seen at 1300 and 1500 cm^{-1} is due to C=O arising owing to bridging type

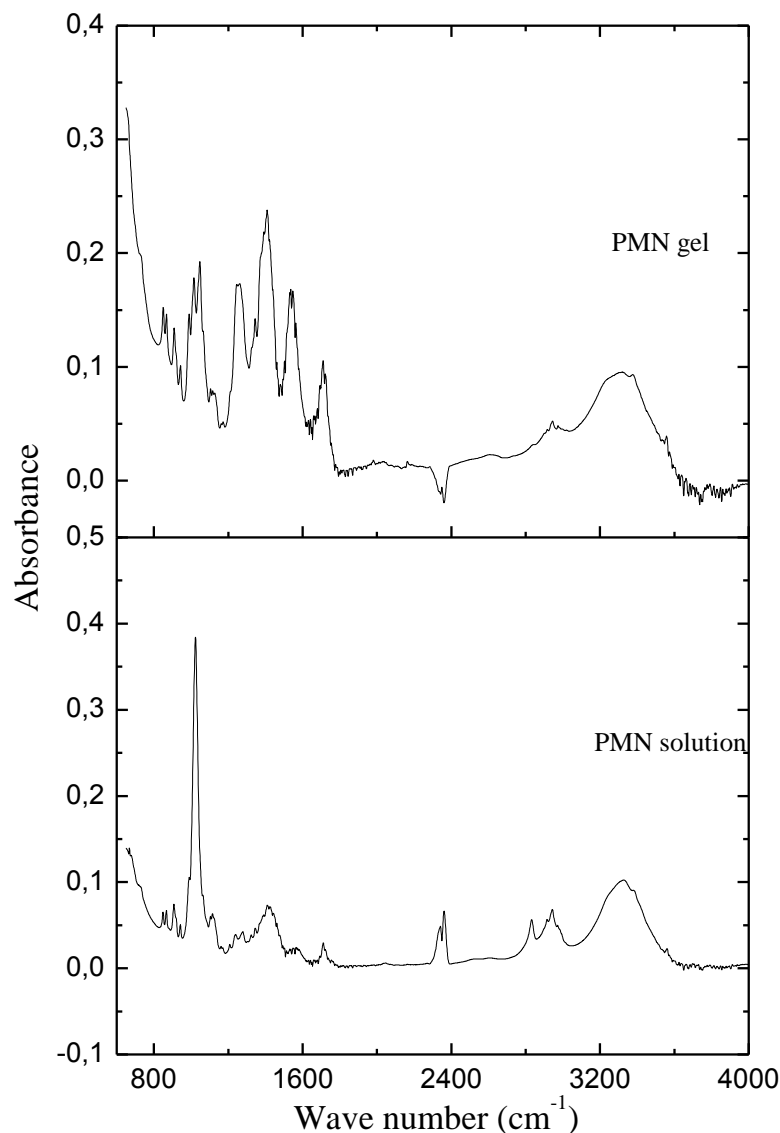


Figure 4.11 FTIR spectra of undoped PMN solution and gel samples.

metal-acetate bonding (M-OCOO-M) (Culha et al. 2009). The band at 1444 cm^{-1} is the C-O stretching frequencies and that at 1000 cm^{-1} is due to weakly bound acetic acid molecule (HOOC-R). Notice that the spectra of the samples, which were heat treated at 25, 100 and 200 °C were nearly similar. However, the OH band has shifted slightly toward lower frequencies as seen in Figure 4.12. Upon increasing heat treatment temperature from 25 to 600 °C, the frequencies of O-H, C-H, C=O and M-OCOO-M bands decreased (Culha et al. 2009). The spectrum of PMN precursor powders annealed at 500 and 600 °C, which shows an absence of absorption bands corresponding to organics and hydroxyls indicating complete removal of organics

and hydroxyls. The common features that appear below 900 cm^{-1} corresponds to the stretching vibrations of Pb=O , Mg=O and Nb=O , and also to the contributions of Pb-O , Mg-O and Nb-O bonds. In the spectrum of $500\text{-}600\text{ }^{\circ}\text{C}$, the band at as 500 cm^{-1} may be assigned to the vibration of PMN bands appear at high temperatures (Culha et al. 2009).

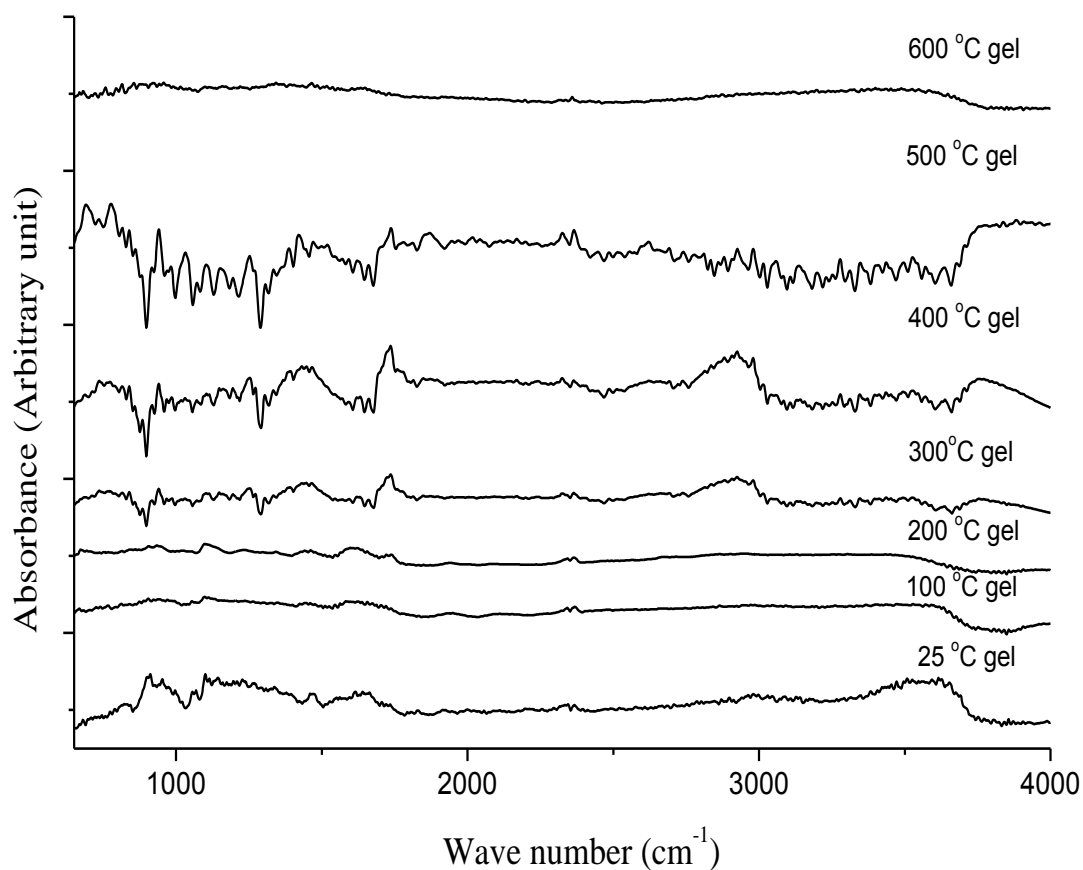


Figure 4.12 FTIR absorbance spectra of PMN gel samples at heat treated at different temperatures.

The influence of annealing temperature on the structure for the PMN thin films annealed at $100\text{ }^{\circ}\text{C}$ – $800\text{ }^{\circ}\text{C}$ shown in Fig. 4.13 illustrates the expected results. In these samples, there is an absence of absorption bands corresponding to organics and hydroxyls indicating complete removal of organics and hydroxyls. This result is the same as that of the PMN precursor powders annealed at 500 and $600\text{ }^{\circ}\text{C}$. Broadly speaking, the common properties that appear below 1600 cm^{-1} corresponds to the stretching vibrations of Pb=O , Mg=O and Nb=O and also to the contributions of Pb-O , Mg-O and Nb-O bonds. This is believed to be due to the oxidation of Pb , Mg and

Nb and the formation of PMN based perovskite structure. In the spectrum of 100 °C - 800 °C, the band at $\approx 500 \text{ cm}^{-1}$ may be assigned to the vibration of PMN bands appear at high temperatures and the band at $\approx 2400 \text{ cm}^{-1}$ may be assigned to the vibration of C-O appear at 300 °C - 800 °C.

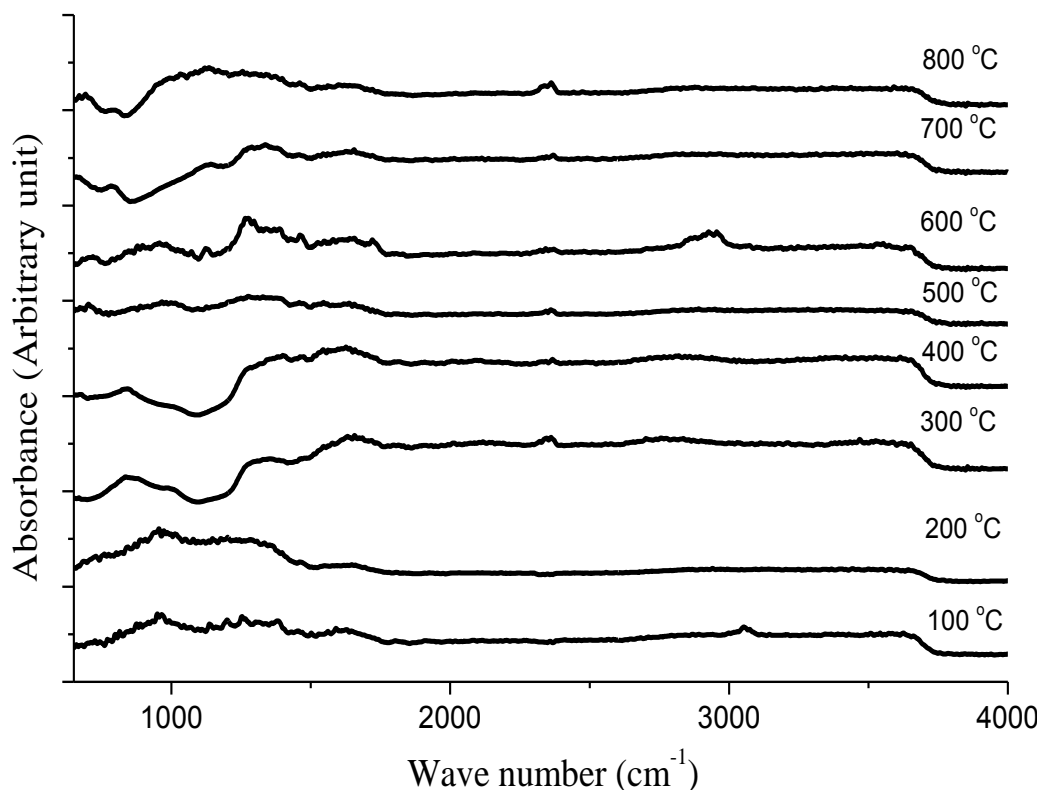


Figure 4.13 FTIR absorbance spectra of PMN coating samples heat treated at different temperatures.

Figures 4.14 and 4.15 demonstrate FTIR absorbance spectra of Er and Eu doped PMN xerogel samples which were dried at room temperature for 24 hours in air. The bands at 3500 and 4000 cm^{-1} are due to O-H species in Er and Eu doped PMN gel samples which were dried at 25 °C, and those at 2000–2300 cm^{-1} is due to C-H stretching frequencies. The band seen at 1600 cm^{-1} is due to C=O arising since the samples possess bridging type metal-acetate bonding (M-OCO-M). The band at 1000 and 1300 cm^{-1} is the C-O stretching frequencies and that at 600-850 cm^{-1} is due to weakly bound acetic acid molecule (HOOC-R). The spectra of the samples which was dried at 25 °C, were nearly similar. But, the OH band has shifted slightly towards lower frequencies as seen in Figures 4.14 and 4.15. Once increasing the

percentage of erbium and europium from 0.01 to 0.07, the frequencies of O-H, C-H, C=O, C-O and M-OCOO-M bands increased.

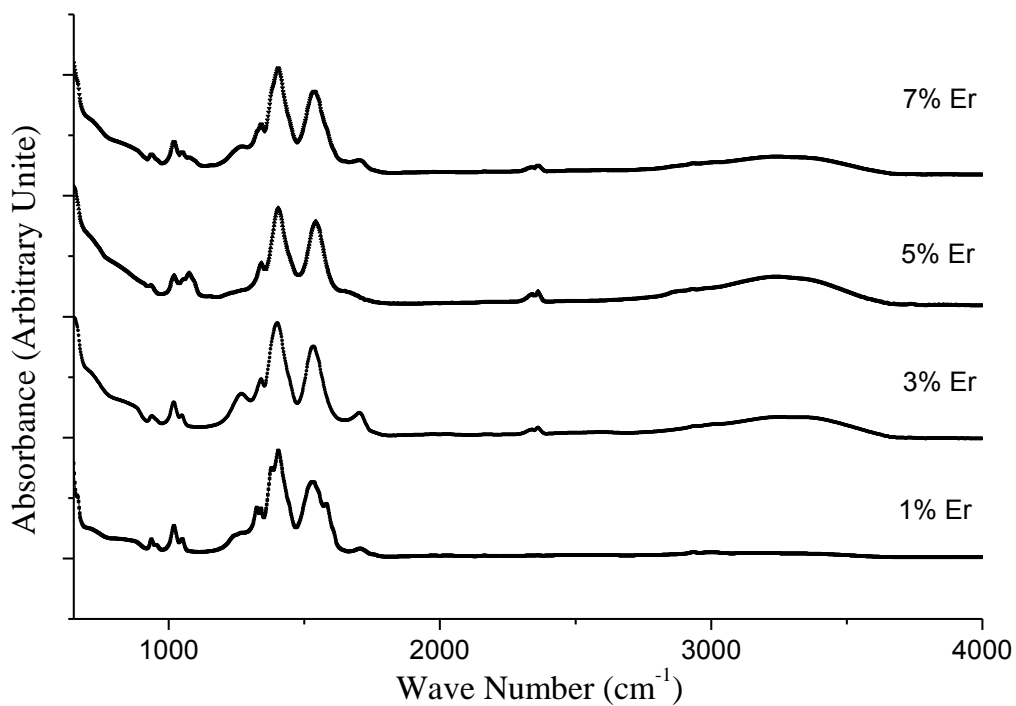


Figure 4.14 FTIR spectra for different amount of erbium doped PMN gels.

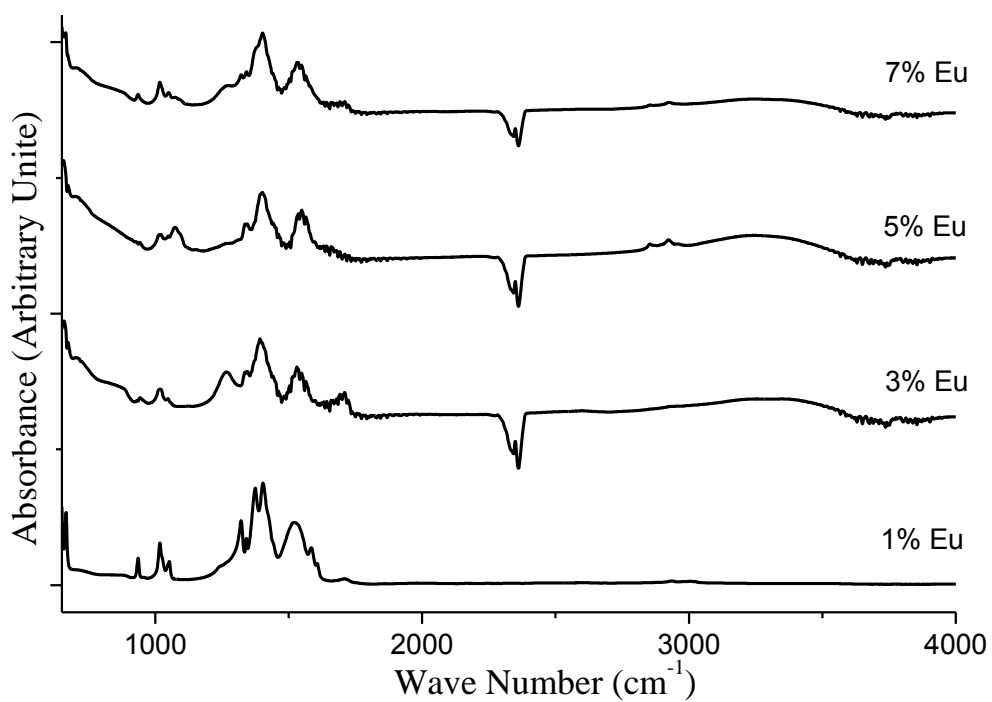


Figure 4.15 FTIR spectra for different amount of europium doped PMN gels.

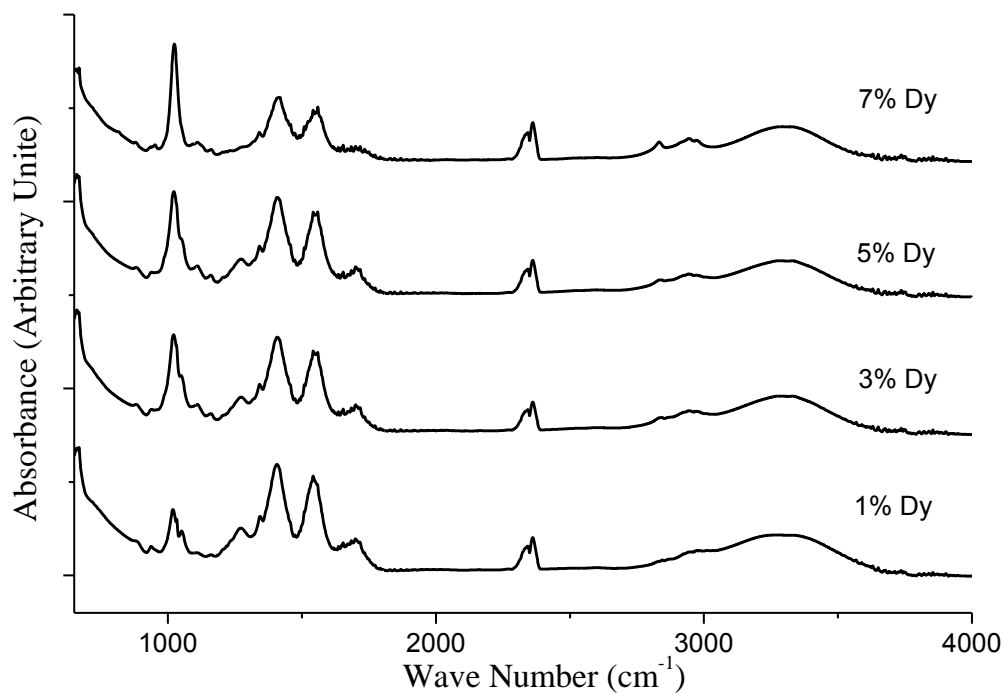


Figure 4.16 FTIR spectra for different amount of dysprosium doped PMN gels.

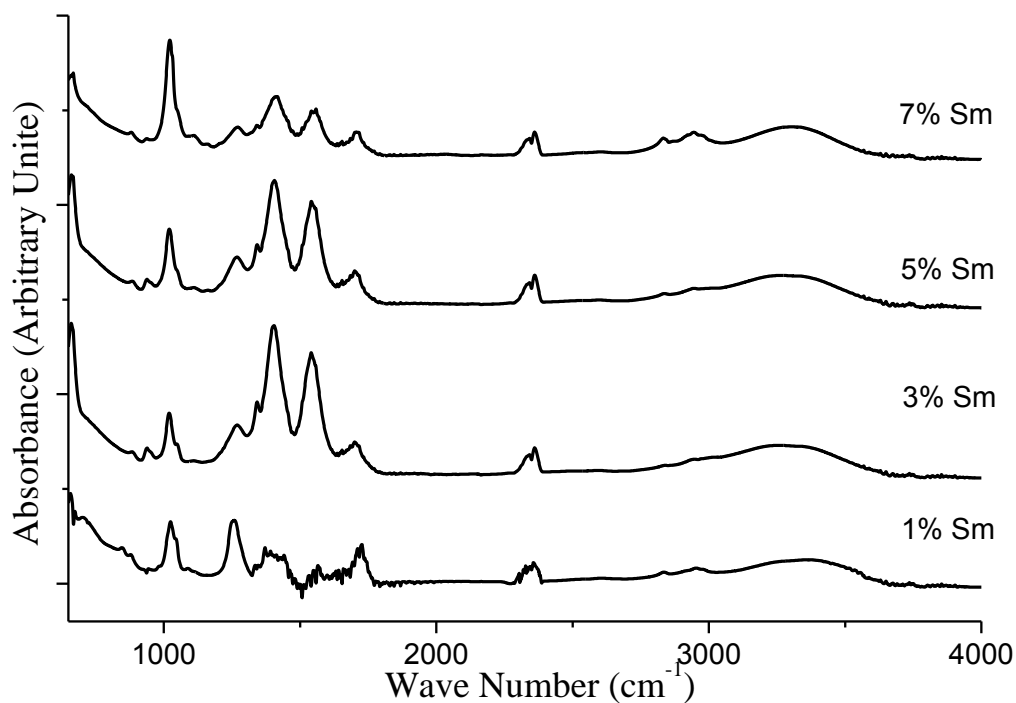


Figure 4.17 FTIR spectra for different amount of samarium doped PMN gels

Figures 4.16 and 4.17 signify FTIR absorbance spectra of Dy and Sm doped PMN xerogel samples. In this study, the xerogel powder samples were dried at room temperature for 24 hours in air. The bands at 3500 and 4000 cm^{-1} are due to O-H

species in Dy and Sm doped PMN xerogel samples, and those at 1700–2800 cm^{-1} is due to C-H stretching frequencies. The band seen at 1450 cm^{-1} is because of C=O arising due to bridging type metal-acetate bonding (M-OCOO-M). The band at 1000 and 1300 cm^{-1} is the C-O stretching frequencies and that at 400-900 cm^{-1} is by virtue of weakly bound acetic acid molecule (HOOC-R). It was found that the spectra of the samples which was dried at 25°C, were nearly similar. Nonetheless, the OH band has shifted slightly towards lower frequencies as seen in Figures 4.16 and 4.17. When the percentage of Dy and Sm dopants was increased from 0.01 to 0.07, the frequencies of O-H, C-H, C=O, C-O and M-OCOO-M bands increased.

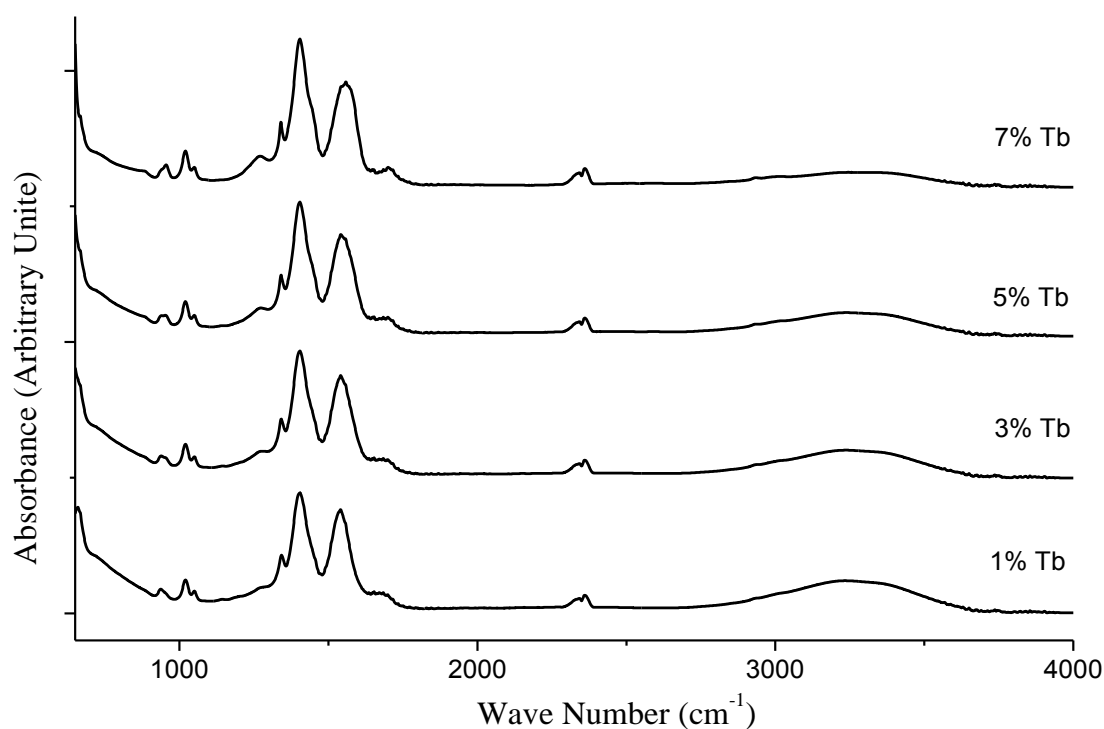


Figure 4.18 FTIR spectra of different amount of terbium doped PMN xerogels

As for the structure of Tb doped PMN xerogels, the samples were dried at room temperature for 24 hours in air. Figure 4.18 denotes FTIR absorbance spectra of Tb doped PMN xerogel samples. In these samples, the similar results were obtained just like Er, Eu, Dy and Sm PMN xerogels and explained for Tb doped PMN. The bands at 2800 and 3700 cm^{-1} are because of O-H species in Tb doped PMN xerogel samples, and those at 2300 cm^{-1} is due to C-H stretching frequencies. The band seen

at 1450 cm^{-1} is due to C=O arising due to bridging type metal-acetate bonding (M-OCOO-M). The band at 1000 and 1300 cm^{-1} is the C-O stretching frequencies and that at $650\text{--}900\text{ cm}^{-1}$ is due to weakly bound acetic acid molecule (HOOC-R). The spectra of the samples which were dried at $25\text{ }^{\circ}\text{C}$, were nearly similar. But, the OH band has shifted slightly towards lower frequencies as can clearly be seen from Figure 4.18. Upon increasing the percentage of Tb dopant from 0.01 to 0.07, the frequencies of O-H, C-H, C=O, C-O and M-OCOO-M bands increased.

4.3 Phase Analysis

X-ray diffraction (XRD) patterns of PMN powders and thin films were determined by means of a Rigaku diffractometer with a $\text{Cu K}\alpha$ irradiation (wavelength, $\lambda=0.15418\text{ nm}$). Measurements were performed by applying voltage of 40 kV and current of 30 mA . Scans were made over the range $2\theta=15\text{--}80^{\circ}$ in increments of 2° .

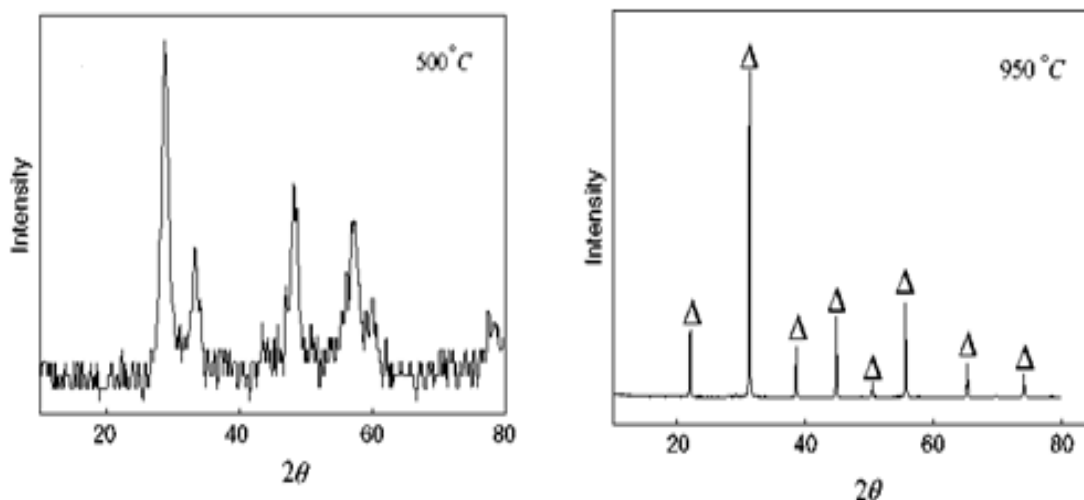


Figure 4.19 XRD patterns of the PMN samples prepared using methanol. Samples were calcined at (500°C) and (950°C) (Deliormanli 2008).

One of efficient ways to obtain the process optimization is to scan XRD patterns of the PMN powders after DTA-TG and FTIR analysis. More precise data will illustrate in XRD results for the process optimization in the production of PMN

based materials. To comparatively discuss XRD results of PMN based materials, the knowledge from literature was scrutinized in detail. Figure 4.19 describes the diffraction patterns of the PMN based samples prepared using methanol (Deliormanli 2008). XRD patterns of PMN powders which have pure perovskite (Lion 2004) and X-ray diffraction pattern of $\text{Pb}_{1.83}\text{Mg}_{0.29}\text{Nb}_{1.71}\text{O}_{6.39}$ pyrochlore produced by partial oxalate method and sintered at 1250 °C for 2.5 hours in air by its Miller indices (hkl) (Mergen et al) as shown in Figure 4.20.

Figure 4.20 identifies XRD profile of the pure perovskite structure and pyrochlore phase. XRD patterns of the PMN powders prepared by alkoxide route are presented in Figure 4.21, showing that the samples were calcined formerly at 500 °C and then sintered at 950 °C and 1100°C for 2 hours. Based on the results, the preliminary experiments seem promising to obtain the perovskite structure. $\text{Pb}(\text{Mg}_{0.333}\text{Nb}_{0.667})\text{O}_3$ phases were found from XRD patterns. It is clear that the intensity of diffraction peaks changed depending on temperatures and maximum perovskite phase was obtained at 950°C. The XRD diagram of the powders prepared by combination 3 calcined formerly at 500 °C and then 950 °C and 1100 °C for 2 hours. According to the results of the preliminary experiments combination 3 seems promising to obtain the perovskite structure.

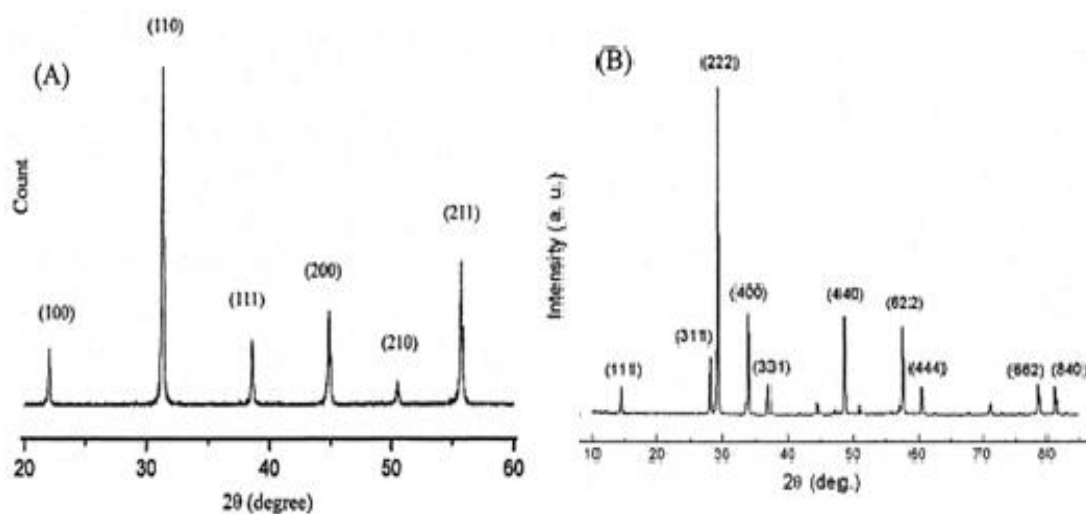


Figure 4.20 XRD patterns of PMN powders. (A) PMN powder, pure perovskite (Lion 2004), (B) X-ray diffraction pattern of $\text{Pb}_{1.83}\text{Mg}_{0.29}\text{Nb}_{1.71}\text{O}_{6.39}$ pyrochlore produced by partial oxalate method and sintered at 1250 °C for 2.5 hours. Peaks are labeled by its Miller indices (hkl) (Mergen et al).

The PMN thin films on n-type Si wafer easily crystallized into perovskite phase after 730 °C annealing for 1 hour, as indicated by Figure 4.22 and 4.23. However, the peaks had very low intensity and were broader compared with that by lower annealing temperature (<600°C for 1 hour, Figure 4.22). Using the peak intensity as a reference, this implied that higher temperature grew the PMN grains in the film and their tetragonal crystalline structure becomes more fully developed (hence more diffracting planes).

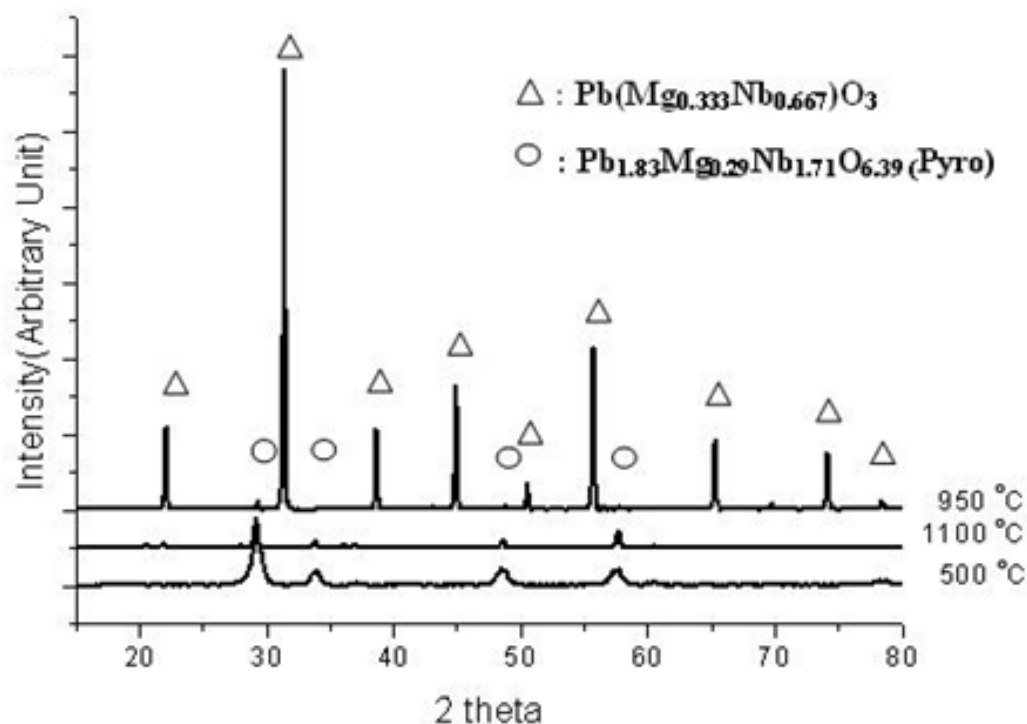


Figure 4.21 XRD results of PMN powders obtained at various temperature.

XRD confirmed the thin film had the desired perovskite phase (Figure 4.23). X-ray penetration depth for PMN was estimated to be about 2 μm . So understandably, XRD of 6-layer film shows less substrate information than the thinner, 1-layer one and the tetragonality of PMN thin films was much lower than their powder counterparts (Figure 4.22), which implies that the substrate may have a strong effect in limiting PMN thin films' ferroelectric properties (the so-called "clamping effect").

After the final deposition and sintering, the films were studied by XRD and SEM for their phases, thickness and grain size. For electrical property measurements, Ag

electrodes were applied onto the annealed film surface as top electrodes. The film was uniform in color, which relates to its thickness, and in morphology, which appeared to be free of cracks.

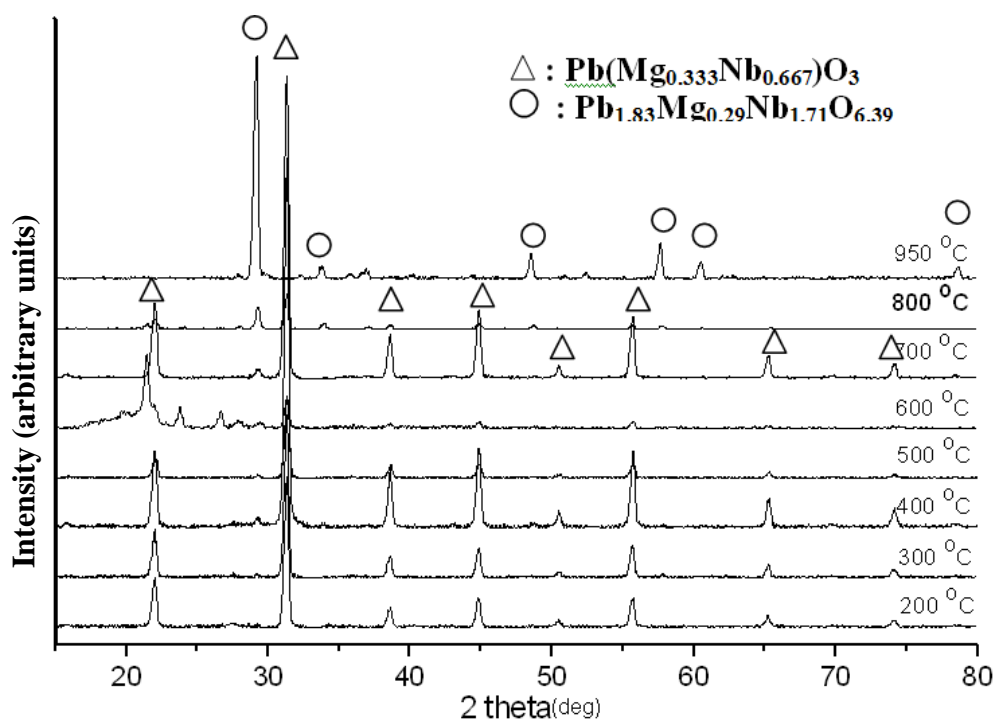


Figure 4.22 XRD results of PMN coatings produced on n-type Si substrates depending on various temperatures.

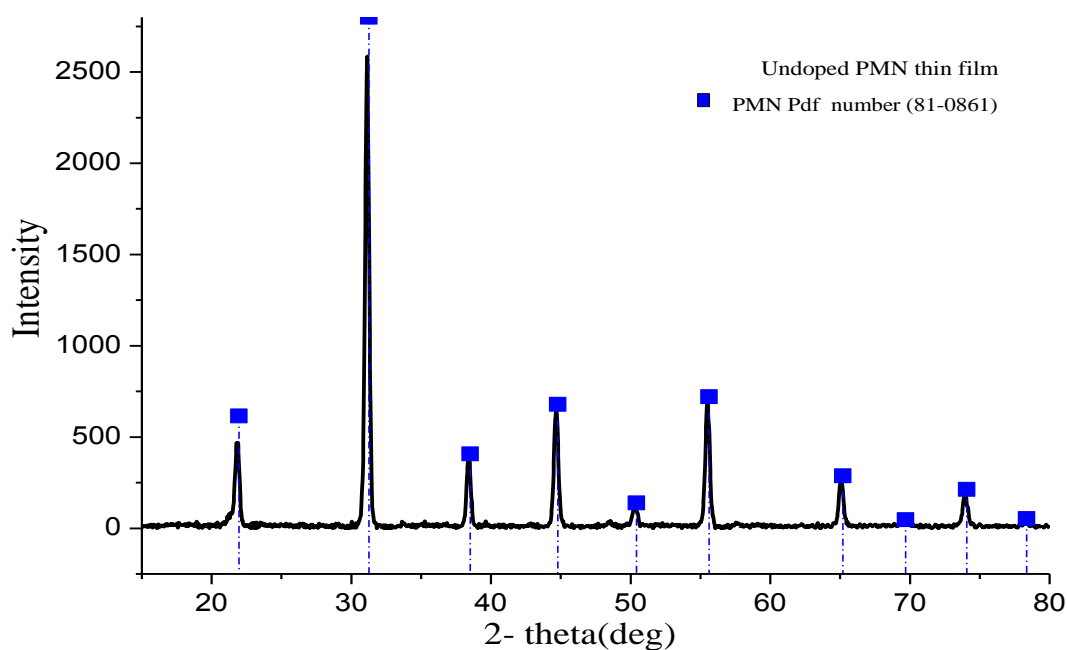


Figure 4.23 XRD pattern of pure PMN thin film produced at 730 °C for 1 hour in air.

XRD patterns of PMN thin films on Si substrate depending on temperature. All of peaks are identified as the diffraction lines $\text{Pb}(\text{Mg}_{0.333}\text{Nb}_{0.667})\text{O}_3$ perovskite and $\text{Pb}_{1.83}\text{Mg}_{0.29}\text{Nb}_{1.71}\text{O}_{6.39}$ pyrochlore phases. This is evidence from Figure 4.22 that the intensity of PMN and pyrochlore phase peaks showed differences when increasing processing temperature.

The XRD pattern clearly revealed the random orientations were obtained. In addition, it clearly showed that the peaks at 700°C are optimum phase of perovskite PMN thin film. A consideration of the structural variations accompanying the pyrochlore–perovskite transformation can give insight into how the dielectric constant might be changed from unit cell to unit cell (Deliormanli 2007-2008).

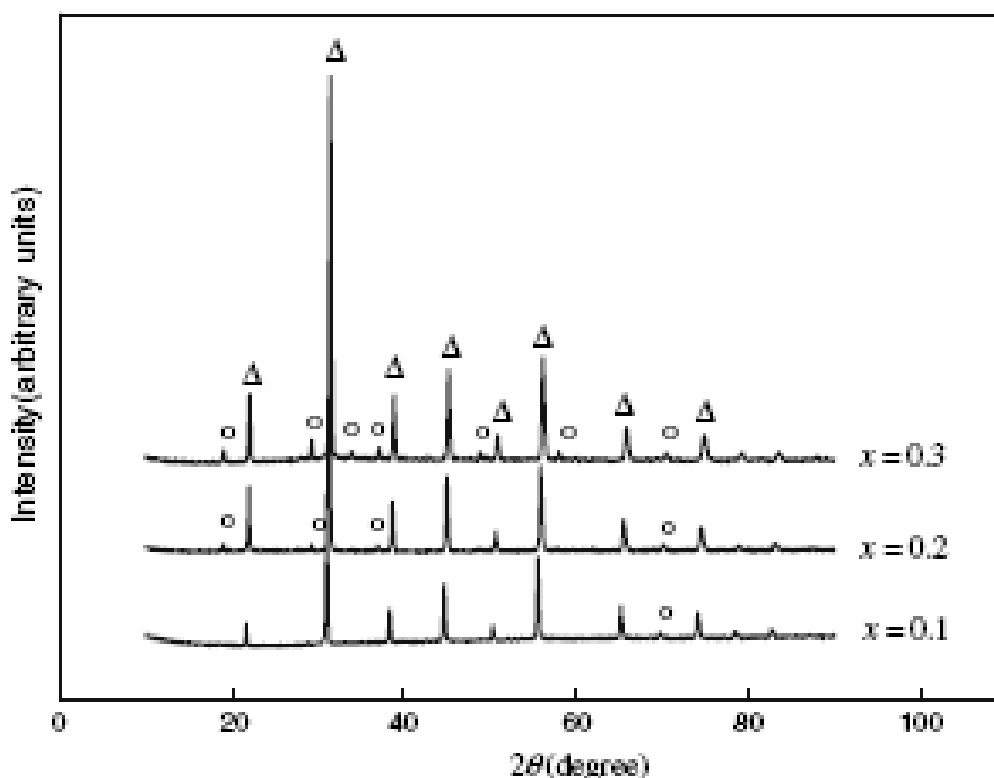


Figure 4.24 XRD results of different amount of Nd doped PMN powders obtained at 1100°C for 2 hours in air (Deliormanli 2008).

The phase formation and electrical properties of piezoelectric ceramics can be modified by using dopants. Effects of rare earth elements (RE) doping on the phase formation and electrical properties of piezoelectric ceramics such as barium titanate

and lead zirconate titanate are well studied. The effect of RE addition on the PMN system has also been studied in the literature to a degree. The effects of adding a fixed amount of rare earth additives on the microstructure and dielectric properties of PMN-PT ceramics. The results of literature pointed out that doping of neodymium (Nd^{+3}) (see in Figure 4.24) resulted in a slight decrease in the grain size and a lowering of the dielectric constant studied effect of lanthanum (La^{+3}) additions on the phase formation of PMN ceramics. The former study indicated that the presence of La^{+3} cations implied an increase in the short range ordering, resulting negative space-charge balance into the ordered domains in PMN. In the majority of these previous studies it is observed that the effects of RE addition has been studied using solid state reactions and at fixed RE compositions (Deliormanli 2008). In the majority of these previous studies it is observed that the effects of RE addition has been studied using solid state reactions and at fixed RE compositions. Also, no published work on the effect of Er^{+3} , Eu^{+3} , Dy^{+3} , Sm^{+3} and Tb^{+3} doping in the PMN system is encountered. Therefore, the aim of the present work is to examine the phase formation and microstructural evolution in RE-modified lead magnesium niobate powders prepared by the sol-gel method.

The XRD patterns presented in Figure 4.25 demonstrates the effect of Er^{+3} doping on the phase formation as a function of Er^{+3} concentration. It is clear that at high concentrations (above 3 mol%) Er^{+3} causes the formation of unwanted pyrochlore phase. According to the results of the effect of Nd^{+3} on the PZT thin films and PMN powders fabrication a pure perovskite phase was obtainable up to 5 wt% and 10 wt% respectively and a pyrochlore phase was found to coexist with perovskite structure beyond this concentration (Deliormanli 2008).

As if the aforementioned issue, we observed that the perovskite phase peaks are slightly higher for the sample that contains 0,01 mol Er^{+3} compared to the undoped sample like in Figure 4.23. Furthermore, Nd^{+3} doping between 1 mol% and 7 mol% did not cause the pyrochlore formation. However, the detrimental effect observed beyond 10 mol%. But Er^{+3} doping between 1 mol% and 7 mol% cause the pyrochlore formation. The best Er^{+3} doped PMN powders were produced using the

solution having 0,01 mol Er^{+3} . All of peaks are identified as the diffraction lines $\text{Pb}(\text{Mg}_{0,333}\text{Nb}_{0,667})\text{O}_3$ and $\text{Pb}_{1,83}\text{Mg}_{0,29}\text{Nb}_{1,71}\text{O}_{6,39}$ (pyro) phase. This is evidence from Figure 4.25 that the intensity of $\text{Pb}_{1,83}\text{Mg}_{0,29}\text{Nb}_{1,71}\text{O}_{6,39}$ peaks increased when increasing Er^{+3} percentages. The XRD patterns clearly presented the random orientations were obtained. It is evident that no texture can exist in the powder.

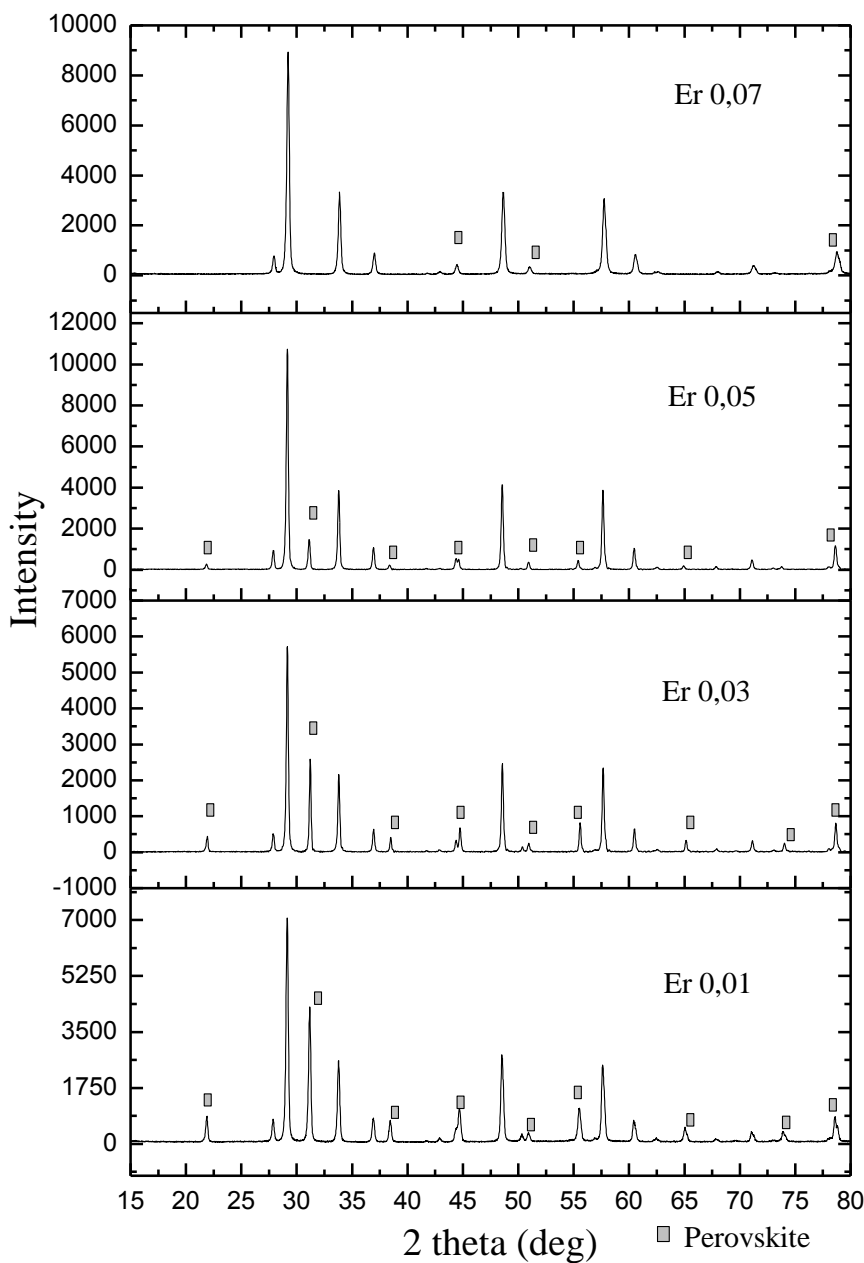


Figure 4.25 XRD results of different amount of Er doped PMN powders obtained at 950°C for 2 hours in air.

Figure 4.26 illustrates XRD patterns of Eu doped PMN powders depending on doping rates of Eu. In this section, Eu was added into the solutions for different concentrations. It was found that the best Eu doped PMN powders were produced using the solution having 5 mol% Eu.

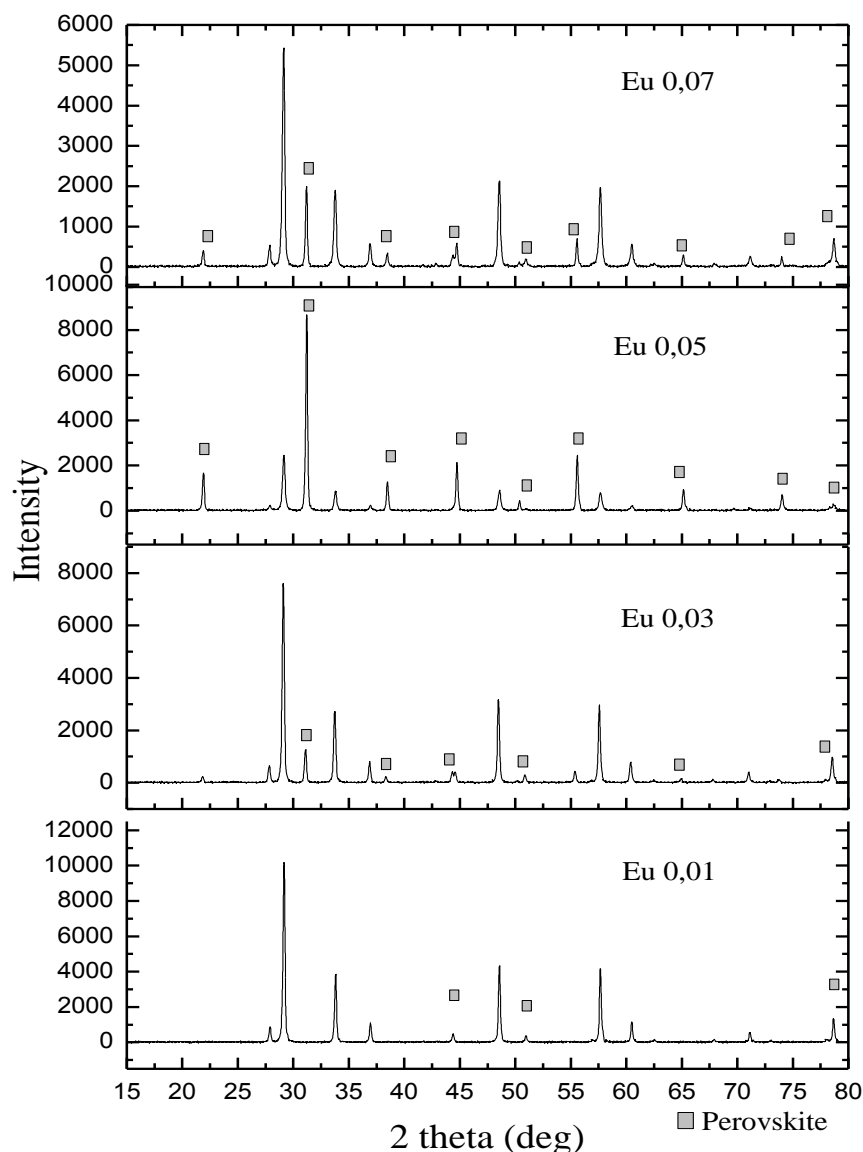


Figure 4.26 XRD results of different amount of Eu doped PMN powders obtained at 950 °C for 2 hours in air.

Note that all of peaks are identified as the diffraction lines $\text{Pb}(\text{Mg}_{0.333}\text{Nb}_{0.667})\text{O}_3$ and $\text{Pb}_{1.83}\text{Mg}_{0.29}\text{Nb}_{1.71}\text{O}_{6.39}$ phases as determined in Er doped PMN powders. This is also evidence from Figure 4.26 that the intensity of $\text{Pb}_{1.83}\text{Mg}_{0.29}\text{Nb}_{1.71}\text{O}_{6.39}$ peaks

decreased when increasing Eu percentage in the sample. It is obviously seen from the XRD patterns that the random orientations were determined. In this case, it can be stated that there is no any texture by reference to the random orientation of Er doped PMN powders. Generally speaking, inasmuch as the texture formation depends on annealing conditions such as temperature, time and specific atmosphere, everything during the annealing process should be under control.

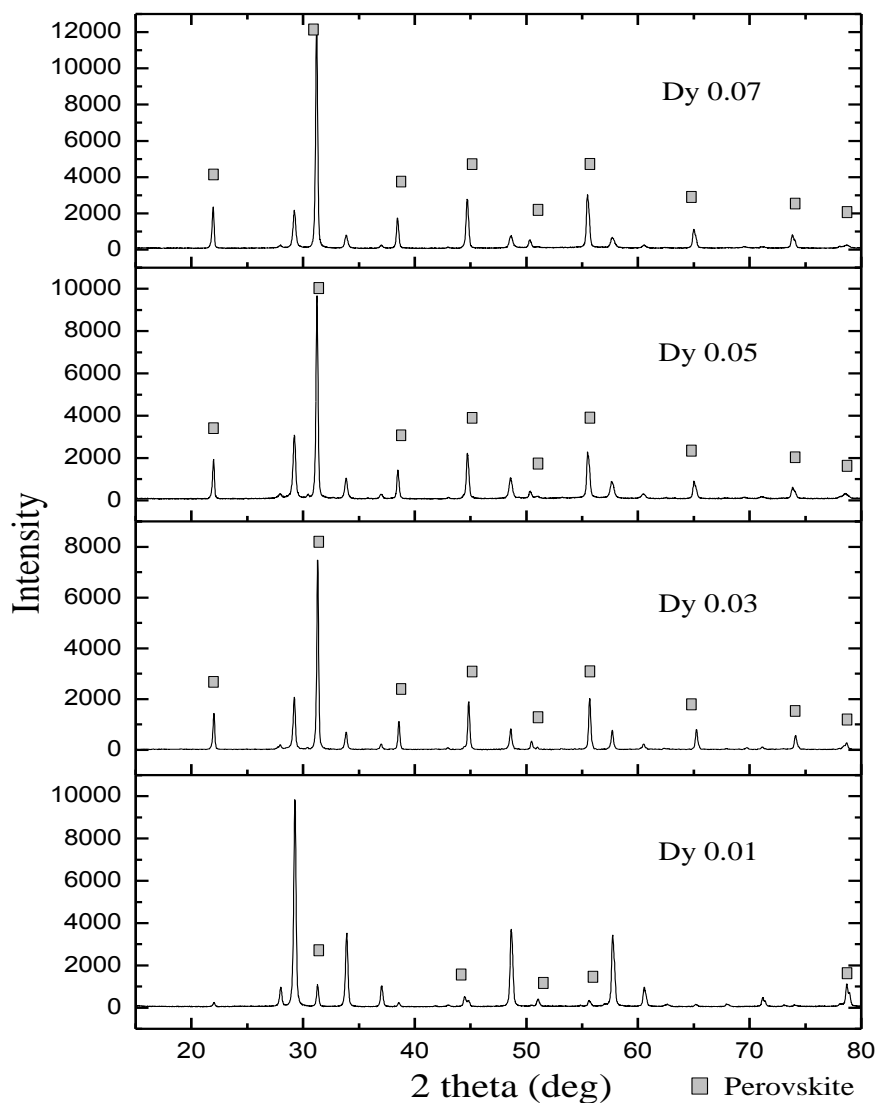


Figure 4.27 XRD results of different amount of Dy doped PMN powders produced at 950 °C for 2 hours in air.

Figure 4.27 depicts XRD patterns of Dy doped PMN powders produced depending on doping rates of Dy element. Here, Dy was added into the solutions

from 0.01 to 0.07 mol concentrations in the solution preparation. Apparently, the best Dy doped PMN powders were produced from the solution having 7 mol % rate. All of peaks are identified as the diffraction lines $\text{Pb}(\text{Mg}_{0.333}\text{Nb}_{0.667})\text{O}_3$ phase. This is evidence from Figure 4.27 that the intensity of $\text{Pb}_{1.83}\text{Mg}_{0.29}\text{Nb}_{1.71}\text{O}_{6.39}$ peaks decreased when increasing Dy percentage. The XRD patterns obviously indicated that pure perovskite PMN peaks can be obtained with increasing Dy percentage in the coating.

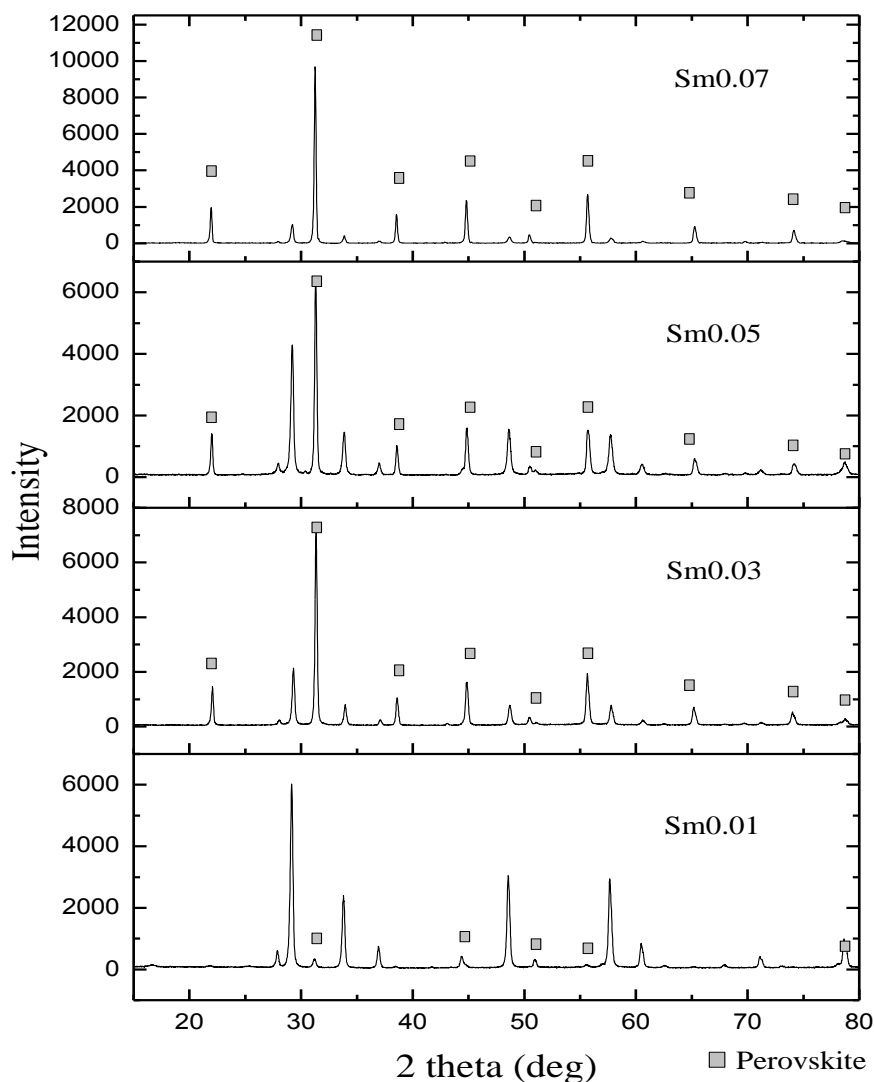


Figure 4.28 XRD patterns of different amount of Sm doped PMN powders obtained at 950 °C for 2 hours in air.

Figure 4.28 presents XRD patterns of Sm doped PMN powders depending on doping rates of Sm. In this section, Sm was incorporated into the solutions from 0.01

to 0.07 mol concentrations. These powders were sintered at 950 °C for 2 hours in air. It was found that the best Sm doped PMN powders were produced using the solution having 7 mol % rate. All of peaks are identified as the diffraction lines $\text{Pb}(\text{Mg}_{0,333}\text{Nb}_{0,667})\text{O}_3$ phase. This is evidence from Figure 4.28 that the intensity of $\text{Pb}_{1,83}\text{Mg}_{0,29}\text{Nb}_{1,71}\text{O}_{6,39}$ peaks decreased when increasing Sm percentage. Additionally, the XRD patterns clarified that pure perovskite PMN phase can be produced with increasing more percentage of Sm mol rates. In addition to these results, we can see clearly from XRD results, Eu and Er dopants have less effect than Dy and Sm dopants to form pure perovskite structure for PMN.

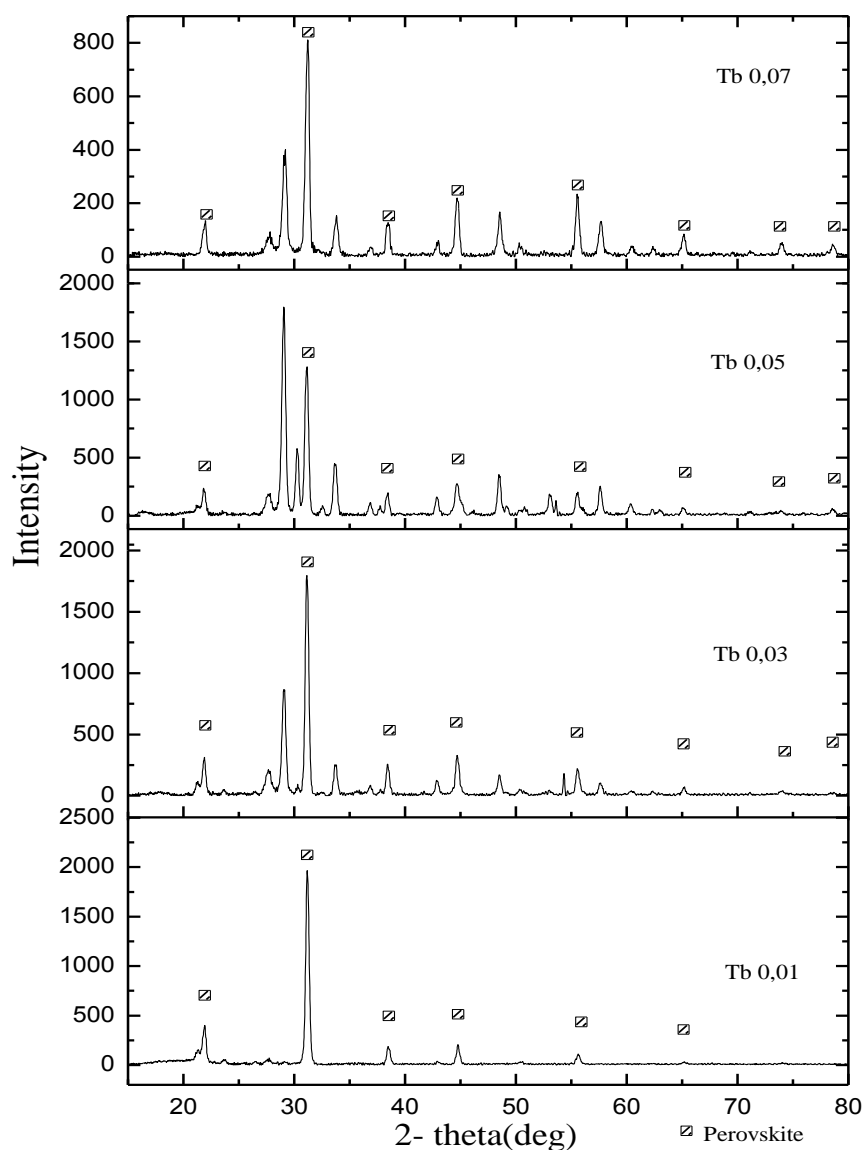


Figure 4.29 XRD results of different amount of Tb doped PMN powders obtained at 950 °C for 2 hours in air.

Attention here is focused on the effect of Tb doping in PMN structure. To illustrate this, XRD patterns of Tb doped PMN powders depending on doping rates of Tb are given in Figure 4.29. With this concept, Tb was added into the solutions from 0.01 to 0.07 mol concentrations. A distinguishable result is that the best Tb doped PMN powders were produced using the solution having 1 mol % rate. It can be noticed that all of peaks are identified as the diffraction lines $\text{Pb}(\text{Mg}_{0,333}\text{Nb}_{0,667})\text{O}_3$ phase. This is clearly evidence from Figure 4.29 that the intensity of $\text{Pb}_{1,83}\text{Mg}_{0,29}\text{Nb}_{1,71}\text{O}_{6,39}$ peaks ideally decreased with increasing Tb percentage. Namely, this is clear from the XRD patterns that pure perovskite PMN phase can be produced with decreasing Tb percent in the powder.

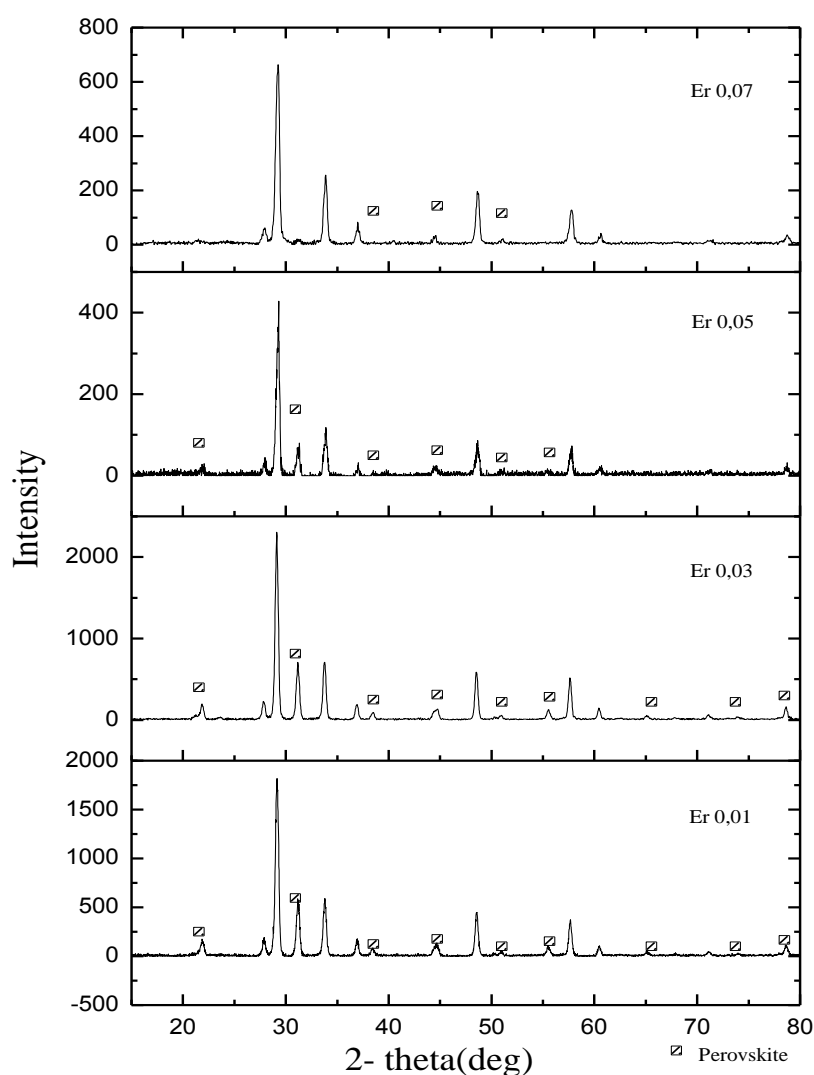


Figure 4.30 XRD patterns of different amount of Er doped PMN thin films produced at 730 °C for 1 hour in air.

It is appropriate to pursue here production procedure of PMN based films fabricated at specific annealing condition depending on dopant content. Figures 4.30 and 4.31 depict XRD patterns of Er doped PMN thin film coatings produced at 730 °C for 1 hour in air depending on different doping rates of Er elements. In this section, Er doped PMN powders were coated onto n-type and p-type Si substrates using dropping technique. The best Er doped PMN thin film with (1 0 0) and (2 0 0) orientations were produced using the powders having 0.01 mol % Er on n-type and Si substrates. All of peaks are identified as the diffraction lines, like Er doped PMN powders patterns, PMN and pyro phase. This is evidence from Figure 4.30 that the intensity of pyro peaks increased when increasing Er percentage.

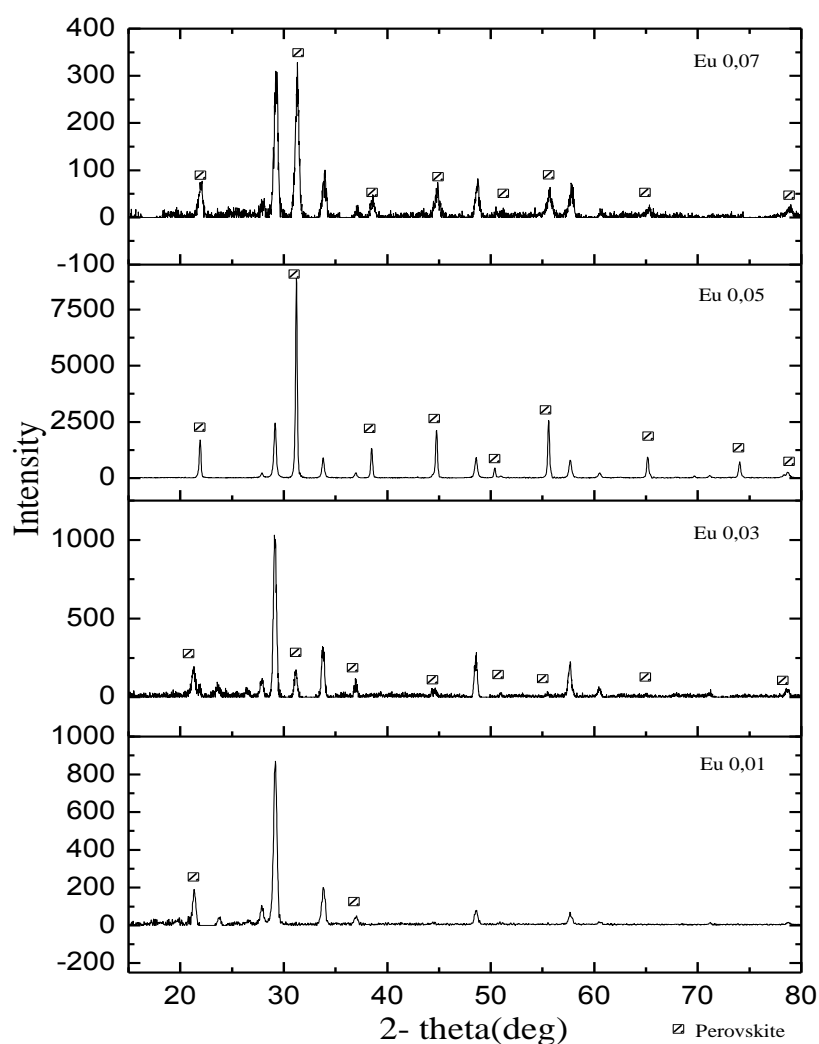


Figure 4.31 XRD results of different amount of Eu doped PMN thin films produced at 730 °C for 1 hour in air.

Figure 4.31 compares XRD patterns of Eu doped PMN coatings depending on doping rates of Eu. In this section, Eu was added into the solutions for different contents such as 0.01 %, 0.03 %, 0.05 % and 0.07 % in mol. It was found that the best Eu doped PMN thin films were produced using the solution having 0.05 mol % Eu. All of peaks are identified as the diffraction lines, for example, $\text{Pb}(\text{Mg}_{0.333}\text{Nb}_{0.667})\text{O}_3$ and $\text{Pb}_{1.83}\text{Mg}_{0.29}\text{Nb}_{1.71}\text{O}_{6.39}$ (pyro) phases. As can be seen from Figure 4.31, the intensity of $\text{Pb}_{1.83}\text{Mg}_{0.29}\text{Nb}_{1.71}\text{O}_{6.39}$ peaks decreased upon increasing Eu percentage in the coatings. The XRD patterns clearly explained that the (1 0 0) and (2 0 0) orientations were obtained after annealing process.

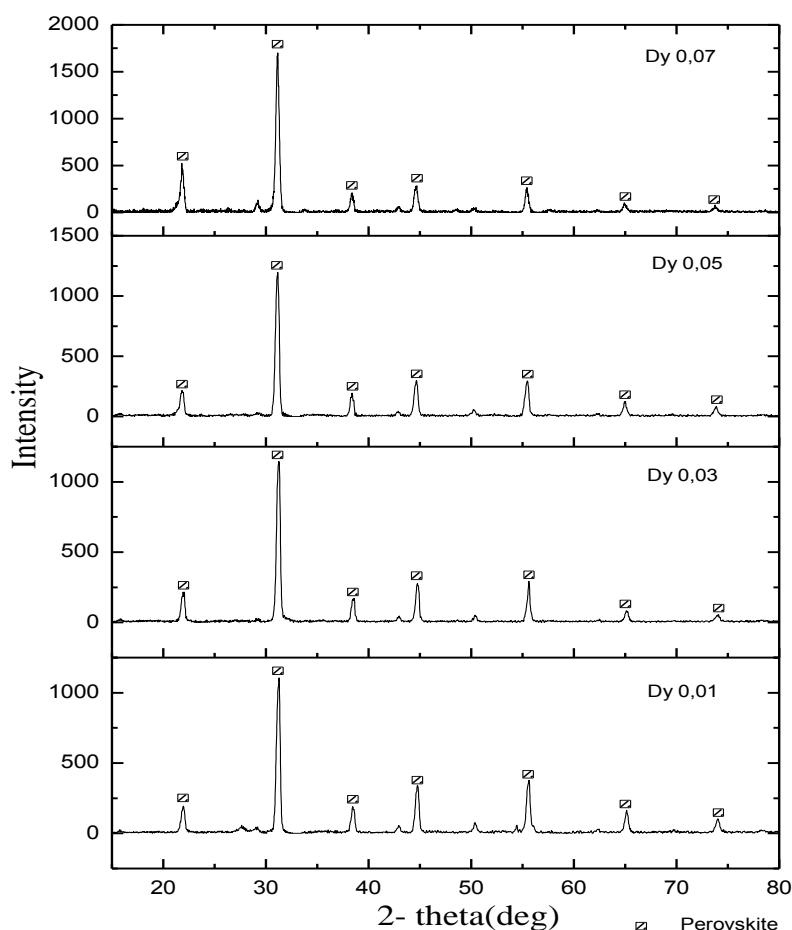


Figure 4.32 XRD patterns of different amount of Dy doped PMN thin films produced at 730 °C for 1 hour in air.

Figure 4.32 indicates XRD patterns of Dy doped PMN coatings depending on doping rates of Dy. Here, Dy dopant was incorporated into the solutions for different

concentrations before coating process. Note that the best Dy doped PMN thin films were produced using the solution including 0.01 % - 0.07 % mol Dy. It was determined that all of peaks are identified as the diffraction lines having $\text{Pb}(\text{Mg}_{0,333}\text{Nb}_{0,667})\text{O}_3$ phase, referred to as perovskite. As is evident from Figure 4.32, the intensity of $\text{Pb}(\text{Mg}_{0,333}\text{Nb}_{0,667})\text{O}_3$ peaks increased with increasing Dy percentage.

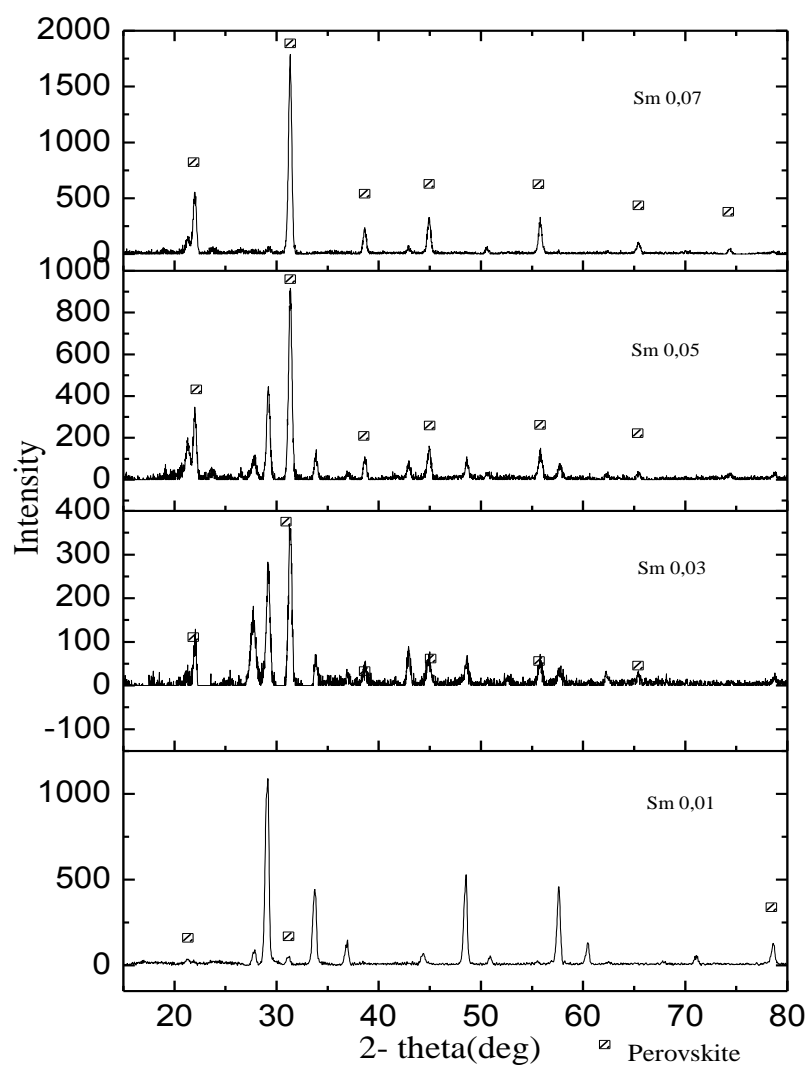


Figure 4.33 XRD results of different amount of Sm doped PMN thin films produced at 730 °C for 1 hour in air.

Figure 4.33 shows XRD patterns of Sm doped PMN coatings depending on doping rates of Sm, which was added into the solutions for 0.01 %, 0.03 %, 0.05 % and 0.07 % concentrations. It was reached that the best Sm doped PMN thin films

were produced through the solution having 0.07 mol % Sm after annealing. Notice also that all of peaks of these coatings are identified as the diffraction lines including $\text{Pb}(\text{Mg}_{0.333}\text{Nb}_{0.667})\text{O}_3$ and $\text{Pb}_{1.83}\text{Mg}_{0.29}\text{Nb}_{1.71}\text{O}_{6.39}$ (pyro) phases. It was found that the intensity of $\text{Pb}_{1.83}\text{Mg}_{0.29}\text{Nb}_{1.71}\text{O}_{6.39}$ peaks decreased when increasing Sm percentage. The XRD pattern obviously showed the (1 0 0) and (2 0 0) orientations were obtained from the coatings.

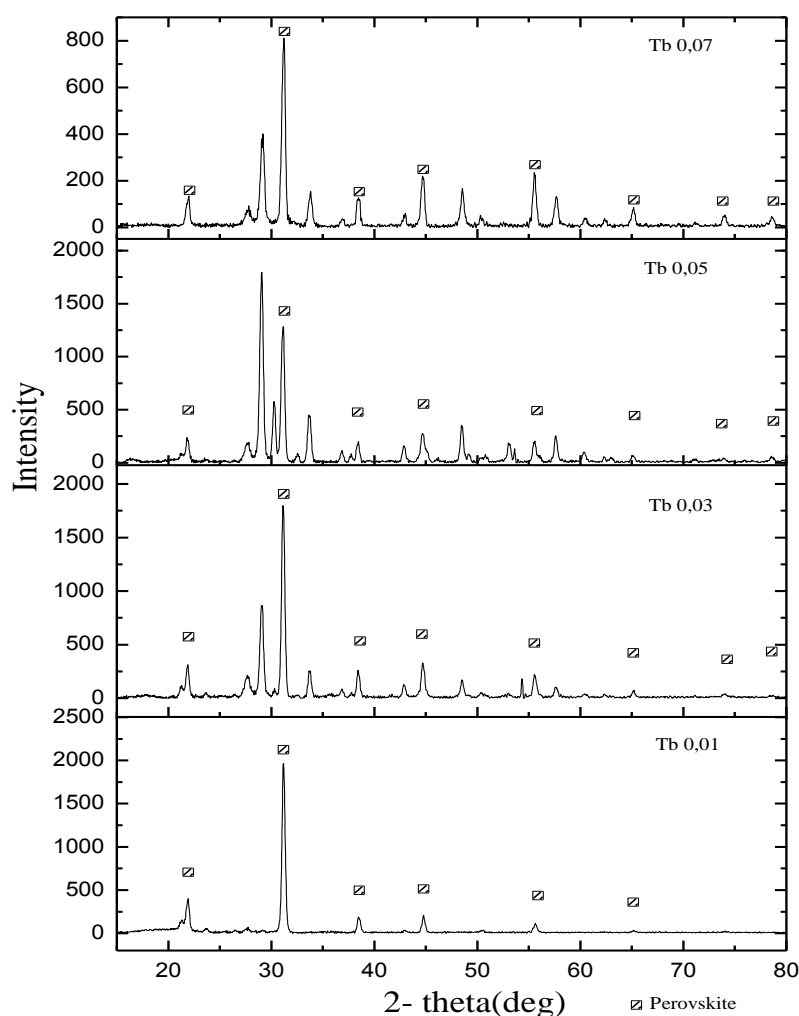


Figure 4.34 XRD patterns of different amount of Tb doped PMN thin films obtained at 730 °C for 1 hour in air.

Figure 4.34 expresses XRD patterns of Tb doped PMN coatings depending on doping rates of Tb. In the last section of XRD analysis, Tb was also added into the solutions for different concentrations. In these type of the coatings, 0.01 %, 0.03 %, 0.05 % and 0.07 % Tb contents were used in the PMN coatings in mol

concentrations. It was accomplished that the best Tb doped PMN thin films were produced using the solution having 0.01 mol % Tb. As mentioned before just like other coatings, all of peaks are identified as the diffraction lines having $\text{Pb}(\text{Mg}_{0.333}\text{Nb}_{0.667})\text{O}_3$ and $\text{Pb}_{1.83}\text{Mg}_{0.29}\text{Nb}_{1.71}\text{O}_{6.39}$ (pyro) phases. This is clearly understood from Figure 4.34 that the intensity of $\text{Pb}_{1.83}\text{Mg}_{0.29}\text{Nb}_{1.71}\text{O}_{6.39}$ peaks increased when increasing Tb percentage. The XRD pattern clearly showed the (1 0 0) and (2 0 0) orientations which we strongly want were obtained in the PMN based coatings. From these results, an important implication was the orientations with (1 0 0) and (2 0 0) in all of coatings. Due to the fact this orientation is not random in the coatings, there have been potential applications in the fabrication of electronic devices. The successful exploitation of the electrical behaviour has been achieved largely through development of the texture in all coatings before the fabrication of the electronic devices. The texture development predominantly relies on heat treatment process of the coatings. On the other hand, this procedure, which account for approximately 100 % of the texture development in the coating production, points out the straightforward annealing conditions. In this annealing technique, an optimum profile of temperature and time not is enough but also environment atmosphere should be control in the furnace during the heat treatment.

Relative amounts of perovskite and pyrochlore phases were determined using the following approximation Equation 4.4 (Deliormanli 2008), and the results shown in Table 4.4:

$$\%pyrochlore = \frac{I_{pyro}}{I_{pyro} + I_{perovskite}} \times 100 \quad (4.4)$$

in which I_{pyro} and $I_{perovskite}$ are the intensity of the major peaks of the pyrochlore (222) and perovskite (100) phases respectively.

A more specialized name for sintering is firing or densification. Another obsolete name is “mature”. The porous green body undergoes a high temperature heat treatment, where significant atomic diffusion happens to eliminate pores and vacancies. In the case of a green tape by doctor blading, the binder was burnt out

completely at 400°C, leaving a porous body for final sintering. The pores of a ceramic are usually closed at 95 % of theoretical density. For piezoelectric ceramics, densities below 95 % usually do not measure up to good properties because the presence of open pores would allow water or other liquid filling, causing increased dielectric loss and reduced volume resistivity. Dielectric strength could also be inferior, making it hard to pole the ceramic (Deliormanli 2007).

Table 4.4 Relative amounts of perovskite and pyrochlore phase of PMN thin films depending on additives rates.

Doping	Doping Ratio (%)	Perovskite Phase (I)	Pyrochlore Phase (I)	Pyrochlore (%)	Perovskite (%)
Pure	0	2586	0	0	100
Er ⁺³	1	587	1817	75.58	24.42
	3	706	2306	76.56	23.44
	5	80	428	84.25	15.75
	7	20	663	97.07	2.93
Eu ⁺³	1	190	870	82.07	17.93
	3	175	1031	85.48	14.52
	5	8894	2455	21.63	78.37
	7	298	310	50.16	49.84
Dy ⁺³	1	2467	297	10.77	89.23
	3	2228	132	5.62	94.38
	5	2358	186	7.34	92.66
	7	3143	355	10.17	89.83
Sm ⁺³	1	230	3059	92.99	7.01
	3	722	1540	68.07	31.93
	5	1719	1180	40.71	59.29
	7	3392	489	12.61	87.39
Tb ⁺³	1	2905	290	9.10	90.90
	3	3013	2069	40.72	59.28
	5	2349	4156	63.72	36.11
	7	1694	1159	40.64	59.36

The sintering temperatures for piezoelectric ceramics are usually well above 1000°C. Barium titanate, for example, densifies in the 1350~1450°C range. PZT typically sinters in the 1200~1300°C range. Under this temperature, the ceramic is subject to PbO evaporation, which can be prevented by maintaining a PbO rich atmosphere around the samples. Often times, PbZrO₃ powder is used to bury the ceramic body together with trace amount of PbO powder. The whole setting is then put in a refractory Al₂O₃ crucible enclosure for sintering. Sometimes a double enclosure is used (Gu 2004).

A typical sintering temperature for PMN-PT is 1250 °C (Kelly 1997) by the columbite method. There have recently been quite a few efforts to sinter PMN-PT at lower temperatures to about 900~1000 °C. A notable example is by a coating method in Dr Huiming Gu's PhD thesis (Gu 2004). Another method is by oxidizing atmosphere coupled with isostatic pressing (Kwon S 2001).

Not only does oxidizing atmosphere helps PMN-PT sintering, but it also reportedly improved properties of the body. Therefore sometimes Pb_3O_4 is intentionally used to create oxygen atmosphere (Chung-Hsin 2000). However, it would be difficult to control the stoichiometry by virtue of the chemical valence in PMN. As a rule of thumb, reducing atmosphere should be avoided because oxygen vacancy binders sintering and reduces the resistivity of the ceramic. In practice, hydrocarbon should be burnt out completely to eliminate carbon residue, which is a major source of reducing atmosphere.

Grain growth is another interesting topic for PMN-PT sintering. Pre-sintered by spark plasma under 30 MPa at 900 °C, abnormal grain growth of 65PMN-35PT to about 0.5 mm in size can be induced by prolonged heating at 1150 °C for 20 hours (Ui jin 2002). PMN-PT grain growth can also be increased by $BaTiO_3$ (Edward 2001), $SrTiO_3$ (Tao Li 1999) and PMN-PT (Tao Li 1998) template grains. Nonetheless, under normal conditions, polycrystalline PMN ceramics usually have a grain size range from 1 to 20 microns.

In our case, two type heat treatment regimes were applied to produce very pure perovskite and textured PMN based materials such as powders and films as a combination of DTA-TG, FTIR and XRD results. For the process optimization, the sintering condition of PMN based powders was chosen as follows: a temperature of 950 °C, a time period of 2 hours, and a furnace environment from air. As far as heat treatment of PMN based thin films is concerned, the annealing condition was chosen like the following procedure: a temperature of 730 °C, a time period of 1 hour, and a furnace environment from air.

4.4 Powder analysis

Particle size analysis was carried out by Mastersizer particle size machine. We have two analysis results about 12 hours prior to grinding mills for the purpose of PMN powder grain size. The powder has micrometer ($d(0.5):67,944 \mu\text{m}$) sizes as shown in Figure 4.35 after ball milling, PMN powder possesses nano scale size distribution ($d(0.5): 414 \text{ nm}$) as seen in Figure 4.36. In order to produce nano-scale powders, the same milling method was applied to doped PMN powders. As nanoparticles get smaller and smaller from micron-size particles, the percentage of atoms on the surface becomes an appreciable fraction of the total number of atoms.

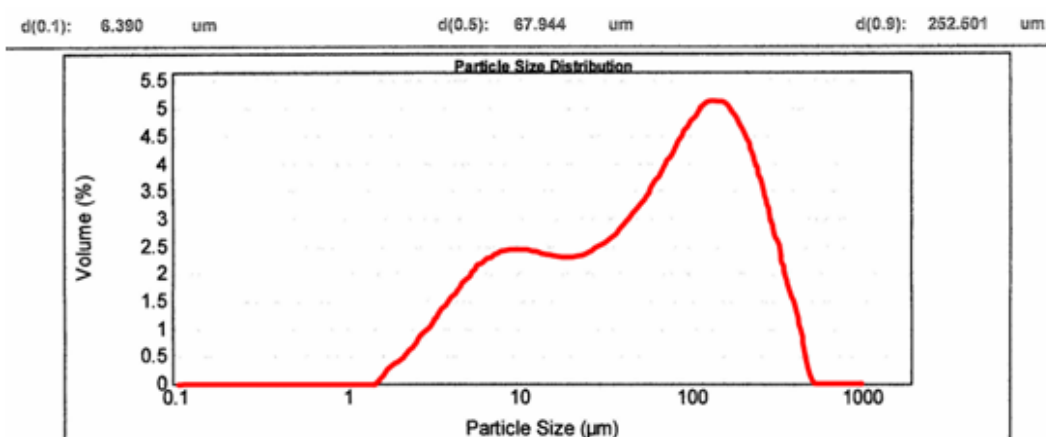


Figure 4.35 Grain size of undoped PMN powders before grinding process.

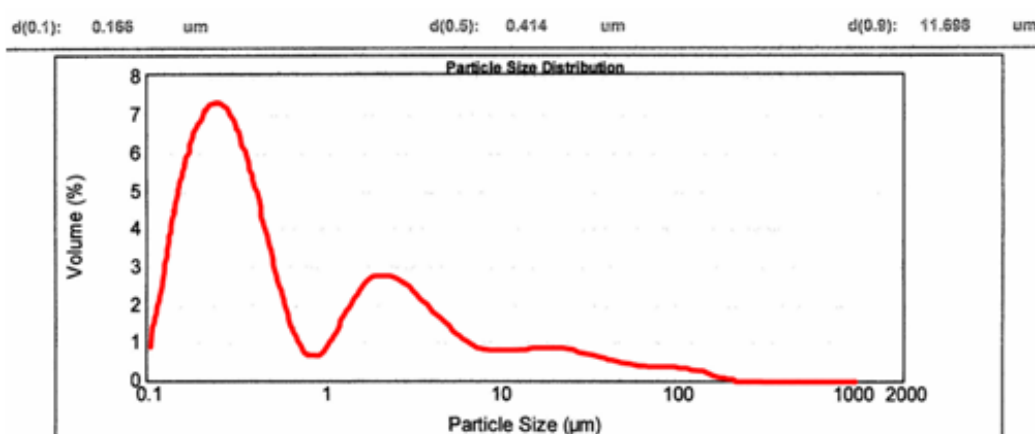


Figure 4.36 Grain size of undoped PMN powders after grinding process for 12 hours in air.

Nano scale PMN based powders stimulated the intensive research, improvement and development in order to realize very good surface qualities of the thin films and

very good electrical properties which will be presented later on. No need to say here, the nanoparticle and nanotechnology dramatically influence the thin film structures, mechanical, electrical properties and consequently improve any electronic device.

4.5 Microstructure Analysis

The surface topographies and characteristics of PMN films on Si substrates were examined by using SEM and AFM. Vacancies, micro cracks and porosities were examined by SEM for determining the effect of ball milling and grain size on the morphology of the thin films. Surface roughness and depths, coating thickness of PMN based materials were observed with the help of AFM. Additionally, elemental analysis of PMN based coatings on Si substrates was investigated through EDS.

4.5.1 SEM-EDS Analysis

Microstructures of the pure and RE⁺³ doped PMN films are given in figures between Figure 4.37 and Figure 4.59 in detail. PMN based films annealed at 730 °C have different surface structures. The Figures show that it is possible to obtain PMN films having continuous and homogeneous microstructure at 730 °C for 1 hour in air. At higher annealing temperatures, abnormal grain growth and the formation of a second phase (pyro) initiate in the PMN based coatings.

One of the most valuable features of dielectric behaviour is how the microstructure of PMN coatings exhibits. Concerning the microstructure of PMN coatings, SEM observation was performed to obtain an optimum sample. Figure 4.37 depicts SEM micrographs of PMN on n-type Si substrate. Crack-free but porous and continuous PMN thin film was produced from alkoxide precursors. All thin films were coated from powder based solutions after producing PMN powders with different size using sol-gel technique. Figure 4.37 denotes SEM micrographs of deposited PMN films using powders prepared before ball milling. SEM examination of PMN shows a porous and having larger particles microstructure on the surface of

the substrate. Figure 4.37 show SEM micrographs of PMN thin films produced from the powder before grinding process.

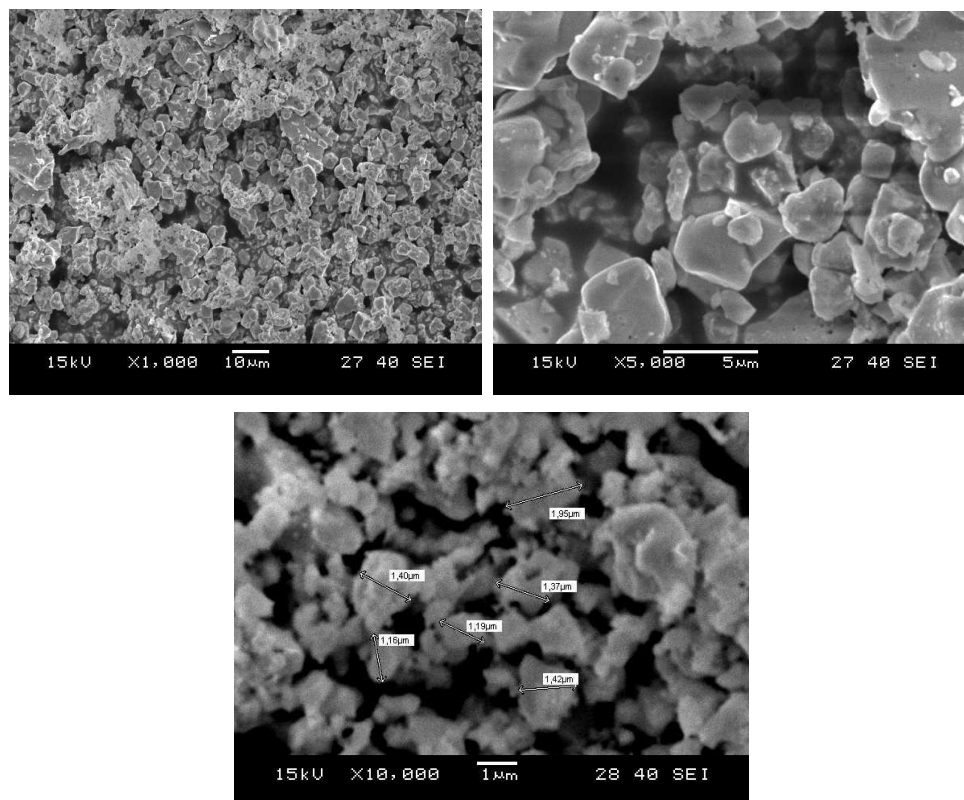


Figure 4.37 SEM images of pure PMN thin films obtained before grinding process at 730 °C for 1 hour in air.

As shown by XRD in Figure 4.23, PMN thick films deposited on Si substrate preserved pure perovskite phase. SEM micrographs in Figure 4.37 showed that the thick films were crack-free structure on Si substrates. The samples heat-treatment at 700°C yielded a homogeneous grain growth to about sub-micron grain size, whilst 800°C heat-treatment resulted in non-uniformity and the appearance of a liquid phase and the thick film appeared to be better sintered.

As stated above, the particle size of PMN has an effect on the PMN coating stability, i.e., larger, micro-PMN were worst coated than the smaller nano-PMN particles. This is confirmed by the EDS analysis (see in Figure 4.39) of the PMN particles from the coating. As illustrated in Figure 4.37 and Table 4.5, the Mg/Nb ratios for micro-PMN particles are much higher than those of submicron-sized

aggregated nano-PMN particles, indicating that the coating of nongrinded particles layer is better for large PMN particles than fine particles. The fine PMN particles were as well coated by grinded particles as shown in Figure 4.38. Although fine PMN particle size may be advantageous for interface adhesion reaction during subsequent heat treatment, the crucial part is preventing the segregation during the colloidal processing of submicron or nanometer-sized PMN powder.

The low-temperature sinterability can also be verified from SEM micrographs, as shown in Figures 4.37 and 4.38. After prolonged heat treatment at 850 °C, an Oswald ripening process happened with grain growth and reduction in grain boundary area. Under higher temperature (1000 °C), grains continued to grow to 10~15 μm .

The micron-sized PMN are pure-perovskite crystalline particles, while the nano-scale sized PMN is amorphous above the 730 °C temperature with no features in its XRD in the 20~40° range of 2θ ($\text{CuK}\alpha$). These two species are well mixed, with fine PMN powder filling the gap between microns sized PMN particles. Moreover, the high surface energy and reactivity of the nano scaled PMN powder are beneficial to the atomic surface diffusion. It is this unique microstructure that makes the PMN precursor powder low-temperature sinterable.

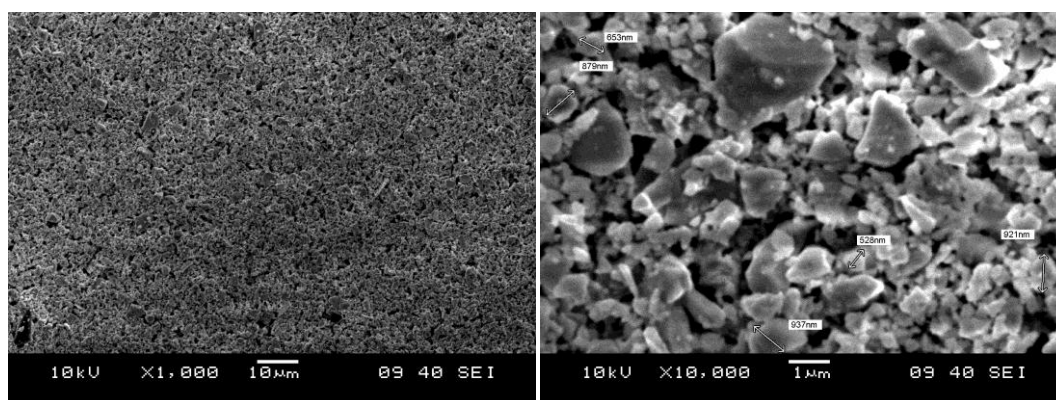


Figure 4.38 SEM images of pure PMN thin films obtained after grinding process at 730°C for 1 hour in air.

In so far as the sintering temperature of 950 °C is higher than the melting temperature of PbO (880 °C), the lead loss will occur from the specimens. The ceramic

piece can be sintered in air without cover or packing powder. The PMN processed by this suspension method has a great potential to be low-temperature co-fired with metallic electrodes or other ceramics.

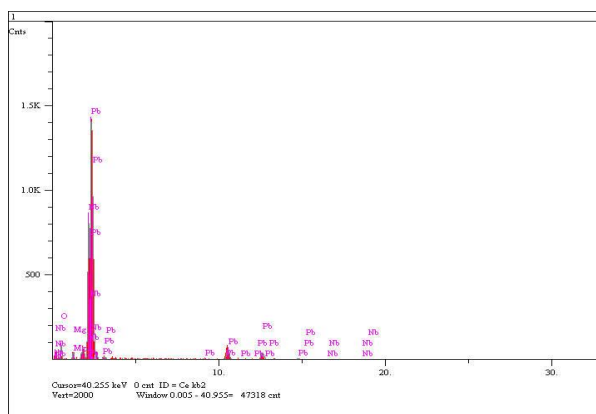


Figure 4.39 EDS analysis result of undoped PMN thin films.

Figure 4.38 has also porous morphology but has smaller nano sized particles compared with the coatings in Figure 4.37. Upon comparing with the SEM images of PMN in Figures 4.37 and 4.38, it can be pointed out that there is remarkable difference in their surface morphologies thanks to fabrication method. In this observation, the effect on film morphology of grinding procedure can be easily seen after 12 hours grinding. Figure 4.37 reveals the vacancies in coating like coating island on substrate. The vacancies are firstly formed in the coating layers and subsequently independent grain growth corresponding to long uncoated regions between two coating vacancies depending on coating thickness and heating process. The morphologies observed in the different regions of the films can be explained by different particle deposition mechanisms acting during the formation and crystallization of PMN powder as seen in Figure 4.37. As demonstrated in Figure 4.37, at bottom part of the film, only powder diffusion into the growing film is active. The atom diffusion is limited at the interface with the Si substrate layer and homogeneous growth of PMN crystalline nuclei takes place. At the top of the film, surface diffusion works very fast and only some PMN nuclei are selected for growth, resulting in larger crystallites, which develop in the directions parallel to the film surface. As seen in Figures 4.38, the same magnification with Figure 4.37, because

of grinding with ball milling for 12 hours, coating thickness was decreased and microstructures were changed. As shown from microstructural observations, a regular surface morphology forms as grain size decrease until 200 nm. These thin films are obtained for the coatings, which applied six cycles on Si substrates.

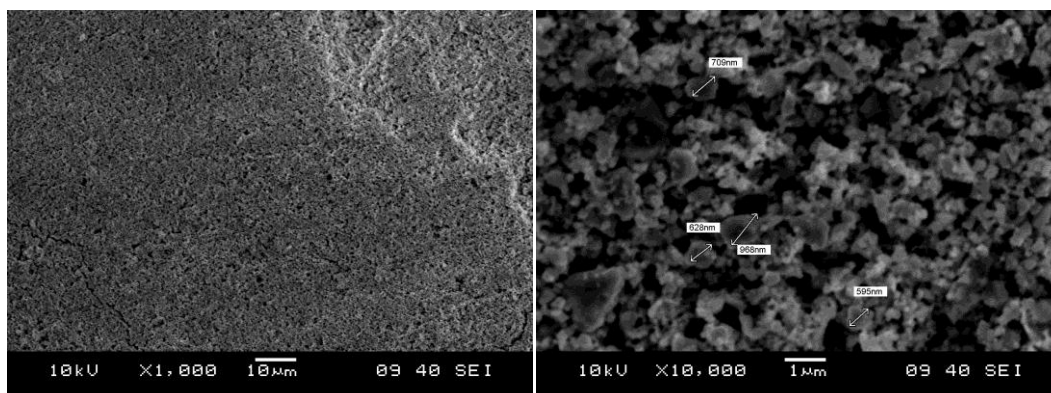


Figure 4.40 SEM images of 1 % Er doped PMN thin films.

Er doped PMN films are given in Figure 4.40 and 4.43. Er doped PMN films sintered at 730 °C for 1 hour in air have porous structures. At the same time, Figures show that it is possible to obtain PMN based films having continuous and homogeneous microstructure at 730 °C.

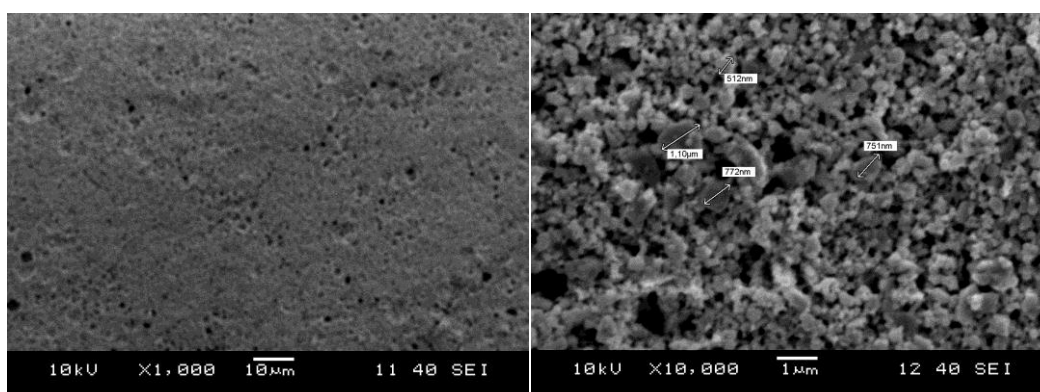
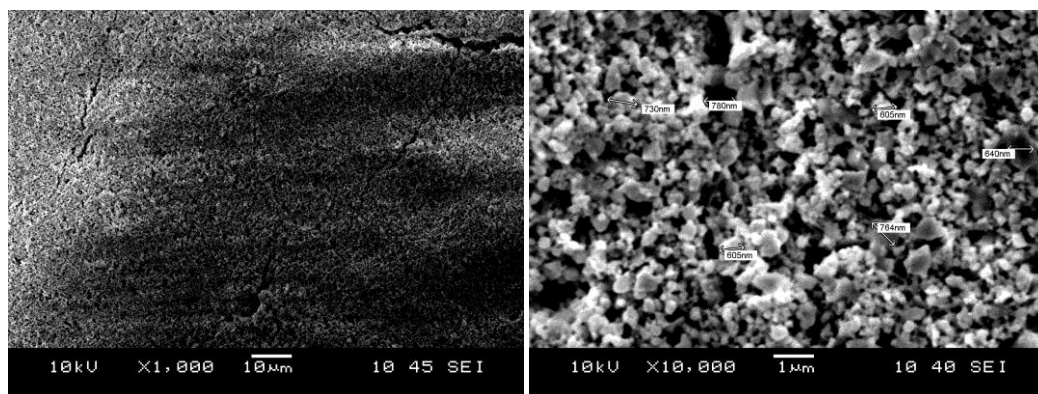
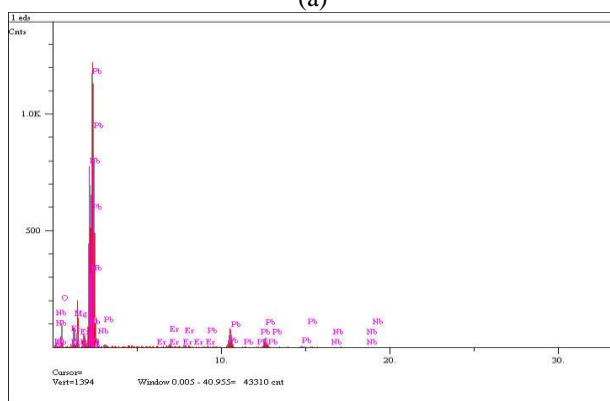


Figure 4.41 SEM images of 3 % Er doped PMN thin films.



(a)



(b)

Figure 4.42 (a) SEM images and (b) EDS analysis of 5 % Er doped PMN thin films.

At higher sintering temperatures abnormal grain growth and the formation of a second phase initiate in the films. Accordingly, PMN films have some micro cracks and porosity except having 0.07 mol % Er. These samples have final thickness of $\sim 0.9 \mu\text{m}$ (see in Table 4.9) after sintering at 730 °C for 1 hour in air.

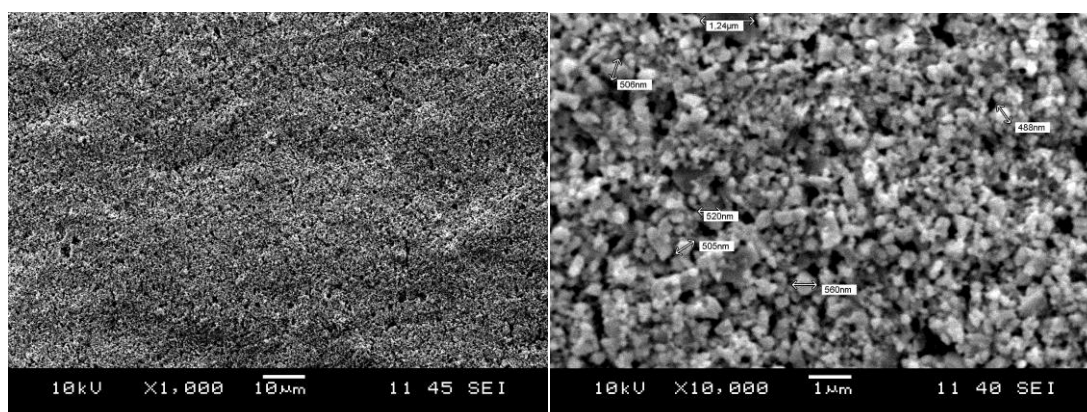


Figure 4.43 SEM images of 7 % Er doped PMN thin films.

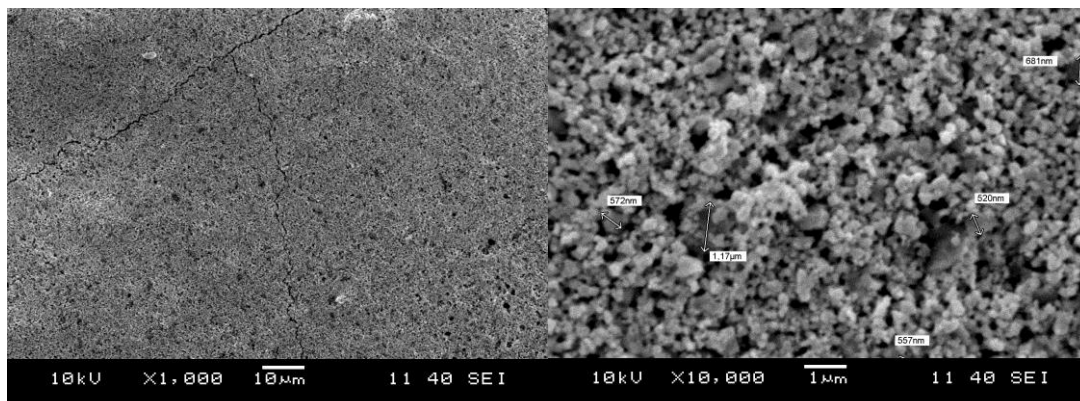


Figure 4.44 SEM images of 1 % Eu doped PMN thin films.

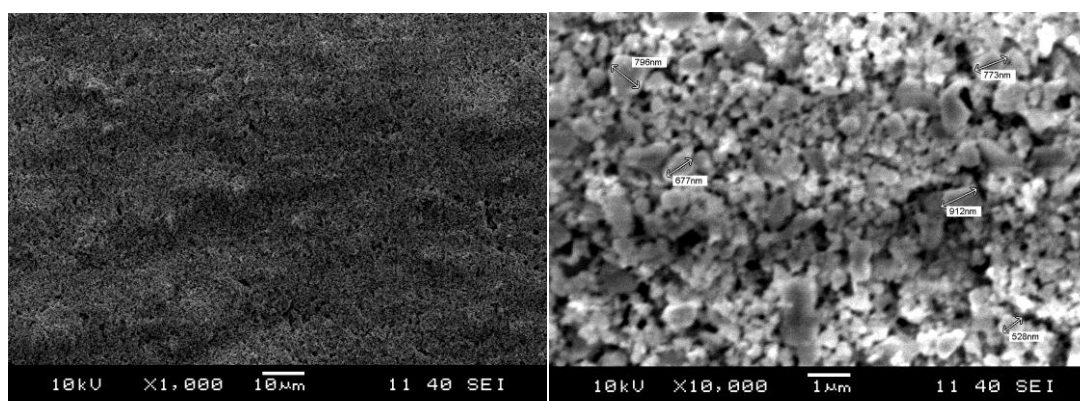
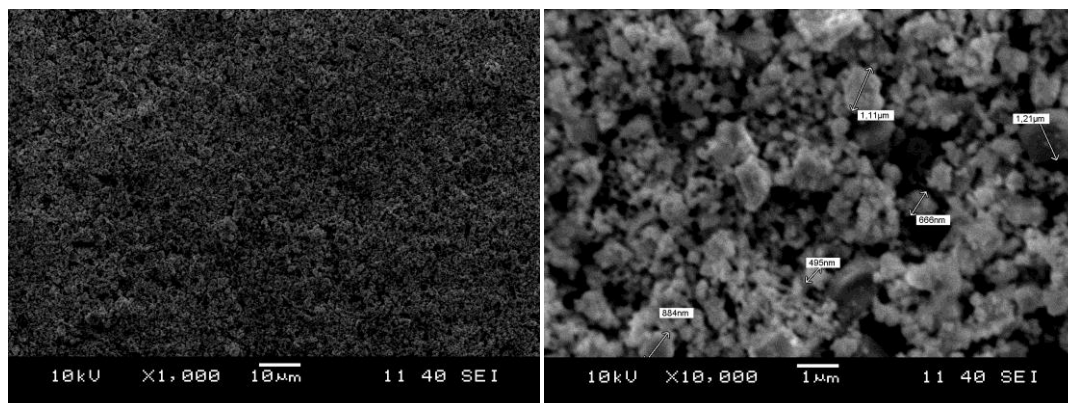
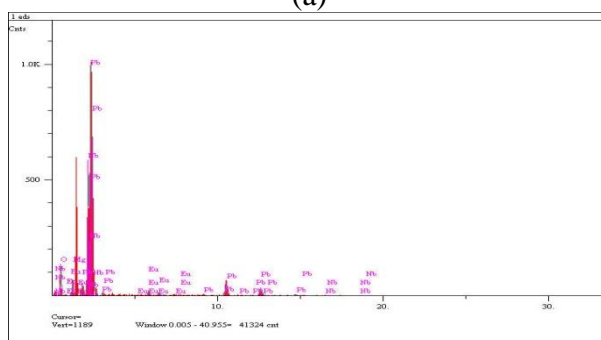


Figure 4.45 SEM images of 3 % Eu doped PMN thin films.

Microstructures of the Eu doped PMN films are given in Figures 4.44, 4.45, 4.46 and 4.47. According to Figure 4.44, PMN films sintered at 730 °C have porous structures. On the other hand, Figure 4.45 shows that it is possible to obtain PMN films having continuous and homogeneous microstructure at 730 °C. At higher sintering temperatures abnormal grain growth and the formation of a second phase initiate. Accordingly, PMN films have some micro cracks and porosity except having 0.03 and 0.05 mol % Eu. These samples have final thickness of $\sim 1 \mu\text{m}$ (see in Table 4.9) after sintering at 730 °C for 1 hour in air.



(a)



(b)

Figure 4.46 (a) SEM images and (b) EDS analysis of 5 % Eu doped PMN thin films.

As shown from microstructural observations, a regular surface morphology forms as optimum doping ratios of Er and Eu. It was observed that particle size of the top layer is larger than that of fewer percentages of doping materials. Thin films are obtained for the coatings which contain few layers. The thickness of film and surface defects increases in accordance with number of dropping. However, more pores and homogeneous structure could be obtained by changing viscosity of the suspensions. Cracking was less extensive in thinner films and very thick films, which were produced using viscous solutions, tended to peel off the substrate completely. In contrast, the films, fabricated using diluted solutions with solvent, are extremely uniform, dense, crack-free and pinhole-free.

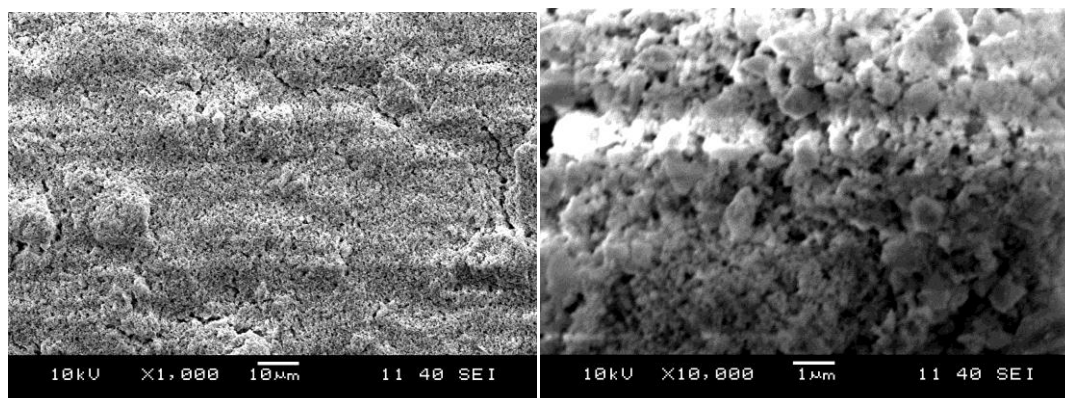


Figure 4.47 SEM images of 7 % Eu doped PMN thin films.

Microstructures of the Dy doped PMN films are presented in Figure 4.48, 4.49, 4.50 and 4.51. Based on Figure 4.48, PMN films annealed at 730°C for 1 hour in air possess micro porous structures. In other words, Figures 4.49, 4.50 and 4.51 demonstrate that it is possible to produce Dy doped PMN films with continuous and homogeneous microstructure increasing doping ratio of Dy at 730 °C since dopant content strongly affects their microstructures. Above this temperature, the variability can, practically speaking, arise during the heat treatment. For example, at higher sintering/annealing temperatures, melting structures and the formation of a second phase from perovskite to pyrochlore initiate in the coatings.

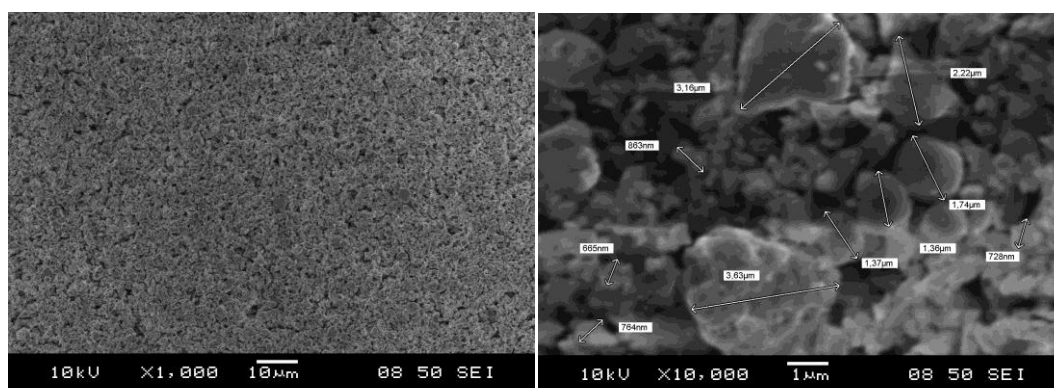


Figure 4.48 SEM images of 1 % Dy doped PMN thin films.

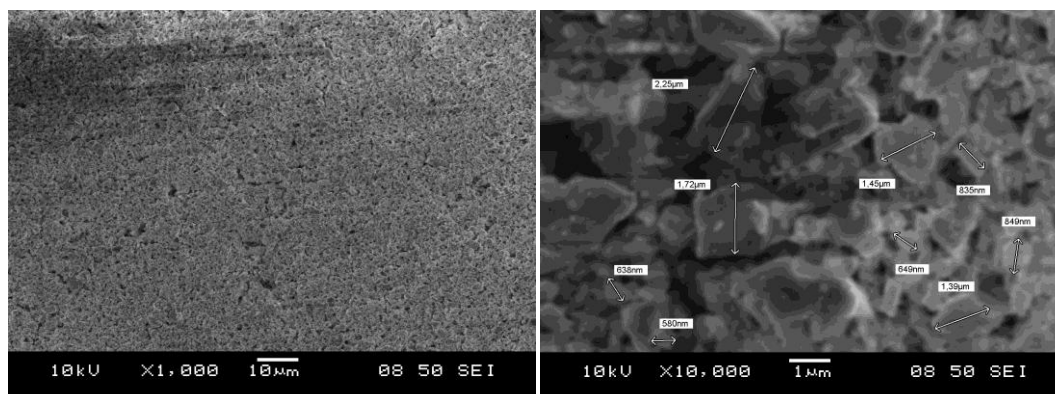
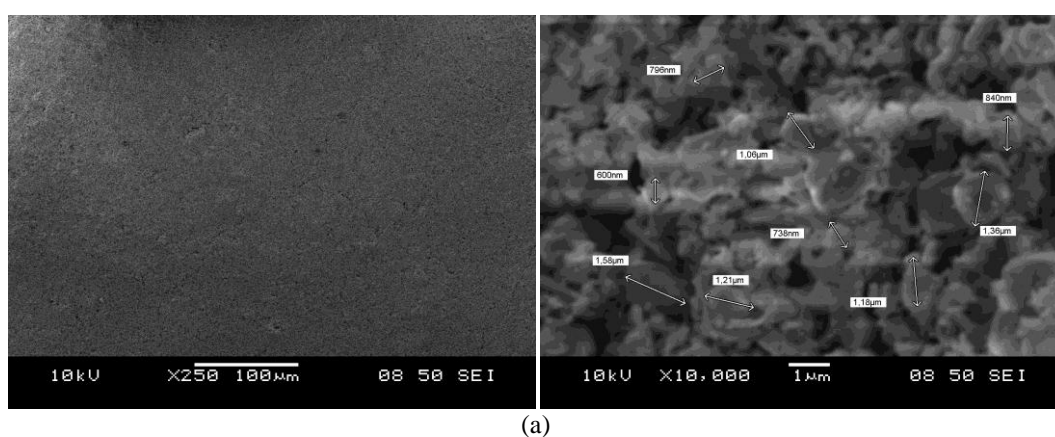
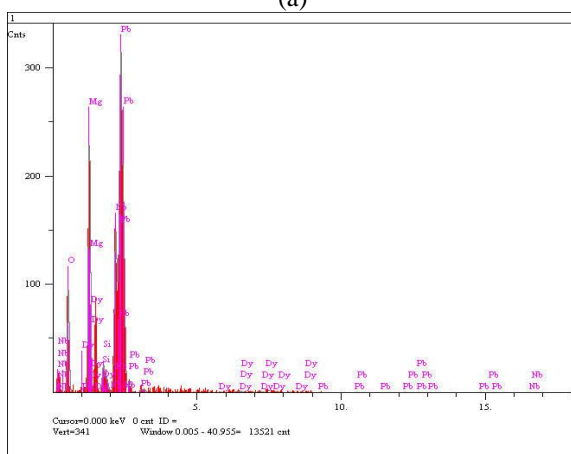


Figure 4.49 SEM images of 3 % Dy doped PMN thin films.



(a)



(b)

Figure 4.50 (a) SEM images and (b) EDS analysis of 0.05 % Dy doped PMN thin films.

In addition to these, PMN films have some micro pores except having 0.03, 0.05 and 0.07 mol % Dy. The final thickness of these coatings are found to be $\sim 1 \mu\text{m}$, as given in Table 4.9, after sintering at $730 \text{ }^\circ\text{C}$ for 1 hour.

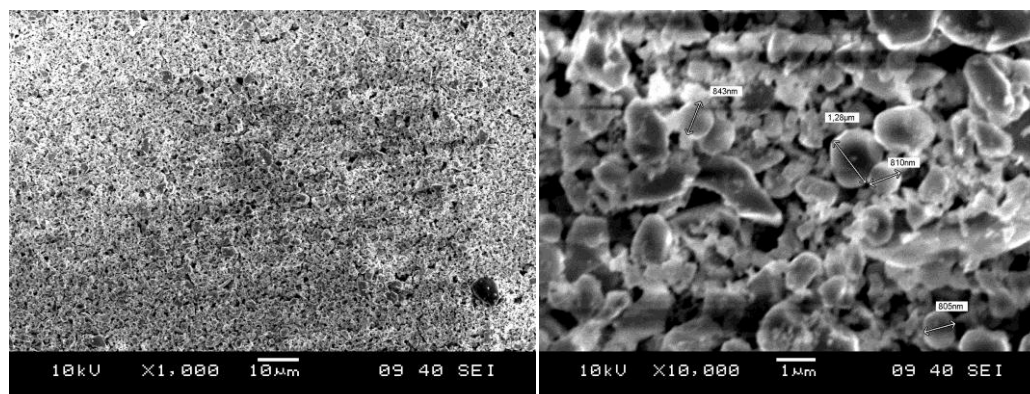


Figure 4.51 SEM images of 0.07 % Dy doped PMN thin films.

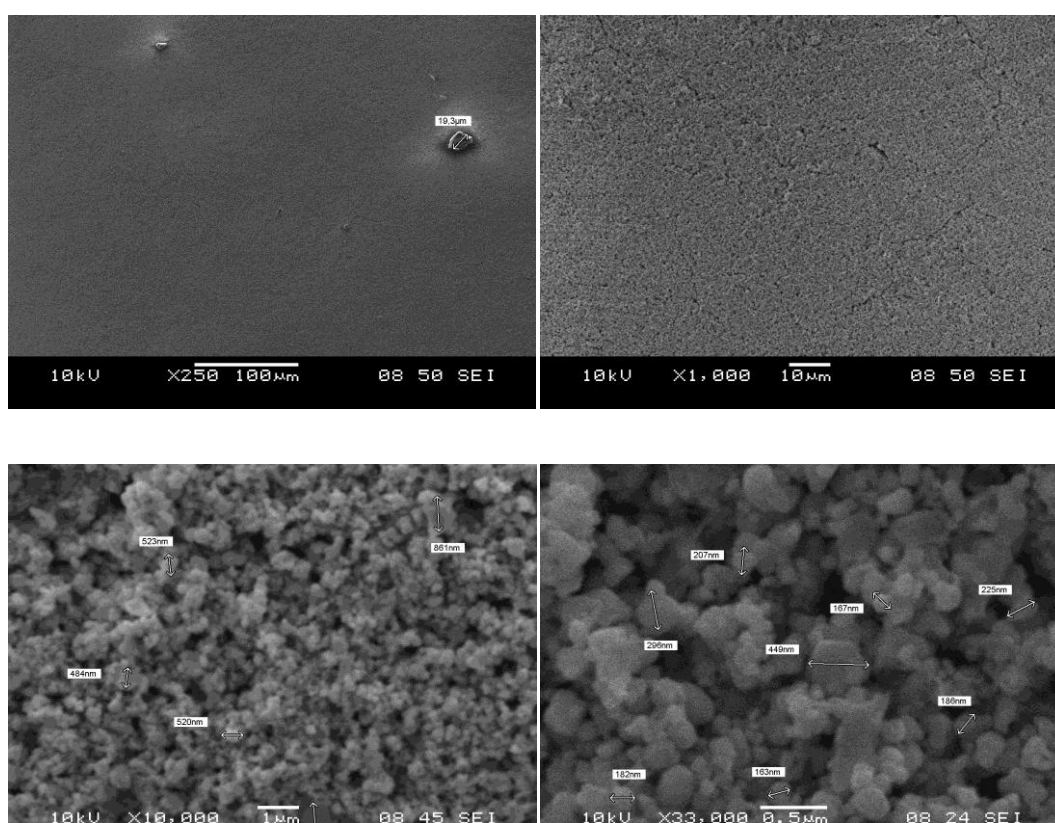


Figure 4.52 SEM images of 0.01 % Sm doped PMN thin films.

Microstructures of the Sm doped PMN films are shown in Figures 4.52, 4.53, 4.54 and 4.55. Depending on the images, Sm doped PMN films annealed at 730 °C for 1 hour in air possesses not porous structures in Figure 4.52. These features open up a good possible applications by improving mechanical and dielectric properties in PMN based coatings. The mechanical and dielectric properties are described in terms of the microstructure of PMN based films. As a parallel to this result, Figure 4.52

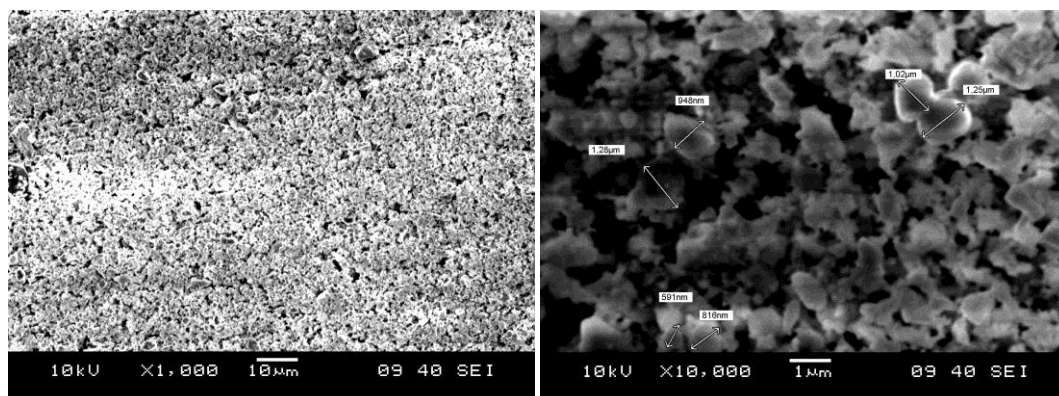
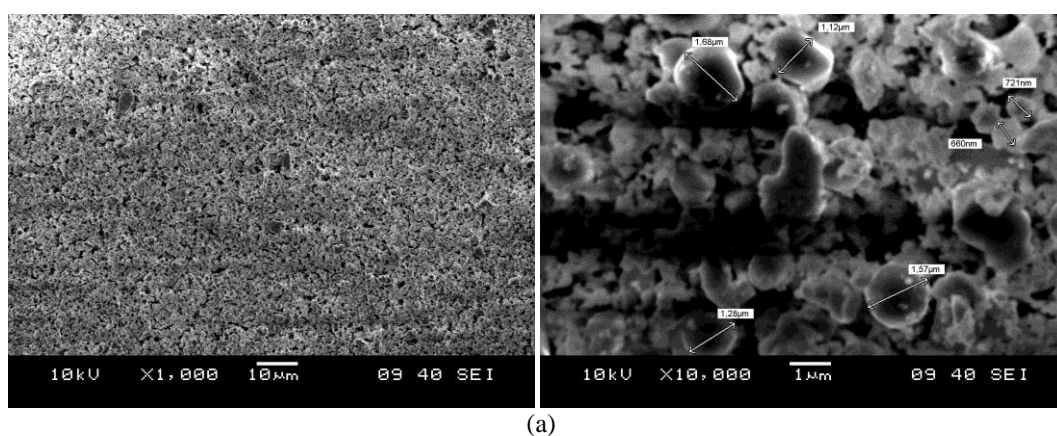
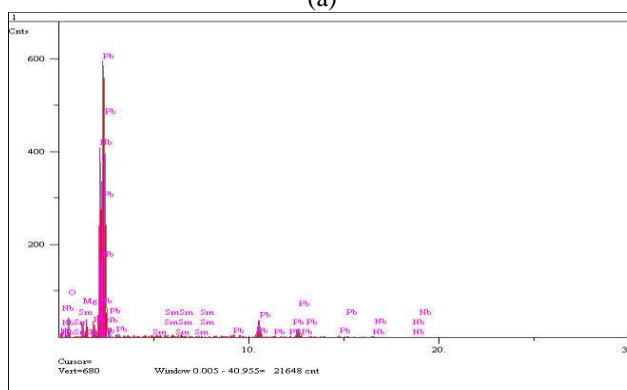


Figure 4.53 SEM images of 0.03 % Sm doped PMN thin films.



(a)



(b)

Figure 4.54 (a) SEM images and (b) EDS analysis of 0.05 % Sm doped PMN thin films.

manifests that it is possible to produce PMN films including continuous and homogeneous microstructure for doping ratio of 0.01 mol % Sm at 730 C. Accordingly, it was found that Sm doped PMN films have some micro pores having 0.03, 0.05 and 0.07 mol % Sm. It can also stated that these samples in coating form have final thickness of $<1 \mu\text{m}$, as referred to as sub-micron, as given in Table 4.9 after sintering at 730 °C for 1 hour in air. After the sintering process, PMN based

coatings densify in terms of temperature and time. Generally speaking, these microstructures regarding as thinner coatings provide less stress concentration which leads to an elimination of microcracking and failure in accordance with annealing conditions and dopant type and content. An estimated coating thickness should be thin as much as possible in the practical applications.

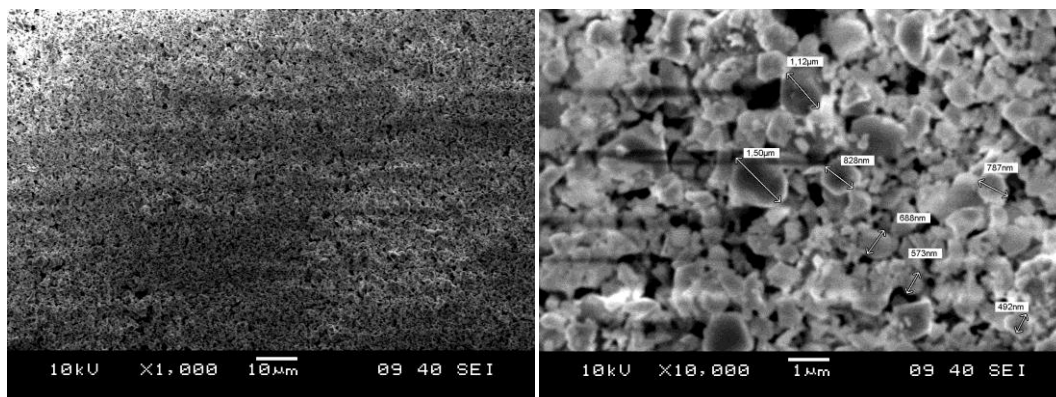


Figure 4.55 SEM images of 7 % Sm doped PMN thin films.

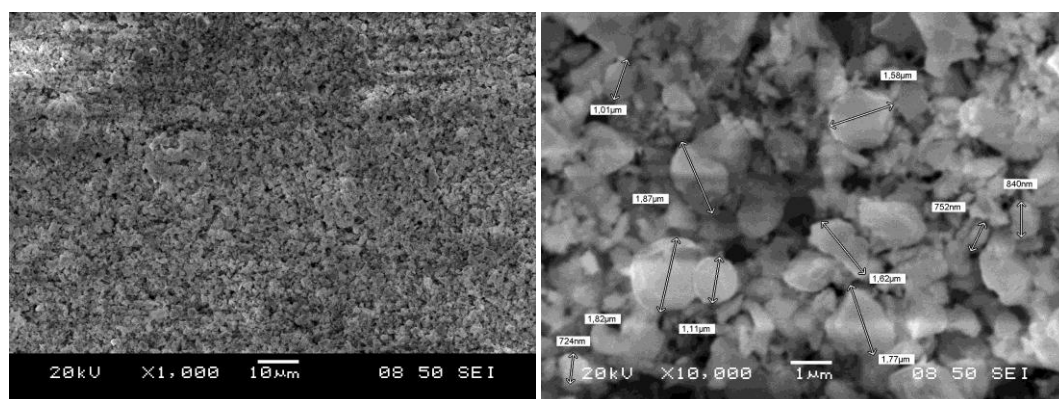


Figure 4.56 SEM images of 1% Tb doped PMN thin films.

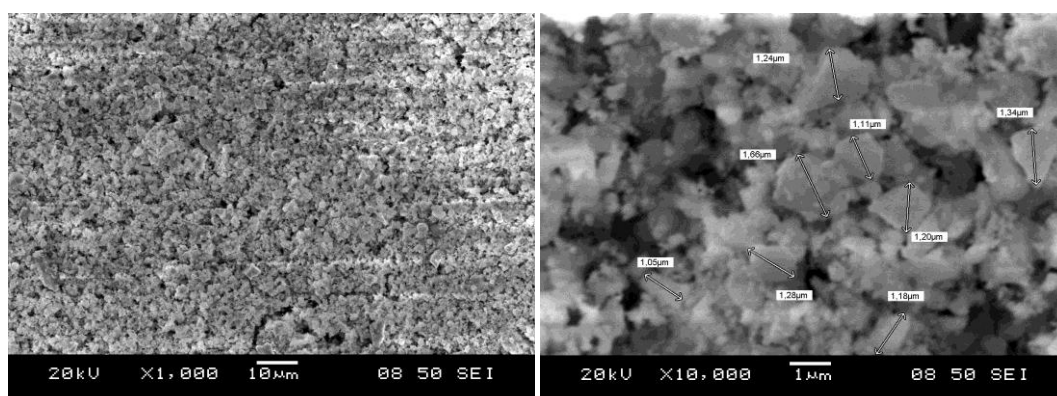


Figure 4.57 SEM images of 3% Tb doped PMN thin films.

To elucidate microstructures of the Tb doped PMN films, Figures 4.56, 4.57, 4.58 and 4.59 were presented depending on Tb content. It is clear from Figure 4.56 that Tb doped PMN films annealed at 730 °C for 1 hour in air possess micro porous structures. At the same time, as stated in Er, Eu, Dy and Sm doped PMN films, Figure. 4.56 clarifies that it is possible to obtain PMN films having well-oriented, continuous and homogeneous microstructure for doping ratio of 0.01 mol % Tb at 730 °C. It was observed from the microstructure that PMN films have some micro pores with 0.03, 0.05 and 0.07 mol % Tb. As can be shown in Table 4.9, final thickness was measured to be <math><1 \mu\text{m}</math> in these samples after sintering at 730 °C for 1 hour.

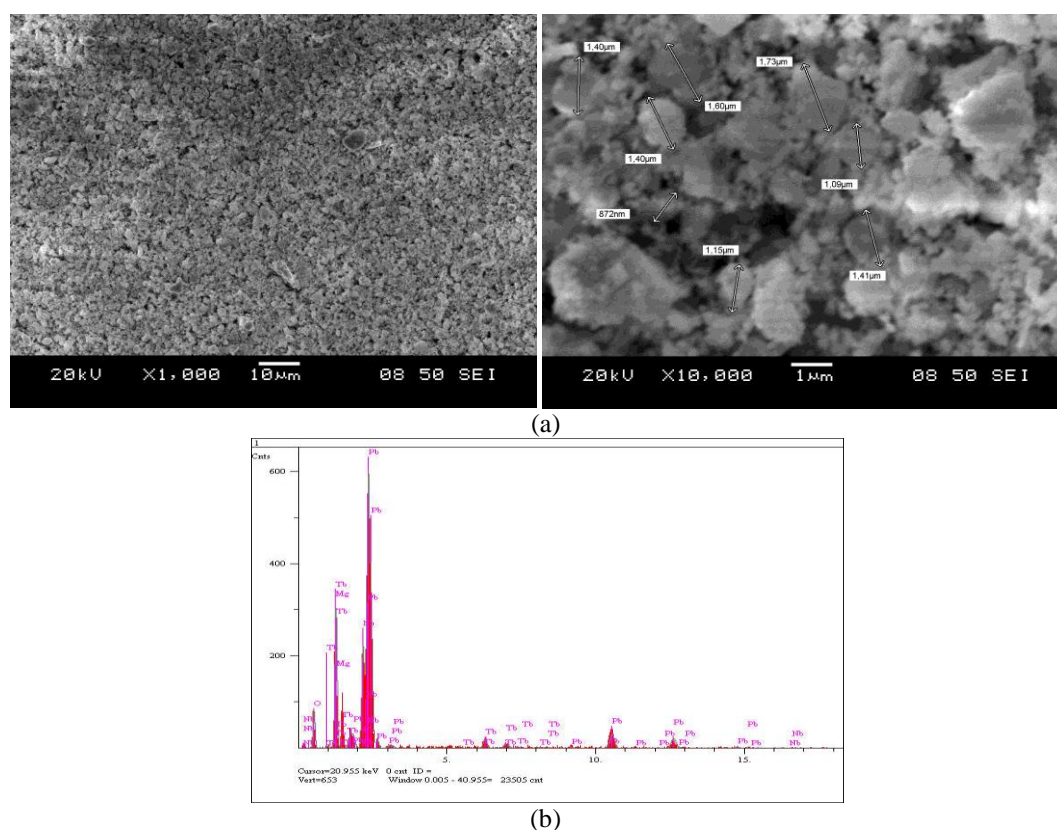


Figure 4.58 SEM images of 0.05 % Tb doped PMN thin films.

As shown by XRD results, PMN based thin films deposited on Si substrate preserved nearly pure perovskite phases. SEM micrographs showed that the thin films on Si substrates were well-oriented, crack-free and homogeneous. The heat-treatment performed at 730 °C for 1 hour in air yielded a homogeneous grain growth to about sub-micron grain size, while the heat-treatment at up to 730 °C observed in

non-uniformity and the appearance of a liquid phase and the thin films appeared to be better sintered.

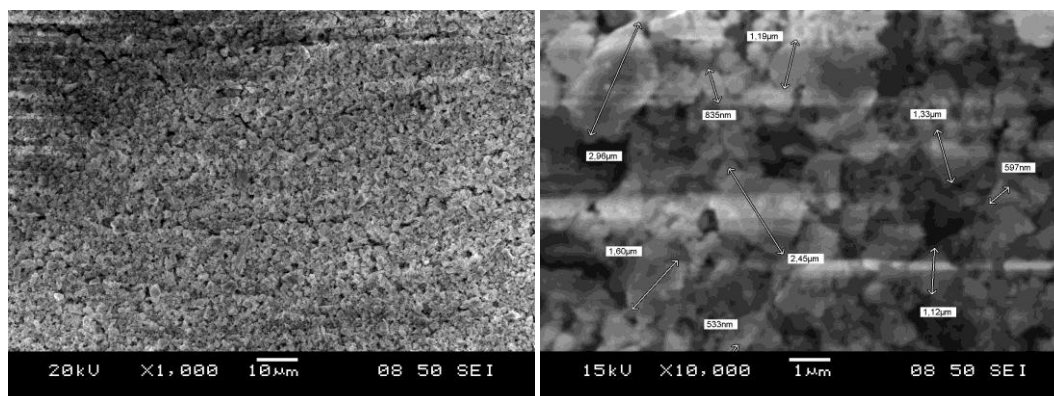


Figure 4.59 SEM images of 7 % Tb doped PMN thin films.

As expressed above, the particle size of PMN has an effect on the coating stability, i.e., larger, micro-PMN were worse coated than the smaller nano-PMN particles. This is confirmed by the EDS chemical analysis of the PMN particles from the coating suspensions. As illustrated in Figures and Table 4.5, the Mg/Nb ratios for submicron-sized aggregated nano scaled-PMN particles are much higher than those of a micro-PMN particle indicating that the coating of PMN layer is better for fine PMN particles than large particles. The average Mg/Nb ratio for the micron-sized PMN particles was the same with submicron-sized PMN particles indicating good PMN coating on the micron-sized PMN particle to allow good electron beam-particle interaction and X-ray generation in the coating layer. In spite of the fact that fine PMN particle size has advantageous for PMN formation reaction during subsequent heat treatment, the crucial part is preventing the segregation during the colloidal processing of submicron or nanometer-sized PMN powders.

The low-temperature sinterability can also be verified from SEM micrographs, as shown in Figures 4.37-4.59. After prolonged heat treatment at 730 °C, one of the fundamental aspects is the interaction energy between the particles which governs the coating behavior. In addition, many factors contribute to the interaction between surfaces, e.g. electrostatic, structural, geometrical, steric, depletion, hydration and hydrophobic forces and, ubiquitously, van der Waals interaction in complete sol-gel

processing. The electrodynamical origin of van der Waals interaction is atomic or molecular electric dipoles by their oscillation or rotation. Depending on the types of interacting dipoles, van der Waals forces can be have contributions from (1) Keesom force (between two permanent dipoles with free rotation); (2) Debye force (between one permanent dipole and one induced dipole); and (3) London force (between two induced dipoles). These forces vary with the inverse sixth power of the distance at atomic or molecular scales (from 1-2Å to several nm) (Bergstrom 1997).

Table 4.5 Chemical compositions of the particles calculated from the EDS spectra.

Sample	Particle size (nm)	Atomic percentage (%)					Mg/Nb ratio
		Mg _K	Nb _K	Pb _K	O _K	Re	
PMN before grinding in Figure 4.37	1300	3.93	24.53	68.59	2.94	-	0.16
PMN after grinding in Figure 4.38	528	4.21	27.07	61.23	6.01	-	0.16
5 % Er doped PMN in Figure 4.42	605	3.44	24.86	59.94	5.86	1.96	0.14
5 % Eu doped PMN in Figure 4.46	495	5.51	23.90	53.79	6.41	4.16	0.23
5 % Dy doped PMN in Figure 4.50	600	1.19	32.79	57.66	6.17	7.23	0.04
5 % Sm doped PMN in Figure 4.54	660	7.23	26.45	54.18	6.01	6.13	0.27
5 % Tb doped PMN in Figure 4.58	872	7.57	23.15	58.49	6.42	2.98	0.32

On a larger scale (e.g., for nano or micron-sized particles), van de Waals forces play their role collectively. Hamaker calculated this collective behavior by a pairwise summation of the individual dipole-dipole interactions (Bergstrom 1997).

In this study, we examine the effects of the size of the nano scaled particle coating experimentally using PMN based coating on Si substrates. Pure and doped PMN based coatings on Si substrates have been shown to be an effective way of promoting the formation of the desired perovskite phase of lead magnesium niobate [Pb(Mg_{1/3}Nb_{2/3})O₃] have many important applications utilizing their high-dielectric properties (Deliormanli 2007). In addition, there have been no studies that examine the effect of particle size on coating, especially when the core particle size is reduced to the nanometer range. The comparison in the coating behavior of micron-sized and nanometer-sized particles will be useful to nanotechnology involving nanoparticles.

A novel suspension method was developed for low-temperature sinterable PMN ceramics near the morphotropic phase boundary. In this method, submicron-sized crystalline PMN was well suspended in a methyl alcohol solution. The PMN precursor powder derived from such solution can be sintered as low as 950°C. This method could be very useful for processing low-temperature co-fired dielectric and piezoelectric ceramics. In the case of niobium-containing perovskites it is necessary to avoid the formation of pyrochlore-type phases if reproducible and optimum mechanical, dielectric and piezoelectric properties are to be achieved as a combination of DTA-TG, FTIR, XRD and SEM-EDS. Depending on these results, we have produced perovskite PMN films and then developed high quality Er, Eu, Dy, Sm and Tb doped PMN ceramic films on Si substrates.

4.5.2 AFM Analysis

One of the main ways to study and characterize nano scale structure of PMN based films is by the use of AFM technique. We begin this section with some introductory comments on the requirement of AFM machine, and then discuss various ways in which it can enhance our understanding of nano scale films. Another important parameter besides phase and morphology is a measure of the thickness deformation under thickness excitation. The thickness deformation would be quite small for the thin PMN based coatings, given the same field as for a bulk sample. In this respect, instruments with Angstrom resolution in height were needed for electronic measurements. AFM is one of the prime candidates.

Figure 4.60 involves an AFM image of the sample surface of pure PMN coating. The grains are 3~5 μm with grains clearly visible. There were concerns on the interaction between the AFM tip and sample surface due to the electrostatic interaction. The depths and surface roughness of PMN based films at 730 °C for 1 hour in air were determined to be in the range of (-1.42) – (1.99) μm . Surface roughness and depth values of the films were regarded as a correlation of temperature and PMN starting solutions.

The AFM tip displacements (hence sample thickness change) on Si were much weaker than that on PMN thin film layer. If we assume that all the other factors are the same for the PMN films and Si substrate, the large response from PMN films must come from the piezoelectric behavior. We would be cautioned that this assumption may or may not hold true since PMN have much higher charge density than Si substrates, and therefore the electrostatic interactions between AFM tip and the surface of the top layers may not be the same. This adds to the complexity in explaining the above experimental results.

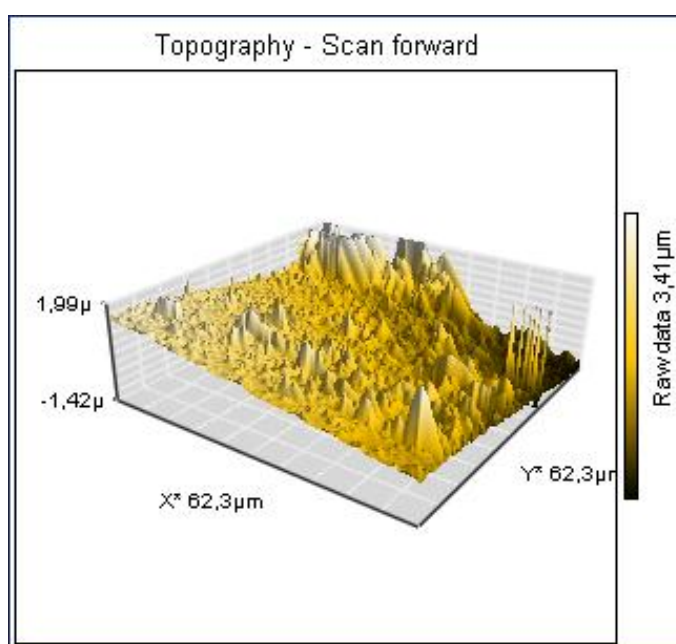


Figure 4.60 AFM image of the surface of pure PMN thin films at 730 °C for 1 hour in air.

Figure 4.61 denotes an AFM image of Er doped PMN coating surface after annealing process. It was found that the grains are $\sim 8 \mu\text{m}$ with grains unclearly visible. The depths and surface roughness of PMN films were determined to be in the range of 4.77-3.8 μm .

An AFM image of Eu doped PMN coating structure is demonstrated in Figure 4.62, showing that their grains are $\sim 8 \mu\text{m}$ with 6 times cycled thin film layer. The depths and surface roughness were determined to be in the range of 5.14-2.77 μm .

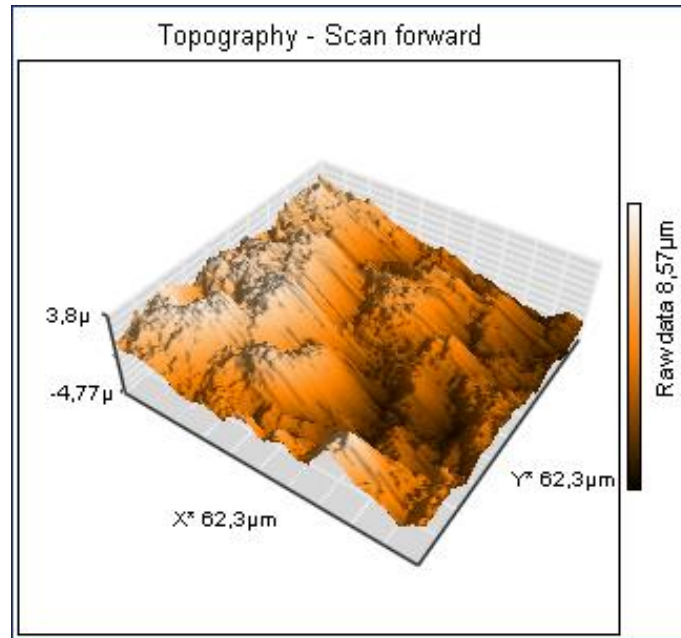


Figure 4.61 AFM image of the surface of Er doped PMN thin films at 730 °C for 1 hour in air.

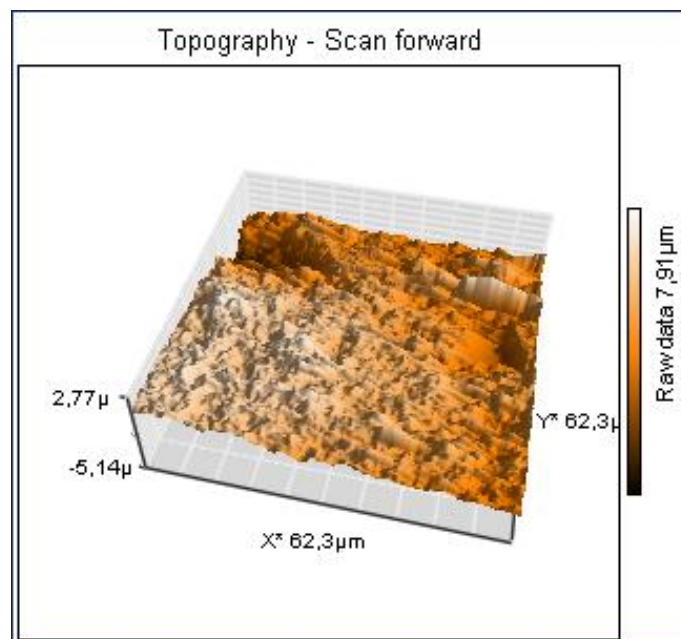


Figure 4.62 AFM image of the surface of Eu doped PMN thin films at 730 °C for 1 hour in air.

Figure 4.63 depicts an AFM image of optimum Dy doped PMN coating after annealing process. It was determined that the grains are 7~8 μ m with grain

boundaries clearly visible. The depths and surface roughness of PMN films annealed at 730 °C were found to be in the range of 758 nm-6.59 μm .

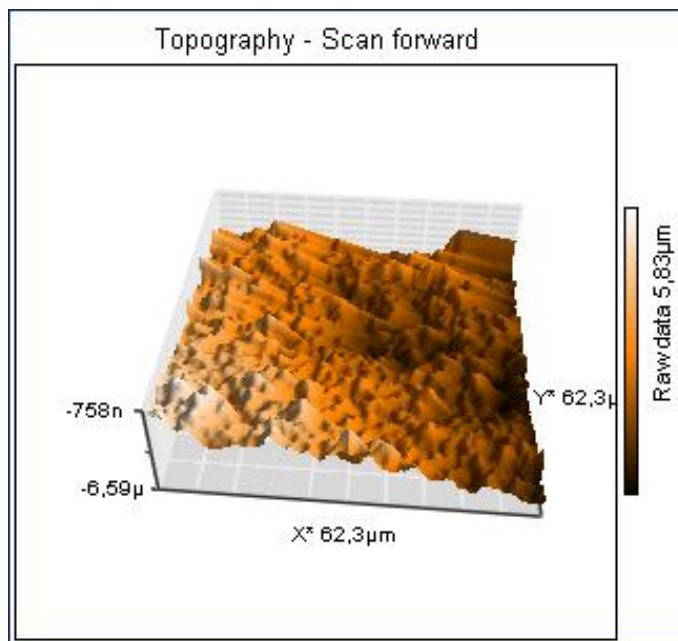


Figure 4.63 AFM image of the surface of Dy doped PMN thin films at 730 °C for 1 hour in air.

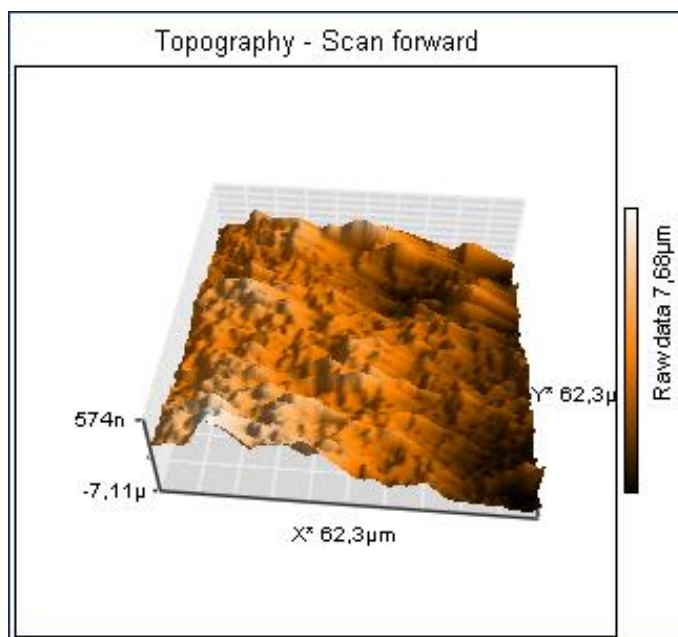


Figure 4.64 AFM image of the surface of Sm doped PMN thin films at 730 °C for 1 hour in air.

As for AFM image of the sample surface of Sm doped PMN coating on Si substrate, it was found that the grains are 7~8 μm with grain boundaries clearly visible (see Figure 4.64). The depths and surface roughness of Sm doped PMN films were determined to be in the range of 574 nm-7.11 μm .

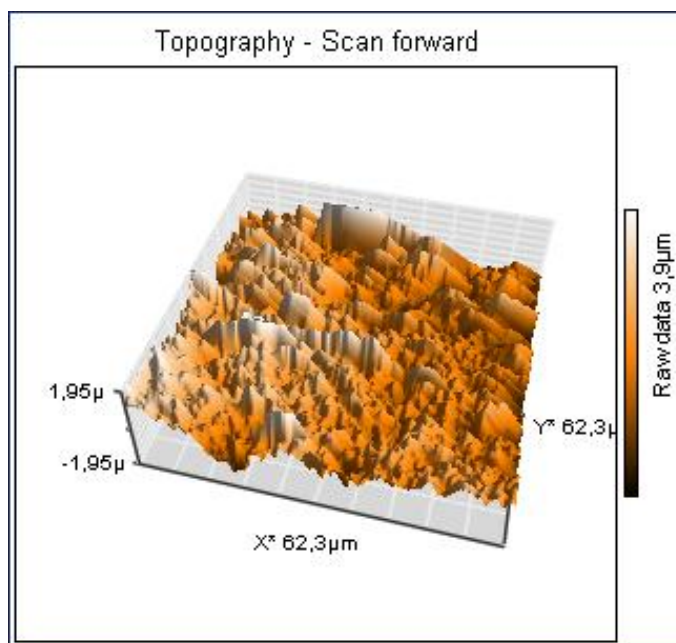


Figure 4.65 AFM image of the surface of Tb doped PMN thin films at 730 °C for 1 hour in air.

Figure 4.65 shows an AFM image of the sample surface of Tb doped PMN coating. In this sample, the grains are $\sim 4 \mu\text{m}$ with grain boundaries clearly visible. The depths and surface roughness of PMN films at 730 °C were determined to be in the range of 1.95-1.95 μm . Now that surface roughness and depth values of the films depends on sol-gel processing such as preparation of the solution and annealing conditions, these parameters vary from coating to coating.

AFM results of PMN based thin films for different rare earth dopants and 5 mol % amount of doping ratio are presented in Figures 4.60, 4.61, 4.62, 4.63, 4.64 and 4.65. Surface roughness of PMN films annealed at 730 °C changed between 150 nm and 175 nm. As marked in the Figures, surface roughness and depth of the samples were measured from different areas of the films. Using those kinds of measurements, surface roughness and depth values of the films were considered a correlation of

different dopant RE and PMN starting solutions. It can be noted here that surface roughness and depth of PMN thin films increase with RE dopants.

4.6 Mechanical Properties

4.6.1 DUH Analysis

Shimadzu Dynamic Ultra Micro Hardness Testing machine is used to determine mechanical properties of PMN based coatings on Si substrates. For these measurements, load of 10 mN is applied to PMN based coatings for determination of hardness and Young's modulus of samples. By using loading-unloading and depth-time curves of PMN based coatings, the numerical values such as hardness and Young's modulus of PMN based specimens were calculated as listed in Table 4.6.

Table 4.6 Indentation results of optimum PMN based coatings.

Optimum Samples of PMN based thin films	Applied Force (mN)	Young's modulus (GPa)	Dynamic Hardness Values at max. force (DHV)
PMN	10	5.76	11.56
1 % Er doped PMN		4.71	3.69
5 % Eu doped PMN		4.07	3.76
5 % Dy doped PMN		7.64	15.12
7 % Sm doped PMN		12.19	21.37
1 % Tb doped PMN		7.63	7.66

Indentation is one of the few ways of measuring mechanical properties of thin PMN based films. It is relatively simple in sample preparation and data acquisition with the help of computer software. Since the sampling region is small microns, local information could be obtained while a large array of indents yields statistical data. With these advantages, indentation experiments were carried out using Shimadzu Dynamic Ultra Micro Hardness Testing machine (Ebeoğlugil 2010).

After aligning the optical microscope and the indenter head, several points to be indented were identified. Commonly used indenter tips are standard Vickers Piramide indenter. In this experiment, Vickers Piramide tip was used because it is

usually employed for Young's modulus measurements. A small load up to 10 mN was used with a time to load of 10 sec for all PMN based coatings. Unload began after holding at max load for 10 sec. Young's modulus was calculated with the initial unloading curve by the software. In the first measurements, average thickness of thin films ($\sim <1 \mu\text{m}$) were selected for indentation.

According to the indentation results, Young's modulus and Dynamic hardness values of pure PMN based coating are 5.76 GPa and 11.56 DHV, respectively. Therefore, hardness and Young's modulus values of the coatings are independent from coating thickness. Young's modulus values of 1 % Er, 5 % Eu, 5 % Dy, 7 % Sm and 1 % Tb doped PMN based coatings for chosen optimum samples are 4.71 GPa, 4.07 GPa, 7.64 GPa, 12.19 GPa and 7.63 GPa respectively. It was found dynamic hardness values of 1 % Er, 5 % Eu, 5 % Dy, 7 % Sm and 1 % Tb doped PMN based coatings for chosen optimum samples are 3.69 DHV, 3.76 DHV, 15.12 DHV, 21.37 DHV and 7.66 DHV, respectively. As can be seen from these results, the Young's modulus and hardness for the six individual samples are quite different, which might have come from the different coating thickness, dopant type and porosity. These results are completely different from PMN bulk materials. Indeed in ferroelectric crystals, some orientations appear to large Young's modulus, while the orientations with the largest d_{33} piezoelectric coefficients are very soft. For example, for $\text{Pb}(\text{Zn}_{1/2}\text{Nb}_{2/3})\text{O}_3\text{-8\%PbTiO}_3$ (PZN-PT), a ceramic very similar to PMN-PT, (111) oriented crystal has $Y_{33}=137$ GPa, with a d_{33} of 83 pm/V, while (001) oriented one had $Y_{33}=7.7$ GPa, with a d_{33} of 2500 pm/V (Seung-Eek 1997). Since there exists (100) and (200) orientations in PMN based coatings, it is difficult to estimate meaningful data like bulk materials. Nevertheless it is important to appreciate the deformation mechanisms leading to thermal and high voltage breakdown of PMN based coatings.

4.6.2 Adhesion Properties

As for adhesion properties of PMN coatings, scratch tester can be performed. In this experiment, the analysis of scratch tester gives critical force values of PMN based specimens. These critical normal force values correspond to be the first peak in

the cartridge output percentage test force graphical curve obtained from scratch tester machine. The resulting effect on the adhesion properties of PMN coatings must be taken into account with this perspective. Bond strengths, critical force and Brinell hardness values of pure PMN coatings are presented in Table 4.7. Hardness value of substrate was converted from Vickers Hardness to Brinell Hardness (H) by using Standard Hardness Conversion Tables for Metal, the adhesion strength (F) of the coatings was calculated as MPa unit by Equation 3.10 (Ebeoğlu 2010). It is clearly seen from Table 4.7 that critical forces of pure PMN coated films at 600 °C, 700 °C and 800 °C have 26.23 mN, 28.54 mN and 46.82 mN, respectively. It is also remarkable that adhesion strength of the films increases from 182 MPa to 248 MPa depending on heat treatment temperature and critical force increase.

Table 4.7 Critical forces and adhesion strengths of pure PMN coating on Si substrates.

Substrate	Brinell Hardness (N.mm ⁻²)	Indenter Radius (µm)	Pure PMN at Different Temperatures	Critical Force (mN)	Adhesion Strength (MPa)
Si	856	15	600 °C	26.23	182
			700 °C	28.54	190
			800 °C	46.82	248

It is clearly seen from Table 4.8 that critical forces of chosen optimum pure, 1 % Er, 5 % Eu, 5 % Dy, 7 % Sm and 1 % Tb doped PMN based coatings annealed at 730 °C have 31.46 mN, 7.95 mN, 3.27 mN, 17.18 mN, 12.62 mN and 30.37 mN, respectively. It is also remarkable that adhesion strength of the films differ from each others. Adhesion strength values of coatings are 200 MPa, 98 MPa, 63 MPa, 146 MPa, 125 MPa and 197 MPa depending on rare earth doping ratios of PMN.

Table 4.8 Critical forces and adhesion strengths of pure and doped PMN coating.

Substrate	Brinell Hardness (N.mm ⁻²)	Indenter Radius (µm)	Optimum samples of PMN based coatings (730 °C)	Critical Force (mN)	Adhesion Strength (MPa)
Si	856	15	PMN	31.46	200
			1 % Er doped PMN	7.95	98
			5 % Eu doped PMN	3.27	63
			5 % Dy doped PMN	17.18	146
			7 % Sm doped PMN	12.62	125
			1 % Tb doped PMN	30.37	197

4.7 Optical Properties

Optical properties of PMN based films on glass substrate are listed in Table 4.9 in details. Refractive index and film thickness of PMN films on glass substrates were measured using UV-Visible Spectrophotometer. It was found that the refractive index of pure PMN thin films was 1.3415. The film thickness of PMN film was determined as 0.960 μm depending on refractive index value.

Table 4.9 Refractive indexes, thickness and band gap values of pure and doped PMN coatings on the glass substrate.

Doping ratio of Rare Earth (mol %)	Refractive index (nD)	Thickness (μm)	Band gap (eV)
PMN	1.34	0.960	3.096
1 % Er	1.51	0.255	2.860
3 % Er	1.51	0.896	2.420
5 % Er	1.47	0.464	3.029
7 % Er	1.51	0.448	3.230
1 % Eu	1.51	0.779	3.993
3 % Eu	1.46	2.184	3.334
5 % Eu	1.52	0.310	3.995
7 % Eu	1.31	0.484	3.831
1 % Dy	1.33	1.190	4.047
3 % Dy	1.30	1.272	2.532
5 % Dy	1.39	0.448	5.224
7 % Dy	1.47	1.746	3.916
1 % Sm	1.51	0.273	3.940
3 % Sm	1.53	0.308	3.967
5 % Sm	1.42	0.281	4.011
7 % Sm	1.48	0.309	3.899
1 % Tb	1.51	0.408	4.020
3 % Tb	1.51	1.428	3.990
5 % Tb	1.53	1.054	3.994
7 % Tb	1.53	0.718	4.034

4.8 Dielectric Properties

Ferroelectric and piezoelectric ceramics cannot be used without well conductive electrodes applied to two opposite faces. Ideally, the electrodes should be very thin, have practically zero electrical resistance, and good chemical and physical durability. It also should allow for attaching leads with good bonding (good pull strength and reliability). These are actually quite stringent and not always obtainable. After all, the

adherence between an oxide ceramic and a metal layer will not be very strong without inter-diffusion induced by bombarding or high temperature.

Silver paste is the most common candidate to use an electrode materials. The importance of sample geometry can be appreciated from Figure 3.36. But it is hard to be applied thinner than several microns. As a result of the organic evaporation from the paste, air gaps may exist between the metal and ceramic layers. Due to such lack of intimate bonding, the gaps acts as a series capacitor with low dielectric constant, lowering the effective capacitance of the ceramic very strongly. If a field is applied, most of the voltage drop is across the gap, which interferes with poling and subsequent using. As a result, some people use silver paste applied on top of sputtered gold film electrode, as electrical contacts (Dong-Hwan 2001).

In the study relative permittivity and real capacity (C') of the PMN thin films prepared according to setup in Figure 4.66 were measured as a function of frequency. It is known that, dielectric constant of PMN is maximum at about $-10\text{ }^{\circ}\text{C}$ and above this temperature dielectric constant decrease with increasing temperature. In this work, the measurements were performed at room temperature ($25 \pm 2\text{ }^{\circ}\text{C}$), therefore the results do not correspond to the maximum relative permittivity values for these samples. Accordingly, Figure 4.66 describes the relative permittivity, ϵ_r , of the PMN samples as a function of frequency. It is obvious that ϵ_r of the PMN samples is dependent on the frequency.

Relative permittivities of the undoped PMN thin films sintered at $600\text{ }^{\circ}\text{C}$, $700\text{ }^{\circ}\text{C}$, $800\text{ }^{\circ}\text{C}$ and $730\text{ }^{\circ}\text{C}$ were measured to be 5980, 7620, 1080 and 31312 at 0.01 Hz, respectively. Similarly, in Figure 4.67, real capacity values of the PMN thin films sintered at $600\text{ }^{\circ}\text{C}$, $700\text{ }^{\circ}\text{C}$, $800\text{ }^{\circ}\text{C}$ and $730\text{ }^{\circ}\text{C}$ is about 0.548, 1.75, 0.49 and 659.51 nano farad (nF) at 0.01 Hz, respectively.

The obtained results showed that under the same conditions ϵ_r values of the PMN based thin film samples are nearly the same compared to previous thin film studies of PMN films. Previous studies related to the electrical characterization of ferroelectric

thick films showed that films may have a lower relative permittivity compared to the bulk ceramics (Deliormanli 2007 and 2008) For example, Gentil et al. measured the relative permittivity of PMN films as 10,000 at 0.1 kHz which is lower than the values of the bulk ceramics (17,800 at 0.1 kHz) under the same conditions. They also found that the decrease of film thickness lead to the decrease of dielectric properties. In this study the lower relative permittivity values in PMN thin films compared to the previous thin film studies may be attributed to the several factors, including higher porosity and higher surface roughness.

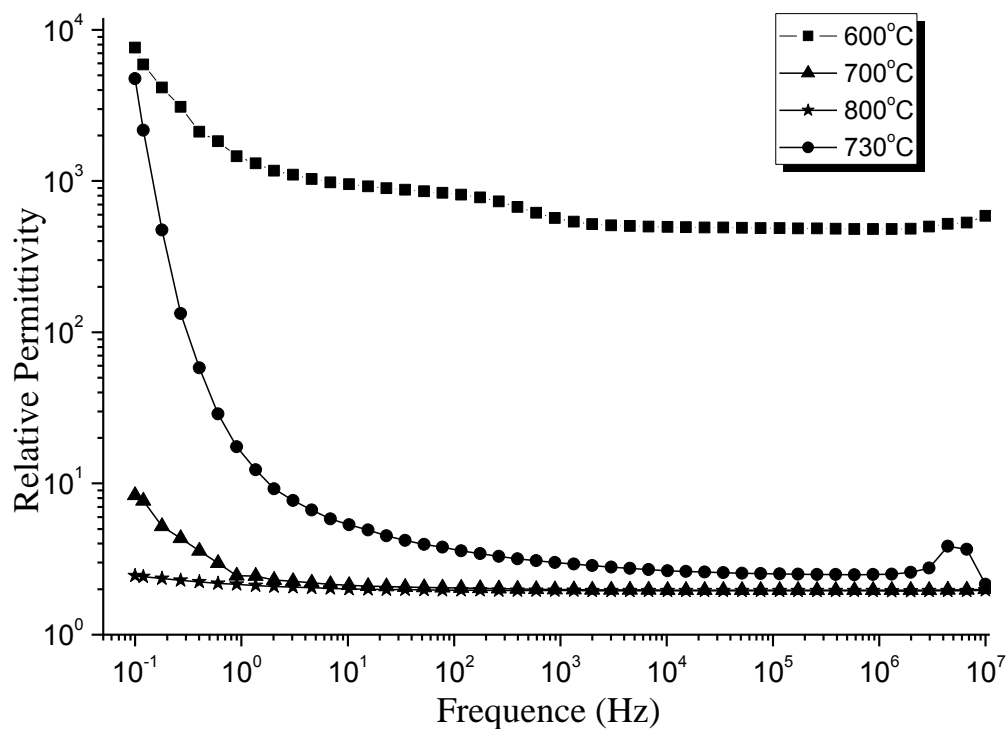


Figure 4.66 Relative permittivities of the PMN thin films suspension method sintered at 600 °C, 700 °C, 730 °C and 800 °C for 1 hour in air.

The most important feature of thin films of PMN is load of storage capability. Therefore, dielectric measurements such as permittivity and capacitance values are extremely important. Measurements of the different heat treatment temperature can be understood from the structure of samples seen approaching 100 % PMN structure and capacitance values of the dielectric coefficient is increased.

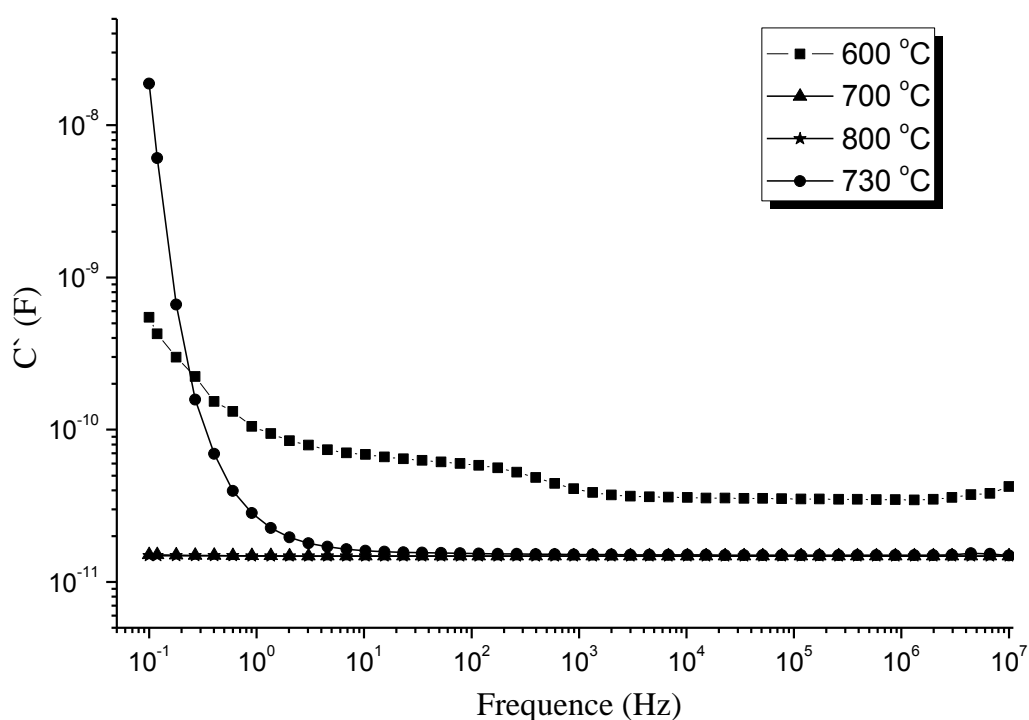


Figure 4.67 Real capacity of the PMN thin films prepared by the suspension method sintered at 600 °C, 700 °C, 730 °C and 800 °C for 1 hour in air.

As shown in Figures 4.66 and 4.67, PMN thin films on Si wafer, a higher annealing temperature is entailed for the thin films electric properties. The dielectric constants are consistent with that of pure PMN film. The low dielectric loss and high resistivity under high field of the annealed PMN thin films indicate good film quality. Further study by Yi-Shih Chiu on Sr-doped PbTiO_3 thin films showed that if the film is somehow (100)-oriented, the dielectric constant can be over 1000 (Chiu 2005). These Figures show the frequency dependence of the dielectric constant of the PMN ceramics. The decrease of dielectric constant with frequency is a typical behavior of a relaxor ferroelectrics.

Optimum sintering temperature (730 °C) improved the dielectric properties of the samples, which may have been due to (1) increased density; (2) increased grain size and (3) the gradual reaction between PMN particles on Si surface and (4) higher adhesion strength between PMN particles and Si substrate at 730 °C. Other samples could not be well-densified at temperatures such as 600 °C, 700 °C and 800°C, and thus their dielectric constants were inferior to that made by the suspension method. It

is believed that the nano-sized powder precipitated from the suspension had small sizes and higher reactivity. There is little dielectric constant variation with regard to frequency, a sign of normal ferroelectrics rather than relaxors. Even though pyrochlore is a problem at 600 °C, 700 °C and 800 °C sintering temperatures, PMN films and were dense enough for dielectric measurements with a fairly large electrode.

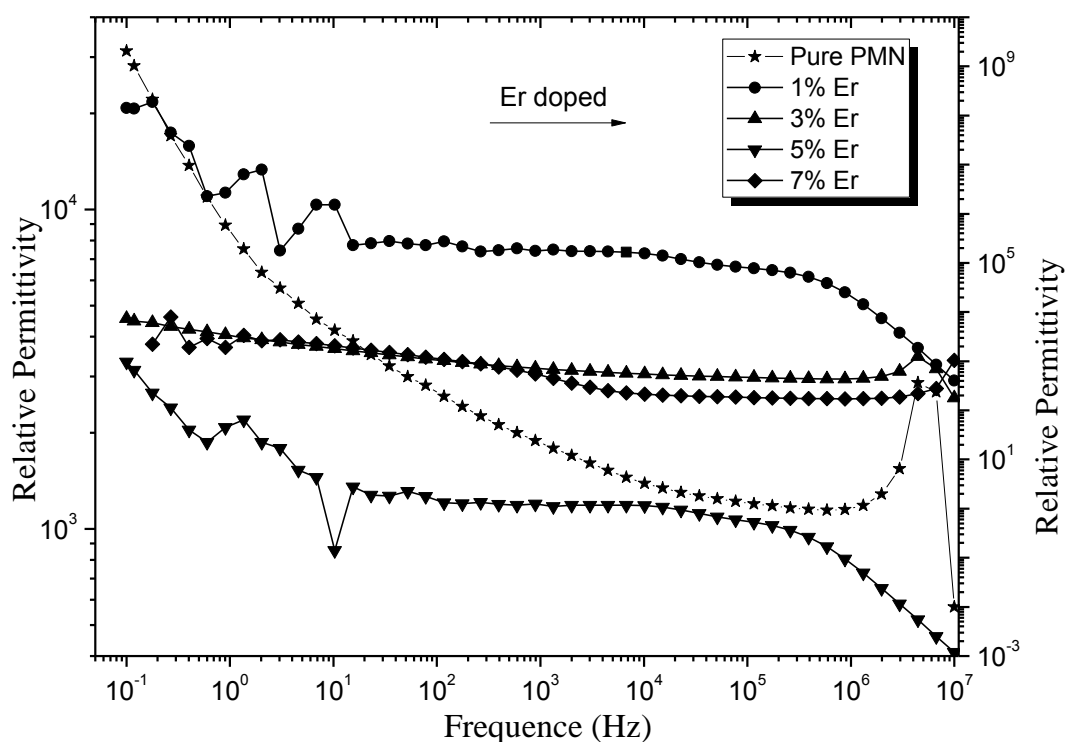


Figure 4.68 Relative permittivities of Er doped PMN thin films obtained suspension method sintered at 730 °C for 1 hour in air.

Figure 4.68 describes the relative permittivity of the Er doped PMN samples as a function of frequency. Relative permittivities of 1 %, 3 %, 5 % and 7 % Er doped PMN thin films sintered at 730 °C were measured as 1.5×10^5 , 1804, 2,8 and 2062 at 10 Hz, respectively. Similarly, in Figure 4.69, real capacity values of 1 %, 3 %, 5 % and 7 % Er doped PMN thin films 730 °C is about 18.8, 8.1×10^{-9} , 1.2 and 1.6×10^{-6} farad (F) at 10 Hz, respectively.

The results showed that under the same conditions capacitance values of the PMN thin film samples are not the same compared to pure PMN thin film values. Previous

results related to the heat treatment. Er doped samples showed that films may have a breakdown treatment in relative permittivity compared to the pure PMN. The coatings generally had lower dielectric constants and capacity than pure PMN counterparts (see Figure 4.68 and 4.69), and the 1 % Er doped sample have giant dielectric constant and capacity than the other doping percentage of Er. This indicates that there is a doping effect in the PMN electrical properties: The thinner the PMN ceramic is, the lower the dielectric constants. As the thickness of the dielectric layers decreases to improve the volumetric efficiency of the capacitors, the electrical behavior of the thin films is expected to differ from that of the bulk materials. Two main reasons can be anticipated to cause this variation. The first one is that at very thin layers the conductivity will be more dependent on the interface. In addition to that, the thin dielectric layers are prepared by different routes than bulk materials leading to variations in the physical properties. The decrease of dielectric constant with frequency is a typical behavior of a relaxor ferroelectric.

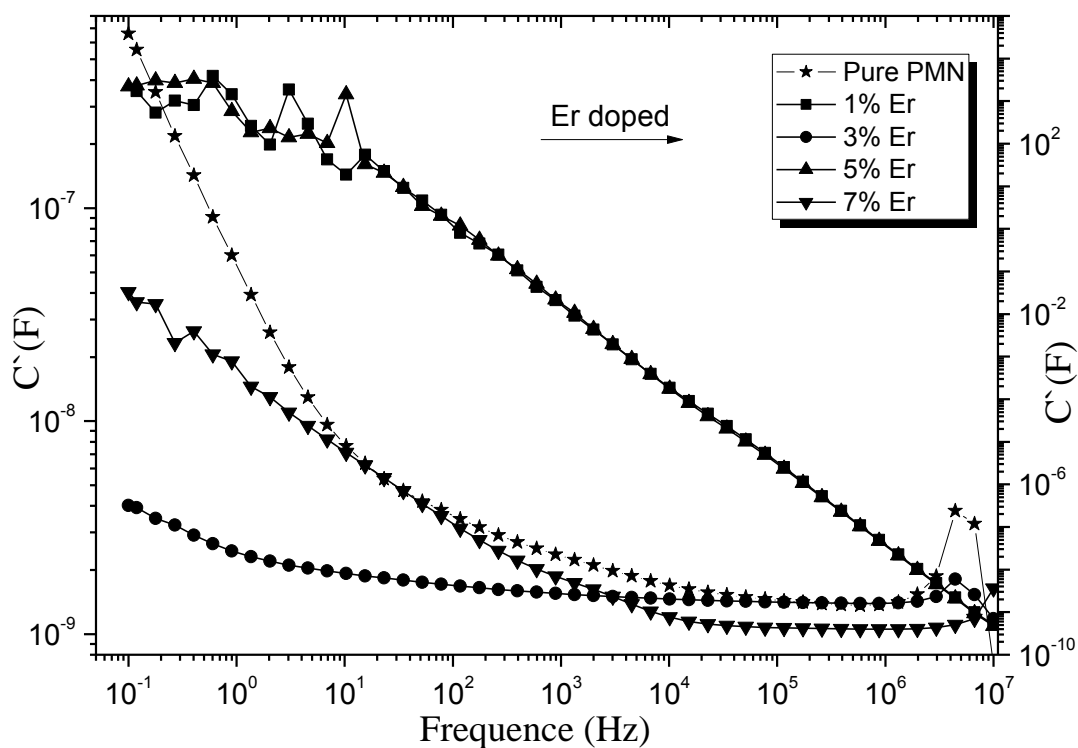


Figure 4.69 Real Capacity of Er doped PMN thin films obtained suspension method sintered at 730 °C for 1 hour.

Figure 4.70 describes the relative permittivity of Eu doped PMN samples as a function of frequency. It was found that relative permittivities of 1 %, 3 %, 5 % and 7 % Eu doped PMN thin films sintered at 730 °C were measured as 27982, 26130, 3648 and 6314 at 10 Hz, respectively. Similarly, it can be seen in Figure 4.71 that real capacity values of 1 %, 3 %, 5 % and 7 % Eu doped PMN thin films 730 °C for 1 hour in air is approximately 0.28, 1.64×10^{-8} , 3.78×10^{-9} and 4.14×10^{-8} farad (F) at 10 Hz, respectively.

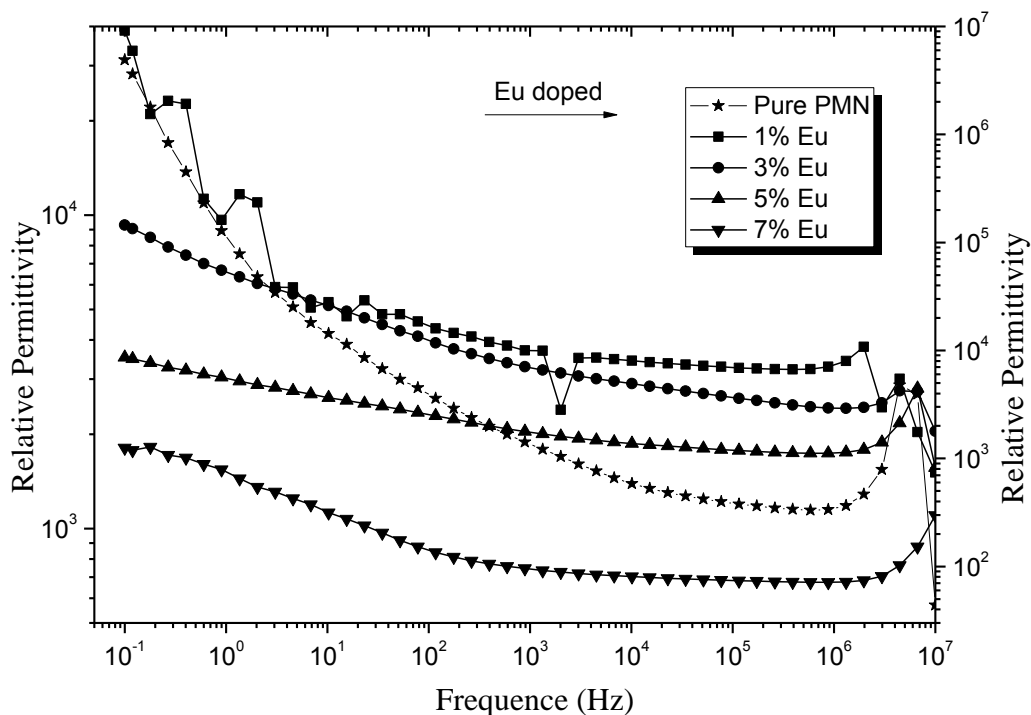


Figure 4.70 Relative permittivities of Eu doped PMN thin films obtained suspension method sintered at 730 °C for 1 hour in air.

As mentioned just before, the obtained results showed that under the same conditions capacitance values of the PMN thin film samples are not the same compared to pure PMN thin film values. Eu doped samples showed that films may have a breakdown treatment in relative permittivity and capacity values compared to the pure PMN. It can be expressed that the coatings generally had lower dielectric constants and capacity than pure PMN samples as indicated from Figures 4.70 and 4.71, and the 5 % Eu doped sample have low dielectric constant and capacity than the other doping percentage of Eu. Moreover, Eu doped coatings exhibit that the same character to Er and we can easily say that the decrease of dielectric constant

with frequency is a typical behavior of a relaxor ferroelectric. This behavior is generally observed that for all samples.

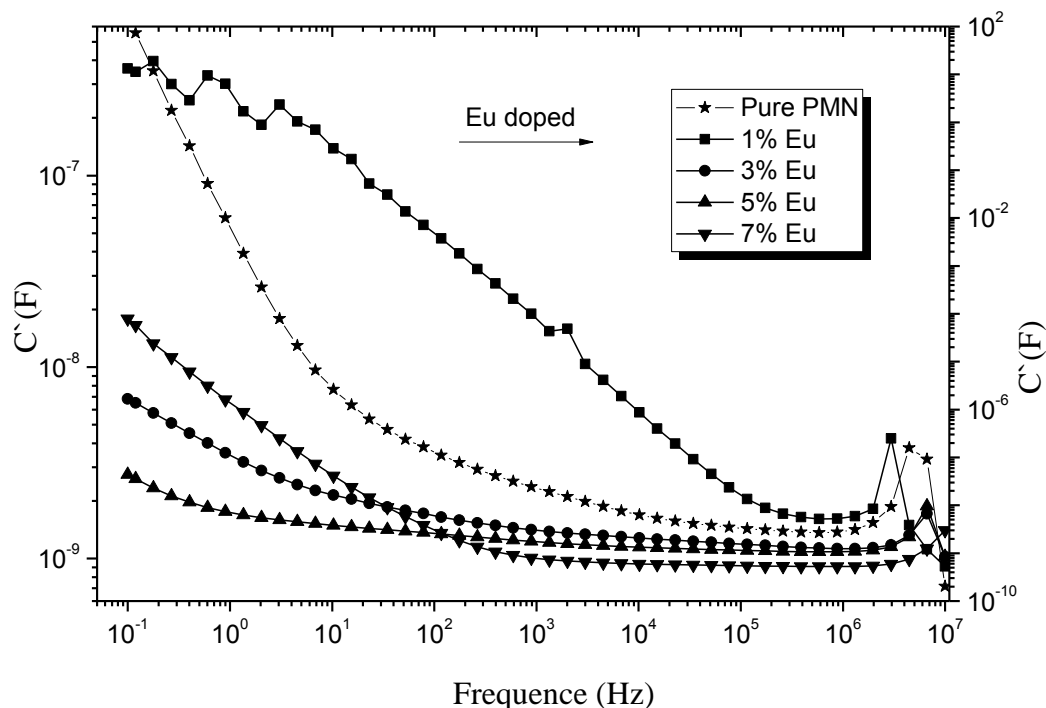


Figure 4.71 Real capacity of Eu doped PMN thin films obtained suspension method sintered at 730 °C for 1 hour in air.

This indicates that there is an effect in the Eu doped PMN on electrical properties: The small percentage of Eu doped PMN ceramic is, the higher the dielectric constants. As the thickness of the dielectric layers decreases to improve the volumetric efficiency of the capacitors, the electrical behavior of the thin films is expected to differ from that of the pure PMN.

The relative permittivity of Dy doped PMN samples as a function of frequency is clarified in Figure 4.72. It was noted here that relative permittivities of 1 %, 3 %, 5 % and 7 % Dy doped PMN thin films sintered at 730 °C were found to be 25169, 4510, 5721 and 1.8×10^5 at 10 Hz, respectively. Similarly, as can be shown from Figure 4.73, real capacity values of 1 %, 3 %, 5 % and 7 % Dy doped PMN thin films 730 °C is nearly 12.56, 2.56×10^{-9} , 2.69×10^{-9} and 20 farad (F) at 10 Hz, respectively.

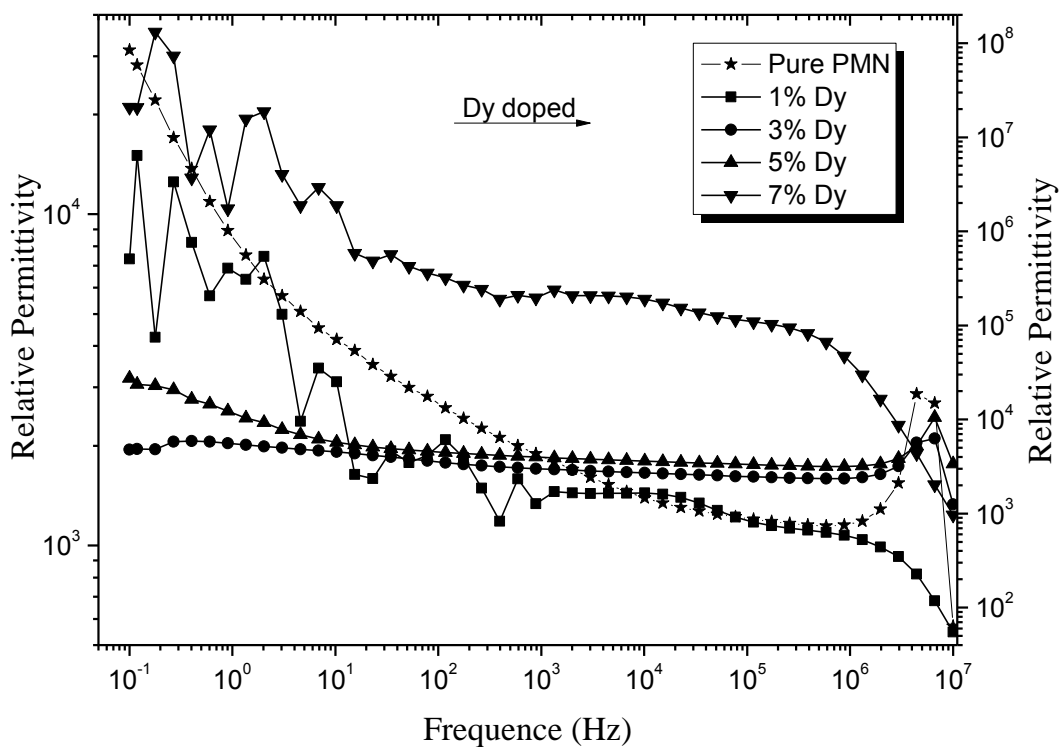


Figure 4.72 Relative permittivities of Dy doped PMN thin films obtained suspension method sintered at 730 °C for 1 hour in air.

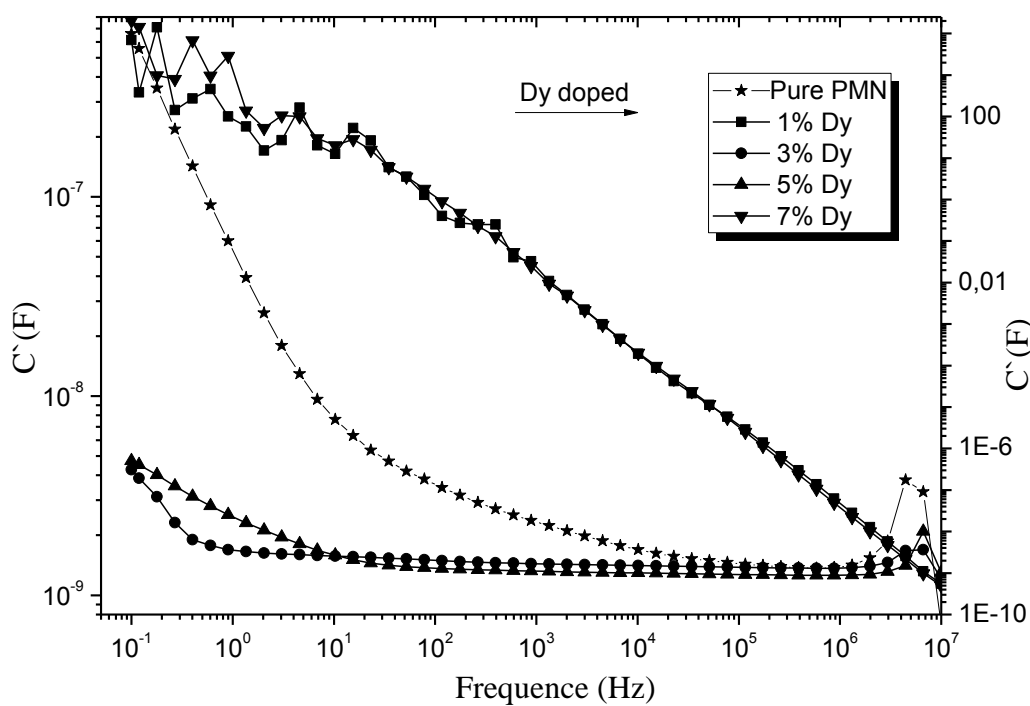


Figure 4.73 Real capacity of Dy doped PMN thin films obtained suspension method sintered at 730 °C for 1 hour in air.

Under the conditions prepared in thin films with the former dopants, capacitance values of the PMN thin film samples are not the same compared to pure PMN thin film and each others. Dy doped PMN films showed that films may have a breakdown treatment in relative permittivity and capacity values compared to the pure PMN at the same frequency. It was found that the coatings generally had higher dielectric constants and capacity than pure PMN samples as shown from Figures 4.72 and 4.73, and the 3 % and 5 % Dy doped PMN film samples possess low dielectric constant and capacity than the other doping percentage of Dy.

Figure 4.74 presents the relative permittivity of Sm doped PMN samples as a function of frequency. In these measurements, relative permittivity of 1 %, 3 %, 5 % and 7 % Sm doped PMN thin films sintered at 730 °C, 1 hour in air were determined as 20608, 353, 85 and 968 at 10 Hz, respectively. In Figure 4.75, real capacity values of 1 %, 3 %, 5 % and 7 % Sm doped PMN thin films is about 11.85, 8.46×10^{-8} , 7.83×10^{-10} and 1.74×10^{-9} farad (F) at 10 Hz, respectively.

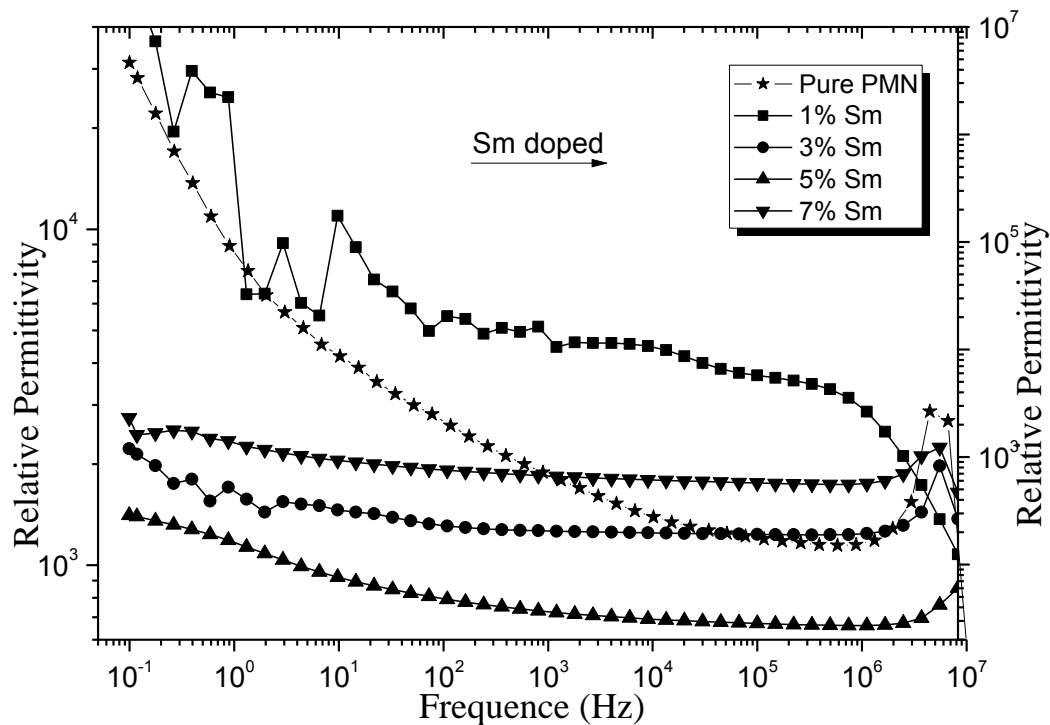


Figure 4.74 Relative permittivities of Sm doped PMN thin films obtained suspension method sintered at 730 °C for 1 hour in air.

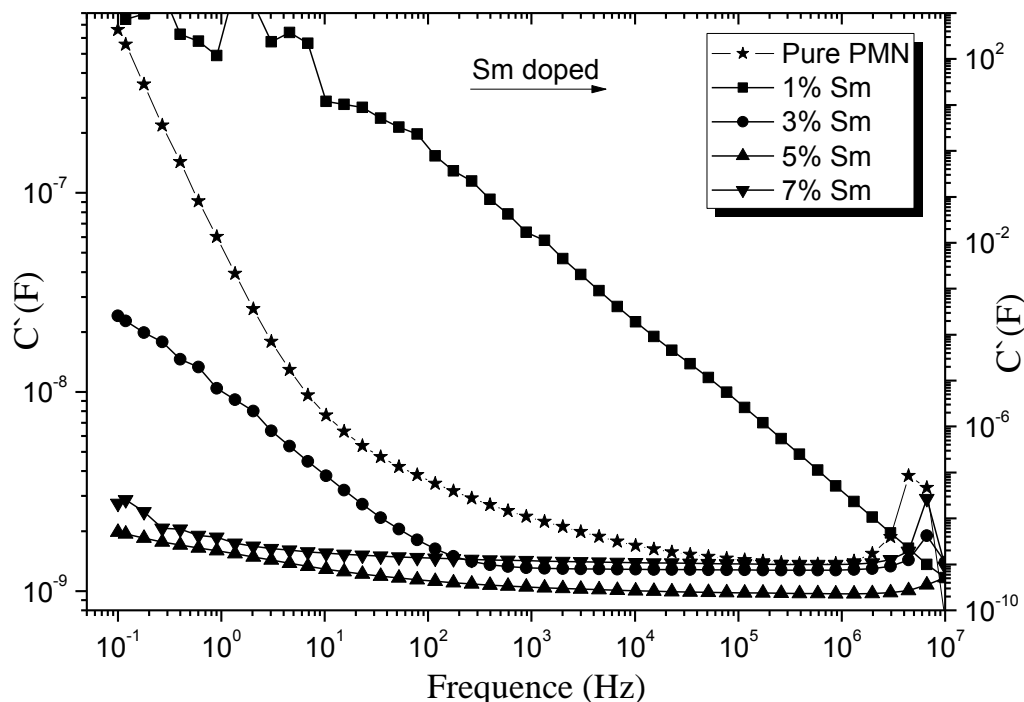


Figure 4.75 Real capacity of Sm doped PMN thin films obtained suspension method sintered at 730 °C for 1 hour in air.

The results showed that under the same conditions the values of Sm PMN thin film samples are not the same compared to pure PMN thin film and each others. Sm doped PMN film samples showed that films may have very small dielectric constant in relative permittivity for 3 %, 5 % and 7 % of Sm and same characteristic capacity values compared to other doping rare earths before at the same frequency. The coatings generally had lower dielectric constants and capacity than pure PMN samples and the 3 %, 5 % and 7 % Sm doped films have low dielectric constant and capacity than the other doping percentage of Sm.

Figure 4.76 denotes the relative permittivity of the Tb doped PMN samples as a function of frequency. Note that relative permittivity of 1 %, 3 %, 5 % and 7 % Tb doped PMN thin films sintered at 730 °C for 1 hour in air were measured as 4418, 22531, 40644 and 29018 at 0.1 Hz, respectively. It is also clear from Figure 4.77 that real capacity values of 1 %, 3 %, 5 % and 7 % Tb doped PMN thin films annealed at 730 °C is approximately 2.51×10^{-7} , 5.35×10^{-8} , 5.02×10^{-9} and 4.84×10^{-8} farad (F) at 0.1 Hz, respectively.

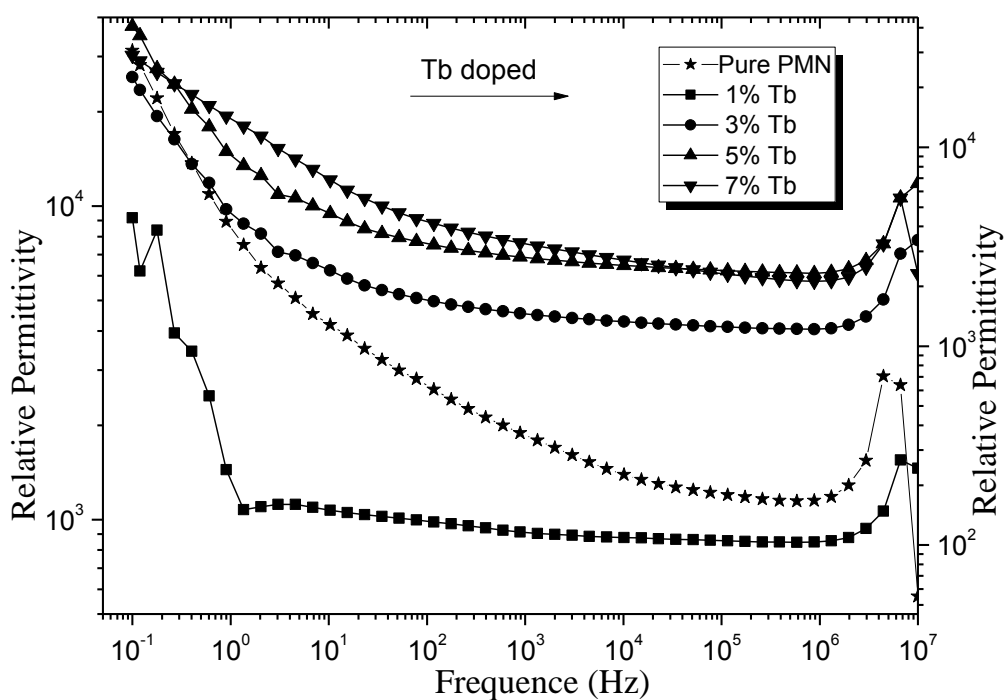


Figure 4.76 Relative permittivities of Tb doped PMN thin films obtained suspension method sintered at 730 °C for 1 hour in air.

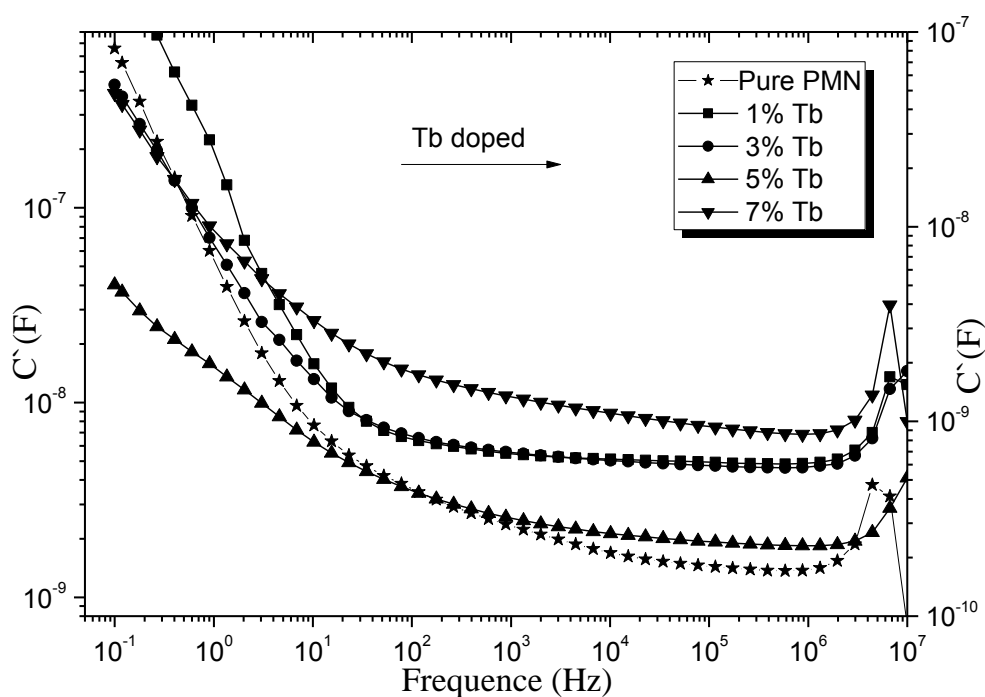


Figure 4.77 Real capacity of Tb doped PMN thin films obtained suspension method sintered at 730 °C for 1 hour in air.

As explained in the preceding samples, capacitance values of the PMN thin film samples are not the same compared to pure PMN thin film values under the same

conditions. Tb doped PMN samples indicated that these films may have the same treatment in relative permittivity and capacity values compared to the pure PMN. It can be said that the coatings generally had higher dielectric constants and capacity than pure PMN samples and the 1 % Tb doped PMN films possess low dielectric constant and high capacity than the other doping percentage of Tb. Furthermore, Tb doped PMN coatings show that the different character to other RE doping and it can be pointed out that the increasing the dielectric constant and capacity occur with increasing the percentage of Tb values. In addition to these, there exists a typical behavior of a relaxor ferroelectric material for Tb doping coatings.

It has been suggested that, in general, larger rare earth cations mainly occupy the A-site (where they act as donor dopants), smaller cations predominantly occupy the B-site (where they act as acceptor dopants) and intermediate ions (Er, Eu, Dy, Sm and Tb) occupy both A and/or B-sites (donor and acceptor dopants). Several investigators have studied the occupancy of rare earth ions in the BaTiO₃ lattice and mixed results have been obtained according to the processing parameters used during the firing. Later on, Tsur et al. revised the rare earth cation substitution in BaTiO₃ and proposed a comprehensive theory in terms of the tolerance factor, thermodynamics and kinetics considerations (Levi 2009).

Dopants that have a strong effect in the dielectric properties of PMN based materials are Er, Eu, Dy, Sm and Tb. It has been reported that doping increases resistance by increasing the reactions in the system. The large variation on the dielectric and capacity with doping content as a function of molar ratio is shown in above presented figures. The formation of the reaction between RE and PMN system reduces the concentration of oxygen vacancies. When added in small amounts RE ions can occupy the A (Pb) site, the B (Mg-Nb) or both sites together depending on the stoichiometry of the perovskite system. The addition of RE may suffer the tightening of the lattice structure when the smaller RE³⁺ replaces Pb⁺⁴.

While the electronic conductivity of RE doped PMN based dielectric materials is low, the large number of charged oxygen vacancies created as compensation causes a

significantly elevated ionic conductivity. The temperature of the ferroelectric phase transition decreases with an increase in RE content (Levi 2009).

Solid solutions of BaTiO₃ and BaZrO₃ have been used as the dielectric material in multilayer ceramic capacitors for several years. The addition of Zr is reported to broaden the permittivity peak and lower the temperature coefficient of capacity. This happens by a decrease in the cubic-tetragonal transition temperature while increasing the orthorhombic-tetragonal and rhombohedral-orthorhombic phase transition temperatures (Levi 2009).

4.9 Current- Voltage (I-V) Characteristics

The current–voltage (I–V) characteristics of pure, Er, Eu, Dy, Sm and Tb doped PMN based coatings on n-Si are shown in Figures 4.78, 4.79, 4.80, 4.81, 4.82 and 4.83. It was found that, at low voltages, the forward current of the coatings increases exponentially with applied voltage like diode. The device indicates a rectifying behavior between PMN and doped PMN on Si semiconductor substrates. It can be noticed that the nanoscaled thin films of PMN/n-Si junctions behave like a Schottky barrier diodes at low voltages.

Current and voltage ranges of pure PMN samples measured at room temperature shown in Figure 4.78 were found to be 51.31 – 23.7 nano Amper (nA) and -50 V - +50 V, respectively. This may result from the high probability of electron and hole recombination in the depletion region or occurrence of tunneling current or presence of an interfacial layer. Notwithstanding we applied huge voltage to the coatings, the PMN coating has very low current characteristics as seen from Figure 4.78.

RE addition is decreased the resistance value and makes the capacitor more conductive. The obtained series current is an important factor in performance of the diode characterized PMN coatings and affects current-voltage characteristic of the capacitor coatings. As seen in Figures 4.79, 4.80, 4.81, 4.82 and 4.83, the current values of Er, Eu, Dy, Sm and Tb doped PMN capacitors were found to be in the

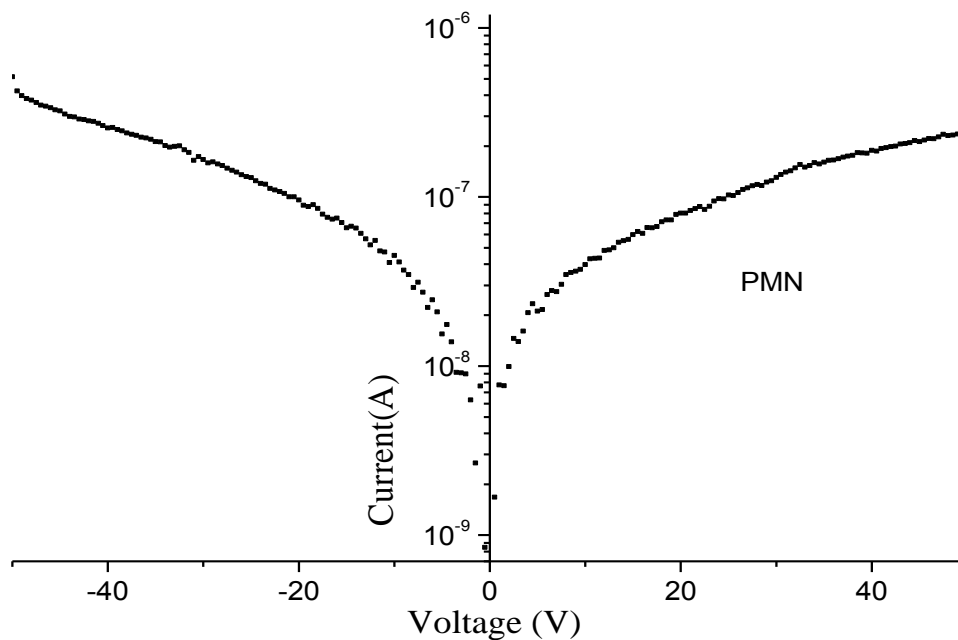


Figure 4.78 The I-V characteristic curve of undoped PMN thin films obtained suspension method sintered at 730 °C for 1 hour in air.

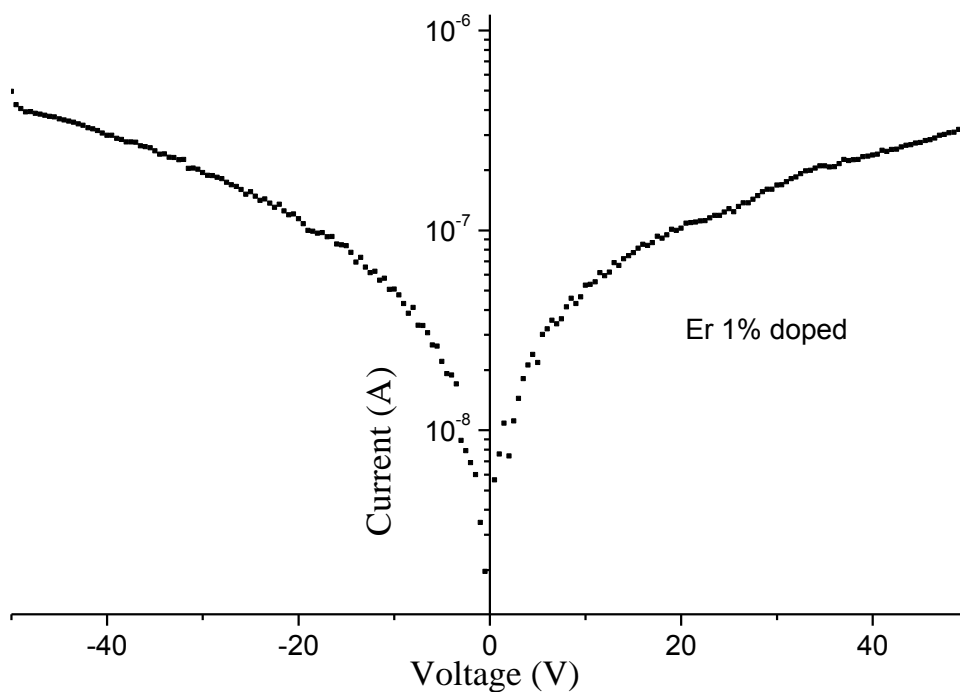


Figure 4.79 The I-V characteristic curve of 1% Er doped PMN thin films obtained suspension method sintered at 730 °C for 1 hour in air.

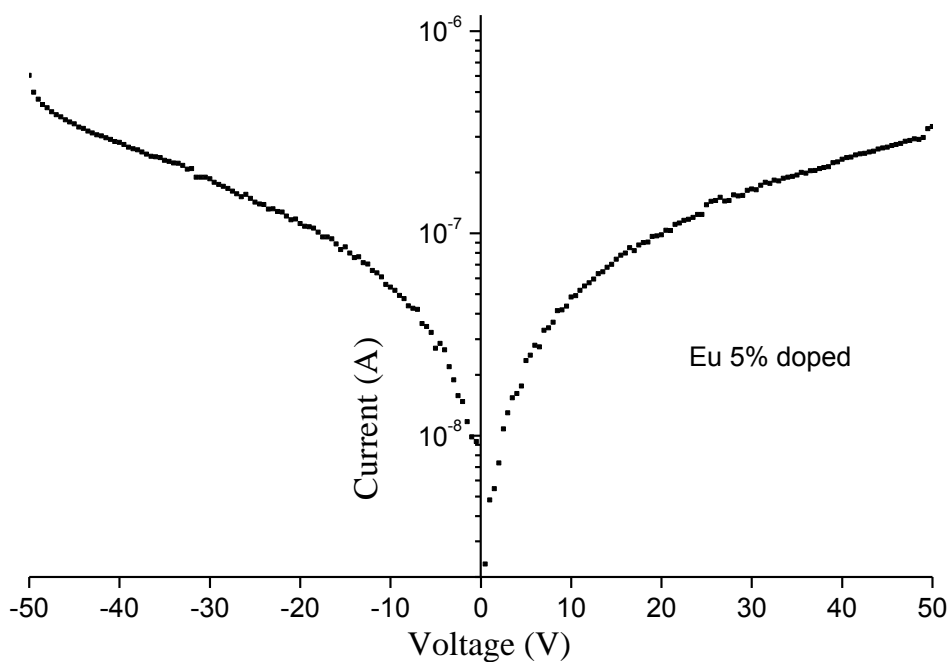


Figure 4.80 The I-V characteristic curve of 5 % Eu doped PMN thin films obtained suspension method sintered at 730 °C for 1 hour in air.

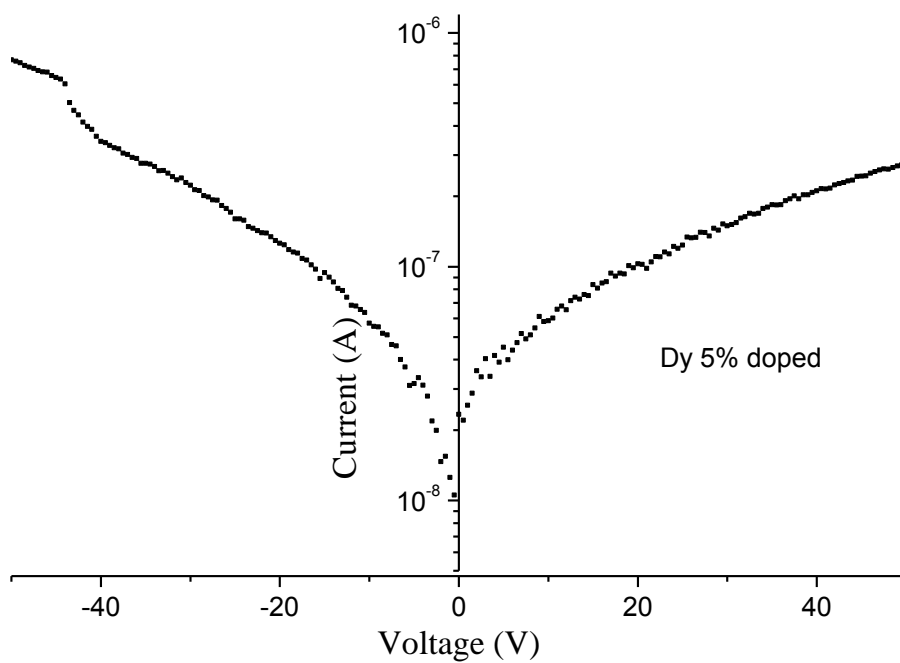


Figure 4.81 The I-V characteristic curve of 5% Dy doped PMN thin films obtained suspension method sintered at 730 °C for 1 hour.

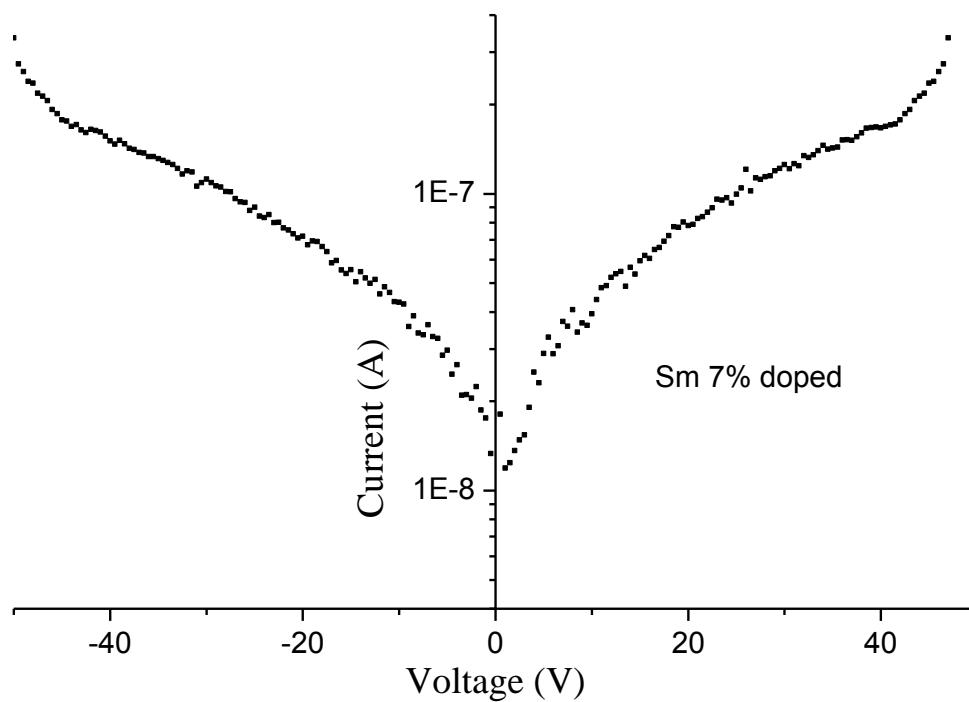


Figure 4.82 The I-V characteristic curve of 7 % Sm doped PMN thin films obtained suspension method sintered at 730 °C for 1 hour.

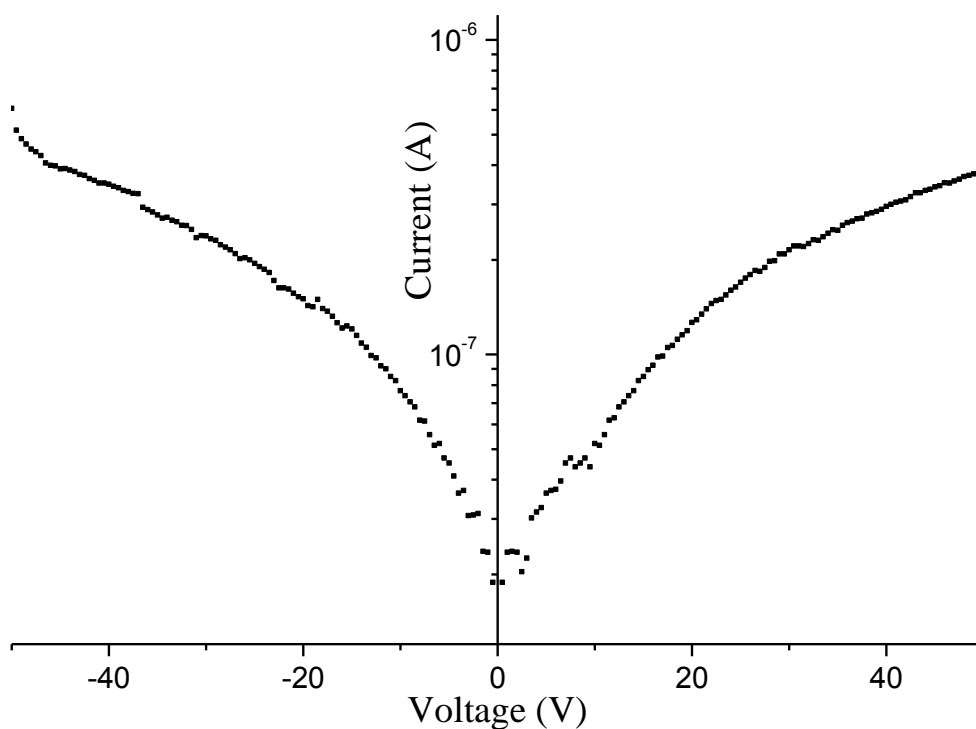


Figure 4.83 The I-V characteristic curve of 1% Tb doped PMN thin films obtained suspension method sintered at 730 °C for 1 hour.

ranges of 49.62-32.15 nA, 56.9-33.7 nA, 76.52-28.15 nA, 33.5-49.75 nA and 60.6-38.4 nA as a function of the applied voltage between -50 V and +50 V, respectively. When the series resistance is low, the I-V curves yield a straight line over a longer ranges. The series conductivity leads to an increase of the voltage across the barrier region.

4.10 Device Applications

The circuit as shown in Figure 4.84 was prepared for measuring charge-discharge time of PMN capacitor. A quick experiment was performed to see whether cantilevers made up of PMN based coatings resonate or not, indicate their dielectric properties. Figure 4.85 presents the resonance spectrum, measured by an TT T-ECHNI-C Oscilloscope MOS-620CH (20MHz), one side of a square piece of Ag-electroded PMN films. The width of the capacitor piece is 1 mm x 1 mm and the thicknesses of the successive layers were configured like Ag(10 μm)/PMN (<1 μm)/Si(520 μm)/Ag(10 μm) architecture.

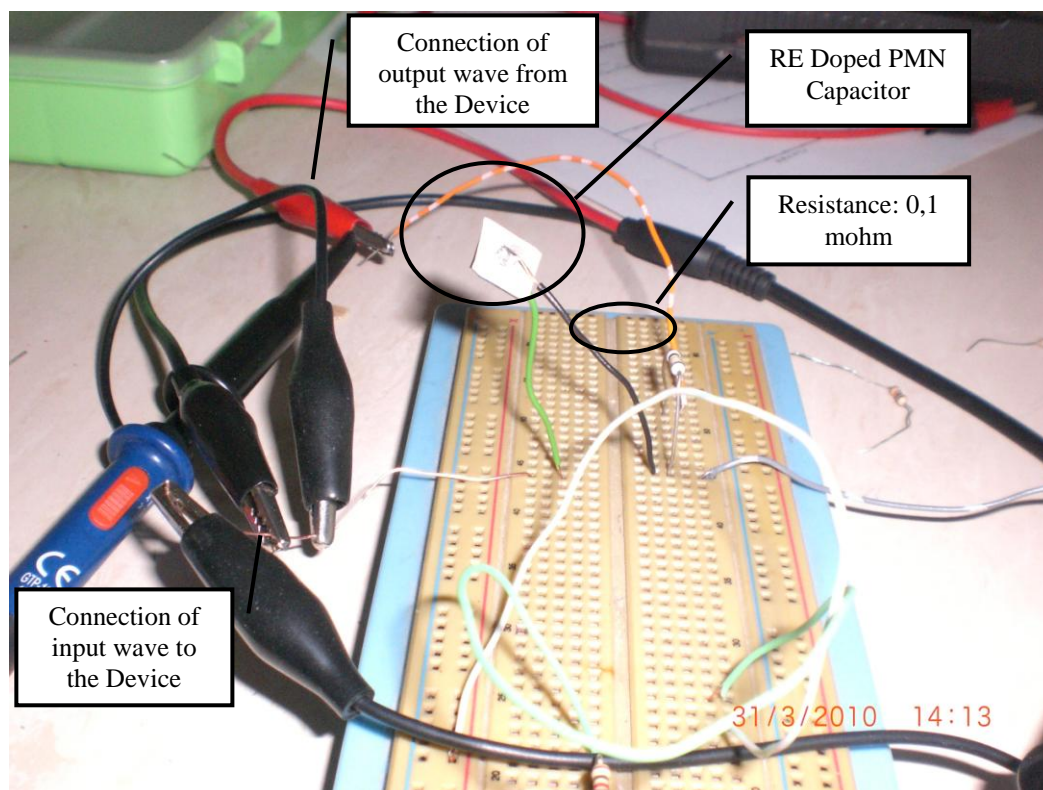


Figure 4.84 R-C device to measure charge-discharge time of PMN capacitor.

It was determined that there were two distinctive resonance peaks, each of which had high quality, as demonstrated in Figures 4.86 and 4.87. The discrepancy between theory and experiment might have come from the error from unfavorable thickness ratios where the thickest layer was the binding Ag paste. Nevertheless, the resonance spectrum of the cantilever indicates that the PMN tape was indeed capacitive behavior under electric voltage generated by the circuit in Figure 4.84 and capable of monitoring resonance peaks.

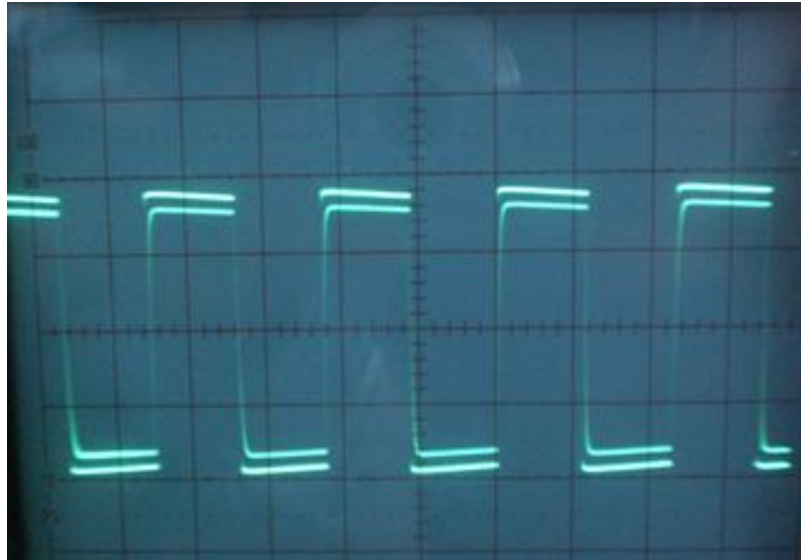


Figure 4.85 Oscilloscope image of PMN capacitor given square wave to the device.

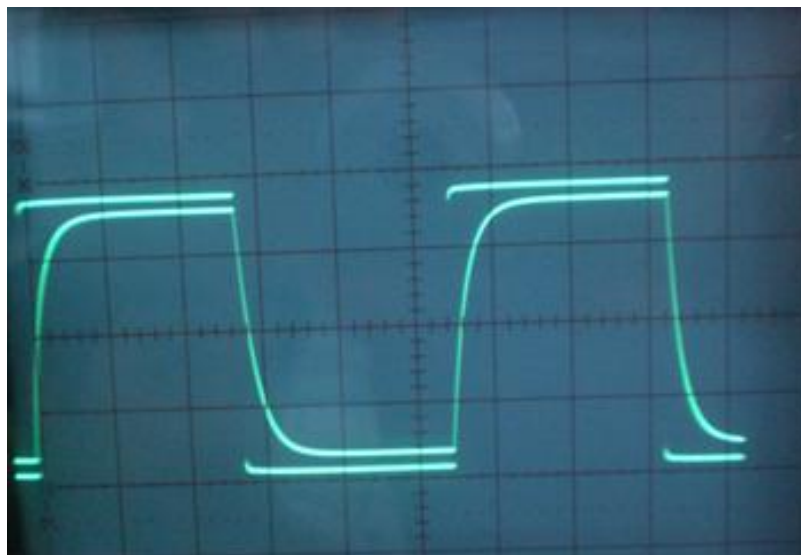


Figure 4.86 Oscilloscope image of output wave for PMN capacitor from the device at 100 Hz.

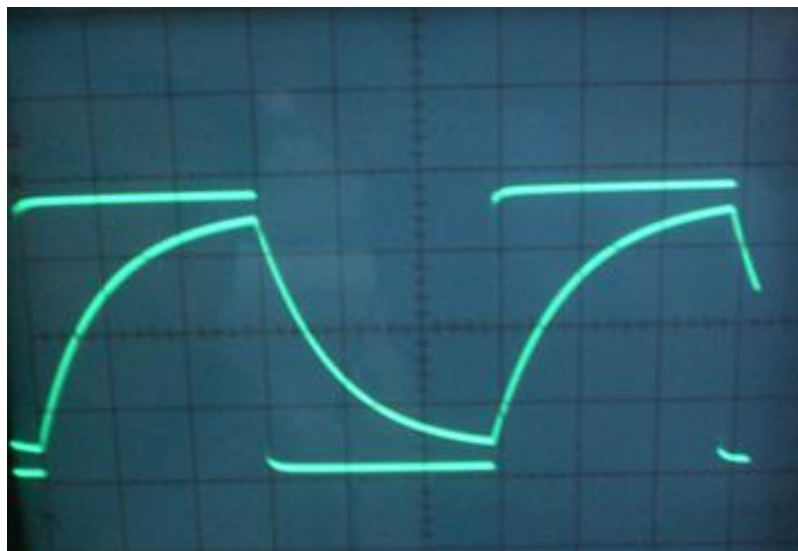


Figure 4.87 Oscilloscope image of output wave for PMN capacitor from the device at 10 kHz.

Figure 4.85 depicts a square wave given to the device. Given a square wave, the upper part wave shows the fill of the capacitor, the lower part shows the drain. The obtained resonans waves of PMN capacitors were shown in Figures 4.86 and 4.87 at 100 Hz and 10 kHz respectively. As can be seen Figures 4.86 and 4.87, whilst the upper parts of the peaks show that the capacitor charged, the bottom parts of the peaks point out that capacitor discharged. The peak distance between two peaks can be calculated charge-discharge time using following Equation 4.5 (WEB_4):

$$T = \frac{1}{RC} = 17 \text{ ms}^{-1} \quad t=17 \text{ ms} \quad (4.5)$$

4.10.1 Example Circuit Diagram

4.10.2 Camera Flash Circuit

After battery is contacted the circuit and turning the switch on, the circuit is in stand by position. If our LED lights, the capacitor is charged and flash is ok for flashing. After that the flashing become with the circuit contact with camera or control switch. Flashing time is illustrated in Figure 4.88. It can be noted that as LED bulb can be seen in the system showing that the capacitor is discharged. Afterwards,

the flashing finish was illustrated in Figure 4.89 and the capacitor charges again and LED lights again. In original circuit, 300 V and 150 μF capacitor was used. With this capacitor, flashing is very well and better than our product, but charging time of this commercial capacitor is very long. It was found that the flashing is not enough with our capacitor, however charging time is too short compared with commercial capacitor.

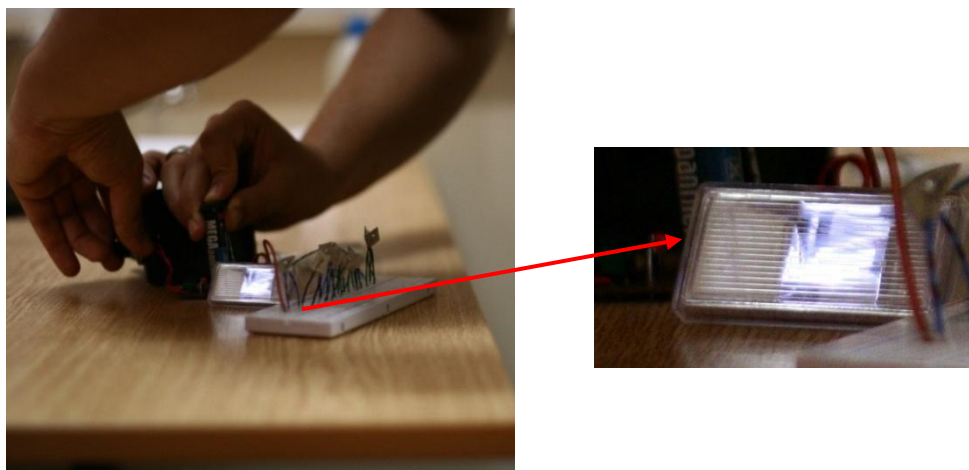


Figure 4.88 Flashing time.

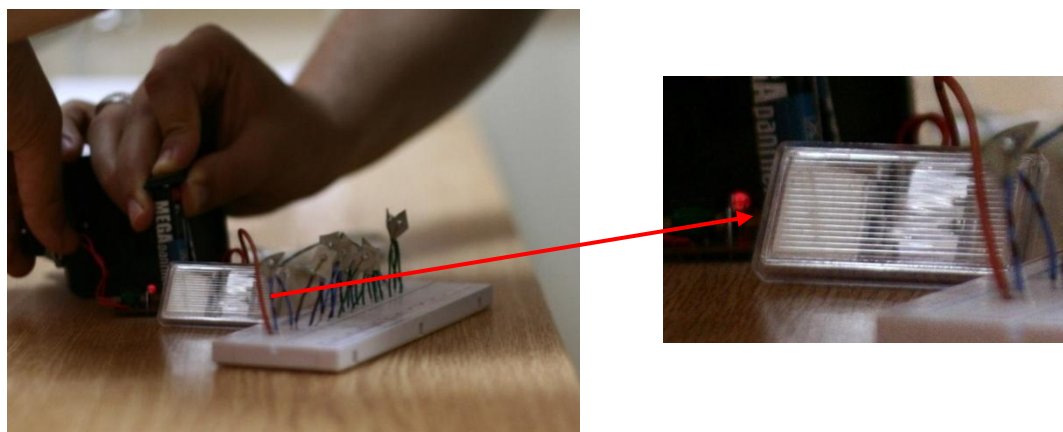


Figure 4.89 Circuit in stand by position.

4.10.3 Durability of the production

Keeping the process parameters on stable levels is always important to have standard products. In the data recording, the process performance provides durability of production. For capacitor production, quantity and properties of precursors in sol-

gel process, stable gelling time, oven regime, milling time and rate, quantity of solvent and powder addition to prepare colloidal suspension, properties of wafers, coating process, sintering time and hygiene conditions of production process are the most important parameters. Optimization of these parameters is required to standardization.

CHAPTER FIVE

CONCLUSION AND FUTURE PLAN

Summarizing the results of this thesis, pure, Er, Eu, Dy, Sm and Tb doped PMN thin films were successfully and separately synthesized on glass and Si substrates from the sol-gel derived PMN powders obtained the solutions prepared from Pb, Mg, Nb, Er, Eu, Dy, Sm and Tb based precursors, solvents and chelating agent for thin film capacitor applications. The summarized results can be outlined as follows:

- 1) In solution characteristics, pH, turbidity and rheological properties of PMN based solutions were obtained. The pH values of the solutions were found to be in the range of 5.85 and 6.00, exhibiting an acidic character which influences hydrolysis, condensation and complexation reactions in the solutions. Powder based precursors are completely dissolved because turbidity value approaches to 0 ntu. Turbidity value of the solutions was measured as 8.42 ntu. The viscosity of PMN ideal solution was measured as a function of time for different temperatures. The increasing temperature caused a gradual decrease in viscosity value. Solution exhibits continuously tendency of formation gel network depending on time. Very interesting gelling behavior was observed to be directly related to the content of RE⁺³ doping.
- 2) For the process optimization, two type heat treatment regimes were suggested to produce very pure perovskite and textured PMN based materials such as powders and films as a combination of DTA-TG, FTIR and XRD results. The sintering condition of PMN based powders was chosen as follows: a temperature of 950 °C, a time period of 2 hours, and a furnace environment from air. The annealing condition of PMN based thin films was the following procedure: a temperature of 730 °C, a time period of 1 hour, and a furnace environment from air.

- 3) In order to produce nano-scale powders, the ball milling was developed and applied to doped PMN powders. Nano scale PMN based powders stimulated the intensive research, improvement and development in order to realize very good surface qualities of the thin films and very good electrical properties.
- 4) The surface topographies and characteristics of PMN films on Si substrates were examined by using SEM and AFM. PMN based films annealed at 730 °C have different surface structures. It was deduced that it is possible to obtain PMN films having well-oriented, crack-free, continuous and homogeneous microstructure. At higher annealing temperatures, abnormal grain growth and the formation of a second phase (pyro) initiated in the PMN based coatings. In addition, the particle size of PMN has an influence on the coating stability, micro-PMN were worse coated than the smaller nano-PMN particles. The Mg/Nb ratios for submicron-sized aggregated nano scaled-PMN particles are much higher than those of a micro-PMN particle indicating that the coating of PMN layer is better for fine PMN particles than large particles.
- 5) A novel suspension method was developed for low-temperature sinterable PMN ceramics near the morphotropic phase boundary. Submicron-sized crystalline PMN was well suspended in a methyl alcohol solution. The PMN precursor powder derived from such solution can be sintered as low as 950°C. This method could be very useful for processing low-temperature co-fired dielectric and piezoelectric ceramics. In the case of niobium-containing perovskites it is necessary to avoid the formation of pyrochlore-type phases if reproducible and optimum mechanical, dielectric and piezoelectric properties are to be achieved as a combination of DTA-TG, FTIR, XRD and SEM-EDS.
- 6) A sol-gel method is developed for RE-doped PMN thin films, using methyl alcohol as the only solvent. RE-doping significantly increases the gelation rate of PMN in methyl alcohol solution and forms colloidal particles in the solution. These particles may have caused inhomogeneity in the thin films and making them more conductive. The dopant also decreases the tetragonality of the derived PMN powder and thin films can be easily

obtained with pure perovskite phase on Si substrates, at temperatures lower than the T_c of bulk PMN materials. The Si substrate substantially reduces the tetragonality of the PMN thin films, compared with that of PMN powders. PMN thin films on Si wafer are more insulative than that on glass substrates. The PMN thin films annealed at 730°C for 1 hour had electrical properties comparable with literature reported data. On the other hand, pure perovskite PMN cannot be easily crystallized from its solution in methanol, making it hard to directly synthesize PMN thin film. The sol-gel process proved to be a good and simple way to make PMN ferroelectric thin films. This sol-gel method was crucial for subsequent PMN processing.

- 7) Both as a coating model and with practical applications in PMN synthesis, PMN coating behavior on Si surface was studied. The fact that PMN can indeed be coated on Si surface indicates that the coating is more due to Coulomb attraction rather than van der Waals interactions. Experimental results also show that core particle size is also important: nanometer-sized core particles are easier to deposit than micron-sized ones. Nano-sized PMN particles further decrease the calcining temperature to about 730°C, in term of its high surface energy and reactivity.
- 8) Using PMN powder synthesized by coating on Si surfaces, PMN precursor suspension was made by dispersing the PMN powder in methanol solution. PMN precursor powder generated from the suspension could be sintered at 730°C for 1 hour, about 500°C lower than conventional oxide processing methods. The lower sintering temperature was found to be related to the unique microstructure in the PMN precursor powder, where crystalline, (sub)micron-sized PMN powder was well mixed with amorphous, nano-sized PMN powder. While the PMN precursor powder derived from the suspension method could be sintered as bulk ceramics, PMN thick film directly deposited from the suspension could not be well sintered on Si wafer and glass substrates up to their applicable temperatures (800°C). Glass was a better substrate than Si wafer, even though PMN films on both substrates showed

dielectric and optical properties much higher than their bulk counterparts. Substrates pose two challenging issues: (1) thermal expansion between the film and substrate may crack the film; (2) inter-diffusion between the substrate and film limiting the highest firing temperature for the film.

- 9) Surface roughness of PMN films annealed at 730 °C changed between 150 nm and 175 nm. It was found that surface roughness and depth of PMN thin films increase with RE dopants.

- 10) It was determined that Young's modulus and Dynamic hardness values of pure PMN based coating are 5.76 GPa and 11.56 DHV, respectively. Young's modulus values of 1 % Er, 5 % Eu, 5 % Dy, 7 % Sm and 1 % Tb doped PMN based coatings for chosen optimum samples are 4.71 GPa, 4.07 GPa, 7.64 GPa, 12.19 GPa and 7.63 GPa respectively. It was found dynamic hardness values of optimum 1 % Er, 5 % Eu, 5 % Dy, 7 % Sm and 1 % Tb doped PMN based coatings for chosen optimum samples are 3.69 DHV, 3.76 DHV, 15.12 DHV, 21.37 DHV and 7.66 DHV, respectively. The adhesion strength of the films increases from 98 MPa to 248 MPa depending on heat treatment temperature and critical force increase.

- 11) It was found that the refractive index, thickness and band gap ranges of PMN based thin films were 1.30-1.51 nD, 0.225-2.184 μm and 2.4-4.1 eV, respectively.

- 12) Dopants that have a strong effect in the dielectric properties of PMN based materials are Er, Eu, Dy, Sm and Tb. It has been reported that doping increases resistance by increasing the reactions in the system. The formation of the reaction between RE and PMN system reduces the concentration of oxygen vacancies. When added in small amounts RE ions can occupy the A (Pb) site, the B (Mg-Nb) or both sites together depending on the stoichiometry of the perovskite system. The addition of RE may suffer the tightening of the lattice structure when the smaller RE^{3+} replaces Pb^{+4} . Using the powder prepared from the precursor suspension method, PMN films were

made with giant dielectric constant responses comparable to that of other previous fabricated PMN ceramics.

- 13) There is a need to remove the substrates and synthesize freestanding PMN films. Drop and spin coating involving organic ligands and dispersant is used very effectively to produce freestanding polycrystalline PMN thin layers with high dielectric constant. We produced polycrystalline films of PMN thin layers that have d_{33} of about ~ 30000 at 0.1 Hz for 0.1 Vrms, higher than that of commercial PMN single crystals. As a result, we have solved the problem of producing ferroelectric ceramics with high dielectric coefficients using a unique suspension coatings approach. The as-obtained PMN films are characterized by virtue of their phase, morphology, optical, mechanical, dielectric, and electrical properties. Dielectric measurement suggests that there is a thickness dependence of the PMN films.

- 14) It was found that, at low voltages, the forward current of the coatings increases exponentially with applied voltage like diode. The device indicates a rectifying behavior between PMN and doped PMN on Si semiconductor substrates. The nanoscaled thin films of PMN/n-Si junctions behave like a Schottky barrier diodes at low voltages. RE addition is decreased the resistance value and makes the capacitor more conductive. The obtained series current is an important factor in performance of the diode characterized PMN coatings and affects current-voltage characteristic of the capacitor coatings. The current values of Er, Eu, Dy, Sm and Tb doped PMN capacitors were found to be in the ranges of 49.62-32.15 nA, 56.9-33.7 nA, 76.52-28.15 nA, 33.5-49.75 nA and 60.6-38.4 nA as a function of the applied voltage between -50 V and +50 V, respectively.

- 15) The circuit was prepared for measuring charge-discharge time of PMN capacitor. The width of the capacitor piece is 1 mm x 1 mm and the thicknesses of the successive layers were configured like Ag(10 μm)/PMN (<1 μm)/Si(520 μm)/Ag(10 μm) architecture. The applicability of the PMN

freestanding films in camera flash applications is demonstrated by making commercial device of conventional camera.

As future plans, pure perovskite PMN can not be easily crystallized from its solution in methanol, making it hard to directly synthesize PMN thin film. It is possible to study a direct synthesis of the PMN thin films to produce PMN nano films and develop dielectric properties of PMN nano sized capacitors. Recently there have been interesting new developments in quantitative imaging of ferroelectric surfaces by Piezoelectric Force Microscopy (PFM). It could be another important tool for the microstructure characterizations of piezoelectric films in the future.

To define the exact nature of interlayers of the PMN/Si substrate and PMN/glass, their structural and mechanical properties should be clarified in the thickness range of 0.1~1 μm with help of structural characterization methods such as synchrotron, AFM and then correlated them to the corresponding property measurements. Well defined dimension and boundary conditions for the miniature samples are crucial. In situ experiments of Raman spectroscopy may also assist to elucidate the reasons for the giant piezoelectric response in these films. Even smaller capacitor with PMN thin films as thin as 100 nm can be produced and tested their capacity in electronics for other applications. The limit to thickness by thin films is probably 100 nm.

REFERENCES

- Ahn, K. H., Kim S. S., & Baik, S. (2003). Thickness dependence of leakage current behavior in epitaxial (Ba,Sr)TiO₃ film capacitors. *Journal of Applied Physics*. 93 (3). pp. 1725-1730.
- Ak, N. F. (2008). *Production of Hydroxyapatite Coating by Sol-Gel Technique on 316l Stainless Steel and Its Corrosion Properties*, PhD Thesis, Dokuz Eylul University.
- Albina, A. (2007). Influence of Carbonaceous Electrodes on Capacitance and Breakdown Voltage for Hybrid Capacitor. *Microelectronics Journal*, 38(4-5), 642-648.
- Alexandrov, P., Koprinarova J., & Todorov, D. (1996). Electrical and Dielectric Properties of Thin r.f. Sputtered TiO₂ vs. Deposition Conditions. *In 9th International School on Condensed Matter Physics*, Varma, Bulgaria: World Scientific.
- Almeida, R. M., & Marques, A. C. (2004). *Characterization of Sol-gel Materials by Infrared Spectroscopy*. In R. M. Almeida, (Volume II.). *Handbook of sol-gel science and technology: processing characterization and applications, characterization and properties of sol-gel materials and products*. (65-90), USA, Kluwer academic, Publishers: Springer.
- Ananta S., & Thomas N. W. (1999). Relationships between Sintering Conditions, Microstructure and Dielectric Properties of Lead Magnesium Niobate. *Journal of the European Ceramic Society*, 19, 629-635.
- Aparicio, R., & Hajimiri, A. (2002). Capacity Limits and Matching Properties of Integrated Capacitors. *IEEE Journal of Solid-State Circuits*, 37(3), 384-393.

- Araki, T., & Hirabayashi, I. (2003). Review of a Chemical Approach to $\text{YBa}_2\text{Cu}_3\text{O}_{7-x}$ Coated Superconductors-metalorganic Deposition using Trifluoroacetates. *Supercond. Sci. & Technol.* 16 R71–R94, PII: S0953-2048(03)25365-3.
- Babooram K., Tailor H., & Ye Z.G. (2004). *Phase Formation and Dielectric Properties of 0.90Pb(Mg_{1/3}Nb_{2/3})O₃-0.10PbTiO₃ Ceramics Prepared by a New Sol-gel Method.* 30, *Ceramics International*, 1411-1417.
- Beltra'n, H., et al. (2000). Sol-Gel Synthesis and Characterization of $\text{Pb}(\text{Mg}_{1/3}\text{Nb}_{2/3})\text{O}_3$ (PMN) Ferroelectric Perovskite. *Chem. Mater.*, 12, 400-405.
- Bergstrom, L. (1997). Hamaker Constants of Inorganic Materials. *Advances in Colloid and Interface Science*, 70, 125-169.
- Bhat, V.V., Angadi, B., & Umarji, A.M. (2005). Diffuse Ferroelectric Phase Transitions in Pb-substituted $\text{PbFe}_{12}\text{Nb}_{12}\text{O}_3$. *Mater. Sci. & Eng. B.* 131, 116.
- Blackman, K.A. (1996). *Processing of Non-Aqueous Tape Cast Ceramic Layers*, MSc. Thesis, University of Illinois at Urbana Champaign.
- Brailenau, A., Ianculescu, A., Zaharescu, M., Pasuk, I., Preda, S., Madarasz, J., et. al. (2004). Phase Formation Study of La-Modified Lead Magnesium Niobate. *Key Eng. Materials*, 1309, 26-48.
- Busch, G., & Scherrer, P. (1935). *Eine neue seignette-elektrische Substanz* *Naturwissenschaften.* 23, 737-737
- Chazono, H., & Kishi, H. (2001). *Dc-electrical degradation of the BT-based material for multilayer ceramic capacitor with Ni internal electrode: Impedance analysis and microstructure.* *Japanese Journal of Applied Physics Part 1-Regular Papers Short Notes & Review Papers*, 40, 5624-5629.

- Cheng, S.D., Kam, C.H., Zhou, Y., Que, W.X., Lam, Y.L., Chan, Y.C., et. al. (2000). Sol-gel Derived Nanocrystalline Thin Films of PbTiO_3 on Glass Substrate. *Thin Solid Films*, 375, 109.
- Chiu, Y.S. (2005). *Synthesis and Characterization of Lead Strontium Titanate Thin Films by Sol-gel Method*. Master thesis, Drexel University.
- Choi, J. D., & M.Choi, G. (2000). Electrical and CO gas sensing of layered ZnO-CuO sensor. *Sensor and Actuators. B69*. 120-126.
- Chung, U-J., e.t al. (2002). Abnormal Grain Growth of $\text{Pb}(\text{Mg}_{1/3}\text{Nb}_{2/3})\text{O}_3$ -35 mol% PbTiO_3 Ceramics Induced by the Penetration Twin. *J. Am. Ceram. Soc.*, 85 (12), 3076-80.
- Chung-Hsin Lu, D.P.C. (2000). Reaction Sintering and Characterization of Lead Magnesium Niobate Relaxor Ferroelectric Ceramics. *Journal of Materials Science: Materials in Electronics*, 11, 363-367.
- Cohen-Stuart, M.A., Cosgrove, T. & Vincent B. (1986). Experimental Aspects of Polymer Adsorption of Solid/Solution Interfaces. *Advances in Colloid and Interface Science*, 24, 143-239.
- Culha, O., Ebeoglugil, M. F., Birlik, I., Celik, E., & Toparli, M. (2009). Synthesis and Characterization of Semiconductor Tin Oxide Thin Films on Glass Substrate by Sol-gel Technique, *Journal of Sol-Gel Science and Technology*, 5, 32-41.
- Culha, O., Zor, M., Gungor, M. A., Arman Y., & Toparli, M. (2009). Evaluating the Bond Strength of Opaque Material on Porcelain Fused to Metal Restorations (PFM) Alloys by Scratch Test Method. *Materials and Design*, 30, 3225-3228.
- Damjanovic, D. (1998). Ferroelectric, Dielectric And Piezoelectric Properties Of Ferroelectric Thin Films And Ceramics. *Reports on Progress in Physics*. 61, 1267-1324.

- Daniels, P., & Ihlefeld, J. (2007). Smart Electrodes for Large Area Thin Film Capacitors, North Caroline State University-Department of Materials Science and Engineering *Dupont Electronic Technologies*. 1-13.
- Dao, M., Chollacoop, N., Van Vliet, K. J., Venkatesh, T. A., & Suresh, S. (2001). Computational modeling of the forward and reverse problems in instrumented sharp indentation, *Acta materials*, 49, 3899–3918.
- Dechakupt, T. (2008). *Influence of Substrate Microstructure on The High Field Dielectric Properties of BaTiO₃ Films*. Ph.D. Thesis, Penn State University.
- Deliormanli A. M., Celik E., & Polat M. (2007). The Isoelectric Point of Lead Magnesium Niobate. *J. Am. Ceram. Soc.*, 90, 3314–3317.
- Deliormanli, A.M. (2007). *Effect of Colloidal Interactions in the Forming of Lead Magnesium Niobate Ceramics*, (Master) Thesis, Izmir Institute of Technology.
- Deliormanli, A.S., Celik, E., & Polat, M. (2009). Preparation of the Pb(Mg_{1/3}Nb_{2/3})O₃ Films by Aqueous Tape Casting. *Journal of the European Ceramic Society*, 29, 115–123.
- Deliormanlı-Şakar, A., & Çelik E. (2008). Phase Formation and Microstructure of Nd⁺³ Doped Pb(Mg_{1/3}Nb_{2/3})O₃ Prepared by Sol-gel Method. *Journal of Material Sci. Mater. Electron* 19, 577-583.
- Dietz, G. W., Schumacher, M., Waser, R., Streiffer, S. K., Basceri, C., & Kingon, A. I. (1997). Leakage currents in Ba_{0.7}Sr_{0.3}TiO₃ thin films for ultrahigh density dynamic random access memories. *Journal of Applied Physics*, 82, 2359-2364.

- Ding, Y. Jin, C. & Meng, Z. (2000). Investigation on the Amorphous–Crystalline Transition and Microstructure of Sol-gel Derived $(\text{Ba}_{1-x}\text{Sr}_x)\text{TiO}_3$ Thin Films. *Materials Research Bulletin*, 35(7), 1187-1193.
- Dong-Hwan, S., et al. (2001). Dielectric Properties of the Perovskite System $\text{Pb}(\text{Mg}_{1/3}\text{Nb}_{2/3})\text{O}_3$ – PbTiO_3 Modified by $\text{Pb}(\text{Mg}_{1/3}\text{Ta}_{2/3})\text{O}_3$ and $\text{Pb}(\text{Zn}_{1/3}\text{Nb}_{2/3})\text{O}_3$. *J. Am. Ceram. Soc.*, 84(6), 1281-1285.
- Ebeoğlugil, M. F., Çulha, O., Çelik E., & Toparlı, M. (2010). Production And Indentation Analysis of $\text{Pb}(\text{Mg}_{1/3}\text{Nb}_{2/3})\text{O}_3$ Capacitor Coatings. *13th International Materials Symposium (IMSP'2010)*, Denizli, Turkey.
- Es-Souni, M., Zhang, N., Iakovlev, S., Solterbeck, C. H., & Piorra, A. (2003). Thickness and Erbium Doping Effects on the Electrical Properties of Lead Zirconate Titanate Thin Films. *Thin Solid Films*. 440.
- Fowler, R. H., & Nordheim, L. (1928). *A-Containing Papers of a Mathematical and Physical Character*. Proceedings of the Royal Society of London Series, 119, 173-181.
- Fujihara, S., Sasaki, C., & Kimura, T. (2001). Crystallization behavior and origine of c-axis orientation in sol-gel derived $\text{ZnO}:\text{Li}$ thin films on glass substrates. *Applied Surface Science*, 180, 341-350.
- Gentil, S., Damjanović, D., & Setter, N. (2004). $\text{Pb}(\text{Mg}_{1/3}\text{Nb}_{2/3})\text{O}_3$ and $(1-x)\text{Pb}(\text{Mg}_{1/3}\text{Nb}_{2/3})\text{O}_3$ – $x\text{PbTiO}_3$ relaxor ferroelectric thick films: processing and electrical characterization. *J. Electroceram.*, 12, 151–161.
- Gu, H. (2004). *Processing of $\text{Pb}(\text{Mg}_{1/3}\text{Nb}_{2/3})\text{O}_3$ – PbTiO_3 by a Novel Coating Approach*, PhD Thesis, Drexel University.
- Güçlü, N. et al. (2006). Depth-Sensing Indentation Study of Superconducting MgB_2 Wire. *Material Characterization*, 57, 166-170.

- Hesselink, F. T., Vrij, A., & Overbeek, J. T. G. (1971). On the Theory of Stabilization of Dispersions by Adsorbed Macromolecules: II Interaction between Two Flat Particles". *Journal of Physical Chemistry*, 75(14), 2094-2103.
- Hiemenz P.C. (1997). *Principles of Colloid and Surface Chemistry*. 3, Marcel Dekker, INC. New York: Basel.
- Hill, J. O. (1991). *For Better Thermal Analysis And Calorimetry*. 3 Canada: International Confederation for Thermal Analysis.
- Holmberg, K., Shah, D. O., & Schwuger, M. J. (2002). *Handbook of Applied Surface and Colloid Chemistry*. 2, John Wiley and Sons.
- Hsi, C.S. et al. (2003). Dielectric Properties of Nanocrystalline Barium Titanate Thin Films Deposited by RF Magnetron Sputtering. *Jpn. J. Appl. Phys.*, 1(42),544-548. <http://www.ceramics.org/ASSETS/6FBA4EED52CF4B07AAD76C6ABCF1C39A/HistoryoftheFirstFerroelectricOxideBaTiO3.pdf>.
- Hunter, R.J. (1995). *Foundations of Colloid Science*, Oxford: UK.
- Hwang, C. S., Lee, B. T., Kang, C. S., Lee, K. H., Cho, H., Hideki, JH., et. al. (1999). *Journal of Applied Physics* 85, 287-295.
- Israelachvili, J. (1991). *Intermolecular & Surface Forces*, Academic Press Limited, San Diego.
- Itagaki, M. et al. (2007). Impedance analysis on electric double layer capacitor with transmission line model. *Journal of Power Sources*, 164(1) 415-424.
- Jaffe, B., Cook, W. R., & Jaffe, H. (1971). *Piezoelectric Ceramics*. Academic Press, London, New York.

- Jillavenkatesa, A., Dapkunas, S. J., & Lin-Sien, L. (2001). *Particle Size Characterization*. NIST Special Publication 960-1.
- Kao, K. C. (2004). Dielectric phenomena in solids. *Elsevier Academic Press*, San Diego.
- Kasap, S., & Capper, P (2006). *Handbook of Electronic and Photonic Materials*. New York: NY.
- Kayatekin, I. (2006). *Synthesis And Characterization Of Buffer Layers And $YBa_2Cu_3O_x$ Superconducting Coatings By Chemical Solution Deposition Method*, MsC Thesis, Dokuz Eylul University.
- Kelly, J., Tantigate, C., & Safari, A. (1997). Effect of Composition on the Electromechanical Properties of $(1-x)Pb(Mg_{1/3}Nb_{2/3})O_3-xPbTiO_3$ Ceramics. *J. Am. Ceram. Soc.* 80(4). 957–964.
- Kim, N., & Jang, S. J. (1991). T.R. Shrout, in Proceedings of the 1990. *IEEE International Symposium on Applications of Ferroelectrics*, 605–609.
- Kim, T. G. et al. (2003). Crystallinity Dependence of Microwave Dielectric Properties in $(Ba, Sr)TiO_3$ Thin Films. *Jpn. Journal of Applied Physics*, 42, 1315-1319.
- King, A. G. (2002). *Ceramic Technology and Processing*. 528. 20-55. Publisher: Noyes.
- Kong, L. B., Ma, J., Zhu, W., & Tan O. K. (2002). Translucent PMN and PMN-PT ceramics from high-energy ball milling derived powders. *Materials Research Bulletin* 37, 23-32.

- Kong, L. B., Ma, J., Zhu, W., & Tan O. K. (2002). Rapid formation of lead magnesium niobate-based ferroelectric ceramics via a high-energy ball milling process. *Materials Research Bulletin*, 37, 459-465.
- Kwon, S. S. E., & Messing, GL. (2001). Low-temperature reactive sintering of 0.65PMN-0.35PT. *Journal of the American Ceramic Society*. 84 (3). 648-650.
- Laughlin, B., Ihlefeld, J., & Maria, J. P. (2004). TEM and Electrical Analysis of Sputtered Barium Strontium Titanate (BST) Thin Films on Flexible Copper Substrates. *MRSS proceedings on ferroelectric thin films XII*, 784, 301–306.
- Levi, R. D. (2009). *Solid Solution Trends That Impact Electrical Design of Submicron Layers in Dielectric Capacitors*. PhD Thesis, The Pennsylvania State University.
- Lewis, J. A. (2000). Colloidal Processing of Ceramics. *Journal of the American Ceramic Society*, 83, (10), 2341-59.
- Lewis, J. A. (2006). Direct Ink Writing of 3D Functional Materials. *Advanced Functional Materials*. 16, 2193-2204.
- Li, T. (1998). Single Crystals of PMN-35PT from Polycrystalline Precursors. *J. Am. Ceram. Soc.*, 88(1), 244.
- Li, T. (1999). Heteroepitaxial growth of bulk single-crystal PMN-32 mol % PbTiO₃ from (111) SrTiO₃. *Journal of Materials Research*. 31-89.
- Lin, T.N., et al. (2005). Microstructure and Dielectric Properties of Sputtered (Ba_{0.3}Sr_{0.7})TiO₃ Thin Films with Amorphous Interfacial Layers. *Japanese Journal of Applied Physics*, 44(7A). 5049-5054.

- Liu, Y. L., Liu, Y. C., Liu, Y. X., Shen, D. Z., Lu, Y. M., Zhang, J. Y., et. al. (2002). Structural and optical properties of nanocrystalline ZnO films grown by cathodic electrodeposition on Si substrates. *Physica B: Condensed Matter* 322, 31-36.
- Lu, H.C. et al. (1999). Structural Properties of Thin Films of High Dielectric Constant Materials on Silicon. *Microelectronic Engineering*, 48(1), 287-290.
- Lufrano, F., Staiti, P., & Minutoli, M. (2003). Evaluation of nafion based double layer capacitors by electrochemical impedance spectroscopy. *Journal of Power Sources*, 124(1), 314-320.
- Luo, H. (2005). *Colloidal Processing of PMN-PT Thick Films for Piezoelectric Sensor Applications*, PhD in Drexel University.
- Ma, J., Zhang, R., Liang, C.H., & Weng, L. (2003). Colloidal Characterization and Electrophoretic Deposition of PZT. *Materials Letter* 57, 4648-4654.
- Marcott, C. (1998). *Infrared Spectroscopy*. In R. E. Whan, (Ed.). ASM Metals Handbooks: 10, materials characterization (5), (239-241). USA: ASM International.
- Maria, J.P. (2005). Preparation of sputtered $(\text{Ba}_{1-x}, \text{Sr}_x)\text{TiO}_3$ thin films directly on copper. *Journal of the American Ceramic Society*. 88(9). 2652.
- Morita K., Mizuno, Y., Chazono, H., Kishi, H., Yang, G. Y., Liu, W. E., et.al. (2007). Electric Conduction of Thin-Layer Ni-Multilayer Ceramic Capacitors with Core-Shell Structure BaTiO_3 . *Japanese Journal of Applied Physics. Part 1- Regular Papers Brief Communications & Review Papers* 46, 2984-2990.
- Morito, K., & Suzuki, T. (2005). Effect of internal residual stress on the dielectric properties and microstructure of sputter-deposited polycrystalline $(\text{Ba}, \text{Sr})\text{TiO}_3$ thin films. *Journal of Applied Physics*, 97, 104107-1 - 104107-5.

- Moulson, A. J., & Herbert, J. M. (2003). *Electroceramics, Materials, Properties, Applications*. (2). Wiley: Chichester.
- Moya, J.S., Lopez-Esteban, S., & Pecharromás, C. (2007). The Challenge Of Ceramic/Metal Microcomposites And Nanocomposites. *Progress in Materials Science*, 52(7), 1017-1090.
- Myers, D. (1999). *Surfaces, Interfaces and Colloids Principles and Applications*. John Wiley and Sons.
- Nagata, H., Ko, S. W., Hong, E., Randall, C. A., & Trolrier-McKinstry, S. (2006). Microcontact Printed BaTiO₃ and LaNiO₃ Thin Films for Capacitors. *Journal of the American Ceramic Society*, 89(9), 2816-2821.
- Napper, D.H. (1977). Steric Stabilization. *Journal of Colloid and Interface Science*, 58(2), 390-407.
- Netz, R.R. & Andelman, D. (2003). Neutral and Charged Polymers at Interfaces. *Physics Reports*. 380, 1-95.
- Newnham, R. E. (1975). *Structure-Property Relations*. Berlin: Springer-Verlag.
- Nielsen, M.C. et al. (1998). Composite and multilayered TaO_x-TiO_y highdielectric constant thin films. Components, Packaging, and Manufacturing Technology, Part B: Advanced Packaging, *IEEE Transactions on [see also Components, Hybrids, and Manufacturing Technology, IEEE Transactions on]*, 21(3).274-280c.
- O'Dwyer, J. J. (1973). *The Theory of Electrical Conduction and Breakdown in Solid Dielectrics*. Clarendon, Oxford.

- Ogden, A. L. (1996). *The Influence of Nonadsorbed Polymer on the Behavior of Weakly Flocculated Suspensions*. PhD Thesis, University of Illinois at Urbana Champaign.
- Oliver, W.C., et al. (1992). An Improved Techniques for Determining Hardness and Elastic Modulus Using Load and Displacement Sensing Indentation. *Journal of Materials Research*, 7, 1564- 1583.
- Overbeek, T. J. H., (1977). Recent Developments in Understanding of Colloid Stability. *Journal of Colloid and Interface Science*. 58(2). 408-422.
- Park, S. (1997). Ultrahigh strain and piezoelectric behavior in relaxor based ferroelectric single crystals. *J. Appl. Phys.* 82(4). 1804~1811.
- Pashley, R. M., & Karaman, M.E. (2004). *Applied Surface and Colloid Chemistry* Wiley and Sons, printed in U.K.
- Pecharroman, C., et al. (2001). New Percolative BaTiO₃-Ni Composites With A High And Frequency-Independent Dielectric Constant (Epsilon (R) Approximate To 80,000). *Advanced Materials*, 13(20), 1541-1544.
- Pierre, A. C. (1998). *Introduction to Sol-gel Processing*, Publisher: Kluwer Academic.
- Polat, M., & Polat H. (2000). A Review of the Theory of Interactions between Particles Dispersed in Aqueous Media, II. Vander Waals Interactions. *Ore Dressing*, 3, 21-48.
- Prume, K., et al. (2002). Modelling and numerical simulation of the electrical, mechanical, and thermal coupled behaviour of Multilayer capacitors (MLCs). *Journal of the European Ceramic Society*, 22(8), 1285-1296.

- Rahaman, M. N. (1995). *Ceramic Processing and Sintering*. Marcel Dekker Inc., USA.
- Randall, C. A., Newnham, R. E., & Cross, L. E. (2004). *History of the First Ferroelectric Oxide BaTiO₃*. Materials Research Institute The Pennsylvania State University.
- Reddy, Vayunandana, Y. K., & Mergel, D. (1997). Frequency And Temperature-Dependent Dielectric Properties Of Batio₃ Thin Film Capacitors Studied By Complex Impedance Spectroscopy. *Physica B: Physics of Condensed Matter*, 391(2), 212-221.
- Reed, J. S. (1995). *Principles of Ceramic Processing. Chapter 26, Tape Casting*, Wiley: USA.
- Rezvan, K. (2005). *ProteinTreated Aqueous Colloidal Oxide Particle Suspensions: Driving Forces for Protein Adsorption and Conformational Changes*, PhD Thesis, Swiss Federal Institute of Technology.
- Sabolsky, E. M. (2001). Kinetics of Templated Grain Growth of 65PMN-35PT. *Journal of Am. Ceramic Soc.* 84(11), 2507.
- Sato, T., & Ruch, R. (1980). *Stabilization of Colloidal Dispersions by Polymer Adsorption*. 9, Surfactant Science Series, Marcel Dekker: USA.
- Sergei, V., & Kalinin, D.A.B. (2002). Imaging mechanism of piezoresponse force microscopy of ferroelectric surfaces. *Phys. Rev. B*, 65, 125408.
- Shaw, D.J. (2003). *Introduction to Colloid and Surface Chemistry*. Butterworth-Heinemann, Elsevier science: printed in Great Britain.

- Shaw, T. M., Trolier-McKinstry, S., & McIntyre, P.C. (2000). The Properties of Ferroelectric Films at Small Dimensions. *Annual Review of Materials Science*, 30, 263-298.
- Stamate, M. D. (2003). On the dielectric properties of dc magnetron TiO₂ thin films. *Applied Surface Science*, 218(1), 318-323.
- Stumm, W. (1992). Chemistry of the Solid-Water Interface Processes at the Mineral-Water and Particle-Water Interface in Natural Systems. John Wiley and Sons Inc. printed in USA.
- Su, B. (1997). *Novel Fabrication Processing For Improved Lead Zirconate Titanate (PZT) Ferroelectric Ceramic Materials*. PhD Thesis. Faculty of Engineering, University of Birmingham. UK.
- Su, B., Pearce, D.H., & Button, T.W. (2001). Routes to Net Shape Electroceramic Devices and Thick Films. *Journal of the European Ceramic Society*. 21, (10), 2005–2009.
- Swartz, S. L. (1982). Fabrication of Perovskite Lead Magnesium Niobate. *Material Res. Bull.*, 17,1245-50.
- Sze, S. M. (1981). *Physics of Semiconductor Devices*. John Wiley & Sons Inc. New York.
- Tadros, T.F. (1986). Control of the Properties of Suspensions. *Colloid and Surfaces* 18, 137-173.
- Tombak, A., et al. (2003). Voltage-Controlled RF Filters Employing Thin-Film Barium–Strontium–Titanate Tunable Capacitors. *IEEE Transactions on Microwave Theory and Techniques*, 51(2).

- Tsao, B. H., Heidger, S., & Weimer, J.A. (2000). Sputtered barium titanate and barium strontium titanate films for capacitor applications. *Applications of Ferroelectrics, 2000. ISAF Proceedings of the 2000 12th IEEE International Symposium on, 2000, 2*, 837-840.
- Uchino K., & Hirose, S. (2001). *IEEE Transactions on Ultrasonics Ferroelectrics and Frequency Control* 48, 307-321.
- Ulrich, R., & Schaper, L. (2003). Putting Passives in Their Place. *IEEE Spectrum*, 40(7), 26-30.
- Valasek, J. (1921). *Physical Review* 17, 475-481.
- Van der Bijl, H. J. (1919). Theory and Operating Characteristics of the Thermionic Amplifier. *Proceedings of the IRE (Institute of Radio Engineers)* 7, 97–126. doi:10.1109/JRPROC.1919.217425.
<http://books.google.com/?id=p14AAAAAMAAJ&pg=PA105&dq=current-voltage-characteristic>.
- Vincent, B. (1974). The Effect of Adsorbed Polymers on Dispersion Stability. *Advances in Colloid and Interface Science*. Vol. 4, p. 193-277.
- Vincent, B., Edwards, J., Emmett, S. & Jones, A. (1986). Depletion Flocculation in Dispersions of Sterically Stabilized Particles. *Colloids and Surfaces*, 18, 261-81.
- WEB_1 Hielscher Ultrasonics GmbH, web site, (1999).
<http://www.hielscher.com/ultrasonics/disperse.htm>.
- WEB_2 PerkinElmer Inc. 1998-2011
http://las.perkinelmer.com/content/TechnicalInfo/TCH_FTIRATR.pdf

- WEB_3 Wikimedia Foundation, Inc., (13.06.2010). RC circuit, 13.06.2010
http://en.wikipedia.org/wiki/RC_circuit.
- WEB_4 Wikimedia Foundation, Inc. (04.07.2009). Rare Earth Elements, 04.07.2009,
http://en.wikipedia.org/wiki/Rare_earth_element.
- Wilson, A. H. (1931). *A-Containing Papers of a Mathematical and Physical Character*. Proceedings of the Royal Society of London Series 133, 458-491
- Wu, C. T., & Lu, F. H. (2001). Electrochemical deposition of barium titanate films using a wide electrolytic voltage range. *Thin Solid Films*, 398, 621-625.
- Yang, G. Y., Dickey, E. C., Randall, C. A., Barber, D. E., Pinceloup, P., Henderson, M. A., et.al. (2004). Oxygen nonstoichiometry and dielectric evolution of BaTiO₃. Part I-improvement of insulation resistance with reoxidation. *Journal of Applied Physics* 96, 7492-7499.
- Yokota, K., et al. (1998). Preparation of titanium-oxide films by solid-state reactions of titanium/silicon-oxide/silicon structures. *Thin Solid Films*, 334(1-2), 109-112.
- Yoshioka, K., Sakai, E., Daimon, M., & Kitahara, A. (1997). Role of Steric Hindrance in the Performance of Superplasticizers for Concrete. *Journal of the American Ceramic Society*, 80(10), 2667-71.
- Zhong, N., Xiang, P. H., Sun, D.Z., & Dong, X.I. (2005). Effect of rare earth additives on the microstructure and dielectric properties of 0.67Pb(Mg_{1/3}Nb_{2/3})O₃–0.33PbTiO₃ ceramics. *Material. Science Eng. B*. 116, 140-145.